2008

Design and field testing of tapered H-shaped Ultra High Performance Concrete piles

Thomas L. Vande Voort
Iowa State University

Design and field testing of tapered H-shaped Ultra High Performance Concrete piles

by

Thomas L. Vande Voort

A thesis submitted to the graduate faculty

in partial fulfillment of the requirements for the degree of

MASTER OF SCIENCE

Major: Civil Engineering (Structural Engineering)

Program of Study Committee:
Sri Sritharan, Co-major Professor
Muhannad Suleiman, Co-major Professor
Lester Schmerr

Iowa State University

Ames, Iowa

2008

TABLE OF CONTENTS

LIST OF FIGURES

LIST OF TABLES

CHAPTER 1: OVERVIEW

1.1. INTRODUCTION TO UHPC AND AASHTO STRATEGIC PLAN

Ultra High Performance Concrete (UHPC) is defined worldwide as concrete with a compressive strength of at least 22 ksi (150 MPa) (Schmidt and Fehling 2005). Recently, Lafarge North America has marketed Ductal®, a UHPC in the form of reactive powder concrete (RPC), which regularly achieves compressive strengths of 26 to 30 ksi (179 to 207 MPa). UHPC can achieve such high strengths because the mixture is designed to eliminate some of the characteristic weaknesses of normal concrete. The use of powder components helps to achieve this goal and also dramatically increases durability compared to normal concrete. A steam heat treatment is usually used with UHPC to improve its strength and durability properties even further. UHPC incorporates steel fibers to improve the material's ductility and tension capacity.

In 2005, the American Association of State Highway Transportation Officials (AASHTO), in their Strategic Plan for Bridge Engineering, identified extending service life and optimizing structural systems as two of the grand challenges in bridge engineering (AASHTO 2005). The strategic plan identified foundations as one important area of research for extending bridge service life. Optimization of geotechnical systems and materials was highlighted as an important area of research for optimizing structural systems. The objective of optimizing structural systems, according to the AASHTO plan is "to understand the advantages and limitations of traditional, newer and emerging materials…and to develop structural systems (optimized materials, details, components, structures and foundations) for bridges and highway structures…to assure a safe, minimum 75-year service life requiring minimal maintenance."

To optimize structural systems, the AASHTO strategic plan also puts a heavy emphasis on the potential for high performance materials, like UHPC, to achieve long-term cost savings, especially in maintenance costs, which are absorbing an increasing share of the funding for bridges. The high cost of the steel fibers in UHPC make the material expensive,

as discussed in detail in Section 2.5.5, so UHPC applications must be optimized to take full advantage of the superior properties of the material and thus reduce section sizes.

The AASHTO strategic plan for bridge engineering mentions UHPC specifically as an emerging high performance material. The plan notes that UHPC may soon be ready for widespread use, but research is needed to develop efficient designs, standards, and details. UHPC has been used for many applications, especially bridge girders and decks, but it has never been used or studied for foundation applications for bridges or other structures. The high strength properties of UHPC suggest that UHPC piles with a reduced section size could be developed with the same axial and bending capacity as some types of conventional piles. The excellent durability of UHPC also promises to reduce or eliminate much of the deterioration that conventional steel and concrete piles experience in bridge foundations. For these reasons, the research team has examined the development and testing of a UHPC pile.

1.2. LIMITATIONS ON CURRENT CONCRETE PILING

Several types of piling are used commonly in bridge applications in the United States. Some small bridges employ timber piles, but more commonly concrete, steel, or composite piles are used. Steel piles are usually either H-piles or pipe piles. Precast concrete piles may be prestressed and are driven into the ground in a similar fashion to steel piles. Cast-in-place concrete piles may also be used. They are formed by placing a reinforcing cage in a drilled hole and filling the hole with concrete. Sometimes cast-in-place piles also employ a pedestal or bulb, an expanded section at the pile tip. Composite piles may be created by filling driven steel pipe piles with concrete or by using plastic or fiber-reinforced polymer (FRP) materials in conjunction with steel or concrete, as described in Section 1.2.3.

Since steel H-piles and precast, prestressed concrete piles are the most common pile types in bridge foundations, the UHPC pile will primarily be compared to these two pile types. Both of these types of piles have certain limitations, especially related to durability and driveability, which are described in the following sections. A brief comparison between composite piles and UHPC piles is also presented.

1.2.1. Precast, Prestressed Concrete Piles

Concrete piles are susceptible to cracking during driving due to tension forces that may develop as the pile is driven into the ground. Figure 1.1 shows a prestressed concrete pile that has cracked due to excessive tension stresses during driving. High amounts of prestressing can be included in precast piles to reduce cracking risks, but large numbers of prestressing strands increase construction difficulties in pile end regions. Additionally, concrete piles sometimes break during driving due to excessive compression stresses in hard soil. Figure 1.2 shows precast concrete piles that were damaged due to high compressive stresses in hard driving. Occasionally, if proper driveability analysis is not conducted, a concrete pile can fail due to compressive stresses from an excessively large driving hammer. Figure 1.3 shows damage to the top of a normal concrete pile from driving with an unsuitably large hammer (Salgado 2006). Precast concrete piles are also susceptible to damage during handling. Jerky movements or improper lifting procedures can crack or even break precast concrete piles (Richardson 1986).

Figure 1.1. Precast, prestressed concrete pile cracked during driving (RTA NSW 2005)

Figure 1.2. Precast, prestressed concrete piles damaged during hard driving (DiMillio 1998)

Figure 1.3. Damage to the tops of driven concrete piles due to unsuitable driving hammer size (Salgado 2006)

Concrete cover on pile reinforcement can be critical in severe environments. Cracks and capillary pores allow corrosive compounds to penetrate the concrete and corrode steel reinforcement. The reinforcement expands as it corrodes, leading to eventual spalling and deterioration of the concrete pile, which can significantly lower the axial and bending capacity of the pile to resist structural loads. Corrosion the reinforcement of a marine pile and spalling of the pile's cover concrete are shown in Figure 1.4. Marine piles are often subject to the most severe corrosion due to the presence of high amounts of chlorides or other water-born contaminants in saltwater. De-icing salts can also cause severe corrosion of reinforcement in many piles in non-marine environments.

Figure 1.4. Prestressed concrete marine pile with spalling and reinforcement corrosion in a marine environment (Port Strategy 2007)

Arsoy et al. (2002) conducted cyclic lateral tests on precast, prestressed piles to simulate the cyclic temperature loading of bridge piles in integral abutments during a 75 year service life, which is the design life recommended by AASHTO (2004). They found that precast, prestressed piles may crack and suffer progressive cracking damage and loss of section under cyclic loading. Thus even service flexural stresses can lead to significant concrete pile deterioration over a bridge's lifetime.

1.2.2. Steel H-Piles

The thin flanges and webs of steel H-piles make these pile sections vulnerable to local buckling during hard driving conditions.

Figure 1.5 shows some steel piles that were badly damaged during hard driving. Figure 1.6 shows the lower portion of a steel H-pile driven into a permafrost soil in Alaska, United States, with an impact hammer (Huck and Hull 1971). Selecting an inappropriate hammer also can lead to damage of steel piles, as shown in Figure 1.7.

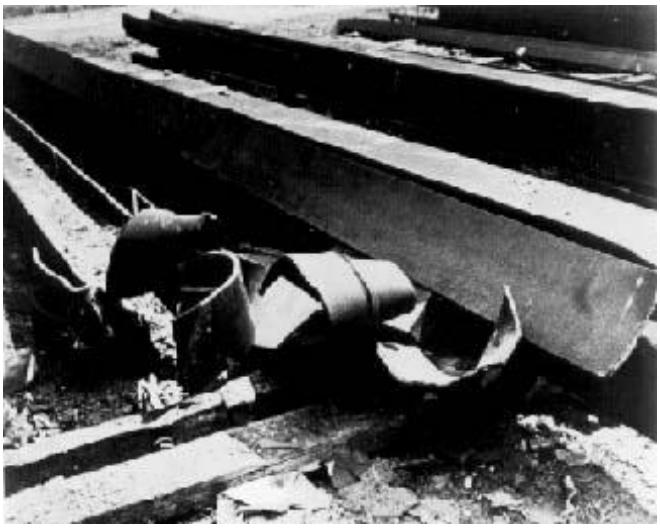

Figure 1.5. Steel piles heavily damaged due to hard driving (DiMillio 1998)

Figure 1.6. Lower portion of steel H-pile driven into Alaskan permafrost with an impact hammer (Huck and Hull 1971)

Figure 1.7. Damage to steel piles due to excessive driving hammer size (Salgado 2006)

Unprotected steel piles are subject to even greater corrosion than concrete piles from chloride attack in environments with saltwater or de-icing salts. Figure 1.8 shows some steel piles with total section loss due to corrosion. Protection measures can be used to attempt to

prevent steel pile corrosion. Typically, no protection measures are used for portions of piles that remain permanently buried in undisturbed soil (Cornfield 1980). Portions of piles continually immersed in water or subject to splashing are usually protected with a protective coating or by providing an increased thickness of steel, such as through steel plates welded to the pile flanges and/or web of the steel pile. One typical protective coating used by the state of Florida consists of an inorganic zinc primer followed by two coats of coal tar-epoxy on all exposed surface of the pile (FDOT 2008). Both of these corrosion prevention measured must be applied before the piles are installed, especially for continually immersed pile segments. Portions of piles exposed to air are sometimes coated with paint to prevent atmospheric corrosion (Cornfield 1980). Each of these corrosion prevention measures can be costly, may be damaged during handling and driving, and may only last up to 30 years themselves (FDOT 2008; Morley 1979). In fact, Morley estimates that protective coatings may only extend overall pile life by five to 15 years.

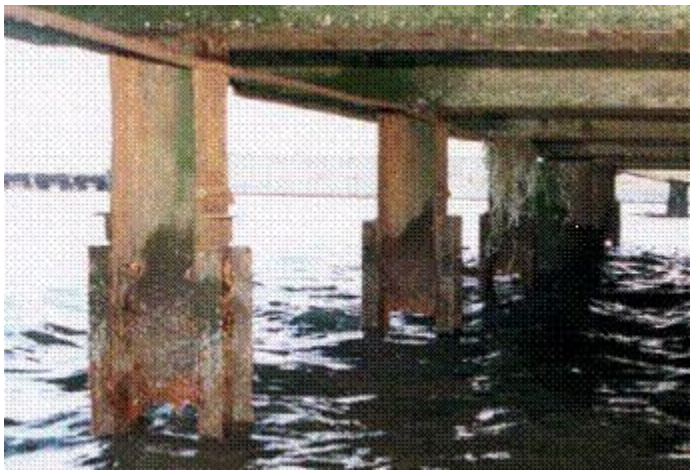

Figure 1.8. Corroded steel piles with loss of section in a marine environment (Juran and Komornik 2006)

Steel piles can also experience significant corrosion in applications supporting integral bridge abutments, such as the deterioration of the pile shown in Figure 1.9 (White et al. 2007). As the bridge experiences temperature changes, piles supporting the integral abutments move laterally, pushing soil laterally as they move. Gaps thus sometimes form under the integral abutments as soil moves laterally, and these gaps may alternately be filled

with air and water, leading to deterioration in the pile near the connection with the abutment. Unfortunately, this loss of section due to corrosion is often very near the location of the maximum moment demand in the steel piles.

Figure 1.9. Corroded H-pile supporting integral abutment (White et al. 2007)

Corrosion of steel piles can have a significant effect on bridge life. Typical corrosion rates for steel piles in are shown in Table 1.1. Using the values shown in Table 1.1, over a 75-year design life, the section area of an HP 10×57 pile, for example, would be reduced by 32 percent under the maximum corrosion rate when buried in undisturbed soil or by 84 percent under the maximum corrosion rate when buried in a disturbed soil, or fill. The pile at the freshwater splash zone would theoretically corrode away completely after 48 years under the average corrosion rate.

Table 1.1. Corrosion rates for steel piles

Pile zone	Average Corrosion Rate in./yr (mm/yr)	Maximum Corrosion Rate in./yr (mm/yr)	Sources
Buried in undisturbed soil	0.0004 (0.01)	0.001 (0.03)	(Morley 1979)
Buried in disturbed soil	—	0.003 (0.08)	(Romanoff 1962)
Submerged in freshwater	0.002 (0.05)	0.003 (0.08)	(Morley and Bruce 1983; Cornfield 1980)
Splash zone in freshwater	0.006 (0.15)	0.013 (0.34)	(Cornfield 1980; Morley and Bruce 1983)

Increased foreign demand for steel has also increased the cost and lead-time required for steel piling. Structural steel prices have risen by more than 125 percent in the period between the beginning of 2004 and the end of 2007 (Grogan 2007). Representatives in the steel industry point out that the lead-times for structural steel are still reasonably short, but since mills are no longer stockpiling steel, projects that use structural steel must be more carefully scheduling (Pinkham 2006).

1.2.3. Composite Piling

Recognizing the problems with traditional steel and concrete piling, particularly those associated with pile deterioration, the FHWA sponsored research by Pando et al. (2006) that examined composite piling as an alternative to traditional types of piling. Composite piles contain materials like plastic or FRP to create durable outer or inner shells on traditional concrete or steel piles or use plastic or FRP instead of concrete and steel entirely. Pando et al. also noted that traditional piles have a limited service life and high maintenance costs when used in harsh marine environments – characteristics that are not consistent with the AASHTO strategic plan. They estimated that costs for repair and replacement of all types of piling systems in the United States are more than $1 billion annually.

Pando et al. (2006) noted that the higher cost of composite piles compared to traditional piles is expected to decrease as composite piles begin to see wider application. They also acknowledged that labor and equipment costs may be lower for composite piles as well, due to their relatively light weight. Finally, they expected composite piles would be economically competitive with traditional piles in some applications when the entire life cycle cost of each alternative is considered. Each of these assumptions could also be made for UHPC piles. Cost reductions are expected as UHPC sees wider application. Equipment and labor costs are lower due to the smaller and lighter sections possible with UHPC. Finally, UHPC boasts a longer service life than normal concrete or steel and reduced maintenance costs.

Composite piling has its own set of concerns. Driveability may be less efficient with composite piling (Pando et al. 2006). The structural properties of composite piles, particularly the low pile stiffness, could result in large deformations when the piles are

loaded. A composite pile composed of recycled plastic and FRP reinforcing, for example, had an elastic modulus of only 490 ksi (3.4 GPa) in material tests by Juran and Komornik (2006). Composite piles also may have reduced surface friction when composite materials are used on the exterior of the pile, as is usually the case (Pando et al. 2006). UHPC avoids many of these concerns. Driveability analysis shown later in this paper confirms that UHPC may be driven with as much or greater ease than normal concrete piles or even steel piles in some situations. UHPC piles have excellent lateral and axial stiffness due to their high elastic modulus of approximately 8000 ksi (55 GPa), even when reduced sections are used (Sritharan et al. 2003). UHPC can also be cast with a variety of surface finishes, and simple casting in wood forms gives UHPC a finish with comparable friction capacity to normal concrete or steel.

1.3. INTRODUCTION TO BENEFITS OF UHPC RELATED TO PILING

This section provides a brief summary of some of the properties of UHPC that make it especially promising for piling applications. For more information on the composition, properties, and application of UHPC, see Chapter 2: Literature Review.

1.3.1. Strength

The 26 ksi (179 MPa) compressive strength of UHPC is approximately five times that of the normal concrete typically used for pile applications. The tensile strength of 1.7 ksi (12 MPa) is also improved over that of normal concrete (Graybeal 2006). The reserve compressive strength, however, makes UHPC an ideal material for prestressing in order to increase tensile and bending capacities. Another advantage for the use of UHPC in precast applications is that no shrinkage occurs after the steam heat treatment used for the material. The modulus of UHPC is also high, as noted above, with a typical value of approximately 8000 ksi (55 GPa).

1.3.2. Handling and Driveability

Since UHPC has greatly improved material strength, sections can be designed with greatly reduced cross-sectional area without compromising pile strength. These reduced

sections are then lighter and easier to handle and transport than traditional concrete piles. In fact, the pile section designed for this project has a weight approximately equal to a similarly sized steel pile. The reduced section allows the UHPC pile to be driven into the ground with more ease than a normal concrete pile, and the high material strengths effectively prevent driving damage.

1.3.3. Durability

UHPC has extremely good durability. The capillary porosity is very low, and the material is extremely resistant to chloride permeability. UHPC experiences virtually no freeze-thaw deterioration even after 800 freeze-thaw cycles (Gao et al. 2006). These properties allow the required concrete cover thickness for steel reinforcement to be reduced and thus permit an even further reduction in section sizes for some applications. The excellent durability properties also suggest that UHPC piles may reduce maintenance costs and help extend the lives of some bridges, particularly those in harsh environments.

1.4. SCOPE OF RESEARCH

The objectives of this research project include the following:

- characterize the behavior of UHPC elements (piles) under loading conditions similar to those expected in the field;
- evaluate the behavior of UHPC piles using large-scale tests and analytical procedures; and
- develop a design concept and demonstrate the potential use of UHPC in geotechnical applications.

1.5. REPORT CONTENT

This report consists of six chapters describing the development and testing of the UHPC pile. A summary of the content of each chapter is presented below.

- Chapter 1 – Introduction: A brief introduction to UHPC and its properties and limitations on traditional concrete and steel piling
- Chapter 2 – Literature Review: A review of published studies describing the composition, microstructure, durability, material properties, and applications of UHPC as well as current pile design practice
- Chapter 3 – Section Design: Description of the design process for designing a section for the UHPC pile and results of the analysis of the pile section, including moment-curvature, interaction diagram, and driveability study
- Chapter 4 – Pile and Test Piece Production: Details of the casting of the UHPC piles and test pieces, including instrumentation and hardened mix properties
- Chapter 5 – Field Testing: Description of the driving of UHPC and steel piles at a bridge site in central Iowa and of the vertical and lateral load tests on UHPC piles and vertical load test on a steel pile as well as test results
- Chapter 6 – Conclusions: Summary of results on UHPC found from casting and load testing and description of future research potential

CHAPTER 2: LITERATURE REVIEW

2.1. 1. HISTORY AND BACKGROUND

2.1.1. Concrete Strength Development

The advent of Ultra High Strength and Ultra High Performance Concrete (UHPC) is a relatively recent development in concrete technology. Figure 2.1 shows that during the advances in the 150 year history of concrete, the strength of concrete commonly used in structural applications has often lagged behind the threshold strengths achieved through material development (Tang 2004). This trend is suspected to be due to an increase in material cost accompanying increases in strength and to a general reluctance to use new materials in practical applications. To reduce the gap between material development and application of new materials in routine design, researchers must optimize the use of UHPC in structural design to take advantage of the incredible increase in strength and other material properties. Then the use of UHPC and other high performance materials can become more common in structural applications.

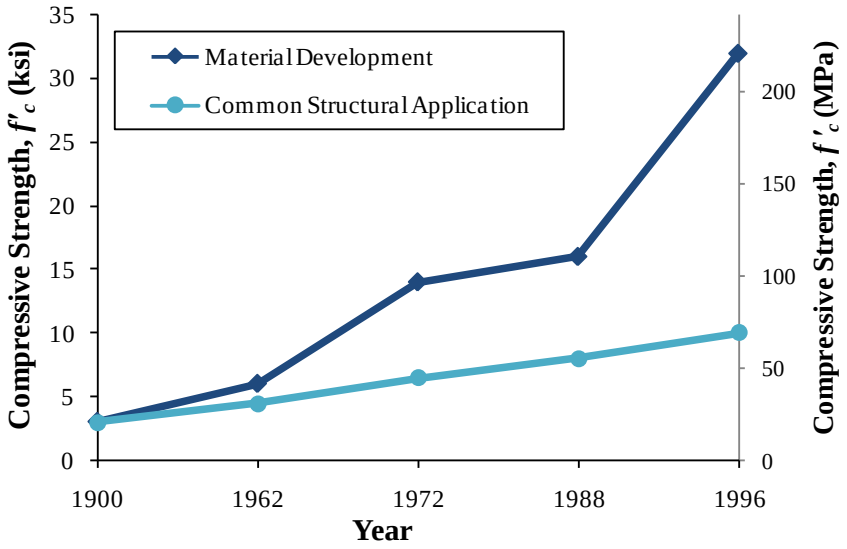

Figure 2.1. Concrete strength development over 100 years (after Spasojevic 2006)

Since durability is significantly improved compared to normal concrete and characteristic weaknesses of concrete are eliminated, the only limiting factor in the application of UHPC is the cost. Optimization is therefore required to see UHPC achieve more common use in structural applications, and optimization can only be accomplished by thoroughly understanding the material behavior and its engineering properties and by adapting to newer, more efficient cross-sectional shapes.

2.1.2. Development of UHPC

UHPC represents a significant departure from the design premise of High Performance Concrete (HPC) mixes. UHPC is the result of the "minimum defect" concept – creating a material with a minimum amount of defects, such as micro-cracks and interconnected pore spaces in order to more closely approach the potential ultimate strength of the components and enhance durability.

Two lines of research have been pursued in developing minimum defect materials, macro-defect free (MDF) and densified small particle or densified system with ultra fine particles (DSP) concretes (Rossi 2005). The MDF approach uses polymers to fill in pores in the concrete matrix. This process requires very demanding manufacturing conditions, including laminating the material by passing it through rollers. MDF concretes, which can have tensile strengths up to 22 ksi (150 MPa), require pressing, are susceptible to water, have a large amount of creep, and are very fragile. DSP concretes contain high amounts of superplasticizer and silica fume. DSP concretes must either use extremely hard coarse aggregates or eliminate them entirely to prevent the aggregates from being the weakest component of the mix. DSP concretes do not require the extreme manufacturing conditions that MDF concretes do, but DSP concretes have a much lower tensile strength and, like MDF concretes, are very brittle. The addition of steel fibers was considered to improve the ductility of each concrete type, but MDF concretes become too viscous and unworkable with the addition of fibers. Therefore DSP concrete was supplemented with fibers, resulting in UHPC.

2.1.3. Types of UHPC

Several types of UHPC have been developed in different countries and by different manufacturers. The main difference between the types of UHPC is the type and amount of fibers used. The four main types of UHPC are Ceracem/BSI, compact reinforced composites (CRC), multi-scale cement composite (MSCC), and reactive powder concrete (RPC). A brief summary of the differences between these types of UHPC is given here.

Ceracem/BSI includes coarse aggregates, which are eliminated in the other types of UHPC (Jungwirth and Muttoni 2004). CRC and MSCC both use high amounts of fiber and use different fiber sizes than those used in RPC (Rossi 2005). RPC's steel fibers occupy two percent of the concrete mixture by volume. RPC has become one of the leading types of UHPC, and one such product is marketed under the name Ductal® by the French companies Lafarge, Bouygues, and Rhodia.

Since RPC is the most commonly available types of UHPC and was used for the laboratory and field experiments in the current study, the term "UHPC" refers exclusively to RPC for the remainder of this paper unless otherwise indicated. Also note that "heat treated" UHPC refers to the standard heat treatment at 194°F (90°C) for 48 hours unless otherwise indicated. In this paper, the properties of a UHPC mix may be assumed to be characteristic of UHPC regardless of fiber content or curing process if such information is not noted.

2.1.4. UHPC Strength Principles

At this point it is useful to take a brief look at how UHPC is able to attain such high strength. Pierre-Claude Aïtcin (2000) described the situation as follows:

> "We know how to make 150 MPa [21.8 ksi] concrete on an industrial basis. Because at such a level of strength it is the coarse aggregate which becomes the weakest link in concrete, it is only necessary to take out coarse aggregate, to be able to increase concrete compressive strength and make reactive powder concrete having a compressive strength of 200 MPa [29.0 ksi]; it is only necessary to confine this reactive powder concrete in thin-walled stainless steel tubes to see the compressive strength increased to 375 MPa [54.4 ksi]; and when the sand is replaced by a metallic powder, the compressive strength of concrete increases to 800 MPa [116.0 ksi]."

This statement not only gives an idea of the potential strength of UHPC, but also reveals that typical HPC mixes are prevented from reaching higher strengths due to defects caused by the coarse aggregates.

Normal concrete and HPC both suffer from a mismatch in the properties of their constituent materials; namely, the aggregate and cement paste have significantly different elastic moduli. The mismatch in elastic moduli is eliminated in UPHC by selecting constituent materials with similar elastic moduli (Gao et al. 2006). A weak transition zone also exists in the interface between the aggregate and paste in normal concrete and HPC (Dowd and Dauriac 1996). Figure 2.2 shows a representation of the force transfer through normal concrete compared to UHPC. The aggregates in normal concrete become inclusions that form a rigid skeleton. When a compressive force is applied, shear and tensile stresses develop at the interfaces between the aggregates, forming small cracks approximately proportional in size to the maximum aggregate diameter. In UHPC, however, the aggregates are a set of inclusions in a continuous matrix, and the aggregate diameters are much smaller. Thus the compressive force can be transmitted by the matrix instead of by a rigid skeleton of aggregates, which reduces the stresses that develop at the paste-aggregate interface. The transmittal of stresses by both the aggregates and the surrounding matrix in UHPC leads to a much more uniform stress distribution, which can reduce potential for shear and tensile cracking at the interface (Richard and Cheyrezy 1995).

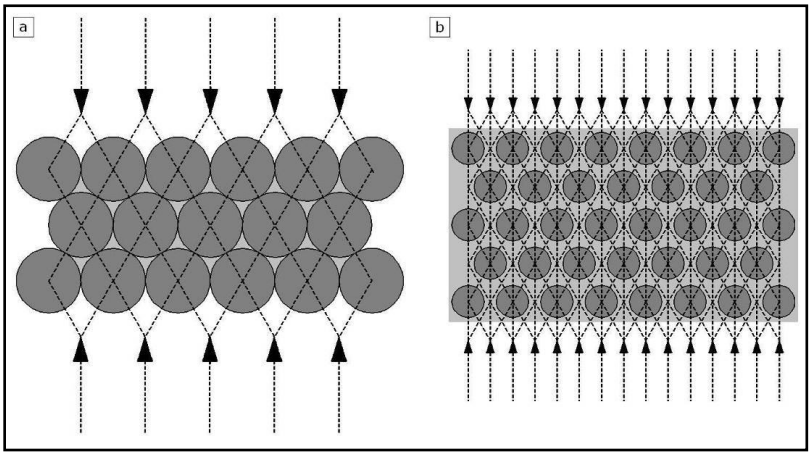

Figure 2.2. Depiction of force transfer through a) normal concrete and b) UHPC (after Walraven 2002)

In normal concrete, the rigid skeleton also prevents some paste shrinkage, resulting in increased porosity. In UHPC aggregates do not block paste shrinkage to a great extent, since the aggregate particles are free to move in the paste with respect to each other (Richard and Cheyrezy 1995). According to the maximum paste thickness theory, however, completely eliminating both the fine and coarse aggregates is not entirely beneficial. Aggregates have a confining effect on cement paste. When the paste thickness between aggregates becomes large, the compressive strength of the material actually decreases (de Larrard and Sedran 1994). Thus, fine aggregate is retained in UHPC to maintain the highest possible compressive strength.

Several authors have identified some of the basic principles used in UHPC (e.g. Ma and Schneider 2002; Richard and Cheyrezy 1995), which can be summarized as follows:

- enhancement of homogeneity by elimination of coarse aggregate;
- enhancement of the packing density by optimization of the granular mixture through a wide distribution of powder size classes;
- improvement of the properties of the matrix by the addition of a pozzolanic admixture, such as silica fume;
- improvement of the matrix properties by reducing water/binder ratio;
- enhancement of the microstructure by post-set heat-treatment; and
- enhancement of ductility by including small steel fibers.

Application of the first five principles without the sixth leads to a concrete with a very high compressive strength without any improvement in ductility. The addition of the steel fibers noted in the last principle helps to improve both tensile strength and ductility (Richard and Cheyrezy 1995).

2.2. MATERIAL AND MICROSTRUCTURE

2.2.1. Typical UHPC Mix

Polystructural theory holds that the overall properties of a material are a function of both macro-level properties (of the overall behavior of the cement and aggregate) and micro-

level properties (of the particles of the modified cement paste with its admixtures) (Sobolev 2004). Thus it is useful to examine the different components of a typical UHPC mix, as well as the microstructural properties of the mix. A typical UHPC mix contains sand, cement, silica fume, crushed quartz, fibers, superplasticizer, and water in the ranges shown in Table 2.1. Table 2.2 shows a typical UHPC mix with the mix components reported in terms of weight per unit volume, mass ratio relative to cement, and volume fraction, which is expressed as a percentage of the total volume.

Table 2.1. Range of UHPC mix components

Component	Typical Range of Weight (Mass) per ft^3 (m^3)
Sand	31 – 87 lb (490 – 1390 kg)
Cement	38 – 67 lb (610 – 1080 kg)
Silica Fume	3.1 – 21 lb (50 – 334 kg)
Crushed Quartz	0 – 26 lb (0 – 410 kg)
Fibers	2.5 – 15.5 lb (40 – 250 kg)
Superplasticizer*	0.6 – 4.5 lb (9 – 71 kg)
Water	7.9 – 16.3 lb (126 – 261 kg)

*Superplasticizer is expressed as the weight of the solid fraction; the liquid fraction is included in the water weight.
(Compiled based on data provided by Dugat et al. 1996, Castellote et al. 2003, Droll 2004, de Larrard and Sedran 1994, Lee et al. 2005, Blais and Couture 1999, Huh and Byun 2005, Xing et al. 2006, Voo et al. 2001)

Table 2.2. Typical UHPC mix components (Cheyrezy and Behloul 2001)

Component	Weight per Cubic Foot (Meter)	Mass Ratio /Cement	Volume Fraction
Sand	61.9 lb (991 kg)	1.430	38.8%
Cement	42.3 lb (693 kg)	1.000	22.7%
Silica Fume	14.0 lb (225 kg)	0.325	10.6%
Crushed Quartz/Fly Ash	13.0 lb (208 kg)	0.300	8.1%
Fibers	9.4 lb (151 kg)	0.218	2.0%
Superplasticizer*	0.90 (14.4 kg)	0.021	1.4%
Water	9.9 (159 kg)	0.229	16.5%

*Superplasticizer is expressed as the weight of the solid fraction; the liquid fraction is included in the water weight.

The selection of the components of UHPC uses the packing density optimization principle. The mix is also proportioned in such a way that the fine aggregates will be a set of movable inclusions in the matrix, rather than a rigid skeleton. Use of smaller particles only to

fill the voids between sand particles would lead to packing optimization, but a rigid skeleton of sand particles would still remain. Figure 2.3 shows the differences between this so-called Apollonian packing (Figure 2.3a) and the "spacing packing" which UHPC uses (Figure 2.3b). In spacing packing, the particle size distribution is chosen such that there is a wide distribution in granular class sizes, and each particle is surrounded by more than one layer of the next smaller particle size. For example, each sand particle would be surrounded by at least two layers of cement particles; each cement particle would be surrounded at least two layers of silica fume particles, etc.

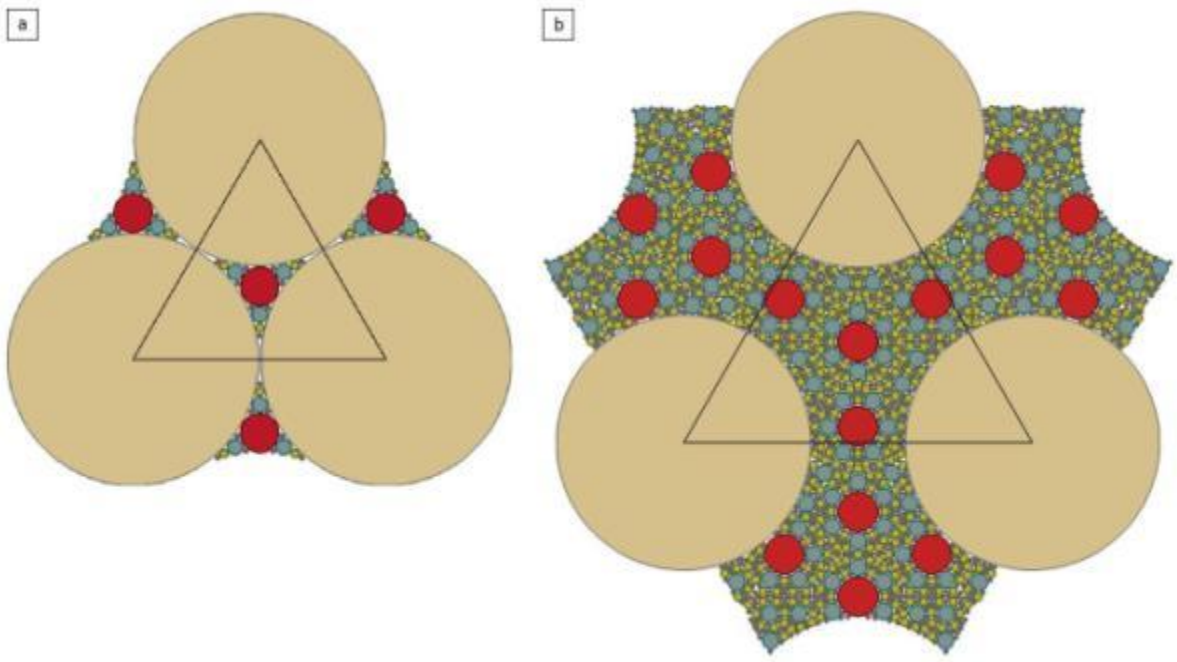

Figure 2.3. Diagrams illustrating a) Appollonian packing and b) spacing packing (after Vernet 2004)

Richard and Cheyrezy (1995) found that maintaining a minimum ratio between the mean diameters of two consecutive granular class sizes of 13 gives the desired spacing packing. In other words a fine aggregate with a mean diameter at least 13 times as large as cement and a silica fume with a mean diameter at least 13 times as small as cement are chosen for the mix. Table 2.3 shows the mean diameters and diameter ranges for the solid particles in the mix.

Table 2.3. Granular class mean diameters and diameter ranges for UHPC mixes (Richard and Cheyrezy 1995, Sobolev 2004, Chan and Chu 2004)

Component	Ratio to Previous Size Class	Mean Diameter	Typical Diameter Range
Steel Fibers*	---	0.50 in (12,700 mm)	-----
Sand	51:1	0.0098 in (250 μm)	0.0059 – 0.0236 in (150 – 600 μm)
Cement	19:1	0.00051 in (13 μm)	< 0.0039 in (< 100 μm)
Crushed Quartz (same class as cement)	1.3:1	0.00039 in (10 μm)	0.00020 – 0.00079 in (5 – 20 μm)
Silica Fume	67:1	0.000006 in (0.15 μm)	0.000004 – 0.000008 in (0.10 – 0.20 μm)

*Note: Steel fiber mean diameter represents the largest dimension of fiber (length); the fiber diameter is 0.006 in. (0.15 mm)

The wide distribution of granular classes helps to not only maximize density and create a more uniform stress distribution when the matrix is loaded but also contributes to the flowability of the mixture. The smaller grains serve as a lubricant, allowing sand particles of the same size to move past each other with minimal interference. Usually, UHPC mixes can be made to be self-compacting, requiring no vibration to place (Walraven 2002). In normal fiber-reinforced concrete (FRC), the coarse aggregate sizes are approximately the same as the fiber lengths, creating interferences between the fibers and aggregates that drastically decrease workability. In UHPC, however, even the largest sand particles are over 20 times smaller than the fiber length, so no such interference occurs. Indeed, the addition of fibers has little effect on workability unless very high fiber volumes are used (Bonneau et al. 1997).

2.2.2. UHPC Components

The following sections present a more detailed description of the role of each component in the UHPC mix.

2.2.2.1 Sand

Sand plays the role of confining the cement matrix to add strength, as noted previously. A variety of quartz sand is usually used, which is not chemically active in the cement hydration reaction at room temperature (Porteneuve et al. 2002).

2.2.2.2 Cement

A typical Portland Cement or other similar cement can be used in UHPC. The only suggestion by Aïtcin (2000) is that the cement used should be coarse cement not rich in C_3S and C_3A. Low shrinkage cements may also be preferred since the high cement content of UHPC can make it more susceptible to high shrinkage.

Interestingly, not all of the cement in the UHPC matrix becomes hydrate due to the low water content of the mix. While the hydrated cement acts as a bonding agent, the unhydrated cement grains can act as high elastic modulus (17,400 ksi or 120 GPa) reinforcing in the matrix (Vernet 2004).

2.2.2.3 Crushed Quartz

Since not all of the cement is hydrated, some of it can be replaced by crushed quartz powder. Experiments by Ma and Schneider (2002) showed that up to 30 percent of the volume of cement can be replaced by crushed quartz with no reduction in compressive strength. Besides reducing the cement requirement, crushed quartz also improves the flowability of a UHPC mix. The improved flow characteristics may be due to a filling effect since the crushed quartz particles are slightly smaller than the cement particles. The explanation for the increased flowability with crushed quartz may also be that fewer cement binding products are produced in the first few minutes of the mixing.

2.2.2.4 Fly Ash or Blast Furnace Slag

Using fly ash or blast furnace slag is an alternative to using crushed quartz for cement replacement. Fly ash also has the lubricating effect (similar to crushed quartz powder), helping make UHPC mixes self-compacting (Walraven 2002). In addition, fly ash may have to be used instead of crushed quartz where the small diameter quartz particles cause respiratory health concerns. Fly ash is readily available from waste products of the coal power industry (Schmidt et al. 2003).

Ground granulated blast furnace slag has also been used to replace cement. Soutsos et al. (2005) found up to 36 percent of the cement could be replaced by blast furnace slag without sacrificing compressive strength or setting time. Yazici (2006) also found cement

replacement of up to 40 percent with either fly ash or blast furnace slag had no detrimental effects on compressive strength. Blast furnace slag can also be used in conjunction with crushed quartz as a cement replacement (Droll 2004).

2.2.2.5 Silica Fume

Silica fume is composed of very small, glassy silica particles which are perfectly spherical. Silica fume has three main functions in UHPC:

- filling the voids in the next larger granular class (cement);
- enhancing lubrication of the mix due to the perfect sphericity of the basic particles; and
- production of secondary hydrates by pozzolanic reaction with the products from primary hydration (Richard and Cheyrezy 1995).

The pozzolanic reaction is the reaction of silica hydrates with $Ca(OH)_2$ (portlandite) produced by the hydration of Portland cement (Ma and Schneider 2002). The portlandite is consumed to produce C-S-H hydrates (Cheyrezy et al. 1995). Silica fume content increases the length of C-S-H chains (and thus concrete strength) produced in hydration (Porteneuve et al. 2001).

The amount of silica fume in a mix is typically about 25 percent of the total binder material (Matte and Moranville 1999). The amount of silica fume theoretically required for the reaction with products of cement hydration is 18 percent. The optimal silica fume content increases to about 25 percent to get the densest mixture, and tests reveal the greatest compressive strength could be achieved with 30 percent silica fume (Ma et al. 2003; Ma and Schneider 2002). In tests of UHPC with silica contents from zero to 20 percent, Xing et al. (2006) found that the maximum flexural tensile strength occurred with a silica fume content of 20 percent, and the maximum compressive strength occurred with a silica fume content of 5 percent. Bond strength between the fibers and the matrix of hardened UHPC also appears to be maximized with a silica fume content of 20 to 30 percent (Chan and Chu 2004).

Silica fumes used in UHPC should be pure with low carbon content, since carbon increases the water requirement and decreases flowability (Schmidt et al. 2003). Also, silica

fume slurry cannot be used because the quantity of water in the slurry often exceeds the total water required for the UHPC mix (Richard and Cheyrezy 1995). Zanni et al. (1996) found that silica fume consumption is highly dependent on heat treatment temperature and duration. Heat treatment will be discussed in more detail later in the Literature Review.

2.2.2.6 Fibers

As stated previously, UHPC without fibers is very strong but very brittle. Fibers are included to increase tensile capacity and improve ductility. Studies using different fiber materials, contents, sizes, and shapes have been conducted by various researchers.

The dense structure of UHPC can lead to poor fire performance if certain measures are not taken. As the concrete heats, interior steam pressure may build in the pores and cause sudden collapse of the UHPC since little extra void space for gaseous expansion exists. A 0.6 percent volume of polypropylene fibers can improve the fire properties of the matrix by melting in the heat of a fire. When the fibers melt at 338°F (170°C), extra void space is created to relieve some of the pressure build-up (Schmidt et al. 2003).

Since steel fibers have a small diameter and could puncture human skin, organic fibers are sometimes used in place of steel fibers where people are expected to have contact with UHPC (Klemens 2004). The organic fibers must be used in applications with lower tensile strength or ductility demands since the structural performance of a member with organic fibers will be reduced compared to the performance with steel fibers.

The workability of any concrete mix containing fibers is a function of both the fiber size and the coarse aggregate size in the mix. Since UHPC typically does not contain coarse aggregates, the dimensions of the fibers are the primary influence on the concrete flowability. MSCC, with its multiple fiber sizes, can reach 11 percent steel fibers by volume without becoming unworkable (Rossi 2005). The upper limit for workability for the 0.25-in. (6-mm) long and 0.006-in. (0.15-mm) diameter fibers in CRC is ten percent according to Rossi (2005) or six percent according to Bindiganavile et al. (2002). The longer fibers for RPC, 0.5-in. (13-mm) long and 0.006 in. (0.15 mm) in diameter, have an upper limit of four percent according to Nielsen (1998) or 2.5 percent according to Rossi (2005). Thus, the workability of UHPC mixes clearly decreases with increasing fiber size. Two percent fiber

volume represents the most common content for UHPC (RPC) and corresponds with the most economic content identified by Richard and Cheyrezy (1995). Figure 2.4 shows an x-ray image of a two percent volumetric fraction of steel fibers in a sample of UHPC. This figure shows the dense packing of fibers in UHPC despite the low volumetric fraction.

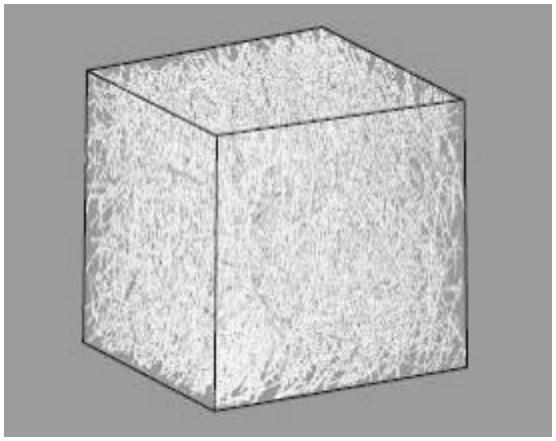

Figure 2.4. X-ray image of fiber distribution in 1.6-in. (40-mm) cube of UHPC (Acker and Behloul 2004)

The behavior of micro-reinforced UHPC with fibers is similar to that of concrete with large-diameter reinforcement. Using 0.5-in. (13-mm) long and 0.006-in. (0.15-mm) diameter fibers with a 0.0098-in. (0.25-mm) average aggregate size is analogous to a 38-in. (0.97-m) long and 0.46-in. (12-mm) diameter reinforcing bar in concrete with 0.75-in. (19-mm) aggregate. Thus, as a reinforcing bar in reinforced concrete carries tension forces across cracks in a concrete member, fibers carry tension forces across micro-cracks in the UHPC.

The orientation of fibers relative to the plane of cracking affects the ductile behavior of UHPC (Bayard and Plé 2003), so care must be taken to properly mix and place UHPC to avoid clustering of fibers and to ensure proper fiber dispersion within each UHPC element.

2.2.2.7 Superplasticizer

Superplasticizers are high-range water reducers composed of powerful organic polymers used to disperse cement particles and silica fume, improving the flowability of UHPC mixes (Aïtcin et al. 2000). Thus, superplasticizers can allow a lower water/cement (w/c) ratio and lower water/binder (w/b) ratio (binder includes both silica fume and cement)

to be used without sacrificing the workability of the mix. Since UHPC uses such low w/c and w/b ratios, the optimum amount of superplasticizer is relatively high, with a solid content of approximately 1.6 percent of the cement content (Richard and Cheyrezy 1995).

2.2.2.8 Water

The water/cement ratio has typically been used as an indicator of concrete strength. Schmidt et al., however, claim that the compressive strength of UHPC cannot be accurately characterized by w/c ratio alone (Schmidt et al. 2003). They note that UHPC can be developed with a w/c ratio as high as 0.40 without a reduction in strength, though porosity may be greatly increased with such a comparatively high w/c ratio. The link between initial porosity and compression strength is also questioned by de Larrard and Sedran (1994), who regard final porosity as a better indicator of strength. Regardless, w/c ratio does affect porosity and have a significant effect on compressive strength, even if it is not the only factor affecting it (Aïtcin et al. 2000).

The goal in a UHPC mix is not to minimize water content, but to maximize relative density. The minimum w/b ratio for a workable mixture is 0.08 (Richard and Cheyrezy 1995). The relative density, however, is not maximized at this w/b ratio, as can be seen in Figure 2.5. As the w/b ratio is increased above the 0.08 minimum, water replaces air without increasing the volume of the mixture up to a w/b ratio of about 0.13. If the w/b ratio is increased beyond this point, additional water increases the volume and thus decreases the density of the mixture. In Figure 2.5, the mixtures represented by the descending branch of the graph have superior performance and workability to those represented by the ascending branch, so the practical optimum w/b ratio used is chosen slightly toward the higher values of w/b ratio to ensure that the w/b ratio of the actual mixture is slightly higher than the theoretical optimum.

Richard and Cheyrezy (1995) thus identified 0.14 as the optimal w/b ratio for UHPC, which agrees exactly with the study by de Larrard and Sedran (1994) using a solid suspension model. Richard and Cheyrezy also agree closely with Gao et al. (2006) and Lee and Chrisholm (2006), who each reported an optimum w/b ratio of 0.15 from experimental test samples. Wen-yu et al. (2004) reported an optimum w/b ratio of 0.16 through their tests.

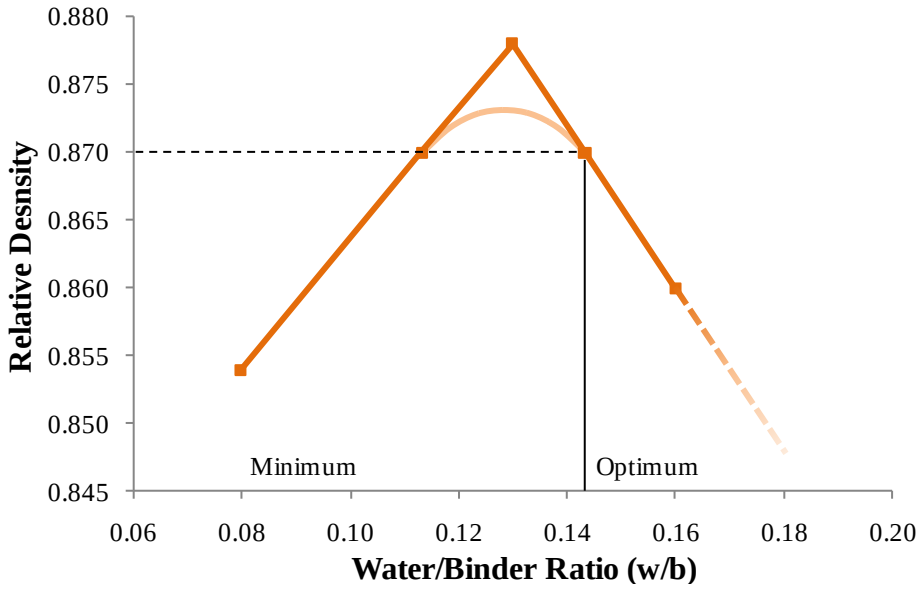

Figure 2.5. Relative density versus water content (after Richard and Cheyrezy 1995)

The research team compiled a total of 68 UHPC mix designs from 59 published sources to determine the range of w/b and w/c ratios. Table 2.4 summarizes the mean and range for the w/c ratios and w/b ratios used in UHPC.

Table 2.4. Low, mean, and high values of w/b and w/c ratio used for UHPC mixes

Mix Property	Low Value	Mean Value	High Value
w/b ratio	0.10 (Voo et al. 2001)	0.17	0.25 (Droll 2004)
w/c ratio	0.13 (Voo et al. 2001)	0.22	0.37 (Soutsos et al. 2005)

2.2.3. Density

Because UHPC has a very compact microstructure, the density is higher than HPC or normal concrete, and the weight per cubic foot is also slightly increased. Table 2.5 shows a comparison among the typical densities of UHPC, HPC, and normal concrete mixes. The density of UHPC is higher than that of normal concrete or HPC, but the slight increase in weight is easily offset by the much higher strength of UHPC. The average reported value for the density of UHPC mixes from 17 published mix descriptions was approximately 157 lb/ft^3 (2510 kg/m^3). A weight density of 155 lb/ft^3 (2480 kg/m^3) was used for design purposes in this study, as suggested by Graybeal (2005).

Table 2.5. Density comparison between UHPC, HPC, and normal concrete

Concrete Type	Typical Density Range
Normal	143 – 150 lb/ft^3 (2290 – 2400 kg/m^3)
HPC	152 – 155 lb/ft^3 (2430 – 2480 kg/m^3)
UHPC	144 – 172 lb/ft^3 (2320 – 2760 kg/m^3)

(Compiled based on data presented by Kosmatka et al. 2002, Ma et al. 2003, Teichmann and Schmidt 2004)

2.2.4. Pressure during Setting

Another way to improve the density of the microstructure of UHPC is to apply a pressure during setting. About 7.3 ksi (50 MPa) of confining pressure is typically used when a pressed UHPC sample is desired. The application of pressure has favorable effects of removing entrapped air and of removing excess water as long as forms are not watertight (Richard and Cheyrezy 1995). Pressure application can also reduce some of the increases in porosity caused by self-desiccation, which is the drop in relative humidity in concrete pores that leads to autogenous shrinkage (Bonneau et al. 1997). In fact, Roux et al. (1996) estimate from some of their tests that pressing UHPC can reduce cumulative porosity by approximately 50 percent. The increase in total density from these effects is estimated as a relative density increase of six percent by Richard and Cheyrezy (1995) and a total compression of eight percent of the initial length by Bonneau et al. (1997).

2.2.5. Heat Treatment

The primary function of heat treatment is to enhance the hydration reactions in concrete to further reduce porosity and enhance other properties of the mixture. Heat treatment temperatures can range from 194 to 752°F (90 to 400°C), and the heat treatments may last from 48 hours to six days. The typical heat treatment used for UHPC is a 48 hour heat treatment at 194°F (90°C).

The rate of development of hydration increases with increasing heat treatment temperature. Zanni et al. (1996) found that hydrate formation at eight hours was ten percent with heat treatment at 194°F (90°C) compared to 55 percent with heat treatment at 482°F (250°C).

The pozzolanic reaction of silica fume depends heavily on the temperature and duration of heat treatment. Consequently, heat treatment has the potential to greatly accelerate the reaction (Zanni et al. 1996; Richard and Cheyrezy 1995).

The increased pozzolanic reaction of silica fume leads to a decrease in porosity. Cheyrezy et al. (1995) claim the overall porosity of UHPC is not changed with heat treatment but the intermediate porosity is converted into small diameter porosity. Roux et al. (1996) confirm this finding and report that sizes of micropores can be reduced several orders of magnitude through heat treatment. Cheyrezy et al. (1995) also found the heat treatment temperature for optimal porosity was 302 - 392°F (150 – 200°C). Heat treatment also improves ratio of bound water to free water in UHPC. In fact, after heat treatment at 742°F (400°C), no free water remains in UHPC according to Cheyrezy et al. (1995).

2.2.6. Hydration

As stated previously, not all of the cement in UHPC hydrates due to the low water content. Figure 2.6 shows the maximum possible degree of hydration as a function of w/c ratio.

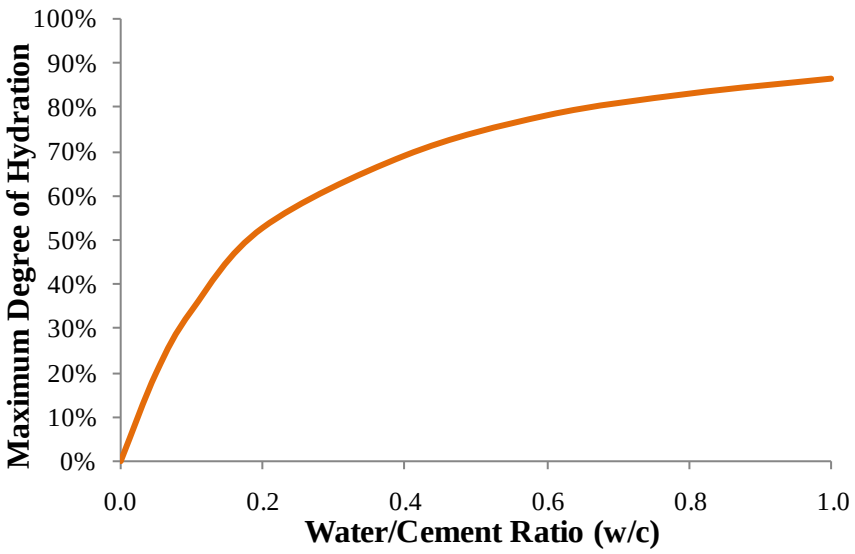

Figure 2.6. Maximum degree of hydration versus water/cement ratio (after van Breugel and Guang 2004)

The figure indicates that the maximum hydration percentage for a w/c ratio of 0.20 is approximately 50%. Estimates of the final hydration percentage of the cement in UHPC range from 31 percent to 60 percent in published studies (e.g., Habel et al. 2006b, Cheyrezy et al. 1995). These estimates agree with the chart from van Bruegel and Guang. A slightly higher degree of hydration can be reached with water or steam curing compared to dry curing (Ay 2004). The unhydrated cement particles make UHPC potentially self-healing. Unhydrated cement particles have the ability to close up small cracks in the matrix when a small amount of additional water is introduced in the area of the crack (Granger et al. 2006; Sritharan et al. 2003). Figure 2.7 shows a self-healed micro-crack in a UHPC specimen.

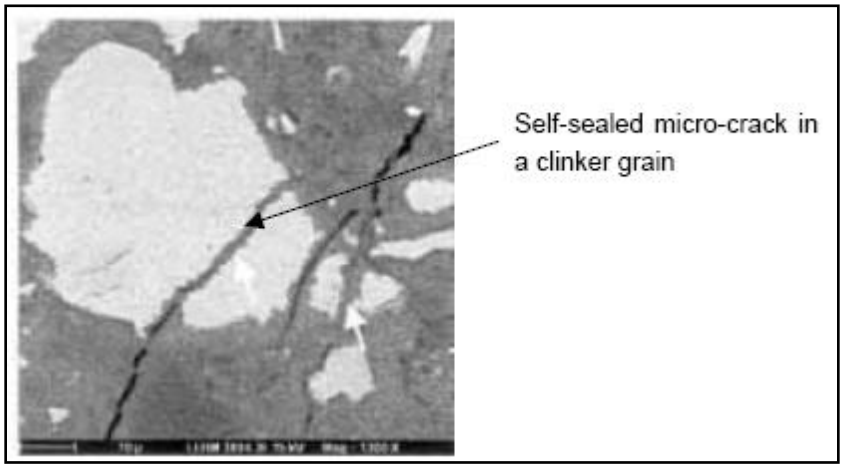

Figure 2.7. Self-healing of UHPC micro-crack (Acker and Behloul 2004)

Estimates of the setting time for UHPC vary widely. Richard and Cheyrezy (1995) identified the setting time as only six to 12 hours, while other estimates of setting time were as high as 40 hours (e.g., Brown 2006). The large discrepancy in setting time is likely due to differences in researchers' definitions of setting time and/or to delays in setting caused by the use of high amounts of plasticizer. Habel et al. (2006b) identified the setting point as the point at which the stiffness of the mix reaches 145 ksi (1 GPa) and autogenous shrinkage begins. From their study, they further determined the setting point of the UHPC mix to be 31.5 hours, which corresponded to 16 percent of the final hydration. Graybeal (2006) defined the initial set and final set using the AASHTO T197 standard test method. He observed that initial set, defined as a penetration resistance of 500 psi (3.4 MPa), occurred approximately

15 hours after casting, and final set, defined as a penetration resistance of 4,000 psi (27.6 MPa), occurred 18 to 20 hours after casting.

The hydration reaction in untreated UHPC initially develops very quickly and then slows down as almost all of the mixing water is consumed, as shown in the hydration model in Figure 2.8. Approximately 96 percent of the final hydration is reached after 28 days after casting, and hydration has virtually ceased at 90 days (Habel et al. 2006b). The equation used to develop the hydration curve shown in Figure 2.8 can be compared with experimental hydration results reported by Loukili et al. (1999). To facilitate the comparison, the 28-day hydration from the experimental results is assumed to correspond to 96 percent of the final hydration, as predicted by the model by Habel et al. Differences can then be seen in early age values, but for concrete ages of three days or greater, differences between the experimental values and the model are less than ten percent. The model by Habel et al. thus provides a conservative estimate of the percent of final hydration and is used as the basis for the plots of the time development of strength and modulus in untreated UHPC shown in later sections.

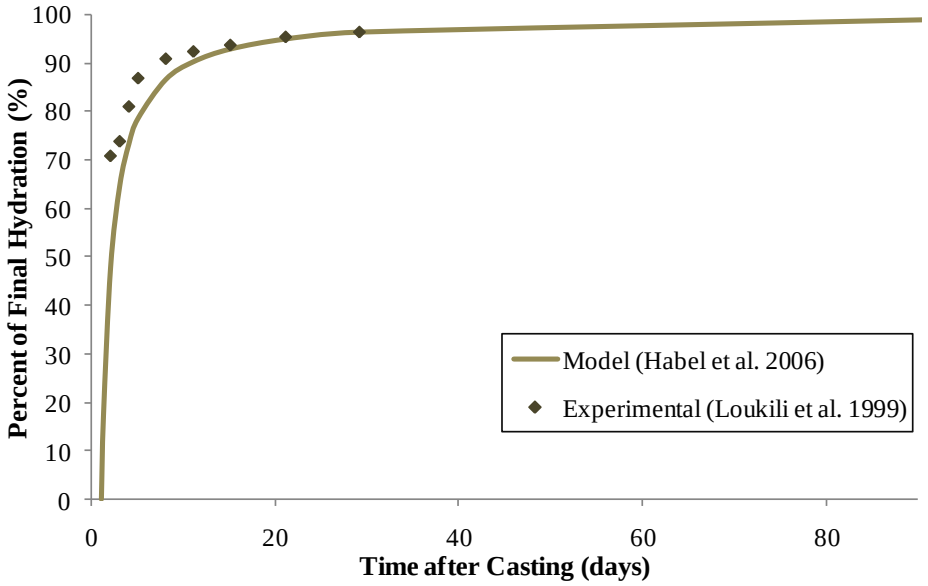

Figure 2.8. Development of percentage of final hydration in untreated UHPC with time (Habel et al. 2006b, Loukili et al. 1999)

2.2.7. Shrinkage and Creep

Two types of shrinkage contribute to the total shrinkage in concrete – autogenous shrinkage and drying shrinkage. UHPC can experience large shrinkage values, but unlike normal concrete, autogenous shrinkage makes up a larger portion of the total shrinkage in UHPC than drying shrinkage according to tests by Schmidt et al. (2003) on untreated UHPC samples and on UHPC samples subjected to the standard heat treatment.

2.2.7.1 Autogenous Shrinkage

Autogenous shrinkage is "the external-macroscopical (bulk) dimensional reduction (volume or linear) of the cementitious system that occurs under isothermal conditions without exchange of moisture or any other substance with the surroundings" (Habel et al. 2006a). In other words, autogenous shrinkage is the component of shrinkage not due to loss of water or material to the surrounding environment.

Autogenous shrinkage is driven by chemical shrinkage. The total volume of hydration products of cement and silica fume is approximately eight percent less than the total volume of the initial components. After mixing, chemical shrinkage proceeds uninhibited until the largest particles in the UHPC mix have no global degrees of freedom (Feylessoufi et al. 2001). The solid skeleton that forms restrains chemical shrinkage, causing air voids in the matrix (Habel et al. 2006a). As a result, the relative humidity in the pores of the concrete decreases rapidly in a process called self-desiccation (Loukili et al. 1999). The self-desiccation causes increased capillary tension in the pores of the UHPC, and the capillary tension drives the shrinkage of the matrix. When the relative humidity drops to approximately 73 to 75 percent, its time rate of change slows dramatically. This nearly constant relative humidity corresponds with a near stop in autogenous shrinkage in UHPC as shown in Figure 2.9 (Loukili et al. 1999; Habel et al. 2006a).

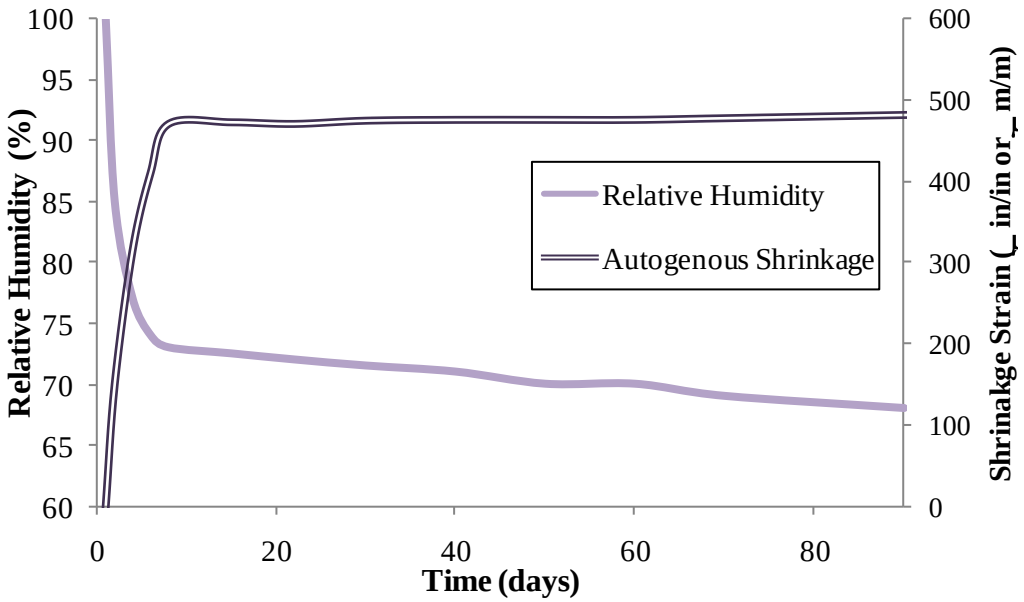

Figure 2.9. Evolution of relative humidity and autogenous shrinkage with time (after Loukili et al. 1999)

With the high autogenous shrinkage possible, cracking is a concern in early-age UHPC behavior. A low w/b ratio and associated high amount of cement make UHPC more susceptible to cracking from high shrinkage, but the improved tensile strength also helps limit cracking behavior. In an experiment by Habel et al. (2006a), the shrinkage stresses induced in restrained UHPC samples reached only 60 percent of the tensile strength the material. Strategies used to control the restraint stresses developed in UHPC due to autogenous shrinkage include heat treatment with steam curing and application of pressure during setting.

2.2.7.2 Drying Shrinkage

Drying shrinkage refers to the volume reduction in the cement matrix resulting from an overall loss of water to the environment through evaporation. As evaporating water is lost by capillary pores in the concrete, the vapor pressure drops and induces tensile stresses in the pores that cause the concrete to shrink (Cement and Concrete Association of Australia 2002). Habel et al. (2006) found that drying shrinkage in UHPC is most intense during the first 20 days, reaching a magnitude of 40×10^{-6} at day 20 and 80 $x10^{-6}$ by day 90. They also noted that the dense matrix of UHPC after 20 days largely prevents moisture exchange with the

environment except in a localized zone at the surface. Cheyrezy and Behloul (2001) found a somewhat higher drying shrinkage of 170×10^{-6} at 90 days.

2.2.7.3 Overall Shrinkage

The time rate of development of shrinkage and the final shrinkage magnitudes are difficult to compare between published studies. Early age shrinkage values can be very high in UHPC, and different methods of shrinkage measurement are able to begin to capture shrinkage magnitudes at different concrete maturities. Cheyrezy and Behloul (2001) indicated linear shrinkage strain while UHPC is still in the liquid phase could be as high as $2120x10^{-6}$. The shrinkage occurring between initial set and final set is estimated as high as $760x10^{-6}$, with final shrinkage (at 90 days after casting) approaching $1400x10^{-6}$, including the portion that occurs during setting.

Graybeal (2006) obtained a useful shrinkage value by embedding a vibrating wire strain gage in a UHPC prism to capture some of the early-age behavior. The shrinkage strain that the strain gage was able to measure more accurately measures the strain that would cause loss of stress in a prestressing strand than the measurements of total strain from the beginning of setting. The total shrinkage of untreated UPHC at 40 days was found to be $790x10^{-6}$. Loukili et al. (1999) confirm this estimate of shrinkage with reported autogenous shrinkage (including early-age behavior) of approximately $875x10^{-6}$ at 40 days and $890x10^{-6}$ at 90 days after casting.

Since early-age shrinkage is so difficult to measure consistently, the time rate of shrinkage is better compared between sources by using shrinkage magnitudes measured relative to the shrinkage at 24 hours after casting. Figure 2.10 shows the total shrinkage measured from one day after casting at seven days and at 90 days. Habel et al. (2006) and Cheyrezy and Behloul (2001) also suggest that including fibers in UHPC can reduce shrinkage up to 10 to 20 percent compared to plain UHPC.

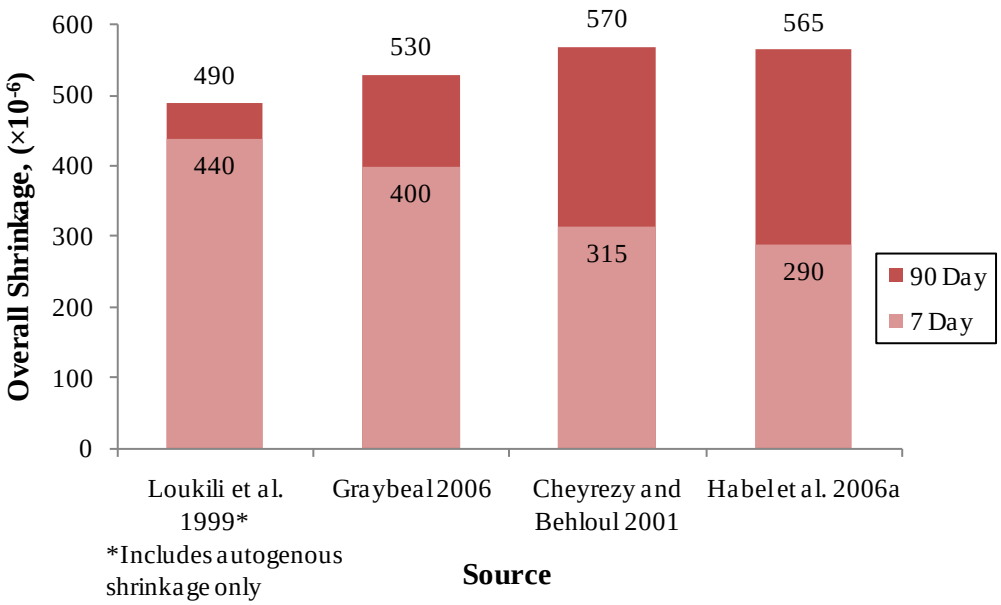

Figure 2.10. Seven day and 90 day shrinkage for untreated UHPC measured from one day after casting

Interestingly, if UHPC is heat treated, nearly all of the shrinkage will take place during the 48 hour, 194°F (90°C) standard heat treatment (Acker 2004, Graybeal 2006). Figure 2.11 shows the difference in UHPC shrinkage development caused by heat treatment.

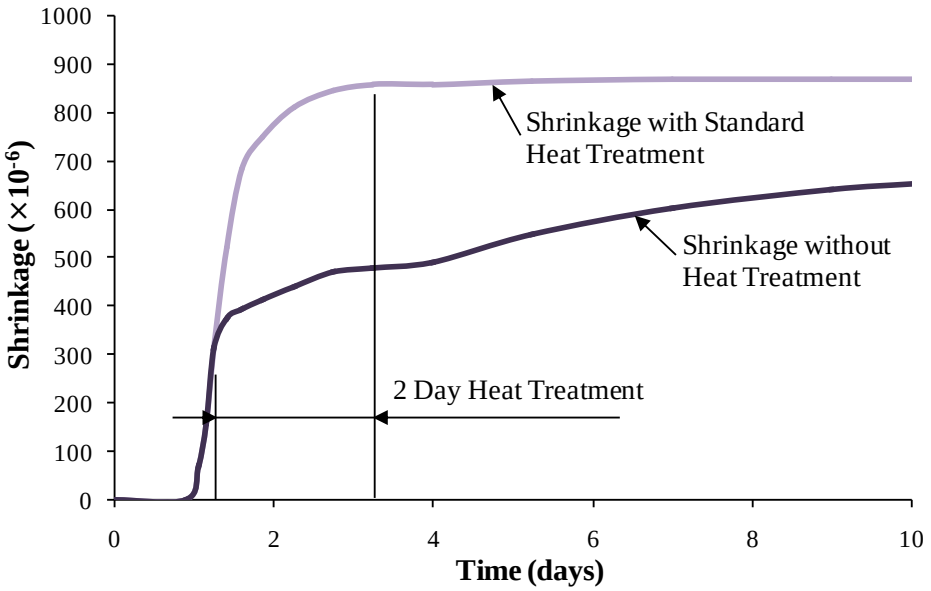

Figure 2.11. Heat treatment effects on UHPC shrinkage (after Graybeal 2006)

2.2.7.4 Creep

Creep is defined as additional deflection or strain in addition to the initial instantaneous strain that occurs when a load is applied to the concrete matrix. The ultimate creep coefficient is 0.78 for untreated UHPC (Graybeal 2006). This is noticeably smaller than the creep coefficient expected for normal concrete, which is in the range of 2.0 to 4.0 (Jones and Cather 2005; Acker and Behloul 2004). Similarly to normal concrete, the value of the creep coefficient for UHPC does appear to be greatly affected by the concrete age at loading (AFGC 2002). Table 2.6 and Figure 2.12 illustrate the how the magnitude of UHPC creep depends on loading age. The figure also shows the reduction in creep achieved through heat treatment, which will be discussed in a following section. Graybeal (2006) measured a specific creep, defined as the ultimate creep per unit stress, of 146×10^{-6}/ksi (21.2×10^{-6}/MPa) for untreated UHPC loaded at 28 days, confirming the accuracy of the Association Française de Génie Civil (AFGC) equation.

Table 2.6. Ultimate Creep and Creep Coefficient for untreated UHPC with different loading ages (AFGC 2002)

Concrete Age at Loading	Specific Creep $\times10^{-6}$/ksi ($\times10^{-6}$/MPa)	Creep Coefficient
1 day	323 (46.9)	2.27
4 days	256 (37.2)	1.80
7 days	224 (32.5)	1.57
28 days	153 (22.2)	1.08

2.3. DURABILITY

The greatly improved microstructure of UHPC not only results in higher compressive strength but also leads to superior durability properties. This makes UHPC both a high strength and a high performance material. The low porosity of UHPC, particularly capillary porosity, leads to great improvements in the durability properties of UHPC. The porosity of UHPC is discussed in the following section, and then various durability properties reported for UHPC are presented and compared to HPC and normal concrete in the following sections. A table and figures summarize the comparisons near the end of the durability

section. The high durability of UHPC may lead to reduced maintenance costs for the material and a possible reduction in the cover concrete required to resist weathering effects compared to normal concrete.

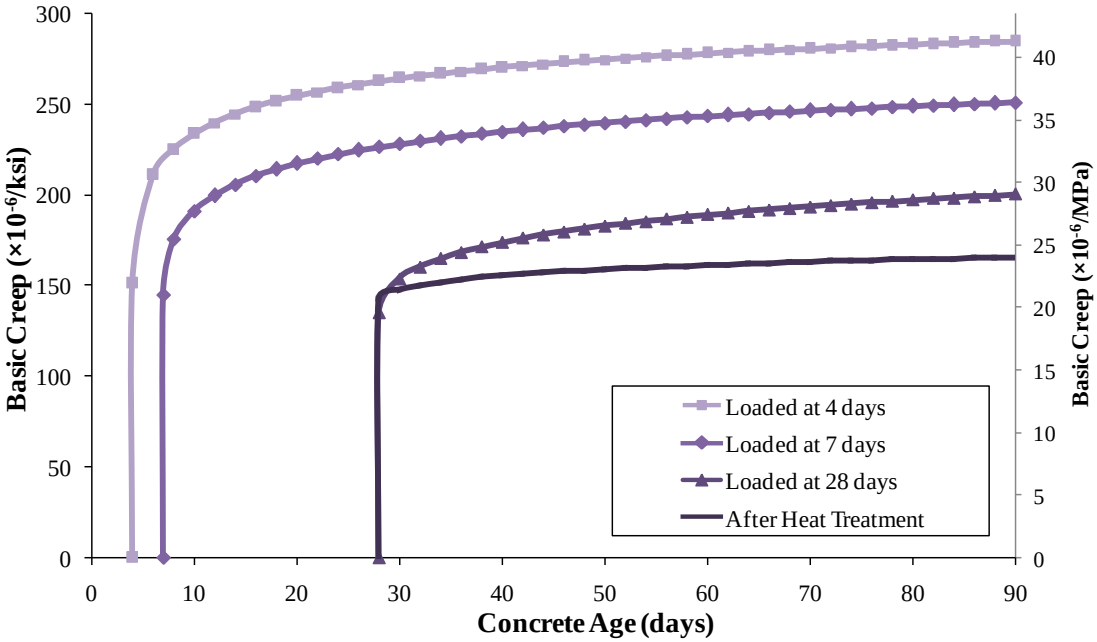

Figure 2.12. Basic creep of UHPC for different loading ages (after AFGC 2002)

2.3.1. Porosity

The porosity of any concrete, including UHPC, is intrinsically related to its durability properties. Referring to UHPC, Perry (2001) notes, "The superior durability characteristics [of UHPC] are due to the low and disconnected pore structure, which is generated as a result of the use of a combination of fine powder materials." Both the total volume of pores and the size of the pores in a concrete matrix can be important for mix durability. Many durability parameters, such as the rate and depth of ingress of contaminants and freeze-thaw damage, are greatly improved if a low volume of disconnected pores can be developed in the material.

The total porosity of UHPC appears to depend on the curing process applied to the material. Measurements of the total porosity range from 4.0 percent to 11.1 percent for UHPC without heat treatment (Schmidt et al. 2003, Acker 2001). When the standard heat treatment is used, however, UHPC has total porosity ranging from 1.1 percent to 6.2 percent

(Cwirzen 2007; Herold and Müller 2004). Figure 2.13 shows the cumulative porosity of both a heat treated and an untreated UHPC sample from a study by Cheyrezy et al. (1995). The total porosity of the untreated UHPC in their study is approximately 8.4 percent, but heat treatment reduces the total porosity of the UHPC sample to only 1.5 percent.

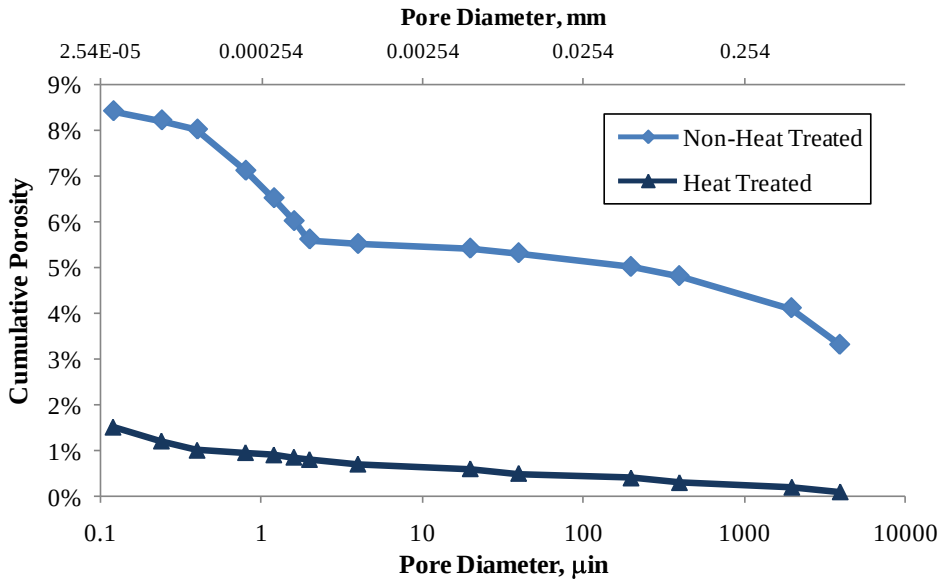

Figure 2.13. Porosity of Heat Treated and Non Heat Treated UHPC (Modified from Cheyrezy, Maret, and Frouin 1995)

Pore sizes large enough to facilitate the movement of water and waterborne contaminants are called capillary pores and are defined as pores with a diameter of 2.4 x 10^{-7} to 2.0 x 10^{-6} in. (6 to 50 nm) (Dallaire et al. 1998). Capillary pores defined as "large capillary pores" have a diameter greater than 2.0 x 10^{-6} in. (50 nm) and may allow larger contaminant particles to penetrate into a matrix. Dowd and Dauriac (1996) report most pores in UHPC have a diameter less than 2.0 x 10^{-7} in. (5.0 nm), and Schmidt et al. (2003) claim capillary porosity is nearly nonexistent in UHPC. Other researchers have reported the capillary porosity in UHPC to be approximately 1.0 to 2.0 percent by volume (Vernet 2004; Teichmann and Schmidt 2004).

The percolation threshold for a concrete is defined as the degree of hydration at which capillary pores become discontinuous. Bonneau et al. (2000) found the percolation threshold of UHPC to be 26 percent. Since the hydration of typical UHPC samples is at least 31

percent, as discussed in Section 2.2.6, UHPC can theoretically obtain zero capillary porosity. By comparison, the percolation threshold of HPC is approximately 54 percent. Sritharan et al. (2003), using a scanning electron microscope, found no interconnected pores on the surface of a cast UHPC sample.

The porosity of UHPC is even more impressive when compared to normal concrete and HPC. Table 2.7 shows the total porosity, capillary porosity, and percolation threshold of normal concrete, HPC, and UHPC.

Table 2.7. Total porosity, capillary porosity, and percolation threshold of normal concrete, HPC, and UHPC

Parameter	UHPC (with typical heat treatment)	HPC		Normal Concrete	
		Value	Ratio to UHPC	Value	Ratio to UHPC
Total Porosity*	6 %	8.3 %	1.4	15.0 %	2.5
Capillary Porosity*	1.5 %	5.2 %	3.5	8.3 %	5.5
Percolation Threshold (% Hydration)†	26 %	54 %	2.1	> 100 % (impossible)	Infinite

*(Teichmann and Schmidt 2004) †(Bonneau et al. 2000)

2.3.2. Freeze-Thaw Effects

2.3.2.1 Relative Dynamic Modulus

If water can seep into concrete through capillary pores, it can freeze and expand when the ambient temperature drops, which could crack or spall the concrete. One typical way to measure freeze-thaw resistance is to determine the ratio between the elastic modulus after a certain number of freeze-thaw cycles and the initial value, expressed as a percentage. Many tests have been performed on UHPC that show it has excellent freeze-thaw resistance. Gowripalan and Gilbert (2000) and Bonneau et al. (1997) found the freeze-thaw resistance to be 100 percent after 300 freeze-thaw cycles, which can be attributed to the lack of interconnected pores in UHPC. The Federal Highway Administration (2004) also found minimal degradation after 600 cycles. Gao et al. (2006) even found 100 percent freeze-thaw resistance after 800 cycles. Also, UHPC samples at the Natural Weathering Exposure Station at Treat Island, Maine, show no significant degradation after over 500 freeze-thaw cycles and 4500 wet-dry cycles in saturated seawater (Vernet 2004). After subjecting UHPC samples to

1000 freeze-thaw cycles, Lee et al. (2005) noted that their the relative dynamic modulus reduces to 90 percent. By comparison, typical relative dynamic moduli after 1000 freeze-thaw cycles for HPC and normal concrete are 78 percent and 39 percent of their initial values, respectively.

2.3.2.2 Salt Scaling

Another measure of durability is the mass lost due to freezing and salt scaling of the surface of concrete. Salt scaling can be an important parameter for structures exposed to saltwater and for concrete used as pavement or for a bridge deck, due to the wide usage of deicing salts. Estimates of salt scaling of UHPC reported in the literature vary from approximately 0.002 lb/ft^2 (8 g/m^2) to 0.013 lb/ft^2 (60 g/m^2) for studies using between 28 and 50 freeze-thaw cycles (Bonneau et al. 1997; Perry and Zakariasen 2004). The wide variation in the measured salt scaling may be due to the use of different testing methods and the level of precision obtainable for each test method. Since the total mass loss for UHPC is so low according to any of the sources (typical limits for concretes are 0.20 to 0.31 lb/ft^2 (1000 to 1500 g/m^2)), the actual mass loss is below the sensitivity threshold in some tests (Vernet 2004; Schmidt and Fehling 2005). The mass lost from salt scaling of HPC and normal concrete are much higher than that of UHPC at 0.031 lb/ft^2 (150 g/m^2) for HPC and 0.31 lb/ft^2 (1500 g/m^2) for normal concrete (Schmidt and Fehling 2005).

2.3.3. Chloride Ions

2.3.3.1 Diffusion Coefficient

Another important durability parameter for concrete is the rate at which chloride ions migrate through the cement paste. The presence of chloride ions near metallic reinforcement is a major cause of corrosion. In the only reported study in which the researchers attempted to determine the diffusion coefficient of UHPC, the coefficient was below the sensitivity threshold of the test. Roux et al. (1996) thus estimated the diffusion coefficient of UHPC to be 2.2 x 10^{-13} ft^2/s (2.0 x 10^{-14} m^2/s). The diffusion coefficients of HPC and normal concrete are 30 to 600 times higher at 6.5 x 10^{-12} ft^2/s (6.0 x 10^{-13} m^2/s) for HPC and 1.2 x 10^{-11} ft^2/s (1.1 x 10^{-12} m^2/s) for normal concrete.

2.3.3.2 Penetration Depth

In addition to the diffusion coefficient, the depth of penetration of chloride ions is also of interest to concrete durability. In a 128-hour long test with an increasing hydraulic pressure from 14 psi (0.1 MPa) to 230 psi (1.6 MPa), the total depth of penetration in UHPC was 0.11 in. (2.7 mm) (Gao et al. 2006). Using a different type of test, Schmidt et al. (2005) report a total depth of penetration of 0.04 in. (1 mm) for a six hour test with an applied 40 V DC voltage. In comparison, these researchers report the chloride ion penetration depth was 0.32 in. (8 mm) for HPC and 0.91 in. (23 mm) for normal concrete from the six-hour long test.

2.3.3.3 Total Charge

Another way to evaluate chloride ion permeability is by measuring the total electric charge passed through a test sample. Graybeal (2006) measured 18 Coulombs as the total charge passed through a 2.0-in. (51-mm) thick UHPC sample subjected to the standard heat treatment and 360 Coulombs for an untreated UHPC sample. Bonneau et al. (1997) report the total charge passed through a 2.0-in. (51-mm) thick heat-treated UHPC sample as 10 Coulombs, and compare this value with HPC at 500 to 1000 Coulombs and normal concrete at 6000 Coulombs for the same sample size. Schmidt et al. (2003), using a 1.4-in. (3.5-mm) sample thicknesses, estimate the total charge passed by heat-treated UHPC as approximately 22 Coulombs, compared to HPC at 216 Coulombs and normal concrete at 1736 Coulombs.

2.3.4. Air Permeability

2.3.4.1 Oxygen

UHPC exhibits extremely low permeability. The permeability of UHPC to oxygen is less than 1×10^{-19} ft^2 (1×10^{-20} m^2) (Vernet 2004). By comparison, the oxygen permeability of HPC is 10 times greater at 1×10^{-18} ft^2 (1×10^{-19} m^2) and of normal concrete is 100 times greater than UHPC at 1×10^{-17} ft^2 (1×10^{-18} m^2).

2.3.4.2 Air (Nitrogen)

Since the main component of air is nitrogen, nitrogen permeability is sometimes investigated in addition to oxygen permeability. Since the air permeability of UHPC is often

near or lower than the sensitivity threshold of the testing apparatus, a wide range of permeabilities have been reported for UHPC. Results from Teichmann and Schmidt (2004) on UHPC, HPC, and normal concrete allow a fairly accurate comparison between the concrete types. The permeability of UHPC to nitrogen is 1×10^{-18} ft^2 (1×10^{-19} m^2), HPC is 4.3×10^{-16} ft^2 (4.0×10^{-17} m^2), and normal concrete is 7.2×10^{-16} ft^2 (6.7×10^{-17} m^2). This comparison shows the air permeability of HPC and normal concrete is 400 to 670 times greater than that of UHPC.

2.3.5. Water Absorption

Since water has the potential to carry many impurities into voids in concrete, the potential for water to be observed in concrete is an important durability parameter. Roux et al. (1996) report that the water absorption of UHPC is less than 0.041 lb/ft^2 (200 g/m^2). Specific values for the water absorption of HPC and normal concrete were not obtained. Schmidt and Fehling (2005) list a water absorption factors for each type of concrete as 1 for UHPC, 11 for HPC, and 60 for normal concrete, but no further details concerning the basis of the factors were given.

2.3.6. Carbonation

The resistance of concrete to carbon dioxide is measured by carbonation depth. Most Several researchers agree that the typical carbonation depth for UHPC after six months is approximately 0.02 in. (0.5 mm) (Perry and Zakariasen 2004; Schmidt et al. 2003). One accelerated carbonation test by Roux et al. (1996) showed no carbonation depth after 90 days exposure to a 100% carbon dioxide environment. The typical carbonation depth after three years is approximately 0.059 in. (1.5 mm) for UHPC, compared to a 0.16 in. (4 mm) for HPC and a 0.28 in. (7 mm) for normal concrete (Schmidt and Fehling 2005).

2.3.7. Reinforcement Corrosion

A common cause of deterioration in typical reinforced concrete is corrosion of the reinforcing steel. Although all of the passive reinforcement can often be eliminated in UHPC members, the inclusion of steel fibers in the UHPC matrix makes corrosion a concern. Roux et al. (1996) found the corrosion rate for UHPC to be less than 4×10^{-7} in./yr (0.01 μm/yr).

Generally corrosion rates of less than 4×10^{-5} in./yr (1.0 μm/yr) indicate no corrosion risk for reinforced concrete members. Visual inspection in the tests conducted by Roux et al. also showed no evidence of corrosion. The corrosion rates for HPC and normal concrete are 25 to 120 times higher at 9.8×10^{-6} in./yr (0.25 μm/yr) and 4.7×10^{-5} in./yr (1.2 μm/yr), respectively.

2.3.8. Resistivity

The low corrosion rate in UHPC is partly due to the high resistance of the material to conducting an electric current. The high volume of steel fibers in UHPC reduces the resistivity of the material, but Roux et al. (1996) show through tests that the resistivity of UHPC is still better than that of HPC or normal concrete. The resistivity of a plain UHPC matrix without fibers is extremely high at 445 kΩ·in. (1130 kΩ·cm), but the addition of 2.0 percent of steel fibers reduces the resistivity to 53.9 kΩ·in. (137 kΩ·cm). In comparison, the resistivity of HPC is only 37.8 kΩ·in. (96 kΩ·cm), and that of normal concrete is 6.3 kΩ·in. (16 kΩ·cm).

2.3.9. Abrasion Resistance

Abrasion resistance in concrete is usually measured as a relative volume loss index. Glass is used as a reference material, which has a relative volume loss index of 1.0 (Dowd and Dauriac 1996). For UHPC, relative volume loss indices range from approximately 1.1 to 1.7 (VSL Proprietary Limited 2003; Perry and Zakariasen 2004). By comparison, the relative volume loss index is 2.8for HPC and 4.0 for normal concrete (Roux et al. 1996).

2.3.10. Comparison of Durability Properties

A summary of average values of various durability parameters discussed above is presented in Table 2.8 for UHPC, HPC, and normal concrete. Also included in this table are the ratios of each durability property of HPC and normal concrete with respect to those of UHPC, which highlight the superior qualities of UHPC. In addition, the durability properties of UHPC, HPC, and normal concrete are compared in graphical form in Figure 2.14 and Figure 2.15, in which the properties are normalized with respect to those of normal concrete. For the parameters compared in Figure 2.14, the smaller values should be considered highly

favorable, while the opposite is true for Figure 2.15. Based on the values reported in Table 2.8 and comparisons presented in Figure 2.14 and Figure 2.15, it is clear that UHPC outperforms both HPC and normal concrete in every durability parameter examined, sometimes by several orders of magnitude.

Table 2.8. Summary of durability properties of UHPC compared to HPC and normal concrete

Parameter	UHPC	HPC		Normal Concrete	
		Value	Ratio to UHPC	Value	Ratio to UHPC
Salt Scaling Mass Lost (28 cycles)	0.010 lb/ft^2 (50 g/m^2)	0.031 lb/ft^2 (150 g/m^2)	3.0	0.31 lb/ft^2 (1500 g/m^2)	30
Chloride Ion Diffusion Coefficient	2.2×10^{-13} ft^2/s (2.0×10^{-14} m^2/s)	6.5×10^{-12} ft^2/s (6.0×10^{-13} m^2/s)	30	1.2×10^{-11} ft^2/s (1.1×10^{-12} m^2/s)	55
Chloride Ion Penetration Depth	0.04 in. (1 mm)	0.32 in. (8 mm)	8	0.91 in. (23 mm)	23
Chloride Ion Permeability Total Charge Passed	10 – 25 Coulombs	200 – 1000 Coulombs	34	1800 – 6000 Coulombs	220
Oxygen Permeability	1×10^{-19} ft^2 (1×10^{-20} m^2)	1×10^{-18} ft^2 (1×10^{-19} m^2)	10	1×10^{-17} ft^2 (1×10^{-18} m^2)	100
Nitrogen Permeability	1×10^{-18} ft^2 (1×10^{-19} m^2)	4.3×10^{-16} ft^2 (4.0×10^{-17} m^2)	400	7.2×10^{-16} ft^2 (6.7×10^{-17} m^2)	670
Water Absorption	0.041 lb/ft^2 (0.20 kg/m^2)	—	11	—	60
Carbonation Depth (3 years)	0.059 in. (1.5 mm)	0.16 in. (4 mm)	2.7	0.28 in. (7 mm)	4.7
Reinforcement Corrosion Rate	4×10^{-7} in./yr (0.01 μm/yr)	9.8×10^{-6} in./yr (0.25 μm/yr)	25	4.7×10^{-5} in./yr (1.2 μm/yr)	120
Abrasion Resistance Relative Vol. Loss Index	1.1 – 1.7	2.8	2.0	4.0	2.9
Relative Dynamic Modulus (1000 cycles)	90%	78%	0.87	39%	0.43
Resistivity	53.9 kΩ·in. (137 kΩ·cm)	37.8 kΩ·in. (96 kΩ·cm)	0.70	6.3 kΩ·in. (16 kΩ·cm)	0.12

(Compiled based on data presented by Lee et al. 2005, Schmidt and Fehling 2005, Roux et al. 1996, Bonneau et al. 1997, Schmidt et al. 2003, Vernet 2004, VSL Proprietary Limited 2003, Perry and Zakariasen 2004)

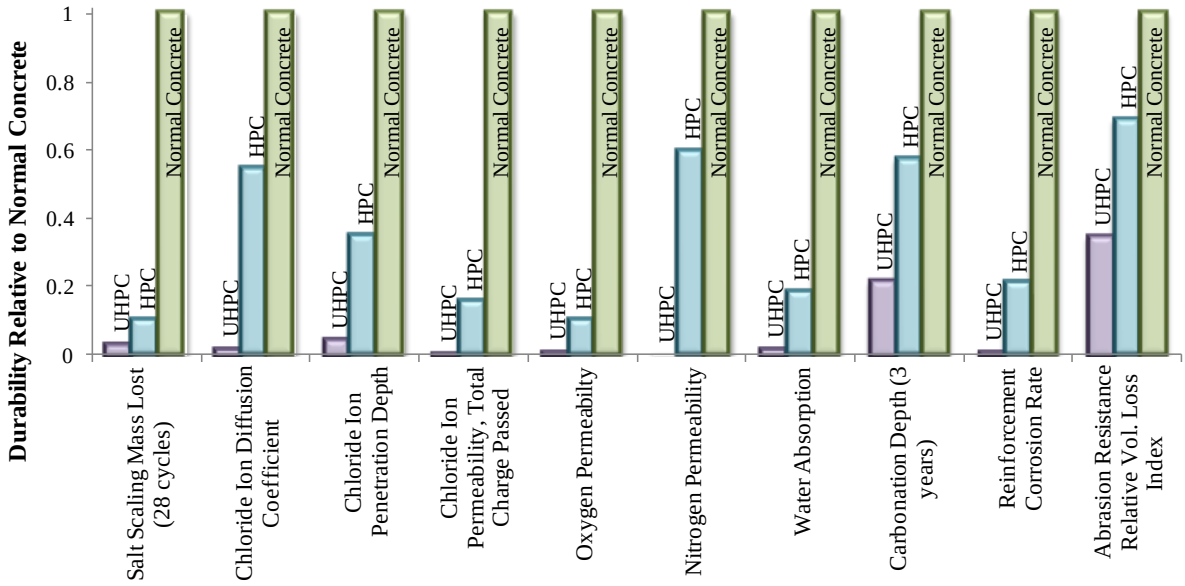

Figure 2.14. Durability properties of UHPC and HPC with respect to normal concrete (smallest values identify the most favorable material)

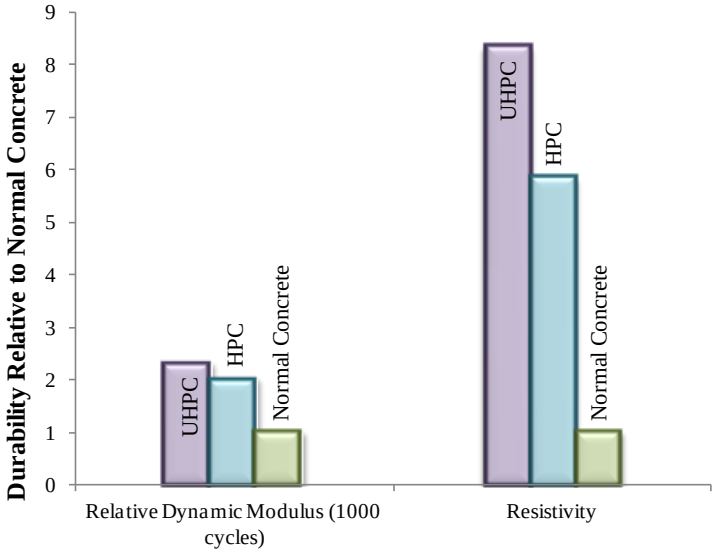

Figure 2.15. Relative dynamic modulus and resistivity of UHPC and HPC with respect to normal concrete (higher values identify the most favorable material)

2.4. MATERIAL PROPERTIES

The most striking aspects of UHPC are its material properties. The compressive strength and elastic modulus of UHPC depend on the type and duration of heat treatment.

This section will discuss results from a wide range of sources on UHPC material properties and summarize, where possible, typical values for each of the properties. Note that the intent of this section is to highlight both the material properties of UHPC and their dependency on heat treatment and fiber content, not to provide absolute maximum or minimum values to be used as a standard.

2.4.1. Compressive Strength

2.4.1.1 Influence of Fibers

Though the increase in tensile strength accomplished by adding fibers to the UHPC matrix cannot be disputed, researchers disagree on whether fibers also increase the compressive strength. Schmidt et al. (2003) remark compressive strength "is practically not increased by the fibers," which occupied 2.5% of the volume of the UHPC mix in their tests. Reda et al. (1999) disagree, but note that the increase due to fibers is not as great as the increase that may be achieved through an appropriate heat treatment, although the observed increase in strength is statistically significant with a fiber content of 2.0 percent. Figure 2.16 compares the compressive strength results for UHPC mixes utilizing different fiber types and contents, including organic fibers and steel fiber contents of 0, 2.0 to 2.5, and 4.0 percent. The results obtained for the same batch of UHPC with different fiber contents allow direct and accurate comparison of compressive strengths. According to the figure, it appears that steel fibers increase the compressive strength of UHPC when compared to the values obtained using organic fibers. Also apparent in this figure is that the compressive strength of UHPC increases with increasing fiber content. The four sources (i.e., Bonneau et al. 1997, Soutsos et al. 2005, Lee and Chrisholm 2006, and Herold and Müller 2004) which reported compressive strengths of UHPC mixes with both 0 percent and 2.0 to 2.5 percent fiber contents show an average increase in compressive strength of 30 percent with the increase in fiber content from 0 to 2.0-2.5 percent. Based on these observations, it is concluded that the type and content of fibers do appear to influence the compressive strength of UHPC.

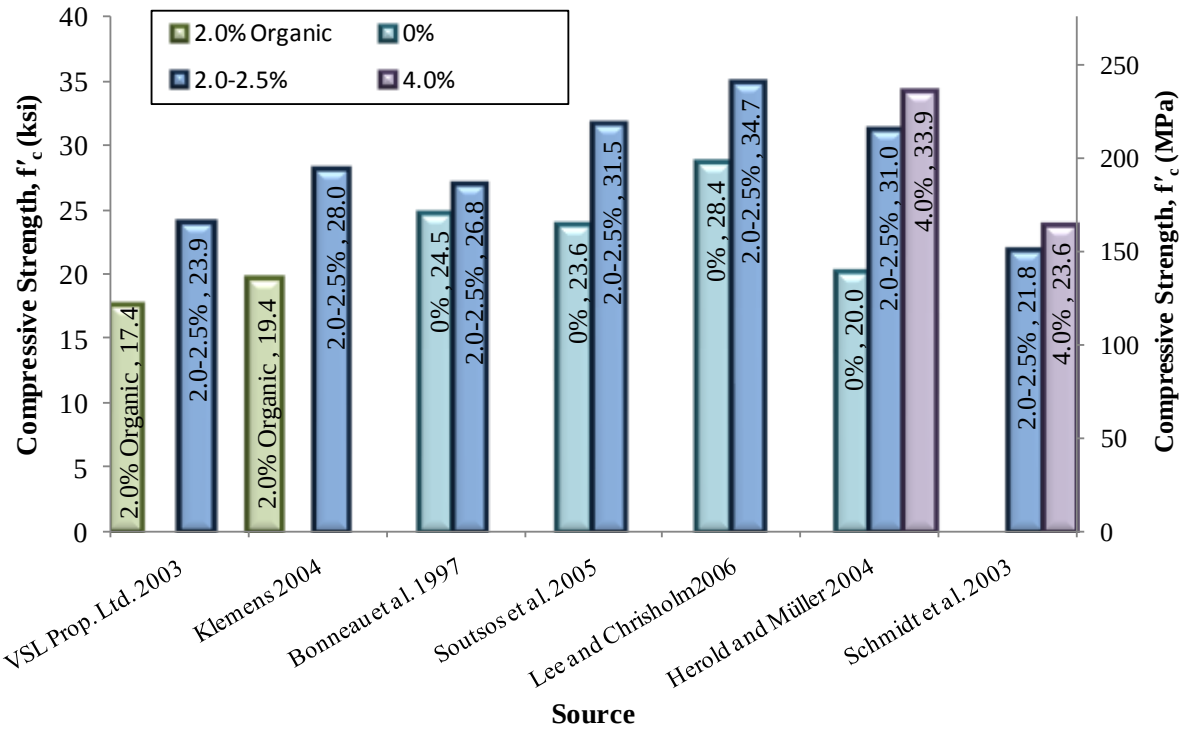

Figure 2.16. Comparisons of compressive strength of UHPC with different types and contents of fibers

2.4.1.2 Influence of Heat Treatment

In addition to low water/binder ratios, use of a proper heat treatment to reduce the final porosity of UHPC can, in turn, greatly increase the compressive strength. Figure 2.17 compares compressive strengths obtained for untreated UHPC, UHPC with the standard heat treatment of 194°F (90°C) for two days, and UHPC with higher temperature heat treatments of 320 – 482°F (160 – 250°C). Note that some the UHPC samples subjected to the high temperature heat treatments were also subjected to a confining pressure while curing. The figure allows comparison of results for different curing regimes obtained from the same sources, ensuring samples were produced and tested under similar conditions. The compressive strength of UHPC generally appears to increase with increasing heat treatment temperature. The compressive strength of UHPC was increased on average by 33 percent for the 194°F (90°C) heat treatment samples with respect the strengths obtained for untreated UHPC. This observation is made used the results reported for both heat treated and untreated UHPC in 15 references (see Figure 2.17).

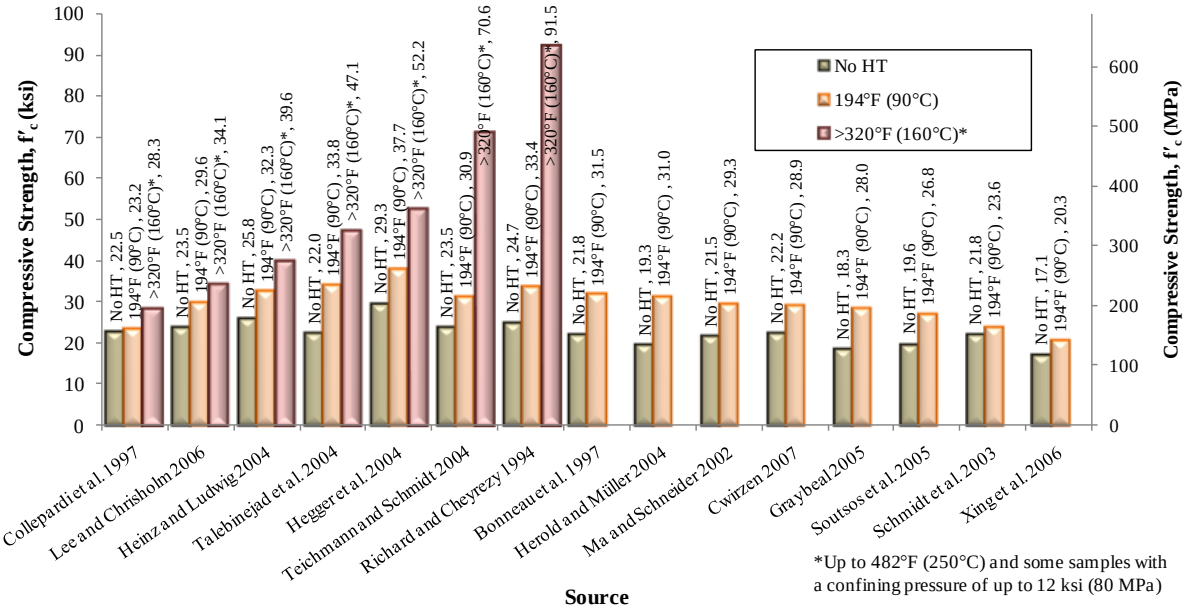

Figure 2.17. Comparisons of compressive strength of UHPC subjected to heat treatment at different temperatures

Interestingly, the same four groups of researchers who tested UHPC without fibers and with 2.0 to 2.5 percent of fibers by volume also studied the compressive strength of untreated UHPC and UHPC with the standard 194°F (90°C) heat treatment. Each of these four groups reported a greater increase in compressive strength due to heat treatment than due to addition of fibers in the UHPC mixes. The average strength increase due to heat treatment obtained for the results reported in the four studies was 42 percent, compared to the 30 percent increase due to the addition of fibers, as previously noted.

A maximum compressive strength of 117.5 ksi (810 MPa) has been achieved by Richard and Cheyrezy (1995) for a UHPC mix incorporating steel aggregates, heat treatment at 752°F (400°C), and application of a 7.3 ksi (50 MPa) confining pressure during setting. This type of extremely high strength UHPC has only been successfully produced in a laboratory and requires a demanding production process. Instead, applying pressure during setting and confining concrete in stainless steel tubes may be a more favorable way to achieve very high compressive strength in UHPC members. The typical confining pressure applied during setting, as noted in Section 2.2.4, is 7.3 ksi (50 MPa). A compressive strength of 55.1 ksi (380 MPa) was achieved by confining UHPC in 0.12 inch (3 mm) thick stainless

steel tubes and applying the 7.3 ksi (50 MPa) confining pressure for the design of the Sherbrooke Pedestrian Bikeway bridge in Canada (Dallaire et al. 1998).

Compressive strengths for normal concrete commonly fall in the range of 4 to 8 ksi (28 to 55 MPa), and compressive strengths for HPC are usually from 12 to 18 ksi (83 to 124 MPa). The compressive strength of UHPC subjected to its standard heat treatment is thus approximately twice that of HPC and five times that of normal concrete.

Figure 2.18 shows theoretical models for the time rate of development of the compressive strength of untreated UHPC reported by Habel et al. (2006b) and by Graybeal (2007). The figure also includes data points from tests on both heat treated and untreated UHPC by Graybeal. Both models were adjusted to assume a set time of 17 hours, as measured by Graybeal. The figure shows UHPC achieves its high compressive strength very quickly. The strength gain from seven to 56 days is 18 percent, according to the model by Habel et al. Graybeal, by comparison, shows a strength gain of 26 percent over the same time period from his model, and measured a strength gain of 41 percent from tests of untreated UHPC. The rate of strength gain is much higher for heat treated UHPC, and the strength increase from seven to 56 days is only 5.0 percent.

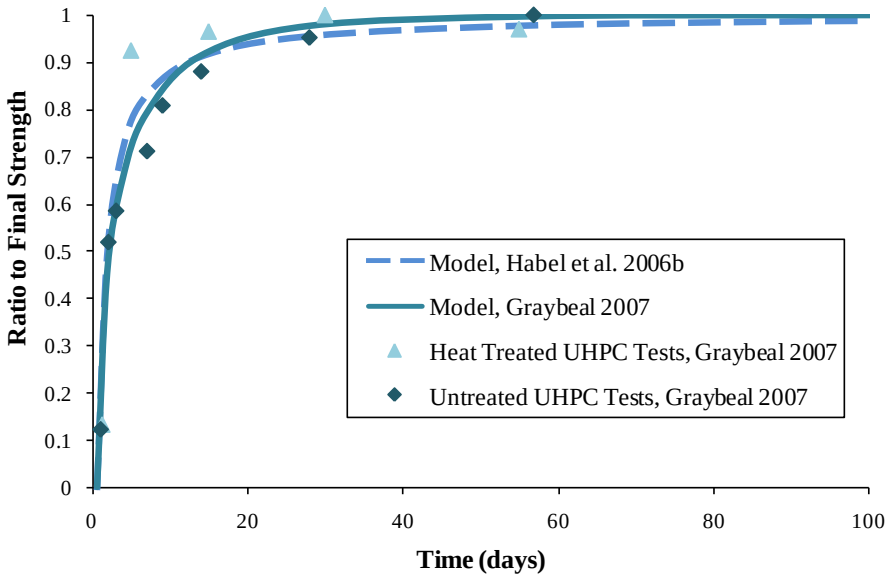

Figure 2.18. Development of compressive strength of UHPC with and without heat treatment

2.4.2. Tensile Strength

2.4.2.1 Direct Tensile Strength

Normal concrete has a low tensile strength, typically between 300 and 700 psi (2.1 to 4.8 MPa) as calculated from expressions by Kosmatka et al. (2002) for the range of compressive strengths noted in the previous section, so building codes and standards typically ignore concrete's contribution to tensile resistance for most structural applications. The tensile strength of HPC for the range of compression strengths noted in the previous section can be estimated as 800 to 900 psi (5.5 to 6.2 MPa) based on expressions by Yin et al. (2002). UHPC, however, develops a much more appreciable tensile strength, even beyond in the post-cracking regime due to the ability of steel fibers in the matrix to bridge micro-cracks. Many researchers, including Bayard and Plé (2003), Cadoni et al. (2004), Habel et al. (2006b), and Rossi (2005), agree that UHPC can also experience some strain-hardening between its first tensile cracking strength and ultimate tensile strength.

Tests by Graybeal (2006) on UHPC mortar briquettes indicate that the first cracking tensile strength of UHPC is 1220 psi (8.4 MPa) and the ultimate tensile strength is 1350 psi (9.3 MPa). Graybeal notes, however, that the small mortar briquette test samples used for this comparison may not accurately represent typical fiber dispersion and orientation in large-scale UHPC members. Therefore, Graybeal also reports a first cracking tensile strength of 1410 to 1600 psi (9.7 to 11.0 MPa) from direct tension tests on UHPC cylinders, in which an epoxy was used to hold the ends of the UHPC cylinders to the testing machine heads. Tests by Graybeal also show the tensile strength of untreated UHPC, at 800 to 1000 psi (5.5 to 6.9 MPa), is lower than that of heat-treated UHPC for the direct tension tests.

Habel et al. (2006b) also developed a model for the development of the tensile strength of untreated UHPC, shown in Figure 2.19. For comparison, the figure also shows the model of the time development of compression strength. The direct tensile strength increases 46 percent from seven to 56 days. Therefore the rate of development of the tensile strength of UHPC is much slower than the rate of development of the compressive strength. Habel et al. note that in normal concrete, the tensile properties develop faster than the compressive properties – the opposite behavior to that observed for UHPC.

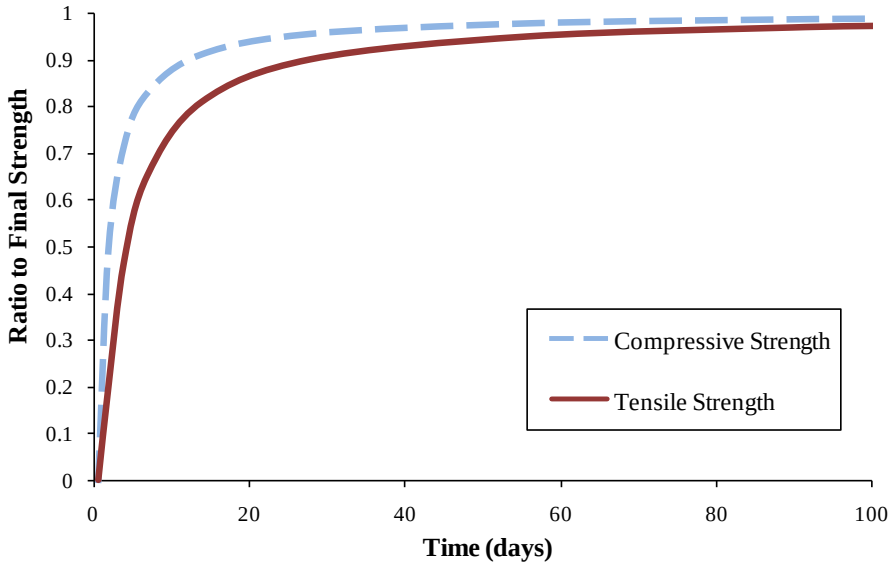

Figure 2.19. Development of strengths of untreated UHPC (after Habel et al. 2006b)

2.4.2.2 Flexural Strength

Many researchers attempt to characterize the flexural strength of UHPC with single- or two-point bending tests on small UHPC prisms. Results from these tests appear to show that the flexural tensile strength of UHPC depends heavily on the size of the prisms used in the test. Figure 2.20 shows that for larger prism cross-sections, the flexural strength of UHPC is much lower than for smaller prisms. Reineck et al. (2004) also show average values of flexural strength for a wider range of prism sizes in Figure 2.21, where "size of prism" refers to the dimension of each equal side of the square cross-sections of the prisms. The higher strengths for smaller beams may be largely due to local alignment of fibers in small prisms. The local alignment leads to relatively more fibers oriented parallel to the long direction of the prism, making a greater proportion of the fibers effective to bridge flexural cracks.

Typical UHPC behavior under flexure is characterized by linear elastic behavior up to the first cracking strength of the material, a strain-hardening phase up to the maximum load, and a strain-softening phase after the maximum load is reached. Figure 2.22 shows a typical load-deflection diagram for UHPC in bending with the typical phases labeled.

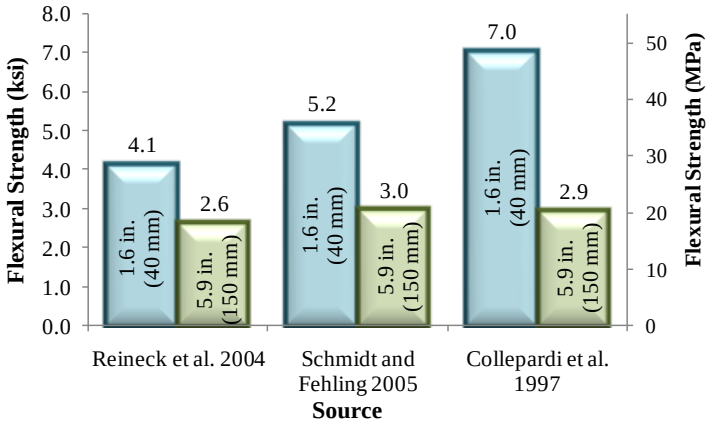

Figure 2.20. Flexural strength of UHPC showing size effect of tested prisms

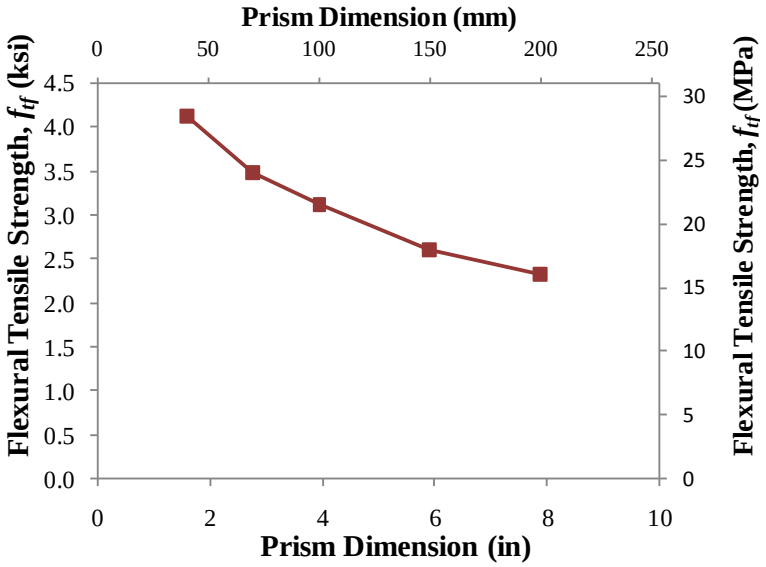

Figure 2.21. Size effect on UHPC flexural strength for wide range of prism cross-sections (after Reineck et al. 2004)

2.4.3. Bond Strength

UHPC also displays high bond strength, allowing anchorage of reinforcement over short distances. Results for the UHPC bond strength have been established using typical deformed reinforcing bars, prestressing strands, and steel fibers. Reported values of bond strengths by different researchers vary widely, so details of published bond strengths are summarized in Table 2.9. For all of the tests shown, the bond strength was calculated as the average stress at the maximum pull-out load on the reinforcement.

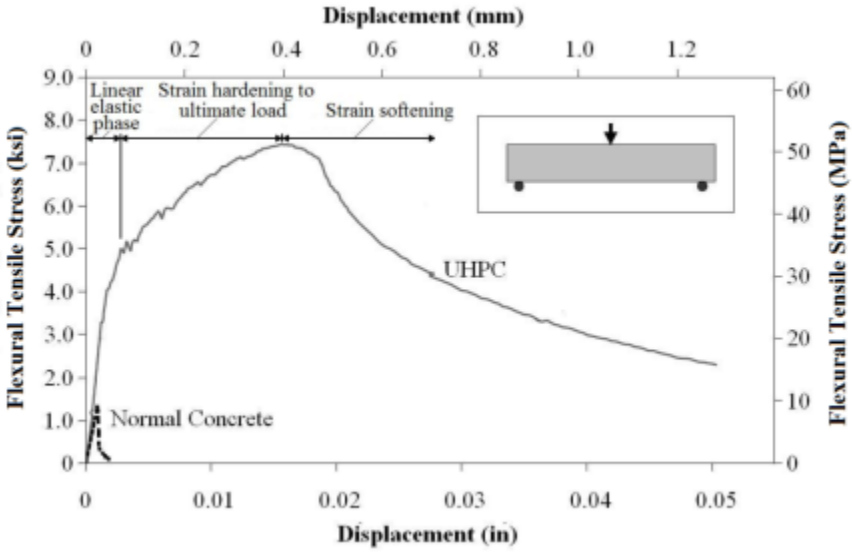

Figure 2.22. Flexural tensile stress-deflection diagram of UHPC under single-point bending (after Acker and Behloul 2004)

Table 2.9. Bond Strength of Various Reinforcement in UHPC

Type of Reinforcement	Diameter in. (mm)	Bond Strength ksi (MPa)	Fiber Content	Heat Treatment	Source
½-in. (13-mm) Steel Fiber	0.006 (0.15)	0.79 (5.5)	None added	Standard	Chan and Chu 2004
½-in. (13-mm) Steel Fiber	0.006 (0.15)	1.67 (11.5)	2%	Not given	Behloul 1996, referenced by Tuchlinski et al. 2006
Epoxy Coated Deformed Bar	⅜ (9.5)	1.84 (12.7)	Approx. 0.5%	Untreated	Lee et al. 2005
Deformed Bar	0.79 (20)	4.12 (28.4)	2%	Standard	Collepardi et al. 1997
Deformed Bar	0.16 (4)	6.7 (46)	2%	Not given	Reineck and Greiner 2004
Deformed Bar	0.39 (10)	8.1 (56)	None	None	Holshemacher et al. 2005
Prestressing Wire	0.20 (5)	1.5 (10)	2%	Standard	Cheyrezy et al. 1998
Prestressing Strand	½ (13)	5.1 (35)	2%	Standard	Cheyrezy et al. 1998
Prestressing Strand	½ (13)	2.2 (15)	2.5%	Not given	Tuchlinski et al. 2006

All reported results in the table agree on the fact that the bond strength of UHPC is high. The excellent bond is a result of the very high tensile strength and elastic modulus of UHPC and is a result of the incorporation of silica fume, which increases the amount of cementitious materials that adhere to the fibers and, presumably to other reinforcement (Chan

and Chu 2004). Holshemacher et al. (2003) also note the dense and homogenous matrix of UHPC increases the bond strength of UHPC, although the lack of coarse aggregates eliminates the advantages aggregate interlock provides for the bond strength of large diameter deformed bars.

The high bond stresses in UHPC lead to very short development and transfer lengths. Tuchlinksi et al. found ½-in. (13-mm) steel prestressing strands with embedded lengths of only 24 in. (61 cm) fractured before pulling out of UHPC (Tuchlinski et al. 2006). They estimate the transfer lengths of ½-in. (13-mm) strands in UHPC to be only 14 in. (35 cm). In tests by Lubbers, both ½-in. (13-mm) and ½-in. oversized strands fractured with embedment lengths as low as 12 in. (30 cm) used for all of her tests (Lubbers 2003).

2.4.4. Cover

Because of its superior strength and durability properties, UHPC requires a smaller thickness of concrete cover on metallic reinforcing compared to normal concrete. The high durability of UHPC helps prevent the ingress of chloride ions and other corrosive elements, and the high tensile strength helps prevent damage due to splitting and spalling, which can occur when the cover concrete does not have enough capacity to help develop the full strength of a prestressing strand or reinforcing bar. Tests by Holshemacher et al. (2005) showed no indication of splitting and no reduction in bond strength when UHPC cover was reduced from 1.8 in (45 mm) to 1.0 in (25 mm) on a 0.6-in. (16-mm) diameter reinforcing bar. In fact, even when the cover was reduced to be equal to the reinforcing bar diameter, the maximum bond stress dropped by only 25 to 30 percent. Splitting, however, has been observed by Schmidt and Fehling (2005) when a 0.39-in. (10-mm) diameter reinforcing bar used a cover thickness of less than 1.0 in. (25 mm). Table 2.10 demonstrates an example of the decreased cover requirement for UHPC for a ½-in. (13-mm) prestressing strand. The cover can be reduced 33 percent without the potential for developing longitudinal cracking according to these tests by Tuchlinski et al. (2006). Reduction of cover thickness in UHPC members can contribute to achieving smaller section sizes, since stirrups and ties can be eliminated in the design of UHPC members.

Table 2.10. Cover and spacing requirements recommended for ½-in. (13-mm) prestressing strands in UHPC by Tuchlinski et al. (2006)

Concrete Type	Strand Clear Spacing	Clear Cover
Normal Concrete	2.0×Diameter	3.0×Diameter
UHPC	1.5×Diameter	2.0×Diameter

2.4.5. Elastic Modulus

UHPC displays linear elastic behavior in both compression and tension up to certain strain limits. For compression, the linear zone has been found to extend to 60 percent of the compressive strength by Dugat et al. (1996) on UHPC subjected to a heat treatment of 194°F (90°C) for six days. Cheyrezy (1999), however, models the elastic portion as continuing to up to 80 percent of the compressive strength on UHPC subjected to the standard heat treatment. Graybeal (2007) also confirms that UHPC has less than five percent deviation from stress-strain linearity up to approximately 80 to 90 percent of the compressive strength for heat-treated UHPC.

Tests by Bonneau et al. (1996) show the elastic modulus of UHPC without fibers is 6700 ksi (46 GPa) compared to 7100 ksi (49 GPa) with a 2.0 percent steel fiber content, an increase of only about 6.5 percent due to the presence of fibers. According to Graybeal (2006), standard heat treatment increases the elastic modulus of UHPC 23 percent from 6200 ksi (42.7 GPa) to 7650 ksi (52.7 GPa). Use of high temperature heat treatment of 482°F (250°F) can increase the elastic modulus further from 8300 ksi (57 GPa) to 10200 ksi (70 GPa), an increase of an additional 23 percent (Richard and Cheyrezy 1994). The elastic modulus of normal concrete with compressive strengths of 4 to 8 ksi (28 to 55 MPa) is typically 3600 to 5100 ksi (25 to 35 GPa) (ACI 2005), and the elastic modulus of HPC with compression strengths of 12 to 18 ksi (83 to 124 MPa) is approximately 4800 to 6400 ksi (33 to 44 MPa), according to the equations shown for HPC in the following section.

The rate of development of the elastic modulus for untreated UHPC is higher than that for the tensile strengths but comparable to that of the compressive strength. Figure 2.23 shows the model of the rate of development of the elastic modulus established by Habel et al. (2006b). The tensile and compressive strength rates of development are also included for

comparison. The increase in elastic modulus is only 13 percent from seven to 56 days for untreated UHPC.

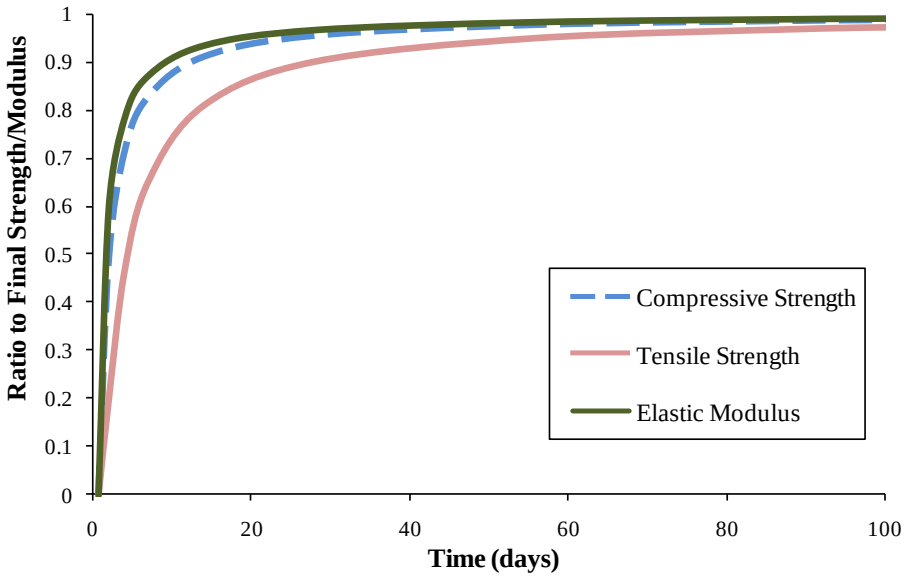

Figure 2.23. Comparison of rate of development of elastic modulus with those of compressive and tensile strength for untreated UHPC (after Habel et al. 2006b)

Many equations have been used to define the relationship between the elastic modulus and the compressive strength of concrete. Equations 2.1 to 2.3 below show some common expressions developed for normal strength concrete. The equation by AASHTO (2004) is specifically limited to a maximum concrete compressive strength of 10 ksi (69 MPa), and the other equations should also not be applied for UHPC. Separate equations have been developed for high performance concrete, shown as Equations 2.4 to 2.6 below. The ACI (1992) equation was developed for concretes with a compressive strength of up to 12 ksi (83 MPa). The equation by Kakizaki et al. (1992) was developed from research on high strength concretes with compressive strengths ranging from 12 to 20 ksi (83 to 138 MPa). Equations 2.7 to 2.10 have been developed specifically for UHPC, although the coefficient in the equation by Sritharan et al. (2003) is based on a single UHPC mix and is not intended for a broad range of compressive strengths.

For normal strength concrete:

$E = 33 \cdot \rho^{1.5} \cdot \sqrt{f_c'} = 63,680 \cdot \sqrt{f_c'}$ $(E = 5288 \cdot \sqrt{f_c'})$ (AASHTO 2004) (2.1)

$E = 57,000 \cdot \sqrt{f_c'}$ $(E = 4730 \cdot \sqrt{f_c'})$ (ACI 318-05) (2.2)

$E = 266,600 \cdot \sqrt[3]{f_c' + 1160}$ $(E = 9500 \cdot \sqrt[3]{f_c' + 8})$ (CEB-FIP 1990) (2.3)

For HPC:

$E = 40,000 \cdot \sqrt{f_c'} + 1000$ $(E = 3300 \cdot \sqrt{f_c'} + 6.9)$ (ACI 363R-92) (2.4)

$E = 43,960 \cdot \sqrt{f_c'}$ $(E = 3650 \cdot \sqrt{f_c'})$ (Kakizaki et al. 1992) (2.5)

$E = 246,900 \cdot \sqrt[3]{f_c'}$ $(E = 20,500 \cdot \sqrt[3]{f_c'})$ (CEB-FIP 1990) (2.6)

For UHPC:

$E = 50,000 \cdot \sqrt{f_c'}$ $(E = 4150 \cdot \sqrt{f_c'})$ (Sritharan et al. 2003) (2.7)

$E = 46,200 \cdot \sqrt{f_c'}$ $(E = 3840 \cdot \sqrt{f_c'})$ (Graybeal 2007) (2.8)

$E = 2,373,400 \cdot \ln(f_c') - 468,910$ $(E = 16,364 \cdot \ln(f_c') - 34,828)$ (Ma et al. 2002) (2.9)

$E = 525,000 \cdot \sqrt[3]{f_c'}$ $(E = 19,000 \cdot \sqrt[3]{f_c'/10})$ (Ma et al. 2004)(2.10)

where E = elastic modulus in psi (MPa) and f_c' = compressive strength in psi (MPa)

Figure 2.24 compares the different equations along with measured compressive strength and elastic modulus values published in the literature. A line representing the mean of the measured values is also shown. The equation by ACI (1992), Equation 2.4, appears to be the best relationship for UHPC of the equations developed for HPC. The best relationship developed specifically for UHPC appears to be that of Graybeal (2007), Equation 2.8. Note that no more than two of the measured values shown were provided by any one researcher; therefore, the data set is not dominated by values from Sritharan et al. (2003), Graybeal (2007), Ma et al. (2002), or Ma et al. (2004).

2.4.6. Stress-Strain Behavior

Typical compressive stress-strain behavior for a UHPC cylinder is shown in Fig. The stress-strain behavior of a normal concrete is also shown for comparison. The high strength and modulus and high ultimate compressive strain values can be clearly observed. Stress-strain models developed for UHPC are described in Section 3.1.

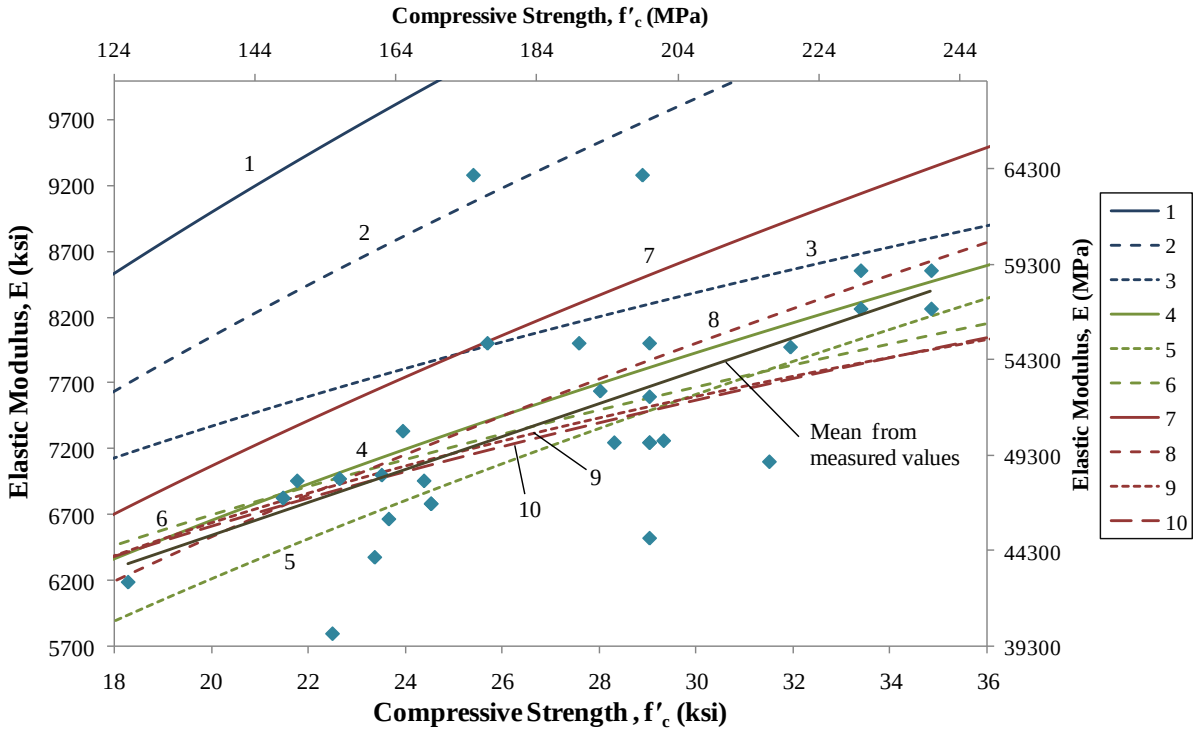

Figure 2.24. Comparison of various equations suggested for elastic modulus of UHPC with measured experimental data

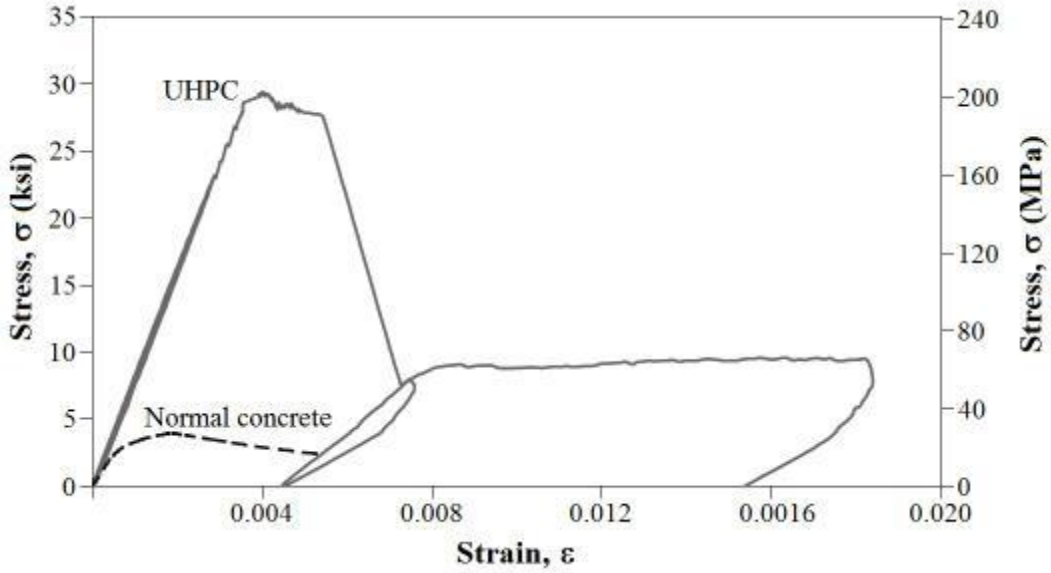

Figure 2.25. UHPC compressive stress-strain behavior from tested cylinder (Acker and Behloul 2004)

2.4.7. Poisson Ratio

An important parameter, particularly for plate, shell, and slab structures, is the Poisson ratio. The Poisson ratios reported by various researchers range from 0.13 by Voo et al. (2001) to 0.22 by Dugat et al. (1996). The average reported ratio was approximately 0.18, which is in the 0.15 to 0.20 range of typical Poisson ratios for normal concrete.

2.4.8. Fracture Energy

Flexural fracture energy represents the total amount of work that must be done on a concrete beam to achieve complete failure. The large amount of energy required to pull out or fracture the steel fibers in the matrix gives UHPC a much greater fracture energy than normal concrete. Fracture energy in UHPC subjected to standard heat treatment ranges from 0.114 kip/in. (20,000 J/m^2) to 0.270 kip/in. (47,300 J/m^2) (Gowripalan and Gilbert 2000; Dugat et al. 1996). For UHPC with short fibers and heat-treated at 482°F (250°C), however, the fracture energy is reduced to between 0.007 kip/in. (1220 J/m^2) and 0.013 kip/in. (2200 J/m^2) (Dugat et al. 1996).

The rate of development of fracture energy is slower than the rates of development of the elastic modulus, compressive strength, and tensile strength. This slow development is most likely due to the fact that fracture energy depends largely on bond strength, which, as stated previously, is affected by the tensile strengths and elastic modulus of the UHPC mix. Figure 2.26 shows the time rate of development of the fracture energy reported in untreated UHPC by Habel et al. (2006b). The tensile and compressive strength and elastic modulus rates of development are also included for comparison purposes. The increase in fracture energy is 93 percent from seven to 56 days for untreated UHPC.

Since normal concrete and HPC exhibit virtually no post-cracking flexural strength, the fracture energy of UHPC is relatively very high. Gilliland (1996) estimates the fracture energy of UHPC to be 250 times that of typical HPC, and Richard and Cheyrezy (1994) report the fracture energy of normal concrete to be only 0.0006 (110 J/m^2).

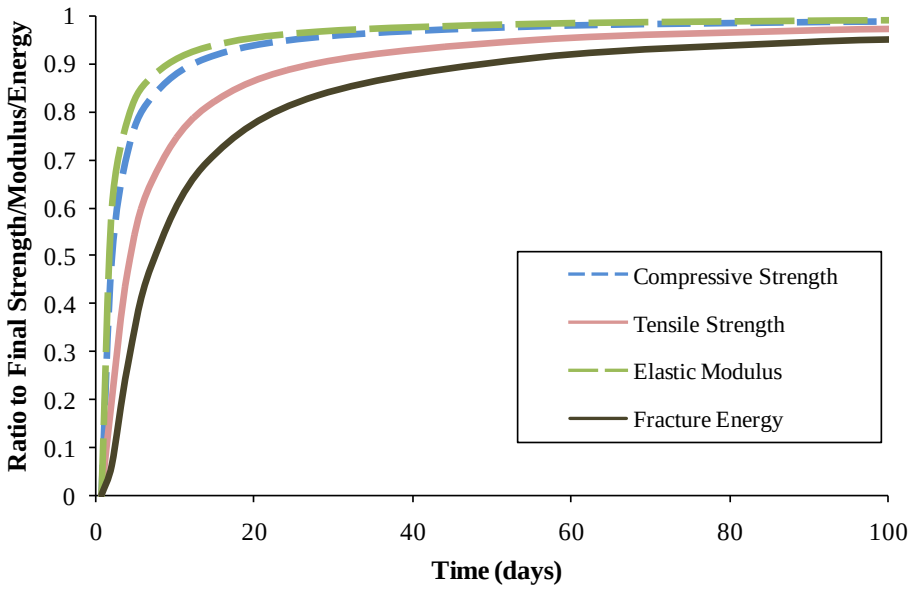

Figure 2.26. Development of fracture energy and other properties of untreated UHPC without heat treatment (after Habel et al. 2006b)

2.4.9. Strain Limits

2.4.9.1 Compression

Graybeal (2006) notes that the compressive stress-strain response of heat-treated UHPC deviates from linearity by five percent before the peak compressive stress is reached – at a strain of 3620×10^{-6} compared to the strain of 4100×10^{-6} at peak stress. Graybeal also reports that the strain of untreated UHPC at its peak compressive stress is slightly lower at 3500×10^{-6}. According to Sritharan et al. (2003), however, linear elastic behavior of heat-treated UHPC occurs essentially up to failure, which corresponds to a compressive strain of 3200×10^{-6} in their study. Dugat et al. (1996) agree that the strain of heat-treated UHPC at peak compressive stress is 3200×10^{-6}, but Gowripalan and Gilbert (2000) and Ma et al. (2004) place it slightly higher at 3500×10^{-6} and 4400×10^{-6}, respectively.

2.4.9.2 Flexural Tension

For flexural loading, close agreement can be found between reported results for cracking tensile strain. Graybeal (2005) estimates the cracking strain as 300×10^{-6}, compared to 321×10^{-6} by Sritharan et al. (2003) and 330×10^{-6} by Dugat et al. (1996). The ultimate

tensile strain is estimated as 5000×10^{-6} to 7000×10^{-6} by Richard and Cheyrezy (1995) and as 7500×10^{-6} by Dugat et al. (1996). Gowripalan and Gilbert (2000) offer Equation 2.11 to estimate the ultimate tensile strain of a UHPC member in bending. Note that for the typical 0.5-in. (13-mm) fibers used in UHPC, any beam with a depth of 50 in. (130 mm) or less would have an ultimate tensile strain of $10{,}000\times10^{-6}$ according to Equation 2.11.

$$\varepsilon_{tu} = {L_f}/{1.2\cdot D} \le 0.01 \tag{2.11}$$

where L_f = length of fibers and D = depth of beam

2.4.10. Deflection Behavior

Klemens notes that as UHPC undergoes well-dispersed micro-cracking as it experiences large deflections, rather than developing large localized cracks (Klemens 2004). Figure 2.27 shows micro-cracking due to a flexural test on a UHPC prism. During tests by the Federal Highway Administration (FHWA) (2002), a 36-in. (91-cm) deep, 80-ft (24-m) long UHPC bridge girder deflected 12 in. (250 mm) without forming any visible cracks, even under three times magnification. The total deflection in the girder was approximately 19 in. (480 mm) before flexural failure. The girder is shown in Figure 2.28 at 17 in. (430 mm) of deflection.

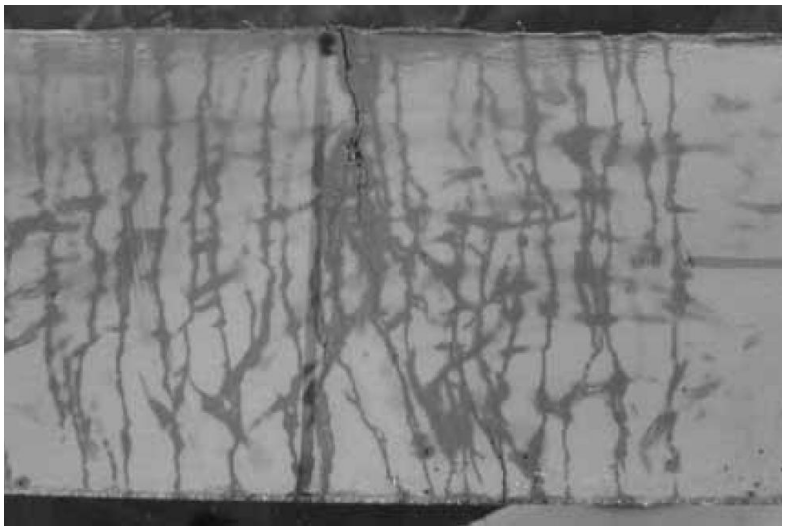

Figure 2.27. Micro-cracking observed during a flexural prism test (Acker and Behloul 2004)

Figure 2.28. An 80-ft (24-m) girder showing a deflection of 17 in. (430 mm) (Graybeal 2005)

2.5. 5. APPLICATIONS

Applications utilizing UHPC have begun to display the uses and potential challenges presented by the material. A summary of some of the applications of UHPC is presented in this section.

2.5.1. General Advantages

Since UHPC can lead to longer span structures with reduced member sizes compared to normal or high strength concrete, a significant reduction in volume and self weight should be expected with UHPC members. Figure 2.29 shows UHPC, steel, prestressed, and reinforced concrete beams with equal moment capacities. Interestingly, the UHPC beam requires only half the section depth of the reinforced or prestressed concrete beams, which in turn reduced its weight by 70 percent or more. The UHPC beam also has the same section depth as the steel beam, which, in this case, is only slightly lighter than the UHPC member.

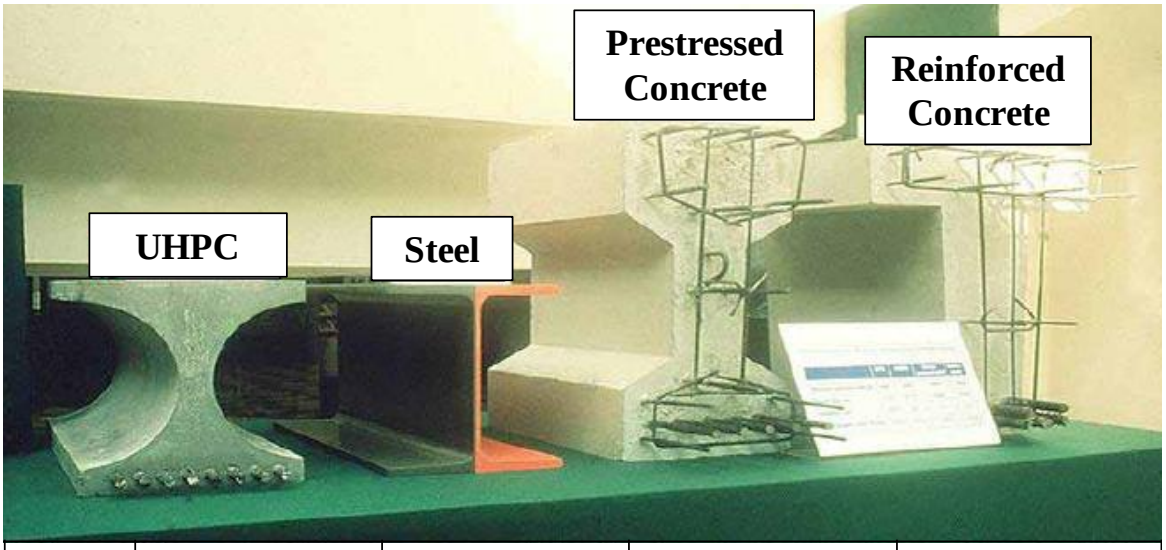

Material	UHPC	Steel	Prestressed Concrete	Reinforced Concrete
Depth	14 in. (360 mm)	14 in. (360 mm)	28 in. (700 mm)	28 in. (700 mm)
Weight	94 lb/ft (141 kg/m)	75 lb/ft (110 kg/m)	313 lb/ft (466 kg/m)	355 lb/ft (528 kg/m)

Figure 2.29. UHPC, steel, prestressed, and reinforced concrete beams with equal moment capacities (after Perry 2006)

Savings in the total amount of materials required may also be realized with UHPC in other types of applications besides flexural members. The cross-sectional area of UHPC compressive members may be reduced compared to normal concrete due to UHPC's high compressive strength, although the reduction in cross-section for those members may be restricted by slenderness ratios. By using UHPC, the cross-sectional area of some 55-ft (17-m) tall columns in a cement silo in Detroit, Michigan, were reduced by 75 percent compared to normal concrete (Klemens 2004). These reductions in material accompany reductions in dead weight and increases in usable floor or overhead space. Figure 2.30 shows UHPC may also be used to reduce cross-sectional area compared to normal concrete in piping applications.

The superior durability properties of UHPC are also advantageous in terms of service life and reduced maintenance costs. Many of the typical deterioration problems associated with concrete reinforcement can be alleviated in UHPC due to its dense matrix and the reduction or elimination of steel reinforcement that is typically required in concrete members.

Figure 2.30. Reduction in pipe wall thickness of UHPC (right) compared to an equivalent pipe in normal concrete (left) (Droll 2004)

UHPC can be a very visually appealing building material as well. The smaller cross-sections can lead to a more elegant appearance for the structure. The high strengths even allow for previously impossible geometries to be constructed, some of which can be accomplished without the use of any steel reinforcement. UHPC can also be given a high-quality surface finish due to the fineness of the matrix. UHPC can even be painted with a synthetic painting technique similar to that used by the auto industry (Dowd and Dauriac 1996).

2.5.2. Workability

As noted previously, the workability of normal concrete is usually significantly reduced when fibers are included in the mix. Due to the fineness of the constituents of UHPC, however, interference issues between aggregates and fibers do not exist to the same degree as they do in concretes with coarse aggregates. Therefore a reduction in workability is only expected when fiber contents greater than 2.5 to 4.0 percent by volume are used (Bonneau et al. 1997, Nielsen 1998, Rossi 2005). In fact, UHPC can be practically self-placing, requiring no internal vibration. External vibration may be required for some UHPC applications, but simply vibrating the forms for a short time will cause the material to flow easily into place (FHWA 2002).

2.5.3. Constructability

2.5.3.1 Precast Applications

The lighter weight and reduced sizes of many UHPC members also allows UHPC members to be transported more easily than larger normal concrete members and the use of lighter capacity cranes when placing precast UHPC members. The high early strength and rapid strength development allow pretensioning to be applied in UHPC members at an early age (Holschemacher and Klotz 2003). This feature combined with the benefits of curing UHPC through heat treatment makes this material well suited for precast applications. However, precasters who have not yet worked with the material have many concerns about casting UHPC in their plants using existing equipment. Bierwagen and Abu-Hawash (2005) summarize the following precaster concerns about UHPC:

- the high cost for UHPC, which is discussed in detail in Section 2.5.5, means that any wasted material or rejected elements constitute a more significant loss;
- the time required to batch a mix is longer, and the time required to clean the mixers is also longer due to the use of large amounts of sand and fibers;
- the high energy mixing required could damage the mixers;
- the entire concrete quantity to be cast for a member must be produced before placement can begin;
- The high shrinkage requires modification of forms or specifically timed releases of prestressing strands and form removal; and
- long setting and curing time ties up the precasting beds for a longer period.

Bierwagen et al. also reported that the compressive strength at release, which was 14 ksi (97 MPa), was too low compared to the 28-day strength to allow designers to take full advantage of the 28-day strength (Bierwagen and Abu-Hawash 2005).

Despite the concerns listed above, UHPC members have been successfully cast in precasting plants, including the casting of the members for the Sherbrooke pedestrian bridge in Sherbrooke, Canada (Aïtcin et al. 2000). Despite the possible challenges in the precasting process, most researchers agree that precast, prestressed applications represent the greatest

potential for UHPC production since the heat treatment of precast members can be easily achieved and since the high compressive strength of UHPC allows the material to be heavily prestressed to improve tensile capacity (Richard and Cheyrezy 1995).

2.5.3.2 Cast-in-Place Applications

A significant advantage in UHPC in cast-in-place applications can be realized over normal or high performance concrete since large amounts of the reinforcement typically required in concrete members can be eliminated with the use of UHPC, greatly expediting the construction process. A concern with UHPC application, when compared to normal concrete in cast-in-place construction, is that care must be taken to ensure adequate dispersion of fibers throughout the cast-in-place members.

2.5.4. Sustainability

2.5.4.1 Material Requirements

The use of UHPC may translate to savings in the total materials required for the design of various structures. Although UHPC has a higher cement content per cubic yard than normal concrete, structural members typically require fewer cubic yards of material, and as a result, the total quantity of cement used is about the same or perhaps even less for UHPC design solutions than those from normal concrete (Walraven 2002). Walraven also estimates that the total amount of aggregates, in which he includes both fine and coarse aggregates, used in structural members may be decreased by 30 percent with the use of UHPC compared to normal concrete. (Note that the amount of coarse aggregates is reduced 100 percent.) Racky (2004), in his own study, determined that while the cement content in UHPC may be as much as twice that in normal concrete, the amount of UHPC required for a large column application was only 44 percent of the normal concrete alternative, which supports Walraven's hypothesis.

Fly ashes used in UHPC can also be obtained as by-products from the power industry. By employing material that would otherwise be wasted, UHPC represents a step towards sustainability. The use of more mineral components and powders in place of cement for

concrete applications is a step toward sustainability and helps to meet the sustainability mandates that may soon be implemented by some government agencies (Aïtcin 2000).

2.5.4.2 Lifecycle

Although too few applications of UHPC currently exist to allow a reliable comparison with normal concrete for average life-cycle durations and costs, most researchers agree the excellent durability properties of UHPC should increase the longetivity of structures while minimizing maintenance costs (Racky 2004; Blais and Couture 1999). Aïtcin (2000) notes that unlike normal concrete, UHPC can be recycled several times before being used as granular road base. This recyclability is attributed to the fact that not all of the cement in UHPC is hydrated during hardening, and unhydrated cement is therefore available for future reactions.

2.5.5. Cost

2.5.5.1 Comparison over Time

UHPC is much more expensive than normal concrete. Much of the cost of UHPC comes from its steel fiber reinforcement, so the cost of the material is largely contingent on the cost of this component. In 1996, Bonneau et al. (1996) estimated the price of UHPC with fibers in Europe as \$1070/yd^3 (\$1400/m^3). Aïtcin (2000) reported a lower 1996 price of UHPC in Europe at \$760/yd^3 (\$1000/m^3). Aïtcin reported the price had decreased to \$570/yd^3 (\$750/m^3) by the year 2000, which agrees fairly closely with Blais and Couture (1999) who reported a price of \$250/ton (\$246/tonne) or \$520/yd^3 (\$750/m^3) in 1999. As usage of UHPC becomes more common, the cost per cubic yard is expected to decrease significantly. Aïtcin (2000) predicts the cost of UHPC will soon reduce to \$460/yd^3 to \$500/yd^3 (\$600/m^3 to \$650/m^3) in Europe. The cost of UHPC in North America as of the year 2007 was comparatively high at approximately \$2000/yd^3 (\$2620/m^3) but is also expected to reduce with increased application in North America.

2.5.5.2 Comparison with Other Materials

According to the Engineering News Record (ENR) (2008), the average cost of a cubic yard (0.76 m^3) of 5000 psi (35 MPa) concrete in 20 United States cities was \$99 in January

2008. If $570/yd^3 ($750/m^3) is used as the cost for UHPC, UHPC is 5.8 times more expensive than normal concrete on a volumetric basis. Many argue, however, that the ability to use a lower volume of UHPC and the superior performance of the material warrant a comparison not volumetrically with normal concrete but by weight with steel. ENR (2007) reports the average cost of 100 lb (45 kg) of structural steel as $41 in November 2007. Assuming a 150 lb/ft^3 (2400 kg/m^3) unit weight for normal concrete, 155 lb/ft^3 (2480 kg/m^3) for UHPC, and 490 lb/ft^3 (7850 kg/m^3) for steel, the prices of each material per ton (1.02 tonne) can be compared, as shown in Table 2.11.

Table 2.11. Cost per unit weight comparison of normal concrete, UHPC, and structural steel

Material	Cost	Ratio to UHPC
Normal Concrete	$49/ton ($48/tonne)	1:5.6
UHPC	$270/ton ($270/tonne)	1:1
Structural Steel	$810/ton ($800/tonne)	3.0:1

2.5.5.3 Other Cost Factors

Additional cost advantages with UHPC over normal concrete include reduced construction times and increased usable floor space or overhead clearance. The use of longer spans with UHPC members could reduce the number of required piers and pier foundations for some bridge applications. The predicted longer service life and lower maintenance costs of UHPC could lead to even more cost benefits of UHPC. Also, increasing lead times required for structural steel may lead to cost advantages for UHPC in addition to the possible cost per unit weight advantage outlined above.

Interestingly, Aïtcin (2000) reports that the Quebec Ministry of Transportation determined that the initial cost of an 8 ksi (55 MPa) bridge was eight percent less than that of an identical 5 ksi (35 MPa) bridge without taking increased service life into account. Therefore, it is reasonable to expect a cost saving when using ultra high performance materials like UHPC.

2.5.6. Optimization

As noted in the introduction to this literature review, increases in concrete strength have not been accompanied by immediate applications in structural design. New materials like UHPC with their associated higher costs and greater uncertainties need to be optimized to make them competitive with current materials. Optimization of structural sections can be a challenge because as section dimensions are reduced, the stiffness of the member may also be reduced. UHPC, however, has a high elastic modulus, so the stiffness of normal concrete and UHPC members may be similar.

Spasojevic (2006a) recognized that excessive optimization of a material for a certain stress range may cause deflection criteria to control the design of a structural member rather than strength criteria. Spasojevic applied topological optimization, a procedure used to find a structural shape with maximum stiffness for a given volume of material, to design optimized UHPC cross-sections. Her research indicates a ribbed slab may be a possible optimized application of UHPC for bridge decks.

Others have speculated that the hourglass or X-shaped beam, shown in Figure 2.29, may be an optimal shape for UHPC beams (Dowd and Dauriac 1996). Bonneau et al. (1996) conducted a comparative study between UHPC and normal concrete box girders. This study indicated that a box girder with the same depth, top area, and required loading could be constructed with a cross-section using 38.2 ft^2 (3.55 m^2) of UHPC compared to a 111.4 ft^2 (10.35 m^2) cross-section using normal concrete. By this optimization, UHPC requires three times less material than normal concrete, and the resulting UHPC girder is much lighter than the normal concrete alternative.

2.5.7. Constructed Applications

UHPC has already been implemented in many construction projects around the world. A summary of projects in which UHPC has been successfully used is presented in this section.

2.5.7.1 First Uses of UHPC

UHPC (specifically in the form of RPC or Ductal®) was developed in the 1990s by three French companies: Bouygues, Lafarge, and Rhodia (Brown 2006). The first structure in the world to be constructed out of this type of UHPC was a pedestrian and bicycle bridge over the Magog River in Sherbrooke, Quebec in July 1997 (Blais and Couture 1999; Dowd and Dauriac 1996). This structure is one of the highlighted projects discussed in more detail in a following section. Another early use of the material was precast, prestressed UHPC beams and girders for a cooling tower at the Cottenom Nuclear Power Plant in France in 1999 (Lafarge North America 2007). Figure 2.31 shows some of the casting beds for the 2,600 precast UHPC beams and girders that were produced for the exchange body of the cooling tower. UHPC was chosen by Electricité de France for this project as a lightweight and durable alternative that would reduce foundation loads and yet be able to withstand freeze-thaw cycles in an aggressive environment.

Figure 2.31. View of precasting area for UHPC beams for Cottenom Nuclear Power Plant (Lafarge North America 2007)

Some of the earliest research into designing UHPC mixes was conducted to develop a material for use as the inner wedge and outer barrel in a nonmetallic anchorage system, according to Reda et al. (1999). UHPC has been used for anchor blocks in seawall anchors on Reunion Island, where 6300 plates were used to stabilize a sea wall (see Figure 2.32). The UHPC plates were cost competitive with the cast iron alternative, and the low maintenance associated with the durability of UHPC led to additional cost savings of 18 percent (Lafarge

North America 2007). UHPC anchors, also shown in Figure 2.32, were used in Calgary, Alberta, Canada for a post-tensioned, soil anchor precast retaining wall system in front of a bridge abutment.

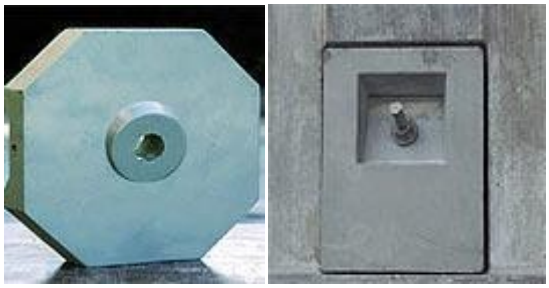

Figure 2.32. Anchor plates for seawall on Reunion Island (left) and soil wall in Calgary (right) (Lafarge North America 2007)

2.5.7.2 Bridges

As mentioned previously, the first UHPC structure in the world was a pedestrian bridge in Sherbrooke, Canada, completed in 1997. In 2002, another UHPC pedestrian bridge, the Footbridge of Peace in Seoul, South Korea, was inaugurated (Lafarge 2007). By using UHPC, the designers were able to create a very elegant 400-ft (120-m) long concrete arch bridge. The bridge uses a 4-ft (1.1-m) deep pi-shaped girder section. The deck is 17-ft (4.3-m) wide and only 1¼-in. (3-cm) thick (Lafarge North America 2007).

UHPC was used for the first time in Japan in the Sakata Mirai footbridge, a 164-ft (50-m) long single-span structure completed in 2002 (Lafarge 2007). The Sakata Mirai bridge uses external prestressing, and the total weight of the bridge is only about one fifth of the weight of an equivalent normal concrete structure (Rebentrost and Cavill 2006). The Yokemuri footbridge has also been constructed with UHPC in Yagamata, Japan. UHPC was chosen for this 116-ft (35-m) long, 37-in. (95-cm) deep box girder bridge because of its resistance to the extreme temperature changes in the region (Lafarge 2007).

In Auckland, New Zealand, footbridges have been constructed out of UHPC at Papatoetoe and Penrose light-rail transit (LRT) stations (Rebentrost and Cavill 2006). The footbridges each consist of multiple 66-ft (20-m) pi-shaped girder spans, and they serve as pedestrian railway crossings. Each span consists of two post-tensioned match-cast UHPC

segments. The main advantage of the UHPC spans is the reduced weight, which results in reduced seismic forces, easier erection, and reduced loads on the substructures.

A UHPC footbridge has also been constructed in the Chryso plant in Sermaises, France (Lafarge 2007). The 62-ft (19-m) walkway is supported on pillars and contains no reinforcement. It was chosen instead of the traditional wood and steel alternative and can carry six times the required design load. UHPC's fire resistance properties, discussed previously in Section 2.2.2.6, are particularly important in this application, considering the close proximity of large quantities of chemicals.

Schmidt and Fehling (2005) report that Germany has also constructed a long-span UHPC pedestrian bridge. They also identify UHPC vehicular road bridges in Germany and the Netherlands but do not give many details of these bridges. The first UHPC vehicular bridge in North America, the Mars Hill Bridge, was constructed in Wapello County, Iowa, United States (Brown 2006). The Mars Hill Bridge is one of the highlighted UHPC projects and is described in more detail in a later section.

The Shepherd Creek Road Bridge in New South Wales, Australia, has been constructed using UHPC beams and permanent UHPC formwork panels overlain by a reinforced concrete deck (Rebentrost and Cavill 2006). The four-lane bridge uses 24-in. (600-mm) deep, 49-ft (15-m) long UHPC beams spaced 4.3 ft (1.3 m) apart. The weight of the UHPC beams was reported to be half much as the alternative normal concrete beams, and the UHPC formwork panels were only 1.0-in. (25-mm) thick.

UHPC in the form of BSI or Ceracem has been used for two bridges over a highway near the city of Bourg-Lès-Valence, France (Semioli 2001). A 62-ft (19-m) long UHPC bridge over a railroad has also been constructed in Saint-Pierre-la-Cour, France (Billon 2006). The 41-ft (12.6-m) wide bridge supports a continuous reinforced concrete road and a bicycle lane and weighs half as much as the normal concrete alternative. Figure 2.33 shows some of the bridges and footbridges described above.

2.5.7.3 Columns

Four UHPC columns were used to support an elevated floor in a cement silo in Detroit, Michigan, United States (Lafarge North America 2006b). The 55-ft (17-m) tall

columns are 30-in. (76-cm) square and reinforced with only four ½-in. (13-mm) diameter prestressing strands. The columns were a quarter of the size of the normal concrete alternative and were erected in just one day. UHPC was also used in columns in the Queen Sofia Museum in Madrid, Spain (Lafarge 2007). The 13-in. (32-cm) diameter steel columns were filled with UHPC, representing the first cast-in-place UHPC project. The addition of UHPC increased the flexural and compressive capacity of the 52-ft. (16-m) tall columns.

Figure 2.33. Examples of UHPC bridges and footbridges: a) Footbridge of Peace in South Korea, b) Shepherd Creek Road Bridge in Australia, c) Sakata Mirai footbridge in Japan, and d) Papatoetoe footbridge in New Zealand (Perry 2006, Lafarge 2007, Billon 2006)

2.5.7.4 Roofs and Canopies

The first long-span roof in the world made from UHPC was completed in 2001 on a clinker silo in Joppa, Illinois, United States (Construction Innovation Forum 2003). The light weight of the UHPC roof did not negatively impact the foundation design of the 58-ft (18-m) diameter silo. The roof consists of 24, ½-in. (13-mm) thick ribbed panels, which support a mechanical penthouse. The UHPC roof took only 11 days to install, compared to 35 days for steel roofs on nearby silos.

One of the most famous UHPC structures in the world is the Shawnessy LRT station in Calgary, Canada, shown in Figure 2.34. The design flexibility afforded by UHPC allowed the architect to fulfill their desire for a free-flowing form design for this structure. Full-scale load tests were used to ensure the satisfactory behavior of the 24 UHPC architectural shell canopies that were used for the station prior to their installation. The canopies are only 0.79-in (20-mm) thick and shield waiting passengers from the weather (Perry 2006). Each pair of canopy pieces is supported on a single UHPC column.

Figure 2.34. Shawnessy LRT station with UHPC canopies (Perry 2006)

2.5.7.5 Urban Environment

UHPC has been used to manufacture acoustic panels for the Monaco underground train station (Lafarge North America 2007). The thin and light UHPC panels were cast with small holes to aid in their acoustic properties. The nonflammable panels are resistant to impact and create an aesthetically pleasing, bright environment for passengers. Acoustic panels have also been used along a roadway in Châtellerault, France, because of their resistance to car pollution and de-icing salts (Lafarge 2007).

UHPC has been used for façade panels for the Rhodia Research Center in Aubervilliers, France (Lafarge 2007). UHPC can also be made into decorative panels, since the panels can be cast with many different surface finishes and can be dyed or painted. UHPC also finds applications in sculptures, most notably the Martel Tree in Boulogne-

Billancourt, France (Lafarge North America 2007). The tree, shown in Figure 2.35, is made entirely out of UHPC, and some pieces of the structure feature a member thickness of only 2.5 in. (6 cm).

Figure 2.35. Martel Tree sculpture made of UHPC (Deem 2002)

UHPC can also be used for urban furniture. One example is eight bus shelters in Tucson, Arizona, United States, that protect passengers from extreme sun and heat (Lafarge North America 2006). A white UHPC premix with organic fibers was used, and it was selected as the best solution compared to six other construction materials. Other urban furniture includes benches and planters (Perry 2006). UHPC can also be used for interior furnishings, including tables, chairs, countertops, sinks, planters, tiles, and even security-type applications like safes (Perry 2006).

2.5.8. Researched Applications

2.5.8.1 Bridge Components

Because of their high loads, long spans, and sometimes harsh environments, bridges represent one of the areas of greatest potential for UHPC. Some of the completed or ongoing research on using UHPC in bridge applications includes:

- Steel-free post-tensioning: some of the first research involving UHPC was directed to develop nonmetallic anchorage systems, as noted previously (Reda et al. 1999).
- Steel-free bridge decks: composite panels composed of UHPC and cast-in-place fiber-reinforced concrete (FRC) show strong potential according to research by Hassan and Kawakami (2005).
- Ribbed deck slabs: an optimized UHPC deck consisting of a ribbed upper slab could be used for box girder bridges. The resulting system would provide a reduction in weight while maintaining sufficient stiffness and easy prefabricated construction (Spasojevic 2006a).
- Box girders: a UHPC box girder with the same depth, load requirements, and top area could be constructed with only one third of the total amount of material compared to normal concrete, as previously noted (Bonneau et al. 1996).
- Π-shaped girders: two 70-ft (21.3-m) long, 8-ft (2.4-m) wide Π-shaped girders have been designed by researchers at the Massachusetts Institute of Technology (MIT) and installed in an experimental test bridge at FHWA's testing facility in McLean, Virginia, United States (Lafarge 2007).
- Protective layers: UHPC may be used compositely on normal concrete structures to protect them. One concept uses UHPC for an abrasion layer and for the curb, barrier, and deck edge on a normal concrete box girder (Cadoni et al. 2004).

2.5.8.2 Other Structures

The dual benefits of high strength and high durability give UHPC potential for a wide variety of uses. Some of the research on non-bridge structural members includes:

- Impact-resistant structures: research on the CRC type of UHPC indicates the material is less sensitive than normal strength FRC to impact loading rate (Bindiganavile et al. 2002).
- Earthquake-resistant structures: research is being conducted on using prestressed UHPC elements for earthquake-resistant structures because of UHPC's high strength and ductility (Deem 2002).

- Spherical dome roof: a 390-ft (120-m) diameter dome has been designed using 1.2-in. (30-mm) thick stiffened UHPC plates and post-tensioned arching beams (Cheyrezy 1999).
- Railway walkway braces: the deterioration of existing concrete footwalk braces led to consideration of UHPC as an alternative. The ductility of UHPC provides warning to maintenance staff before the walkway braces fail (Yan and Yan 2006).
- Nuclear waste containers: containers used for storage of radioactive waste are required to resist impact without losing integrity. UHPC is being considered since current FRC containers do not meet requirements (Toutlemonde and Sercombe 1999).
- Hot water tanks for solar energy storage: the high density of UHPC and its high strength and ability to be used in prefabricated shell elements make it a promising material for underground hot-water tanks (Reineck et al. 2004).
- Well cover plates: UHPC has been researched as a ductile and cost-effective alternative to cast-iron cover plates on wells and underground civil structures (Feng et al. 2006).

2.5.8.3 Theorized Applications

Some applications of UHPC have not actually been researched at this point but are interesting areas of possible future research and application. These theorized applications include the following:

- tunnel liners (Dallaire et al. 1998);
- reservoirs, caissons, and coatings (Roux et al. 1996);
- gas tanks, defense shelters, bunkers, structures of military and strategic importance, crash barriers, and heavy-duty runways (Bindiganavile et al. 2002); and
- heavily loaded industrial floors and transportation routes, sheet piling, and flood barriers (Schmidt et al. 2003).

2.5.9. Highlighted Projects

2.5.9.1 Sherbrooke Pedestrian Bridge

The UHPC pedestrian bridge in Sherbrooke, Canada, is a 10-ft. (3.0-m) deep open-web space truss spanning 197 ft (60 m) (Blais and Couture 1999). The deck acts as the top chord of the truss, while a double beam is used as the bottom chord. The truss diagonals are sloped in two directions.

The deck in this bridge is 1.2-in. (30-mm) thick and 11-ft (3.3-m) wide. The deck has two longitudinal ribs, each with an 8×12 in. (200×300 mm) cross-section, and transverse stiffening ribs at 4.1-ft (1.25-m) spacing. The diagonal members are 10.5-ft (3.2-m) long and 6-in. (150-mm) in diameter and use specially designed mini-anchorages to connect them with the chords because of the space limitations in the chords. Each diagonal member uses only two greased and sheathed ½-in. (13-mm) diameter strands for prestressing. Post-tensioning in the bridge consists of two tendons in the top chord, one in each longitudinal rib, and two tendons in each of the two bottom chords, as shown in Figure 2.36. Three other sets of longitudinal tendons, each containing two tendons, are also harped along the length of the bridge.

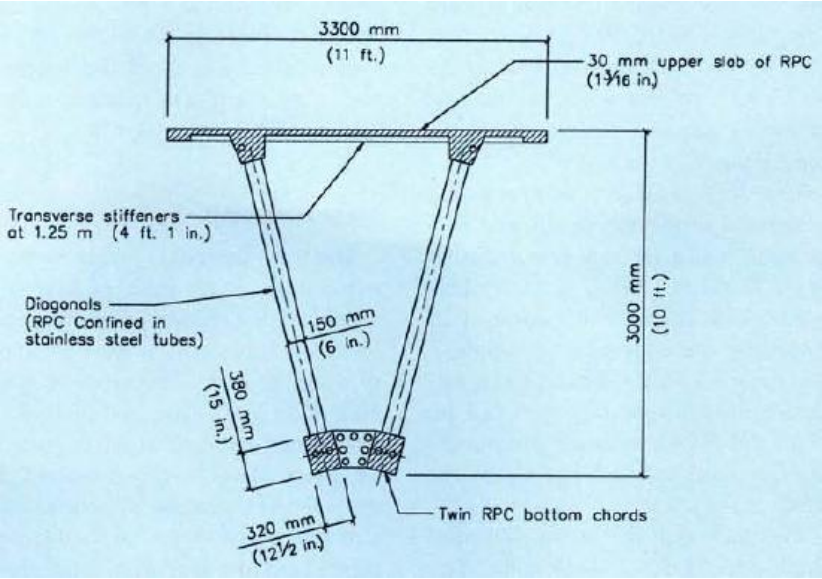

Figure 2.36. Cross-section of Sherbrooke bridge truss (Blais and Couture 1999)

The UHPC used in the Sherbrooke bridge has a compressive strength of 29 ksi (200 MPa). The UHPC in the diagonals of the bridge, however, was confined in 0.08-in. (2-mm) thick stainless steel tubes to achieve a compressive strength of 50 ksi (345 MPa). Since this bridge was the first UHPC structure in the world, it was designed conservatively. During the design of the bridge, no tension was permitted in the diagonal members at the service or ultimate limit states, and no tension was permitted in the bottom chord at the service limit state.

The bridge was prefabricated in six segments, each 33-ft (10-m) long. Adjoining segments of the bridge were match-cast to ensure a close fit. The quality control program at the precasting plant proved that it was possible to produce UHPC with specified properties consistently throughout the casting process, even for large members. Figure 2.37 shows a freshly cast UHPC segment for the Sherbrooke bridge.

Figure 2.37. Sherbrooke bridge segment just after form removal (Blais and Couture 1999)

A single additional post-tensioned tendon was used to tie the three segments in each half of the bridge together at the site before erection. Each half segment of the bridge weighed only 55 tons (50 tonnes) and thus could be lifted and placed with ordinary cranes. The on-site erection time was reduced to less than four days. Figure 2.38 shows the placement of the second half segment of the bridge, while Figure 2.39 shows the completed pedestrian bridge.

Figure 2.38. Placement of the second half segment of the Sherbrooke bridge on the falsework bent (Blais and Couture 1999)

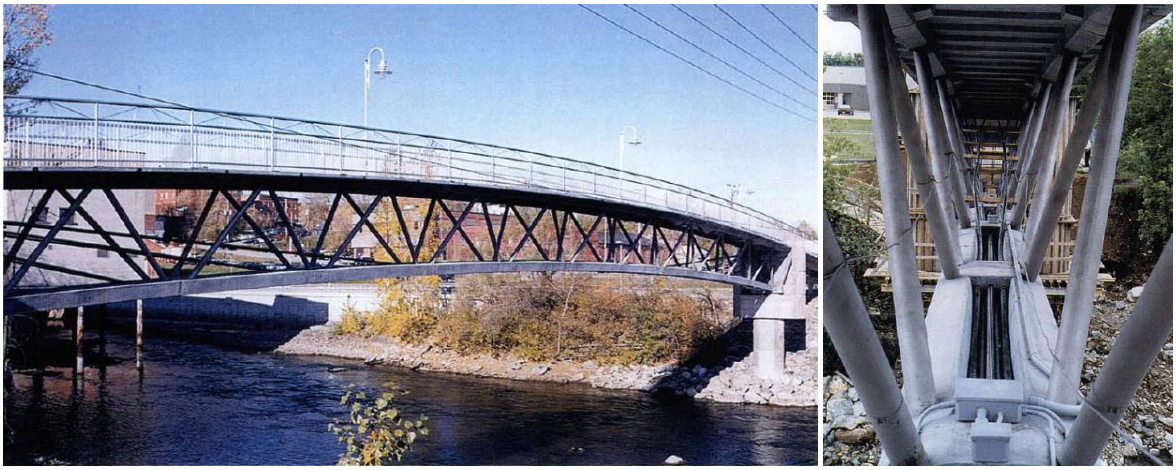

Figure 2.39. Views of the completed Sherbrooke pedestrian bridge (Blais and Couture 1999)

2.5.9.2 Wapello County Mars Hill Bridge

The Mars Hill Bridge in Wapello County, Iowa, United States, is the first UHPC vehicular bridge in North America. The UHPC bridge resulted from efforts of researchers at Iowa State University's (ISU) Center for Transportation Research and Education (CTRE)

seeking an opportunity to use UHPC in a real application (Bierwagen and Abu-Hawash 2005). The bridge is 110-ft (33.5-m) long and has a 24.5-ft (7.5-m) wide roadway.

The dimensions and strand layout of the UHPC girders of this bridge are shown in Figure 2.40. The girders used for the bridge are based on a standard 45-in. (1140-mm) deep bulb tee girder commonly used in Iowa. The section was modified by reducing the thickness of the top flange by 1.0 in. (25 mm), and the web and bottom flange each by 2.0 in. (51 mm), for an overall depth of 42 in. (1070 mm). The beams included 49, 0.6-in. (15-mm) diameter prestressing strands, five of which were draped. Sixteen of the strands were also debonded in the end regions to prevent development of excessive tensile stresses in the girders due to prestressing.

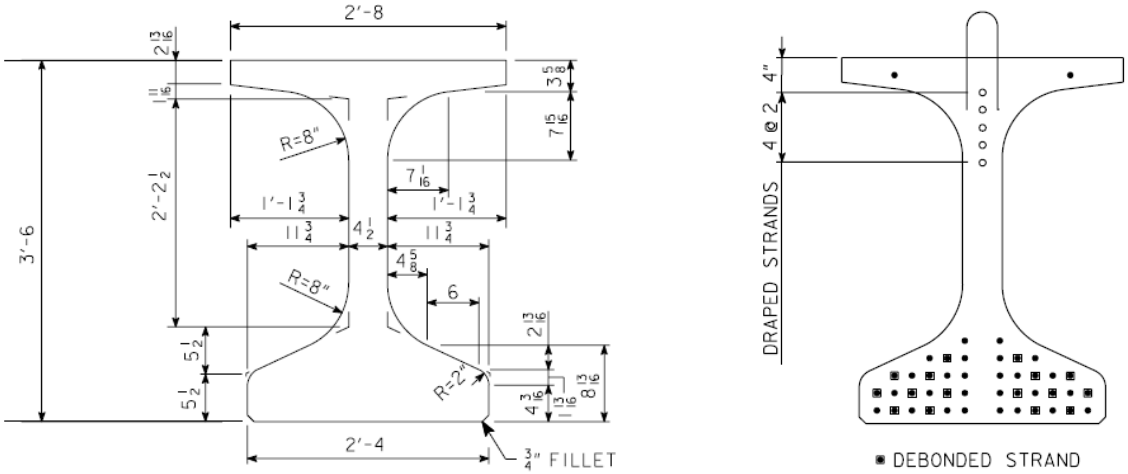

All dimensions in inches

Figure 2.40. UHPC girder dimensions and strand layout for Mars Hill Bridge in Iowa (Bierwagen and Abu-Hawash 2005, Degen 2006)

The Mars Hill Bridge used only three girders at 9 ft, 7 in. (2.9 m) spacing with 4 ft (1.2 m) overhangs. The bridge would have required four girders and three spans (instead of one) if it had been designed with normal concrete. The UHPC girders contained no mild steel apart from the U-shaped bars used near the top to ensure composite action with the 8-in. (200-mm) thick cast-in-place normal concrete deck.

Researchers at ISU also tested a 71-ft (22-m) long UHPC girder to verify the flexural and shear behavior prior to the construction of the actual bridge (Degen 2006). The UHPC

girders for the test and for the actual bridge were cast in Winnipeg, Manitoba, Canada (Brown 2006). Construction of the Mars Hill Bridge began in August 2005, and the bridge was opened for public use in January 2006. Figure 2.41 shows the completed Mars Hill Bridge.

Figure 2.41. A view of completed Mars Hill Bridge (Bridge Engineering Center 2007)

2.5.9.3 Prefabricated Concrete Sheet Piles with Steel Fibers

Grünewald (2004) performed experiments on self-compacting fiber-reinforced concrete (SCFRC) to develop a mix suitable for applications in precast sheet piles. To be able to use thin walls for the prestressed sheet piles, Grünewald actually applied many of the same principles used in UHPC. He reduced the length of the steel fibers to only 0.5 in. (13 mm) and limited the maximum aggregate size to 0.04 in (1 mm), making the mix somewhat similar to UHPC. The mix contained slightly less silica fume than the amount typically used in UHPC, however, and no heat treatment was applied during curing.

Nonetheless, the SCFRC was able to achieve a compressive strength of 10.8 ksi (74.3 MPa) only 24 hours after casting and 19.5 ksi (134.3 MPa) at 28 days. The reported tensile strength was about 0.9 ksi (6 MPa) at one day and 2.0 ksi (13.5 MPa) at 28 days (Walraven 2004). Each sheet pile segment was prestressed with 18, ½-in. (13-mm) prestressing strands (Grünewald 2004). The optimized sheet pile had a flange thickness of only 2.0 in. (50 mm), and a web thickness of 1.8 in. (45 mm), providing a concrete cover thickness of only 0.63 in. (16 mm) for the prestressing strands. Figure 2.42 depicts the prestressing strands and partial

formwork used for the SCFRC sheet piles, which used about one third of the volume of material that the conventional 4.7-in. (120-mm) thick, 9.4 ksi (65 MPa) concrete sheet piles would require (Walraven 2004). A SCFRC sheet pile is shown next to conventional concrete sheet piles in Figure 2.43.

Figure 2.42. Prestressing strands and formwork used for production of SCFRC sheet piles (Walraven 2007)

Figure 2.43. Comparison of a) SCFRC and b) conventional concrete sheet piles (Grünewald 2004)

Additional advantages of the SCFRC piles over conventional concrete sheet piles include the absence of any mild reinforcement, the ability to be stacked, easy handling, the ability to be transported in larger quantities, and improved driveability into the ground

(Grünewald 2004). The price of the SCFRC sheet piles was reported to be comparable to that of the conventional concrete alternative (Walraven 2004).

The confined spaces in the formwork for the SCFRC piles actually caused the fibers to orient with the longitudinal flow through the forms as the material was poured from the top. The tensile properties of the piles in the longitudinal direction were thus increased, but the tensile strength in the transverse direction, which is important for the shear keys that connected the flanges of adjoining sheet piles, was not benefited by this fiber orientation. Tests showed, however that the shear capacity of the keys was still sufficient.

A total of six SCFRC sheet piles were cast, and three were driven into the ground with a vibratory hammer, as shown in Figure 2.44 (Grünewald 2004). The installation time for each of the 41-ft (12.5-m) long piles was only seven to 15 minutes. The installation process was not modified for the thin-walled SCFRC sheet piles, and the connections (shear keys), experienced only very minor damage. Grünewald reported that the sheet piles performed as expected, although details of further tests are not given.

2.6. PILE DESIGN

Piles are generally used in groups, but the design of piles is typically based on the capacity of a single pile in soil. The design of a single pile may be governed by the geotechnical resistance that the soil can provide or by the structural resistance of the pile.

2.6.1. Geotechnical Resistance

Piles derive their resistance from bearing resistance at the pile tip or from accumulated skin friction along the length of the pile or a combination of the two. In general, the pile resistance can be represented by Equation 2.12. This equation assumes that the ultimate (maximum) tip resistance and skin friction resistance occur at the same displacement.

Figure 2.44. Views of a) to c) the driving process for SCFRC sheet piles and d) the completed view (Walraven 2007, Walraven and Schumacher 2005)

$$Q_u = Q_p + Q_f - W_p \tag{2.12}$$

where: $Q_u =$ ultimate geotechnical resistance

$Q_p =$ end bearing or tip resistance

$Q_f =$ skin friction or shaft resistance

$W_p =$ weight of pile (usually negligible)

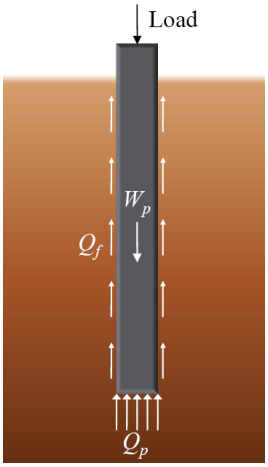

Figure 2.45. Skin friction and end-bearing resistances of a typical pile

The tip resistance can be represented as a bearing stress multiplied by the cross-sectional area of the tip of the pile, as shown in Equation 2.13 (Prakash and Sharma 1990). Equation 2.14 shows that the skin friction is also represented as a stress multiplied by an area. In this case, the area is the surface area of the pile, represented by the pile perimeter multiplied by the length, and the stress represents a friction force per unit area. Although these equations do not provide a good estimate of pile capacity when compared with load test results, they provide the theoretical basis of pile resistance.

$$Q_p = A_p \cdot \left(c \cdot N_c + \frac{1}{2} \cdot \gamma \cdot B \cdot N_\gamma + \gamma \cdot D_f \cdot N_q \right) \tag{2.13}$$

$$Q_f = \sum_{l=0}^{l=L} p \cdot f_s \cdot \Delta l \tag{2.14}$$

where: A_p = pile tip cross-sectional area

c = cohension of underlying soil

N_c, N_γ, N_q = nondimensional bearing capacity parameters, dependent on angle of internal friction of soil

γ = unit weight of underlying soil

B = pile width or diameter

D_f = depth of pile tip below ground surface

p = pile perimeter

f_s = unit shaft friction over length Δl

L = length of pile over wihich skin friction is mobilized

Prakash and Sharma (1990) list the following methods available for calculating the axial geotechnical compression capacity of driven piles:

- static analysis using soil strength parameters;
- empirical analysis using standard field tests;
  - Standard Penetration Test (SPT);
  - Cone Penetration Test (CPT);
  - pressuremeter test;
- dynamic driving resistance;
  - pile driving formulas;
  - wave equation; and
- full-scale pile load tests.

More details on each of these methods can be found in several textbooks and design manuals, including the reference by Prakash and Sharma (1990) and a Federal Highway Administration (FHWA) report on design and construction of pile foundations (1998).

Another factor that can control the design of driven piles is the amount of allowable settlement that the pile can experience. The allowable settlement of a pile foundation is usually dictated by the maximum displacement criteria for the structure it supports. The total settlement of a pile is the sum of the elastic settlement of the pile, the settlement caused by the load at the pile tip, and the settlement caused by the load along the pile shaft (Das 2004). Procedures for calculating pile settlement are given Das (2004), Prakash and Sharma (1990), and others.

Poulos (2006) notes that at least 80 percent of the total pile settlement typically occurs immediately after loading. Computer analysis may be required for some pile settlement calculations due to the nonlinear nature of the soil settlement components. Poulos noted that consideration of nonlinear effects is most important for piles in sand, piles with an enlarged base or pedestal, and bored piles with a large diameter.

2.6.2. Structural Resistance

The structural resistance of axially loaded piles is usually based on a design axial stress or load for the pile. When allowable stress design (ASD) was the common design methodology, piles were designed to meet an allowable stress criterion under unfactored loads. Load factor design (LFD), however, utilizes different factors on the loads applied to structural components to better represent load uncertainties. Now load and resistance factor design (LRFD) has been adopted by the American Association of State Highway Transportation Officials (AASHTO) and by many state departments of transportation (DOT). LRFD utilizes factors greater than one on loads, as does LFD, and also includes resistance factors with values less than one, according to the degree of uncertainty associated with each type of resistance, to ensure a suitable safety margin in design. The resistances calculated according to LRFD design procedures represent ultimate limit states, whereas ASD design resistance represents a service limit state.

2.6.2.1 Steel H-Piles

Table 2.12 shows the stress limits on steel H-piles currently in use in 21 different state DOTs, according to each agency's bridge design manual or geotechnical design division. The stress limits presented in the table assume that the H-piles are adequately braced against buckling by the surrounding soil. For comparison, the stress limits used in 1983 are also shown as reported by the FHWA (Davisson et al. 1983). Note that stress limits cannot be directly compared between ASD, LFD, and LRFD because each design method uses different load factors. Table 2.12 also shows the stress limits for piles used by the American Society of Civil Engineers (ASCE) (ASCE 1996). The AASHTO ASD and LFD limits are contained in the *Standard Specifications for Highway Bridges* (AASHTO 2002). The LRFD limits are from the *AASHTO LRFD Bridge Design Specifications* (AASHTO 2004).

Table 2.12. Steel H-pile compressive stress limits from 1983 and 2008 for state DOTs, AASHTO, and ASCE

State or Agency	1983 Stress Limit ksi (MPa)	2008 Stress Limit ksi (MPa)*		Current Design Policy	Notes
		Good Driving	Severe Driving		
AASHTO LRFD (2004)	—	$0.60 \cdot F_y$	$0.50 \cdot F_y$	AASHTO LRFD	Deterioration shall be considered as described in Section 10.7.1.8
AASHTO LFD (2002)	—	$0.85 \cdot F_y$	—	AASHTO LFD	
AASHTO ASD (2002)	9.0 (62)	$0.33 \cdot F_y$	$0.25 \cdot F_y$	AASHTO ASD	Design shall consider that piles may be subject to corrosion
ASCE (1996)	—	$0.35 \cdot F_y$	—	ASCE 20-96	Engineer should evaluate possible deterioration that limits the life of the pile or reduce its structural capacity
Alaska	—	$0.60 \cdot F_y$	$0.50 \cdot F_y$	AASHTO LRFD	
Arizona	—	$0.60 \cdot F_y$	$0.50 \cdot F_y$	AASHTO LRFD	Use F_y = 36 ksi (250 MPa); H-piles generally used as friction piles
California	10.0 (69)	$0.60 \cdot F_y$	$0.50 \cdot F_y$	AASHTO LRFD	
Colorado		$0.60 \cdot F_y$	$0.50 \cdot F_y$	AASHTO LRFD	Minimum H-pile area = 15.5 in.^{2} (100 cm^2)
Florida	9.0 (62)	$0.60 \cdot F_y$	$0.50 \cdot F_y$	AASHTO LRFD	Sacrificial steel thicknesses due to corrosion: Corrosion Level — Slight — Moderate — Extreme Corrosion Measures — 0.075 in — 0.150 in — 0.225 in No Corrosion Measures — 0.090 in — 0.180 in — 0.270 in
Georgia	—	$0.60 \cdot F_y$	$0.50 \cdot F_y$	AASHTO LRFD	Use 36 ksi (250 MPa) design stress, though 50 ksi (345 MPa) piles are available; only HP 10×42, 12×53, 14×73, 14×89, and 14×102 shapes are used
Illinois	9.0 (62)	$0.27 \cdot F_y$ (end bearing only) $0.70 \cdot F_y$	—	AASHTO LRFD	Resistance factor = 0.50 for pile resistance; for end bearing steel piles, max nominal resistance = $0.54 \cdot F_y \cdot A_s$; structural design resistance factor = 0.70
Iowa	—	6.0 (41) typical Up to 12.0 (83) for conditions as noted	—	AASHTO ASD	9 ksi (62 MPa) design stress is allowed for end bearing piles on rock with SPT N-values of 100-200 or combined end bearing and friction piles on rock with N-values ≥ 200; 12 ksi (83 MPa) design stress is permitted for the same cases, except it may only be used for piers and with approval from the Soil Design Section and Assistant Bridge Engineer

* The equations shown are limits on the service axial stresses of the pile, not the driving stresses. The separate stress conditions listed for good and severe driving are meant to account for possible pile damage during driving.

Table 2.12. continued…

State or Agency	1983 Stress Limit ksi (MPa)	2008 Stress Limit ksi (MPa)		Current Design Policy	Notes
		Good Driving	Severe Driving		
Louisiana	9.0 (62)	9 (62)	—	AASHTO LRFD	Former design manual limits lateral load to 4.95 kip (22 kN)
Massachusetts	9.0 (62)	$0.85 \cdot r \cdot F_y$ = $0.66 \cdot F_y$	—	AASHTO LFD	Eccentricity factor, r = 0.78 for steel H-piles; piles subjected to corrosion should have appropriate thickness reductions
Minnesota	—	$0.60 \cdot F_y$	$0.50 \cdot F_y$	AASHTO LRFD	Maximum lateral load for 50 ksi (345 MPa) steel HP 10×42 = 24 kip (107 kN), for HP 12×53 = 32 kip (142 kN), for HP 14×73 = 40 kip (178 kN)
Missouri	—	$0.60 \cdot F_y$	$0.50 \cdot F_y$	AASHTO LRFD	Generally HP 10×42 piles are used, but HP 12×53 and HP 14×73 are allowed
Montana	—	9 (62) for preliminary design	—	AASHTO LRFD	Limit of 202 kip (900 kN) design load for any pile to maintain contractor competitiveness
Nebraska	—	$0.60 \cdot F_y$	$0.50 \cdot F_y$	AASHTO LRFD	HP 12×53 is the smallest section that can be used for a bearing pile; maximum lateral load for HP 10 = 5 kip (22 kN), for HP 12 = 7 kip (31 kN), for HP 14 = 9 kip (40 kN)
Nevada	9.0 (62)	$0.60 \cdot F_y$ (LRFD) $0.33 \cdot F_y$ (ASD)	$0.50 \cdot F_y$ (LRFD) $0.25 \cdot F_y$ (ASD)	AASHTO LRFD and ASD, whichever is specified by bridge engineer	Apply corrosion adjustment to steel piles; steel H-piles used for bearing piles – typically HP 10 and HP 12 sections; ASD only: allowable lateral load for HP 10 or 12 = 5 kip (22 kN), for HP 8 = 4 kip (18 kN); ASD only: allowable compressive geotechnical capacity is half of the ultimate axial compressive geotechnical capacity
New York	9.0 (62)	$0.60 \cdot F_y$	$0.50 \cdot F_y$	AASHTO LRFD	
Pennsylvania	Up to 14 (97)	$0.45 \cdot F_y$	$0.35 \cdot F_y$	AASHTO LRFD	Use 1/16-in. (1.6-mm) thickness reduction for up to 1/16 in. (1.6 mm) of expected corrosion; for steel piles on soluble bedrock, use $0.25 \cdot F_y$ with F_y = 36 ksi (250 MPa)
Tennessee	—	$0.60 \cdot F_y$	$0.50 \cdot F_y$	AASHTO LRFD	
Texas	9.0 (62)	$0.60 \cdot F_y$	$0.50 \cdot F_y$	AASHTO LRFD	
Virginia	9.0 (62)	$0.33 \cdot F_y$	$0.25 \cdot F_y$	AASHTO ASD	
Washington	—	9 (62) on tip	—	AASHTO LRFD	H-piles are not to be used in material with only moderate density

Table 2.12 shows that most states have now adopted AASHTO LRFD for their steel H-pile design policy. The stress limits imposed by each state, however, vary considerably. For example, a 50 ksi (345 MPa) yield strength steel H-pile could have an axial compressive design stress ranging from 9 ksi (62 MPa) to 35 ksi (241 MPa), even among the LRFD design criteria set forth by the different DOTs. Note that some of the stress limits reported reflect geotechnical concerns rather than structural limit states. For example, the Iowa DOT uses its 6 ksi (41 MPa) stress limit to prevent the need for settlement calculations on piles that do not achieve significant end-bearing resistance (Iowa DOT 2007). Permissible lateral loads given by the different states also vary widely, even within LRFD design, ranging from 4.95 kip (22 kN) to 32 kip (142 kN) for an HP 12×53 pile, for example.

Note also that reductions in thickness due to corrosion can have a significant effect on the design load for steel piles. If no corrosion measures are used on an HP 10×42 pile with extreme corrosion in Florida, for example, only 37 percent of the cross-sectional area of the pile can be considered effective for resisting structural loads. The $\frac{1}{16}$-in. (1.6-mm) thickness reduction used by Pennsylvania allows 85 percent of the area of the HP 10×42 to be used for design. Also interesting to note is that some states use steel H-piles only in end-bearing situations and some others use them only as friction piles.

2.6.2.2 Precast, Prestressed Concrete Piles

Table 2.13 shows the compressive stress limits on precast, prestressed concrete piles currently in use in 21 different state DOTs and by AASHTO and ASCE. Again, the limits assume the piles are adequately braced against buckling by the surrounding soil.

The table shows that about one third of the states never or rarely use precast, prestressed concrete piles for bridge applications. Of the states that specify the design axial loads for a 16-in. (41-cm) square pile, for example, design loads range from 38 tons (39 tonnes) to 210 tons (213 tonnes). Prestressed bridge piles are typically 12-in. (30-cm) to 36-in. (91-cm) in depth, and a square cross-section is the most common pile shape. Prestressed concrete pile compressive strengths are typically 5.0 ksi (34 MPa), although strengths ranging from 4.0 ksi (28 MPa) to 8.0 ksi (55 MPa) are also used in some states.

Table 2.13. Precast, prestressed concrete pile compressive stress limits for state DOTs, AASHTO, and ASCE

State or Agency	2008 Compressive Stress Limit Base Equation	Multiplier, κ		Current Design Policy	Notes
		Spirals	Ties		
AASHTO LRFD	$0.75 \cdot \kappa(0.85 \cdot f_c' \cdot A_g - A_{ps} \cdot E_{ps}(\varepsilon_{pe} - \varepsilon_{cu} + \varepsilon_{ce}))$	0.85	0.80	AASHTO LRFD	Compressive strength at time of driving shall not be less than 5.0 ksi (34 MPa); minimum f_{pe} = 700 psi (4.8 MPa)
AASHTO LFD	$\phi \cdot \kappa(0.85 \cdot f_c' \cdot A_g - A_{ps} \cdot E_{ps}(\varepsilon_{pe} - \varepsilon_{cu} + \varepsilon_{ce}))$	ϕ = 0.75 κ = 0.85	ϕ = 0.70 κ = 0.80	AASHTO LFD	Design shall generally be based on f_c' = 5.0 ksi (34 MPa) but an increase to f_c' = 6.0 ksi (41 MPa) is permitted
AASHTO ASD	$0.33 \cdot f_c' - 0.27 \cdot f_{pe}$	—	—	AASHTO ASD	Limit is on gross cross-sectional area of concrete; design shall consider that deterioration of piles can occur
ASCE	$0.33 \cdot f_c' - 0.27 \cdot f_{pe}$	—	—	ASCE 20-96	Minimum f_c' = 4.0 ksi (28 MPa); minimum f_{pe} = 700 psi (4.8 MPa)
Alaska	$0.75 \cdot \kappa(0.85 \cdot f_c' \cdot A_g - A_{ps} \cdot E_{ps}(\varepsilon_{pe} - \varepsilon_{cu} + \varepsilon_{ce}))$	0.85	0.80	AASHTO LRFD	
Arizona	Not used	—	—		
California	$0.75 \cdot \kappa(0.85 \cdot f_c' \cdot A_g - A_{ps} \cdot E_{ps}(\varepsilon_{pe} - \varepsilon_{cu} + \varepsilon_{ce}))$	0.85	0.80	AASHTO LRFD	
Colorado	$0.75 \cdot \kappa(0.85 \cdot f_c' \cdot A_g - A_{ps} \cdot E_{ps}(\varepsilon_{pe} - \varepsilon_{cu} + \varepsilon_{ce}))$	0.85	0.80	AASHTO LRFD	Minimum f_c' = 4.5 ksi (31 MPa) for precast members
Florida	$0.75 \cdot \kappa(0.85 \cdot f_c' \cdot A_g - A_{ps} \cdot E_{ps}(\varepsilon_{pe} - \varepsilon_{cu} + \varepsilon_{ce}))$	0.85	0.80	AASHTO LRFD	Minimum 18-in. (46-cm) square piles for bridges, 24-in. (61-cm) for extremely aggressive environments; maximum bearing resistance is 300 T (305 t) for 18-in. (46-cm), 360 T (366 t) for 20-in. (51-cm), 450 T (457 t) for 24-in. (61-cm), and 600 T (610 t) for 30-in. (76-cm) piles
Georgia	$0.75 \cdot \kappa(0.85 \cdot f_c' \cdot A_g - A_{ps} \cdot E_{ps}(\varepsilon_{pe} - \varepsilon_{cu} + \varepsilon_{ce}))$	0.85	0.80	AASHTO LRFD	14-in. (36-cm), 16-in. (41-cm), 18-in. (46-cm), and 20-in. (51-cm) square piles available; 24-in. (61-cm), 30-in. (76-cm), and 36-in. (91-cm) piles with approval
Illinois	$0.15 \cdot f_c'$ (end brg only) $0.75(0.85 \cdot f_c' \cdot A_g - A_{ps} \cdot E_{ps}(\varepsilon_{pe} - \varepsilon_{cu} + \varepsilon_{ce})$	—	—	AASHTO LRFD	Resistance factor = 0.50 for pile resistance; for end bearing precast piles, max nominal resistance = $0.30 \cdot f_c' \cdot A_g$
Iowa	$0.33 \cdot f_c' - 0.27 \cdot f_{pe}$ (for 12-in. (30-cm) square pile only	—	—	AASHTO ASD	Maximum load for 14-in. (36-cm) square pile = 33 T (34 t), for 16-in. (41-cm) = 38 T (39 t); 12-in. (30-cm) pile may be used for stub abutments or piers; larger piles may only be used for pile bents; concrete piles to be used only in friction or combined friction and end bearing cases
Louisiana	See notes	—	—	AASHTO LRFD	Simplified method: maximum axial load is 85 T (86 t) for 14-in. (36-cm) square pile, 100 T (102 t) for 16-in. (41-cm), 115 T (117 t) for 18-in. (46-cm), 180 T (183 t) for 24-in. (61-cm), 300 T (305 t) for 30-in. (76-cm), 400 T (406 t) for 36-in. (91-cm)

Table 2.13. continued…

State or Agency	2008 Compressive Stress Limit Base Equation	Multiplier, κ		Current Design Policy	Notes
		Spirals	Ties		
Massachu-setts	$\phi r(0.85 \cdot f_c' \cdot A_g - A_{ps} \cdot E_{ps}(\varepsilon_{pe} - \varepsilon_{cu} + \varepsilon_{ce}))$	$\phi = 0.75$ $r = 0.85$	$\phi = 0.70$ $r = 0.80$	AASHTO LFD	
Minnesota	Not used	—	—		Cast-in-place piles sometimes used
Missouri	Not used	—	—		Concrete filled steel pipe piles sometimes used
Montana	Not used	—	—		Concrete filled steel pipe piles sometimes used
Nebraska	$0.75 \cdot \kappa(0.85 \cdot f_c' \cdot A_g - A_{ps} \cdot E_{ps}(\varepsilon_{pe} - \varepsilon_{cu} + \varepsilon_{ce}))$	0.85	0.80	AASHTO LRFD	Allowable lateral load for 14-in. (36-cm) square pile = 7 kip (31 kN)
Nevada	$0.75 \cdot \kappa(0.85 \cdot f_c' \cdot A_g - A_{ps} \cdot E_{ps}(\varepsilon_{pe} - \varepsilon_{cu} + \varepsilon_{ce}))$ (LRFD) $0.33 \cdot f_c' - 0.27 \cdot f_{pe}$ (ASD)	0.85 —	0.80 —	AASHTO LRFD and ASD, as spec. by bridge engineer	Minimum $f_c' = 4.0$ ksi (28 MPa); maximum $f_c' = 5.0$ ksi (34 MPa); concrete piles are rarely used; typical piles are 12-in. (30-cm) to 18-in. (46-cm) square or octagonal piles used as friction piles; ASD only: allowable lateral load for 12-in. (30-cm) square pile = 5 kip (22 kN), for 15-in. (38-cm) = 4 kip (18 kN); ASD only: allowable compressive geotechnical capacity is half of the ultimate axial compressive geotechnical capacity
New York	$0.75 \cdot \kappa(0.85 \cdot f_c' \cdot A_g - A_{ps} \cdot E_{ps}(\varepsilon_{pe} - \varepsilon_{cu} + \varepsilon_{ce}))$	0.85	0.80	AASHTO LRFD	Minimum $f_c' = 4.0$ ksi (28 MPa)
Pennsyl-vania	$0.45 \cdot \kappa(0.85 \cdot f_c' \cdot A_g - A_{ps} \cdot E_{ps}(\varepsilon_{pe} - \varepsilon_{cu} + \varepsilon_{ce}))$	0.85	0.80	AASHTO LRFD	Minimum $f_c' = 5.0$ ksi (34 MPa); maximum $f_c' = 8.0$ ksi (55 MPa) without approval
Tennessee	$0.75 \cdot \kappa(0.85 \cdot f_c' \cdot A_g - A_{ps} \cdot E_{ps}(\varepsilon_{pe} - \varepsilon_{cu} + \varepsilon_{ce}))$	0.85	0.80	AASHTO LRFD	
Texas	See note	—	—	AASHTO LRFD	Maximum Allowable Pile Service Loads: (T = tons, t = tonnes) Size [in. (cm)] | 16 (41) | 18 (46) | 20 (51) | 24 (61) Abutment, Trestle bent | 75 T (76 t) | 90 T (91 t) | 110 T (142 t) | 140 T (142 t) Footing | 125 T (127 t) | 175 T (178 t) | 225 T (229 t) | 300 T (305 t)
Virginia	$0.33 \cdot f_c' - 0.27 \cdot f_{pe}$	—	—	AASHTO ASD	Design shall ordinarily be based on $f_c' = 5.0$ ksi (34 MPa) or up to $f_c' = 8.0$ ksi (55 MPa) when economical; $f_c' = 8.0 - 10.0$ ksi (55 – 69 MPa) can be used with approval
Washing-ton	Generally not used	—	—	AASHTO LRFD	Guide axial loads: 330 kip (1470 kN) for 13-in. (33-cm) square pile, 420 kip (1870 kN) for 16-in. (41-cm) pile, and 600 kip (2670 kN) for 18-in. (46-cm) piles; maximum allowed loads: 1000 kip (4450 kN) for 18-in. (46-cm) piles, 1500 kip (6670 kN) for 24-in. (61-cm) piles

2.7. PILE DRIVABILITY ANALYSIS AND THE WAVE EQUATION

Another important aspect of pile design is ensuring the piles may be driven into the ground with relative ease and without damaging the piles. An analysis of driving systems and driving stresses must take dynamic effects into account.

2.7.1. History of Pile Driving Analysis

The first pile driving formula was reportedly put forth in 1820 by Eytelwein (Graff 1965). Then between about 1930 and 1960, many formulas were developed based on a simple energy equation, Equation 2.15. This equation is the basis of the Engineering News Record (ENR) formula, as well as many others.

$$W_R \cdot h = R \cdot s \tag{2.15}$$

where: $W_R =$ weight of pile driving ram
$h =$ drop height of ram
$R =$ soil resistance
$s =$ set distance of pile

The main differences between various equations based on this energy concept are the ways that each one accounts for energy losses that occur in the driving system (Graff 1965). Each equation uses different constants or factors to approximate these losses, usually based on empirical results. Unfortunately, the empirical parameters are often based only on a limited range of soil types, pile types, loads, or other variables. Thus for any given pile, soil, and driving system, the different equations may give widely varying results. This erratic distribution of driving formula results has led some engineers to abandon dynamic pile formulas as an approach for determining pile capacity.

The wave equation, which describes the mechanics of force transmission along an elastic rod subjected to an impact, was suggested by A.E. Cummings in 1940 as the dynamic pile driving formula most likely to give accurate results (Graff 1965). Unfortunately, before the development of electronic computers, no practical method existed for solving the differential equation representing the wave equation. In 1962, however, E.A. Smith (1962) published a paper detailing the mathematical solution of the wave equation for piles that

could be applied for computer programming. The basic equations for solution of the wave equation as well as the input parameters and driving system models are described in the following section.

Wave equation analysis programs were developed by several private corporations and by the U.S. Department of Transportation and FHWA. The two most common programs used today are the Texas Transportation Institute (TTI) program and GRLWEAP – the wave equation analysis of pile driving developed by Goble, Rausche, and Likins (PDI 2005). GRLWEAP 2005 was the program used for the driveability analysis in this study.

2.7.2. The Wave Equation

2.7.2.1 Hammer, Pile, and Soil Models

Figure 2.46 shows the wave equation model of the hammer, pile, and soil system during driving. The pile ram or hammer is represented by a mass or weight, W_1, falling through a height equal to the stroke of the hammer. For short, heavy, and rigid hammers, this representation of the hammer as a rigid object without elasticity is sufficient, but for long, slender hammers, the hammer may be represented by a series of weights and springs (Smith 1962). The hammer cushion is represented as a spring with an appropriate stiffness, k_1, and no weight. The helmet is represented by another rigid weight or mass, W_2. The pile then consists of a series of weights and springs representing, respectively, the weight and stiffness of the pile itself. Note that the pile springs, k_2 through k_9 in the figure, can transmit both tension and compression forces, but the hammer cushion spring, k_1, can transmit only compression forces. In the cases where a pile cushion is used, which is typically the case for concrete and timber piles, the stiffness of the cushion must be combined with the stiffness of the spring at the top of the pile according to Kirchoff's law, as shown in Equation 2.16. Note that the axial stiffness of each element of the system can be calculated by multiplying the elastic modulus and area of the element and dividing by the thickness or length.

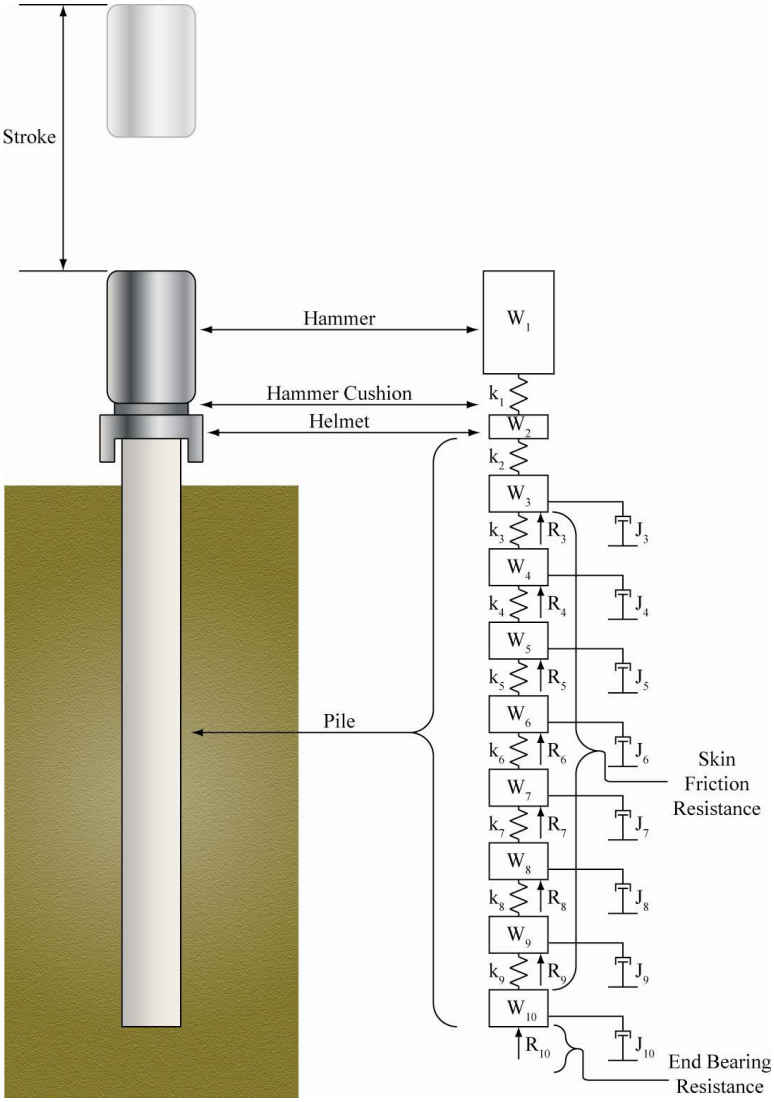

Figure 2.46. Model of hammer, pile, and soil for wave equation analysis (after Graff 1965)

$$\frac{1}{k_2} = \frac{1}{k_{pc}} + \frac{1}{k_2'} \tag{2.16}$$

where: k_2 = combined stiffness of top pile spring

k_{pc} = stiffness of pile cushion

k_2' = initial stiffness of top pile spring

The resistance of the soil is represented by vertical forces, R_i, acting on each pile element, including the pile tip. The total geotechnical resistance of the pile is then the sum of these forces. The resistance-displacement diagram of the soil is modeled as shown in Figure

2.47. The soil compresses elastically for a distance termed the quake and then plastically for a distance that represents the set (Smith 1962). When the load is removed, the soil rebounds elastically over the quake distance but the permanent set of the soil remains. In order to account for the dynamic effects of the soil resistance, a soil damping term, J_i, is included, as represented by the dashpots in Figure 2.46. The soil damping term models the increase in resistance when the soil is experiences a rapidly applied displacement compared to a slower displacement.

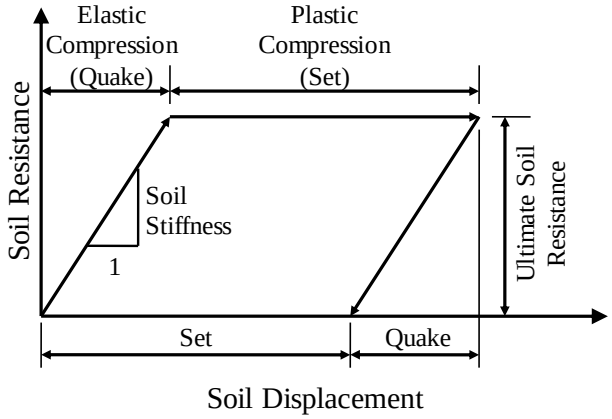

Figure 2.47. Soil resistance-displacement relationship used in wave equation analysis (after Smith 1962)

The actual driving forces are represented by the hammer striking the hammer cushion with a specified velocity. The hammer cushion then undergoes a displacement, which corresponds to a force in the spring that represents the cushion. The force in the spring causes an acceleration of the weight that represents the helmet below it. The displacement of the helmet then displaces the first pile spring, and the process continues down the length of the pile. The time increment used in the calculations of the model must be sufficiently small so that the transmittal of the stress wave from one pile element to another can be captured. Smith estimated this time increment as 0.00025 to 0.00033 sec for pile segment lengths from 8 to 10 ft (2.4 to 3.0 m) (Smith 1962).

2.7.2.2 Required Input

The driving hammer's rated energy, weight, efficiency, and stroke are needed to calculate the velocity of the hammer at the time of impact with the hammer cushion. To determine the stiffness of the spring representing the hammer cushion, the elastic modulus of the cushion material, the thickness of the cushion, and the cross-sectional area of the cushion are usually specified, as well as the coefficient of restitution for the cushion. The same parameters are required for the pile cushion, if one is included in the driving system. For the helmet the only required input is the weight. The pile's cross-sectional area, length, and elastic modulus are also required inputs. In addition, specifying the pile material type allows the program to define an appropriate time increment for calculations. Non-uniform piles may also be modeled by changing the cross-sectional properties of pile segments along the length of the pile.

The required soil information for a wave equation analysis of pile driving depends on what type of analysis is being performed. For every type of analysis, the user must input the soil quake, or elastic deformation capacity, and damping factors. The damping factor will typically be greater at the pile toe than along the shaft, since the soil directly underneath the pile is displaced more rapidly than the soil along the shaft as the pile penetrates into the ground. Smith recommends a quake of 0.10 in (2.5 mm) and damping constants for the shaft and toe of the pile of 0.05 and 0.15, respectively (Smith 1962). These quake and damping values are modified for different types of soils by others, as noted in Table 2.14 and

Table 2.15, respectively.

Table 2.14. Shaft and toe quake for pile wave equation analysis (GRL Engineers 2001)

Quake Type	Soil Type	Pile Type	Quake in. (mm)
Shaft	All soil types	All pile types	0.10 (2.5)
Toe	All soil types and soft rock	Open-ended pile types	0.10 (2.5)
	Dry or very dense/hard soils	Displacement piles w/diameter D	D/120
	Submerged or loose/soft soils	Displacement piles w/diameter D	D/60
	Hard rock	All pile types	0.04 (1)

Table 2.15. Shaft and toe damping factors for pile wave equation analysis

Soil Type	Shaft Damping	Toe Damping	Source
Non-Cohesive Soils	0.05	0.15	(GRL Engineers 2001)
Cohesive Soils	0.20	0.15	
Rock	0.05	0.05	Foundation Soils Information Chart (Dirks and Kam 2003)
Boulders, Gravel, Gravelly Sand, and Packed Sand	0.10	0.05	
Medium Sand and Fine Sand	0.10	0.10	
Silty Clay, Sandy Clay, Firm Sandy Glacial Clay	0.12	0.12	
Silt, Firm Clay	0.15	0.12	
Firm Glacial Clay and Firm Silty Glacial Clay	0.15	0.15	

If a bearing graph is the only required output, the only other soil information required is the distribution of the soil resistance along the pile and at the pile tip. For simple cases, a percentage of end bearing resistance compared to skin friction resistance is specified, based on static analysis, and the skin friction is assumed to act uniformly along the length of the pile. Alternatively, some wave equation programs, such as GRLWEAP 2005, allow the user to specify the distribution shape of the skin friction resistance in addition to specifying the proportion of the resistance provided by end bearing (PDI 2005). Finally, the desired range of ultimate soil resistances to be analyzed must be entered.

A bearing graph shows the user how much soil resistance can be expected for different numbers of blows per inch of driving with the chosen driving system. The bearing graph can also report expected compression or tension stresses in the pile at these various resistances as a check on pile capacity. A driveability analysis, however, is used to analyze pile behavior throughout the driving process, instead of only when the pile is completely in the ground and nearing its ultimate resistance and penetration. A driveability analysis requires additional inputs of the perimeter of the pile and values (not just proportions) of the

unit skin friction of the soil on the pile and the total end bearing resistance, based on static analysis. Thus, instead of calculating driving parameters for a range of possible resistances at the end of driving, driveability analysis enables the calculation of driving parameters for one user-specified resistance over the entire range of pile penetration depths. Thus, driveability analysis enables the designer to estimate not only what the maximum stresses in the pile will be but also where they occur along the length of the pile and at what point in the driving process they are expected. A driveability analysis can also give further insight into the expected performance of the chosen hammer throughout the driving of any pile instead of just at the end of driving.

2.7.2.3 Calculation Process

The calculation process for the solution of the wave equation involves computing the forces, displacements, and velocities of each component of the driving system for each time interval. The displacements, velocities, and forces for each are considered constant over this small time interval and are used to calculate new values for the next time interval. Equations 2.17 to 2.24 show the set of calculations performed at each time interval, *n*, for each segment of the driving system model, *i* (Smith 1962).

$$V_{IMPACT} = \sqrt{\frac{E_h \cdot \varphi \cdot g}{W_1}} \tag{2.17}$$

$$D_i = d_i + v_i \cdot \Delta t \tag{2.18}$$

$$R_i = (D_i - D_i') \cdot K_i'(1 + J_i \cdot v_i) \tag{2.19}$$

$$C_i = D_i - D_{i+1} \tag{2.20}$$

$$F_i = C_i \cdot K_i \tag{2.21}$$

$$Z_i = F_{i-1} - F_i - R_i \tag{2.22}$$

$$V_i = v_i + Z_i \frac{\Delta t \cdot g}{W_i} \tag{2.23}$$

$$R_u = \sum_{i=3}^{m} R_i \tag{2.24}$$

where: V_{IMPACT} = velocity of the driving hammer at impact
E_h = rated energy of the driving hammer
φ = efficiency of driving hammer
g = acceleration of gravity
D_i = displacement of soil and pile segment i in time interval n
d_i = displacement of soil and pile segment i in time interval n-1
v_i = velocity of pile segment i in time interval n-1
Δt = time increment
R_i = resistance of soil acting on pile segment i in time interval n
D_i' = soil plastic displacement in time interval n
K_i' = soil stiffness
J_i = soil damping constant
C_i = compression in spring i in time interval n
F_i = force exerted by spring i in time interval n
K_i = spring stiffness
Z_i = accelerating force in time interval n
V_i = velocity in time interval n
W_i = weight of hammer, helmet, or pile segment
R_u = total ultimate soil resistance to driving, including resistance at the pile tip
m = total number of pile segments in model

The plastic displacement of each soil element starts at a value of zero and remains constant unless it is changed according to one of the conditions defined by Equation 2.25 or 2.26. In other words, the plastic displacement of the soil, D_i', lags behind the displacement of the pile segment, D_i, by a value equal to the quake, Q (Smith 1962).

$$D_i' \geq D_i - Q \text{ and } D_i' \leq D_i + Q \text{ for } i = 1,...,m-1 \quad (2.25)$$

$$D_i' \geq D_i - Q \text{ for } i = m \quad (2.26)$$

Additional subroutines can be used to account for the coefficient of restitution for the hammer and pile cushions. Note that the coefficient of restitution for the pile is assumed to be equal to one. The analysis continues until either the displacement of the pile tip stops

changing from one time interval to the next or all of the velocities of the pile and hammer components are simultaneously negative or equal to zero.

For more information on the development of the wave equation for pile driving, see the referenced paper by Smith (Smith 1962). More information on specific wave equation programs can be found in each of the programs' respective user manuals, such as the GRLWEAP user manual (PDI 2005).

2.7.3. Allowable Driving Stresses

The stresses obtained from a wave equation analysis must not exceed the allowable driving stresses for the pile. The 21 state DOTs cited in Table 2.12 and Table 2.13 generally follow the AASHTO recommendations shown in Table 2.16, with the exception of the Pennsylvania DOT, as noted in the table (PENNDOT 2007).

Table 2.16. Driving stress limits for steel and concrete piling (AASHTO 2002, AASHTO 2004, PENNDOT 2007)

Material	Agency or State	Tension	Compression
Steel	AASHTO ASD	$0.90 \cdot F_y$	$0.90 \cdot F_y$
	AASHTO LRFD	$0.90 \cdot F_y$	$0.90 \cdot F_y$
	Pennsylvania DOT	F_y for 36 ksi steel $0.80 \cdot F_y$ for 50 ksi end-bearing piles	Same as tension
Concrete	AASHTO ASD	$3\sqrt{f_c'} - f_{pe}$ (psi) f_{pe} for severe environments	$0.85 \cdot f_c' - f_{pe}$
	AASHTO LRFD	$0.095\sqrt{f_c'} - f_{pe}$ (ksi) f_{pe} for severe environments	$0.85 \cdot f_c' - f_{pe}$
	Pennsylvania DOT	$0.095\sqrt{f_c'} - f_{pe}$ (ksi)	$0.85 \cdot f_c' - f_{pe}$

CHAPTER 3: DESIGN OF PILE SECTION

The properties of UHPC suggest that a reduced size could be used for a UHPC pile compared to typical sections used for precast, prestressed concrete piles without sacrificing the load carrying capacity of the section. UHPC can also use a much higher level of prestressing due to its high compressive strength, which will increase the resistance of the pile to flexural and axial tension. Reductions in the concrete cover on reinforcement and spacing of prestressing strands are possible due to the superior durability properties of UHPC, enabling the high-cost material to be used more efficiently without significantly increasing the cost of the pile or foundation. This chapter describes the process used for designing the UHPC pile cross-section and presents the properties of that optimized section.

3.1. STRESS-STRAIN RELATIONSHIPS

3.1.1. UHPC Stress-Strain Behavior

The stress-strain diagram used for the moment-curvature calculations presented in Section 3.7 and for the design of the UHPC pile section is shown as Figure 3.1. The compression behavior is represented by a tri-linear relationship, which was developed by Gowripalan and Gilbert (2000) and is used by VSL Proprietary Limited. The AFGC (2002) uses a similar stress-strain diagram in compression for their recommendations for UHPC design. Gowripalan and Gilbert's compressive stress-strain model is based on actual compression tests by Acker and Behloul (2004) on UHPC cylinders that included post-peak stress behavior, such as the test results shown Section 2.4.6.

The initial ascending segment of the model has a slope equal to the elastic modulus of the material, or 8000 ksi, which is based on test results reported by Degen (2006) and Graybeal (2006). Then at 85 percent of the compressive strength, the behavior is modeled as a horizontal straight line (zero stiffness) up to a compressive strain of 4000×10^{-6}. The last segment has a negative slope and stiffness, descending to zero strength at an ultimate compressive strain of 7000×10^{-6}. The compressive strength of the UHPC was assumed to be 26 ksi (179 MPa), based on the results reported by Sritharan et al. (2003).

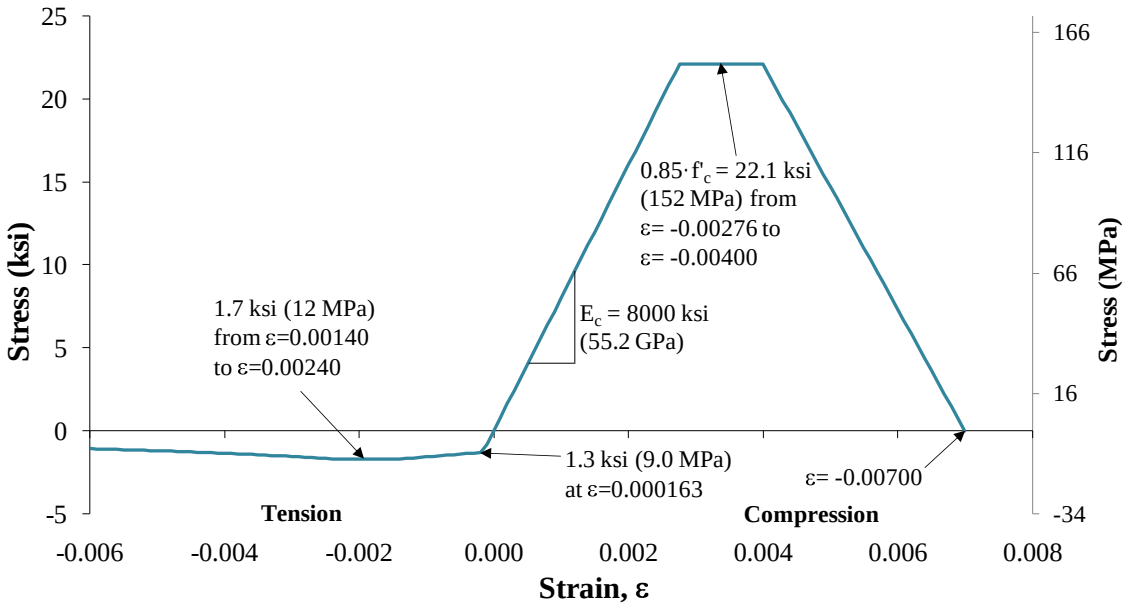

Figure 3.1. UHPC monotonic stress-strain behavior

The tensile stress-strain behavior of UHPC is modeled using Equations 3.1 to 3.4, developed by Bristow and Sritharan (to be published). Bristow and Sritharan also recommended values for the tensile stress-strain variables as shown in Table 3.1.

$$f_t = E_c \cdot \varepsilon \quad \text{for } \varepsilon \le f'_{te}/E_c \tag{3.1}$$

$$f_t = f'_{te} + \frac{f'_{t,MAX} - f'_{te} \quad \varepsilon - f'_{te}/E_c}{0.00125} \quad \text{for } f'_{te}/E_c < \varepsilon \le 0.0014 \tag{3.2}$$

$$f_t = f'_{t,MAX} \quad \text{for } 0.0014 < \varepsilon \le 0.0024 \tag{3.3}$$

$$f_t = f'_{t,MAX} - 0.0672 \cdot \ln(\varepsilon) - 4.062 \quad \text{for } \varepsilon > 0.0024 \text{ until } f_t \text{ reaches 0 ksi} \tag{3.4}$$

where: f_t = tensile stress

E_c = elastic modulus of UHPC

ε = tensile strain (ksi)

f'_{te} = elastic tensile strength

$f'_{t,MAX}$ = maximum tensile strength

Table 3.1. Key parameters defining tensile stress-strain behavior of UHPC (Sritharan and Bristow yet to be published)

Parameter	Value (ksi)	Value (MPa)
Elastic modulus in tension and compression, E_c	8000	55,000
Elastic tensile strength, f_{te}'	1.3	9.0
Maximum tensile strength, f_{te}'	1.7	11.7

The resulting tensile stress-strain behavior, shown in Figure 3.1, is characterized by an initial linear segment with a slope and stiffness equal to the elastic modulus up to a tensile strain of 163×10^{-6}. The initial linear segment is followed by another linear segment with decreased stiffness. At a tensile strain of 1400×10^{-6}, the tensile behavior has zero stiffness up to a tensile strain of 2400×10^{-6}. The behavior thereafter is modeled with an exponentially decreasing negative stiffness as shown in the figure.

3.1.2. Prestressing Steel Stress-Strain Behavior

The stress-strain behavior of prestressing steel is modeled using a trilinear diagram as shown in Figure 3.2. The trilinear diagram was based on the typical stress-strain curve for a 270 ksi () low-relaxation prestressing strand provided by PCI (1999) in the *PCI Design Handbook*. The elastic modulus of the prestressing steel was assumed to be 28,000 ksi (193 GPa), and an ultimate strain of $50{,}000\times10^{-6}$ was assumed.

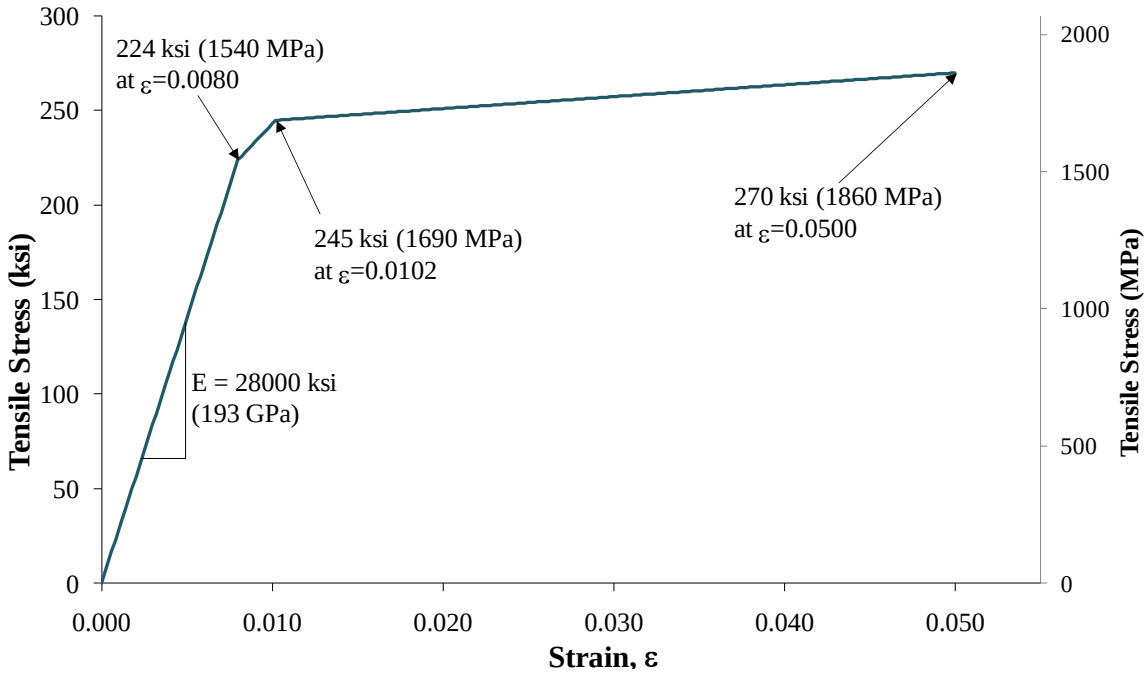

Figure 3.2. Assumed stress-strain behavior for prestressing strands

3.2. SECTION SHAPE

3.2.1. Solid Sections

As described in the literature review, the most common prestressed concrete pile used by state DOTs is a solid square pile. Solid octagonal and solid circular piles are also fairly common in bridge construction in the United States. Solid shapes are relatively easy to form and construct in a precasting plant. Loads transmitted to the solid piles due to driving, soil movements, or applied service loads are also distributed over the large cross-sectional area, resulting in lower stresses on the pile section. Unfortunately, a large number of prestressing strands are required to effectively prestress solid concrete sections due to the large cross-sectional area.

The large areas of the solid pile shapes allow them to develop high bearing resistance in situations where suitable soil for end bearing is present. Solid concrete piles are also typically considered to be displacement piles. The piles displace the soil around them as they penetrate into the ground, which helps to increase skin friction resistance along the piles.

UHPC clearly does not require a large pile cross-sectional area to adequately resist high axial compressive loads. Large amounts of prestressing can also make UHPC sections very effective to resist axial tension and flexural moments. Therefore, at the beginning of the project, hollow UHPC pile sections were considered more favorable than solid sections to use the material economically while maximizing the resistance of the section.

3.2.2. Hollow Sections

Hollow sections are typically formed by casting concrete around a collapsible form in the center of the pile. Hollow square, octagonal, and circular pile cross-sectional shapes, as shown in Figure 3.3, were considered for UHPC. Hollow sections are more efficient than solid sections for resisting flexural moments because the material is concentrated within the section at the extremities, where the maximum flexural stresses are expected to occur.

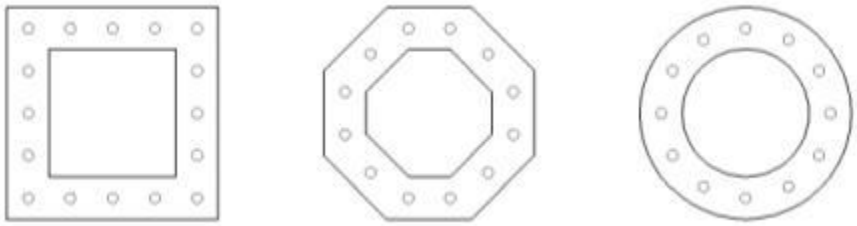

Figure 3.3. Hollow prestressed UHPC sections that were initially considered in the study

All three hollow UHPC sections shown in Figure 3.3 have the advantage of maintaining a large perimeter for developing skin friction resistance. All of these piles should be considered as displacement piles, which provide a large load resistance through skin friction. The tip area available for end bearing is reduced, however, unless the hollow sections are partially filled near the tip.

A major disadvantage of the hollow piles is the increased difficulty in construction due to the need for a collapsible form. The material savings offered by these pile sections might be largely offset by labor and production costs associated with the increased forming time and challenges.

Alternatively, hollow circular concrete piles are sometimes spun-cast. In this process, the appropriate amount of concrete is poured into a cylindrical form containing the reinforcing cage, and the form is spun. The spinning creates a centrifugal effect on the concrete, compacting the material starting from the edges of the cylindrical form and leaving a void in the center. However, the large proportion of steel fibers present in the UHPC mix may add complexity to spin-casting UHPC members. Additionally, since an objective of the study was to design a UHPC pile which could be economically manufactured in a local precasting plant, a spin-casting option for UHPC piles was not considered favorable.

3.2.3. H-Shaped Sections

Since solid sections use too much material, hollow sections are difficult to construct, and some of the properties of UHPC are comparable to those of steel, an H-shaped section was explored for designing UHPC piles. H-shaped pile sections maintain the advantage of efficient use of material that is offered by the hollow sections. Also like hollow pile sections,

an H-shaped pile will have a large perimeter to develop skin friction resistance while minimizing the cross-sectional area of the pile. The H-shaped sections are also much easier to construct in a precasting plant than the hollow sections.

3.2.3.1 Simple H-Shaped Section

Initially, a simple H-shaped section was considered for the UHPC pile, as shown in Figure 3.4. The flanges and web have a constant thickness, and the interior corners between the web and flange are chamfered to prevent stress concentrations in this region. The simple H-shape is very easy to form and can accommodate a large number of prestressing strands with a low volume of UHPC. A concerned for casting this section was that air pockets might form on the flat upper surfaces of the bottom flange as concrete was poured into the section from top to bottom. Therefore, as discussed in the subsequent sections, other H-shapes were considered for the UHPC piles.

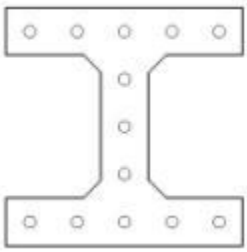

Figure 3.4. Simple H-shaped section considered for UHPC piles

3.2.3.2 X-Shaped Section

As shown in Figure 3.5, an H-shaped section with a web formed by circular arcs, known also as an hourglass or X-shape, was developed. The X-shape eliminates the concerns about forming air pockets on the upper surface of the bottom flange while allowing the possibility of including more prestressing strands in a section than the simple H-shaped section. For example, a 10 by 10 in. (250 by 250 mm) X-shaped section would be able to accommodate 15, ½-in. (13-mm) diameter prestressing strands with the cover and spacing requirements described in a following section, while only 13 strands could be used in a 10 by 10 in. (250 by 250 mm) simple H-shaped section. The additional prestress and the slightly larger cross-sectional area would give the X-shaped section greater flexural capacity than a

comparable simple H-shaped section. The X-shaped section will also not be subjected to stress concentrations in the regions where the flange and web join since the transition is more gradual.

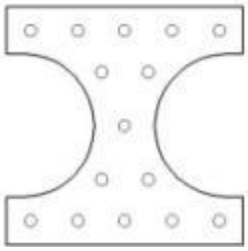

Figure 3.5. X-shaped section considered for UHPC pile

For an equivalent depth and width, the X-shaped section has a greater area than the simple H-shaped section, giving the pile a greater capacity for developing end bearing resistance, while increasing the amount of material needed for the pile. The X-shaped section is also much more difficult to form than the simple H-shape since curved formwork must be used.

3.2.3.3 Tapered H-Shaped Section

Finally, an H-shaped section with a tapered flange thickness was created, as shown in Figure 3.6. The straight surfaces of the tapered H-shape allow for easy forming, while the tapered flanges allow air to escape as concrete is poured into the section. The amount of material used for the tapered H-shaped section is slightly greater than that used for an equivalently sized simple H-shaped section and slightly less than that used for an equivalently sized X-shaped section. A 10 by 10 in. (250 by 250 mm) tapered H-shaped section can accommodate 13 ½-in. diameter prestressing strands, like the simple H-shape, although a reduced number of strands were used in this study. The angle at which the flange and web surfaces intersect is not as acute as in the simple H-shape, so stress concentrations are not as great of a concern. The tapered H-shaped section was the final section chosen for the UHPC pile as part of the current study.

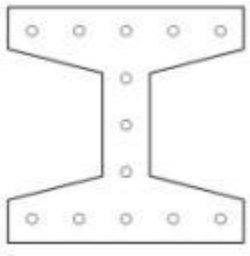

Figure 3.6. Tapered H-shaped section considered for UHPC pile

3.3. 2. SECTION SIZE

Typical concrete bridge pile sizes in the United States range from 12 in. (30 cm) to 36 in. (91 cm), as noted in the Literature Review (See Section 2.6.2.2). Steel H-piles used for bridges are typically HP 10 or 12 in. (250 or 300 mm) sections. The most common pile used by the Iowa DOT (2007) is the HP 10×57, in which 57 denotes the weight per linear foot. Steel piles with a yield strength of 50 ksi (345 MPa) are seeing wide application, although piles with a yield strength of 36 ksi (250 MPa) are still available. Some other common pile sizes used by various state DOTs include the HP 10×42 and HP 12×53.

Pile dimensions (i.e., depth/width or diameter) ranging from 4-in. (100-mm) deep micropiles to 14-in. (360-mm) deep piles were considered for the UHPC section developed in this study. A 10-in. (250-mm) deep by 10-in. (250-mm) wide UHPC pile section was finally chosen, since it matches the outer dimensions of the HP 10×42 and HP 10×57 piles currently in use in many states. This pile size represents a compromise between using as little material as possible and maintaining high flexural, compressive, and tensile strengths for the pile. Since the UHPC pile has the same outer dimensions as the 10-in. (250-mm) deep H-piles, these piles are intended to be driven with the same size helmet as the steel piles, depending on the configuration of the helmet.

3.4. COVER AND SPACING REQUIREMENTS

The required concrete cover for UHPC piles is critical to select of the details of the 10 by 10 in. (250 by 250 mm) tapered H-shaped section. In addition, the required spacing is

critical to determine the optimum size and number of prestressing strands that can be accommodated in the final section.

3.4.1. Concrete Cover on Reinforcing

3.4.1.1 Standards and Specifications for Normal Concrete

The American Concrete Institute (ACI) (2005) in Section 7.7.3 of *ACI 318-05* requires a minimum concrete cover of 1¼ in. (32 mm) for prestressing strands with a diameter of up to ⅝ in. (15.9 mm). The Precast/Prestressed Concrete Institute (PCI) (1999) in the *PCI Design Handbook*, also references the ACI requirement to determine the appropriate cover for prestressing steel. ACI notes that the required cover is for protection against weather and other effects and may need to be increased to enable the full development of the strength of the prestressing strand.

AASHTO (2004) requires a minimum concrete cover on precast, prestressed piles of 2.0 in. (51 mm) for unprotected main reinforcing steel, according to Section 5.12.3 of the *AASHTO LRFD Bridge Design Specifications*. However, this concrete cover requirement may be reduced by 20 percent for concrete with a water/cement ratio not greater than 0.40. AASHTO's *Standard Specifications for Highway Bridges* specifies a minimum concrete cover of 1½ in. (38 mm) for both prestressing steel and main reinforcement (AASHTO 2002). The AASHTO requirements are meant to account for both weathering effects and the ability of the cover concrete to enable the full development of the strength of the prestressing strand.

3.4.1.2 Research on UHPC

The excellent durability properties of UHPC suggest that the thickness of cover necessary to resist weathering effects and prevent corrosion of reinforcement may be reduced compared to the requirements of ACI, PCI, and AASHTO for normal concrete. Research by Tuchlinski et al. (2006) also shows that the concrete cover for prestressing strands that is needed to develop the full strength of the strand is reduced for UHPC compared to normal concrete (See Section 2.4.4). They recommended a concrete cover of 1.5 times the stand diameter for UHPC to ensure that the full strength of the strand can be developed.

Furthermore, in tests of a full-scale UHPC bridge girder at Iowa State University (ISU) (See Section 2.5.9.2), a clear cover as small as 0.84 in. (21 mm) was successfully used on 0.6-in. (15-mm) diameter strands. The two strands with this small cover thickness were located near the top surface of the bottom flange of the girder, and no premature failure of these strands occurred due to the use of a small cover thickness when the girder was tested to flexural and shear failure (Degen 2006). For the UHPC piles, the recommendation of Tuchlinski et al. was followed, which led to a ¾-in. (19-mm) concrete cover thickness for the ½-in. strands. (See Section 3.5 for the details of the strand selection.) A local precaster confirmed that the ¾-in. cover would not cause concerns with casting or releasing prestressing strands in UHPC piles.

3.4.2. Spacing Between Prestressing Strands

3.4.2.1 Standards and Specifications for Normal Concrete

ACI 318-05, Section 7.6.7.1, requires a minimum center-to-center spacing of 4.0 times the nominal strand diameter between prestressing strands (ACI 2005). However, a reduction to this spacing requirement is permitted when strands are used in members with a concrete compressive strength of at least 4000 psi (28 MPa) at the time of prestress transfer. Accordingly, a 1¾ in. (44 mm) center-to-center spacing may be used for ½-in. (13-mm) or smaller nominal diameter strands and a 2.0 in. (51 mm) center-to-center spacing may be used for 0.6-in. (15-mm) diameter strands. The *PCI Design Handbook* states that 2-in. (51-mm) spacing is typically used for all strands up to 0.6-in. (15-mm) diameter (PCI 1999).

AASHTO ASD requires a minimum center-to-center spacing of 2.0 in. (51 mm) for both 0.6-in. (15-mm) and ½-in. (13-mm) diameter strands (AASHTO 2002), but the minimum spacing for $\frac{7}{16}$-in. (11-mm) diameter strands is 1¾ in. (44 mm). AASHTO LRFD, however, requires 2.0-in. (51-mm) spacing for 0.6-in. (15-mm) strands and 1¾-in. (44-mm) spacing for both ½-in. (13-mm) and $\frac{7}{16}$-in. (11-mm) diameter strands (AASHTO 2004).

3.4.2.2 Research on UHPC

As summarized previously in Section 2.4.4, the tests on UHPC by Tuchlinski et al. (2006), suggest that the center-to-center spacing of prestressing strands in UHPC could be

reduced to 3.0 times the nominal strand diameter. The UHPC girder tested at ISU used a typical spacing of 2.0-in. (51-mm) for 0.6-in. (15-mm) diameter strands (Degen 2006), which is a larger spacing than that recommended by Tuchlinski et al.

For UHPC piles, a local precaster recommended a clear spacing of at least 1.5 in. (38-mm) between prestressing strands to allow concrete to freely flow through the section during casting. This clear spacing was chosen for the UHPC pile section, resulting in a center-to-center spacing of 2.0 in. (51 mm) for the ½-in. (13-mm) diameter strands that were eventually chosen for the pile section.

3.5. STRAND SELECTION

Strands sizes of 0.6-in. (15-mm), ½-in. (13-mm), and 7⁄16-in. (11-mm) in nominal diameter were considered for the 10-in. (250-mm) deep tapered H-shaped UHPC pile section. A comparison was made between the dimensions and properties of tapered H-shaped sections with 13 prestressing strands of each size, as shown in Table 3.2. The outer dimensions of the section were adjusted to meet the required concrete cover of 1.5 times the nominal strand diameter and the precaster's required clear spacing of 1.5 in. (38 mm) between strands. The table shows each tapered H-shape section with the minimum dimensions possible to meet the spacing and cover requirements while maintaining a 1.0-in. (25-mm) vertical dimension for the taper on each flange.

The extremely thin section shown for the 7⁄16-in. (11-mm) diameter strands was not used due to concerns about UHPC with fibers being able to freely flow in the tight cover regions during casting. The large amount of prestressing possible in the section with the 0.6-in. (15-mm) diameter strands caused concerns related to stresses in the end regions of the piles, and the slight increase in section dimensions beyond 10 in. by 10 in. (250 mm by 250 mm) was not considered desirable from a driving equipment standpoint. The research team initially selected the 7⁄16-in. (11-mm) strands to be used with the same section dimensions as those shown for the ½-in. (13-mm) strands in the table. The depth at the edge of the flanges of the UHPC pile was also slightly increased to the nearest tenth of an inch or 1.8 in. (46 mm).

Table 3.2. Properties of tapered H-shaped sections with different strand sizes

Strand Size	Section Details (in.)	Properties
0.6 in. (15 mm)	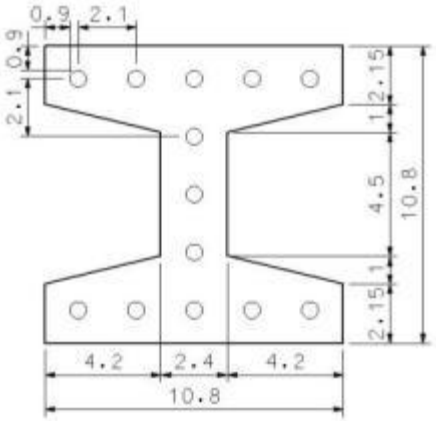	Total concrete area, A_c = 67.58 in^2 (436.0 cm^2) Area of prestressing steel, A_{ps} = 2.82 in^2 (18.2 cm^2) Ratio of A_{ps}/A_c = 4.17%
½ in. (13 mm)	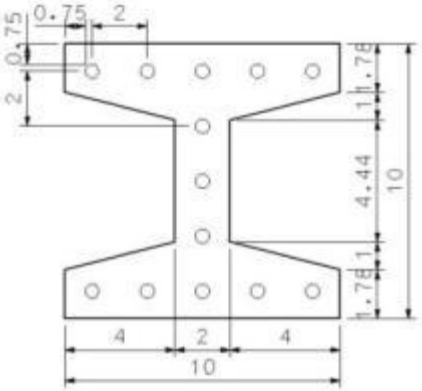	A_c = 54.51 in^2 (351.7 cm^2) A_{ps} = 1.99 in^2 (12.8 cm^2) A_{ps}/A_c = 3.65%
7/16 in. (11 mm)	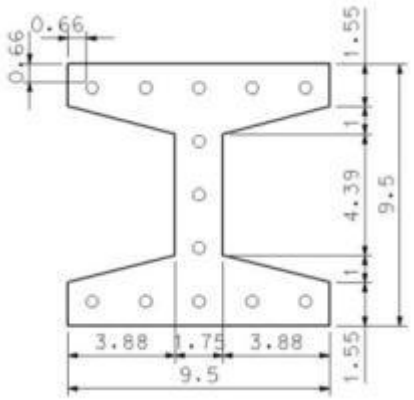	A_c = 46.95 in^2 (302.9 cm^2) A_{ps} = 1.50 in^2 (9.6 cm^2) A_{ps}/A_c = 3.18%

Since ½-in. (13-mm) diameter prestressing strands are more commonly used in prestressing applications throughout the United States than 7/16-in. (11-mm) strands, especially in prestressed concrete piling, the 13 smaller strands were replaced with ten ½-in. (13-mm) diameter strands in this potential UHPC pile section. The ten ½-in. (13-mm) strands

allow the section to be prestressed to almost exactly the same level as 13 7/16-in. (11-mm) strands. The final details of the UHPC pile section are presented in the following section.

3.6. FINAL SECTION DETAILS

The final dimensions of the tapered H-shaped UHPC pile section are compared with an HP 10×57 steel pile in Figure 3.7. The total area of prestressing in the UHPC pile was 1.53 in.^{2} (9.87 cm^2), equivalent to 2.77 % of the total concrete area of the section. A total of ten ½-in. (13-mm) diameter 270 ksi (1860 MPa) low relaxation prestressing strands were used, and the minimum concrete cover and center-to-center spacing on the strands were 0.75 in. (19 mm) and 2.0 in. (51 mm), respectively.

An initial prestress of 75 percent of the ultimate strength of the strands, or 202.5 ksi (1396 MPa) was used in design. As noted previously, an elastic modulus of 8000 ksi (55 GPa) was assumed for UHPC while the corresponding value at the time of prestress transfer at the age of approximately 36 to 48 hours was taken as 5000 ksi (34 GPa). The shrinkage strain in UHPC at the end of the standard heat treatment was assumed to be 450×10^{-6}. The prestress loss associated with this shrinkage strain was 38.7 ksi (267 MPa) or 19.1 percent of the initial prestress.

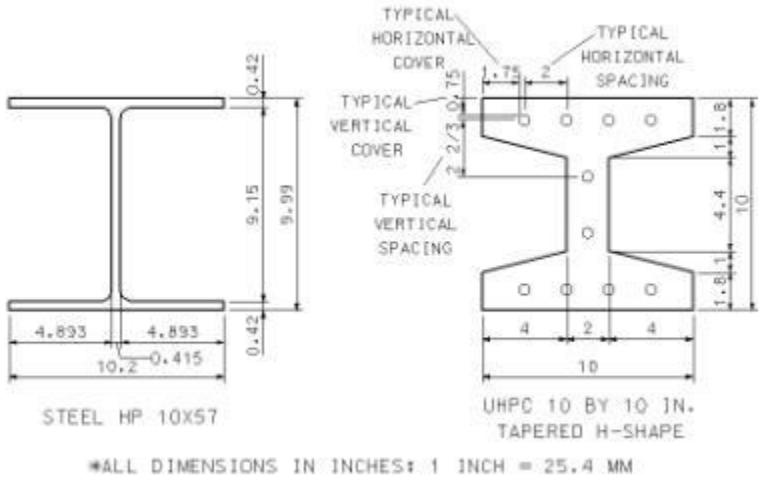

Figure 3.7. Dimensions of HP 10×57 steel pile and UHPC tapered H-shaped pile

Note the UHPC pile does not require ties or other shear reinforcement. Transverse reinforcement was also successfully eliminated in the UHPC girders used in the bridge in Wapello County, Iowa (Degen 2006). The high tensile strength of UHPC, the ability to apply higher prestress to the material, and the presence of fibers in the mix all contribute to improving the capacity of UHPC members to resist shearing forces without supplemental shear reinforcement.

Table 3.3 compares the section properties of the UHPC pile with a comparable HP 10×57 steel pile. The UHPC pile weighs only slightly more than the HP 10×57, although it has a much larger cross-sectional area that can potentially increase the end bearing capacity of the pile. Since the pile driving crane and hammer are often sized based on pile weight, the tapered H-shaped UHPC pile is expected to be driven with the same driving system that is used for an HP 10×57 piles or any other pile with similar weight. Driveability analysis, discussed in a following section, confirms these expectations. The elastic modulus of steel is about 3.6 times higher than that of UHPC. Because the UHPC pile has a much higher moment of inertia and the stiffness of the member is dictated by the E·I term, it is noted that the flexural stiffness of the UHPC pile is only 25 percent less than that of an HP 10×57 steel pile.

Table 3.3. Properties of steel and UHPC pile sections

Property	HP 10×57 Steel Pile	UHPC Pile
Total Area $in.^2$ (cm^2)	16.8 (108)	56.8 (366)
Weight lb/ft (kg/m)	57.2 (85.1)	61.1 (90.9)
Moment of Inertia in^4 (mm^4)	294 (1.22×10^8)	795 (3.31×10^8)
Stiffness term* $kip\cdot in^2$ ($N\cdot mm^2$)	8.53×10^6 (2.25×10^{13})	6.36×10^6 (1.83×10^{13})

*Stiffness term represents the elastic modulus multiplied by moment of inertia (i.e., E·I)

3.7. MOMENT-CURVATURE ANALYSIS

A section analysis spreadsheet was developed to determine the moment-curvature relationship of the UHPC pile section under different axial loads. The spreadsheet uses the assumptions and equations outlined below.

3.7.1. Assumptions

Several assumptions are used in the section analysis calculations, which are:

- Plane sections remain plane;
- Prestress losses occur due to only elastic shortening and shrinkage of UHPC;
- Strands have perfect bonding to UHPC outside the transfer regions, so the change in strain in prestressing strands is equal to the change in strain in concrete at the strand location;
- Effective prestressing is applied at the centroid of the section;
- Bending only occurs about the major flexural axis.
- Initial prestressing does not induce any inelastic strains on the strands; and
- Axial loads on the pile are applied through the centroidal axes with no eccentricity.

Note that the time-dependent prestress losses for UHPC members, creep and relaxation, have very small magnitudes. Assuming an ultimate creep coefficient of 0.29, as reported by Graybeal (2006) for steam-treated UHPC, the total loss due to creep after 75 years under prestressing and an axial compressive load of 200 kips on the UHPC pile would be only 2.1 percent. The loss due to relaxation of the steel strands would be 1.8 percent. UHPC shrinkage takes place almost entirely during steam curing, so it is not a time-dependent loss for UHPC. Note that the last four assumptions are necessary only to simplify the equations used in the spreadsheet, many of which are presented in detail below.

3.7.2. Equations

3.7.2.1 Zero Curvature Strain in Prestressing Steel and Concrete

Prestressing, prestressing losses, and applied axial load each contribute to a uniform strain in the concrete and to a different but equal strain in each prestressing strand. The sum of these strains in UHPC and in prestressing steel are referred to as the zero curvature strains in each material. The loss in prestress due to the elastic shortening of the UHPC member can be calculated using Equation 3.5.

$$\Delta f_{pES} = \frac{f_{pi} \cdot A_{ps}}{2 \cdot A_{ps} + A_c \frac{E_{ci}}{E_p}} \tag{3.5}$$

where: Δf_{pES} = prestress losses due to elastic shortening of UHPC
f_{pi} = initial prestress applied to prestressing strands
A_{ps} = total area of prestressing strands
A_c = total area of UHPC
E_{ci} = elastic modulus of UHPC at time of transfer of prestressing
E_p = elastic modulus of prestressing strands

Determining the loss in prestress due to the shrinkage of UHPC is more complicated, since the prestressing steel actually restrains the free shrinkage of UHPC. Figure 3.8 illustrates the difference between the total free shrinkage (ε_{SH}) and the actual shrinkage strain ($\Delta\varepsilon_{pSH}$) in prestressed UHPC. The prestressing steel experiences $\Delta\varepsilon_{pSH}$, which, in turn, causes the UHPC to experience a tensile stress due to the steel restraint against the free shrinkage of UHPC. Since the tensile force induced in UHPC must be equal to the loss in the prestressing force due to shrinkage, the loss of prestress due to UHPC shrinkage can be calculated using Equation 3.6.

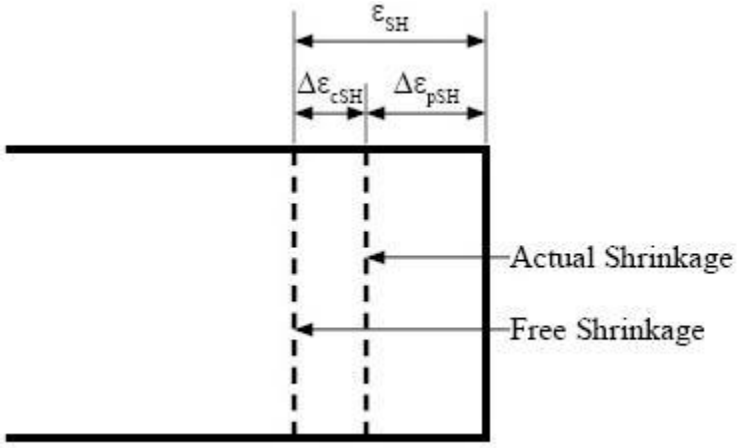

Figure 3.8. Strains in UHPC and prestressing steel due to UHPC shrinkage

$$\Delta f_{pSH} = \frac{\varepsilon_{SH} \cdot A_c \cdot E_p}{A_c + A_{ps} \frac{E_p}{E_c}} \tag{3.6}$$

where: Δf_{pSH} = prestress losses due to shrinkage of UHPC
ε_{SH} = total shrinkage strain of UHPC
E_c = elastic modulus of cured UHPC

Note that the free shrinkage of UHPC does not induce any stress in the concrete. Instead, the restraint of the free shrinkage by the prestressing steel induces the tensile stress in UHPC. This tensile stress can be represented by a strain equal to the difference between the free shrinkage and the actual shrinkage of the UHPC section (see Figure 3.8). This strain induced in UHPC can be determined using Equation 3.7.

$$\Delta\varepsilon_{cSH} = \frac{\varepsilon_{SH} \cdot A_{ps}}{A_{ps} + A_c \frac{E_c}{E_p}} \tag{3.7}$$

where: $\Delta\varepsilon_{cSH}$ = tensile strain in UHPC due to shrinkage

The final component affecting the zero curvature strain in prestressing steel and in concrete is the strain due to the applied axial load on the pile section. Equation 3.8 shows the strain in both concrete and prestressing steel caused by the axial load.

$$\varepsilon_P = \frac{P}{A_c \cdot E_c + A_{ps} \cdot E_p} \tag{3.8}$$

where: ε_P = strain in UHPC or prestressing steel caused by axial load
P = applied axial load

The total initial strains in the prestressing steel and UHPC can then be determined using Equations 3.9 and 3.10, respectively. In each equation, tension effects are positive and compression effects are negative, and at these strains the UHPC section is subjected to zero curvature..

$$\varepsilon_{pZC} = \frac{f_{pi} - \Delta f_{pES} - \Delta f_{pSR}}{E_p} - \varepsilon_P \tag{3.9}$$

$$\varepsilon_{cZC} = -\frac{f_{pi} - \Delta f_{pES} \cdot A_{ps}}{A_c \cdot E_c} + \Delta\varepsilon_{cSH} - \varepsilon_P \tag{3.10}$$

where: ε_{pZC} = strain in prestressing steel at zero curvature
ε_{cZC} = strain in UHPC at zero curvature

3.7.2.2 Strains Due to Curvature

The spreadsheet developed to determine strains at a given curvature uses 100 evenly spaced horizontal slices to represent the UHPC section. The width of the section at the location of each horizontal slice must be specified, as well as the curvature for the section. The location of the prestressing strands and the areas of each are also required input. The spreadsheet can then calculate the area of each horizontal slice, the total areas of UHPC and prestressing steel in the section, the location of the centroid, and the distance from each slice to the centroid.

Since the concrete has a nonzero strain at zero curvature, the neutral axis and the centroid for the section do not coincide. The difference between the distance from the centroid and the distance from the neutral axis for a horizontal slice of the section is illustrated in Figure 3.9.

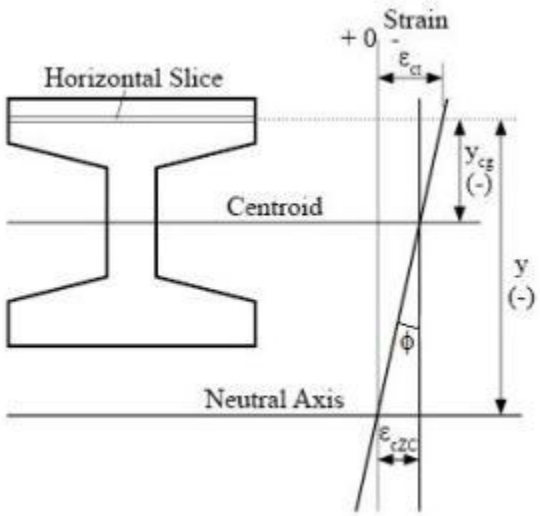

Figure 3.9. Definitions of distance from centroid and distance from neutral axis

The strain in each of the horizontal slices of the UHPC and in each prestressing strand can then be calculated using Equations 3.11 and 3.12, respectively.

$$\varepsilon_{ct} = \phi \cdot y_{cg} + \varepsilon_{cZC} = \phi\left(y - \frac{\varepsilon_{cZC}}{\phi}\right) + \varepsilon_{cZC} = \phi \cdot y \tag{3.11}$$

$$\varepsilon_{pt} = \phi \cdot y_{cg} + \varepsilon_{pZC} = \phi\left(y - \frac{\varepsilon_{cZC}}{\phi}\right) + \varepsilon_{pZC} = \phi \cdot y - \varepsilon_{cZC} + \varepsilon_{pZC} \tag{3.12}$$

where: ε_{ct} = total strain in UHPC
ϕ = curvature about horizontal axis
y_{cg} = distance from centroid, measured positive downward
y = distance from neutral axis, measured positive downward
ε_{pt} = total strain in prestressing steel

When the strain for each horizontal slice and each prestressing strand is calculated for the user-specified curvature, the spreadsheet uses the stress-strain relationships of UHPC and of prestressing steel to calculate the stress for each horizontal slice or strand. The stresses are converted to forces by multiplication by the slice or strand area, and the forces are converted to bending moments by multiplication by the distance to the centroid for each slice or strand. If the sum of all of the forces in the section is not equal to zero, an iterative solution is used to find the location of the neutral axis. When the correct neutral axis is found, the sum of the moments in the section is equal to the total moment resistance associated with the input curvature.

3.7.3. Results

Moment-curvature analysis was performed on the tapered H-shaped UHPC pile section with 24 different axial loads ranging from no axial load to a compressive load of 1064.86 kip, which is the failure load of the section in pure axial compression with the assumption of the pile experiencing no buckling. For each axial load, the calculation process described in the previous section was performed using a total of 26 different curvatures ranging from zero curvature to the ultimate curvature of the section.

The ultimate curvature for each axial load was defined using one of four conditions:

- The strain in the extreme compression fiber reached the assumed ultimate value of 7000×10^{-6}.
- The strain in a prestressing strand reached the assumed ultimate value of $50{,}000\times10^{-6}$.
- The moment resistance of the section decreased to 80 percent of its maximum value.
- The location of the neutral axis depth changed very suddenly, causing a large drop in moment resistance. (This effect is unique to the geometry of the tapered H-shaped section. The moderately sharp decrease in width over the flange tapers may cause the

neutral axis to decrease greatly with only a small increase in curvature. Associated with this change in the neutral axis depth is a sudden decrease in the moment resistance of the section. Since a sudden large drop in moment resistance should be considered a failure, the moment-curvature analysis was stopped when this condition was reached.)

Table 3.4 shows which ultimate condition controlled for each axial load studied for the UHPC section. Note that the second condition of reaching the ultimate strain of the prestressing strand never controlled the ultimate limit state.

Table 3.4. Controlling ultimate condition for different axial loads on UHPC pile section

Axial Loads	Controlling Ultimate Condition
0 – 30 kip (0 – 133 kN)	UHPC extreme fiber compression strain
70 – 330 kip (311 – 1468 kN)	Sudden increase in neutral axis depth
370 – 1065 kip (1646 – 4737 kN)	Decrease to 80 percent of maximum moment resistance

Figure 3.10 shows the moment-curvature responses for various axial loads. The ultimate curvature generally decreases with increasing axial load. The maximum moment resistance increases up to an axial load of about 300 kips (1334 kN) and decreases thereafter.

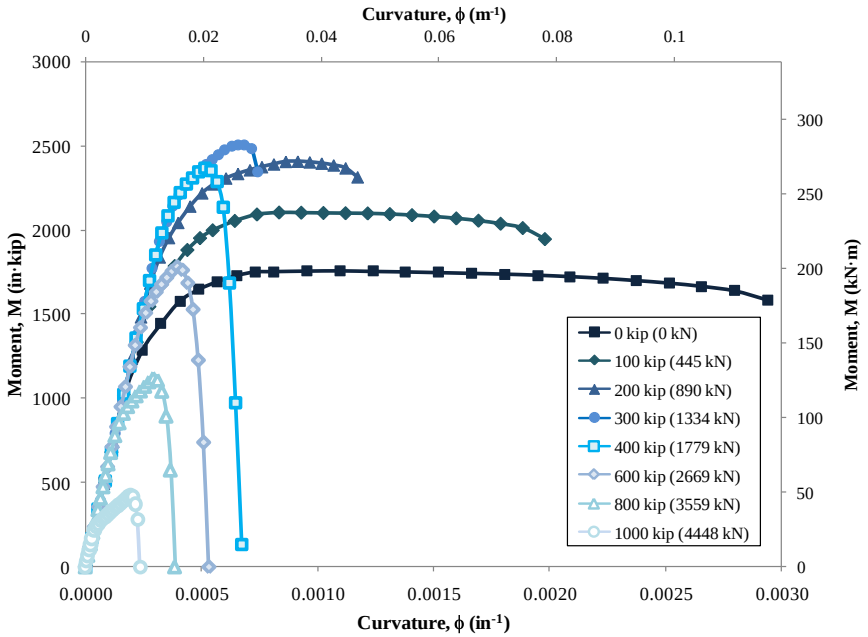

Figure 3.10. Moment-curvature response of UHPC pile section with various axial loads

The curvature ductility of the UHPC pile section was calculated using a bilinear idealized moment-curvature responses for each axial load. Figure 3.11 shows the moment-curvature diagram and an idealized curve for the UHPC pile with a 200 kip (890 kN) axial load. An initial elastic region is observed up to the first yield point, which is defined as reaching the proportional limit of the UHPC in either tension or compression (1.3 ksi [9.0 MPa] and 22.1 ksi [152 MPa], respectively). The first segment of the idealized response was formed by extending the initial elastic portion of the moment-curvature response up to the moment value corresponding with an extreme fiber compression strain of 3200×10^{-6}. This point, referred to as Idealized Point 1, is defined as the yield point for the moment-curvature response. The second segment is formed by connecting the yield point, with a second idealized point (i.e., Idealized Point 2 in Figure 3.11), which is defined by the ultimate curvature and the maximum moment resistance. Curvature ductility can then be calculated using Equation 3.13. The curvature ductility ranges from a maximum of 10.4 at zero axial load to a minimum of 1.8 at an axial load of 450 kip (2002 kN).

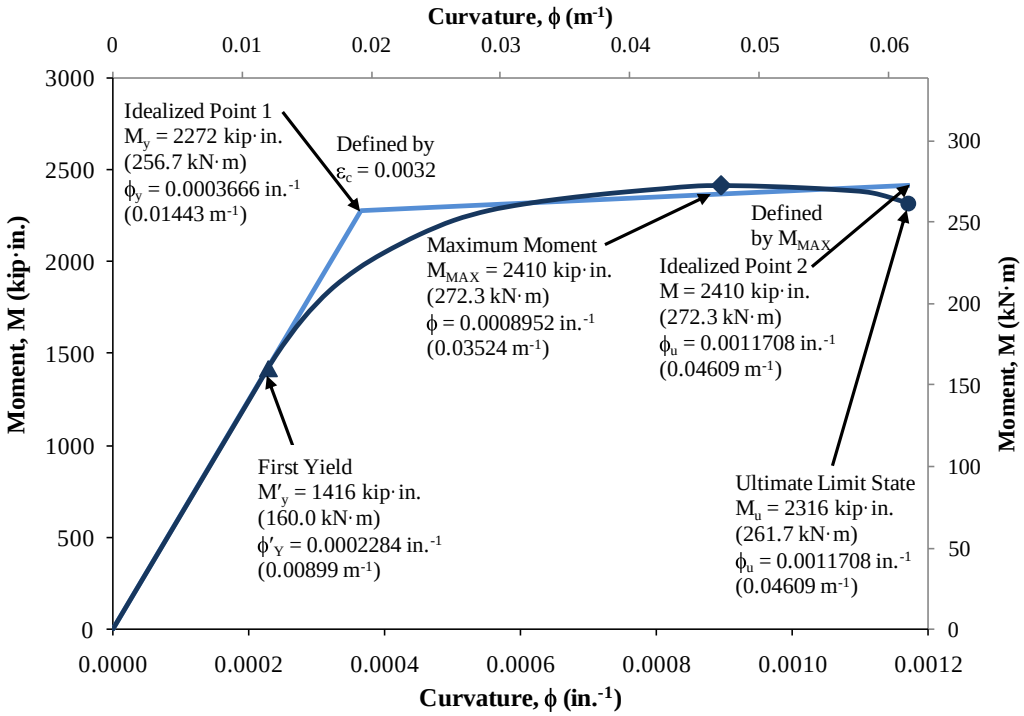

Figure 3.11. Moment-curvature response and idealization for UHPC pile section with a 200 kip (890 kN) axial load

$$\mu_\phi = \frac{\phi_u}{\phi_y} \tag{3.13}$$

Where: μ_ϕ = Curvature ductility
ϕ_u = Ultimate curvature
ϕ_y = Yield curvature

3.8. INTERACTION DIAGRAM

The moment-curvature results can also be used to establish an axial load and bending moment interaction diagram. The interaction diagrams for the 10-in. (250-mm) deep UHPC tapered H-shaped pile and for a Grade 50 steel HP 10×57 are shown in Figure 3.12. The AASHTO LRFD interaction equation was used to determine the interaction behavior of the steel pile (AASHTO 2004). The figure shows the maximum moment resistance of UHPC increases with increasing axial compressive load up to an axial load of 300 kip (1334 kN) and then decreases thereafter.

An interesting comparison can be made between a UHPC pile and steel pile subjected to an equivalent axial load or equivalent axial stress. Figure 3.12 shows a horizontal line representing an axial load of 420 kip, which is equivalent to a 25 ksi (172 MPa) stress (i.e., $0.5 \cdot F_y$) on the HP 10×57. At this level of axial load, the moment capacity of the UHPC pile is 40 percent higher than that of the HP 10×57 steel pile.

UHPC may be used with higher design axial loads (3.4 times higher for the same design stress) and even have higher moment capacity than a steel HP 10×57 pile used to support the same axial loads. An equivalent stress on each pile section can also be compared instead of a comparison using the same axial load for both sections. Figure 3.13 shows the UHPC and steel HP 10×57 pile interaction diagrams with horizontal lines representing a 6.0 ksi (41 MPa) stress on each section. This 6.0 ksi (41 MPa) stress is the current limit imposed by the Iowa Department of Transportation (2007) for bridge piles which do not bear on rock. At this equivalent stress, the UHPC pile can sustain a 240 percent higher axial load than the steel pile, which could lead to reduction in the number of piles needed for a foundation. The corresponding moment capacity of UHPC, however, is 20 percent less than that of the steel pile. Since moment capacity does not typically control the pile design, especially for piles

used in groups to support bridge piers, this reduction in moment capacity for the UHPC pile is not a major concern and will not lead to an increase in the number of piles required for a foundation. Table 3.5 shows a comparison of the moment capacity of the UHPC and steel HP 10×57 piles at various axial stress levels. The moment capacity of the UHPC pile decreases with increasing axial load, even compared to the steel pile, but for any level of axial stress, the axial load of the UHPC pile is increased 240 percent compared to the steel pile. Thus, if an axial stress as high as 12 ksi (83 MPa) is used, even though the moment capacity drops by 45 percent for the UHPC pile compared to the steel pile, the 240 percent greater axial capacity of the UHPC pile may allow a reduction in the number of piles required in a foundation.

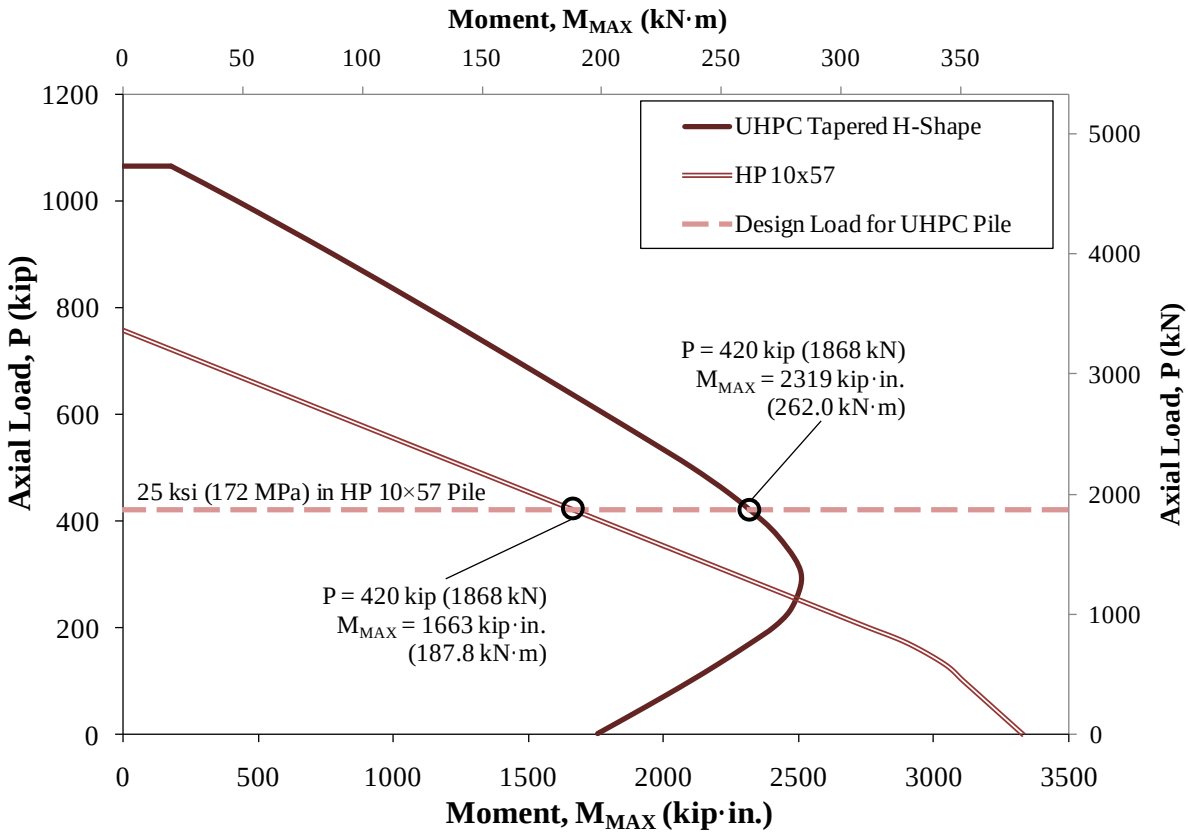

Figure 3.12. Interaction diagram of axial load and moment for UHPC and HP 10×57 pile sections with equivalent axial load shown

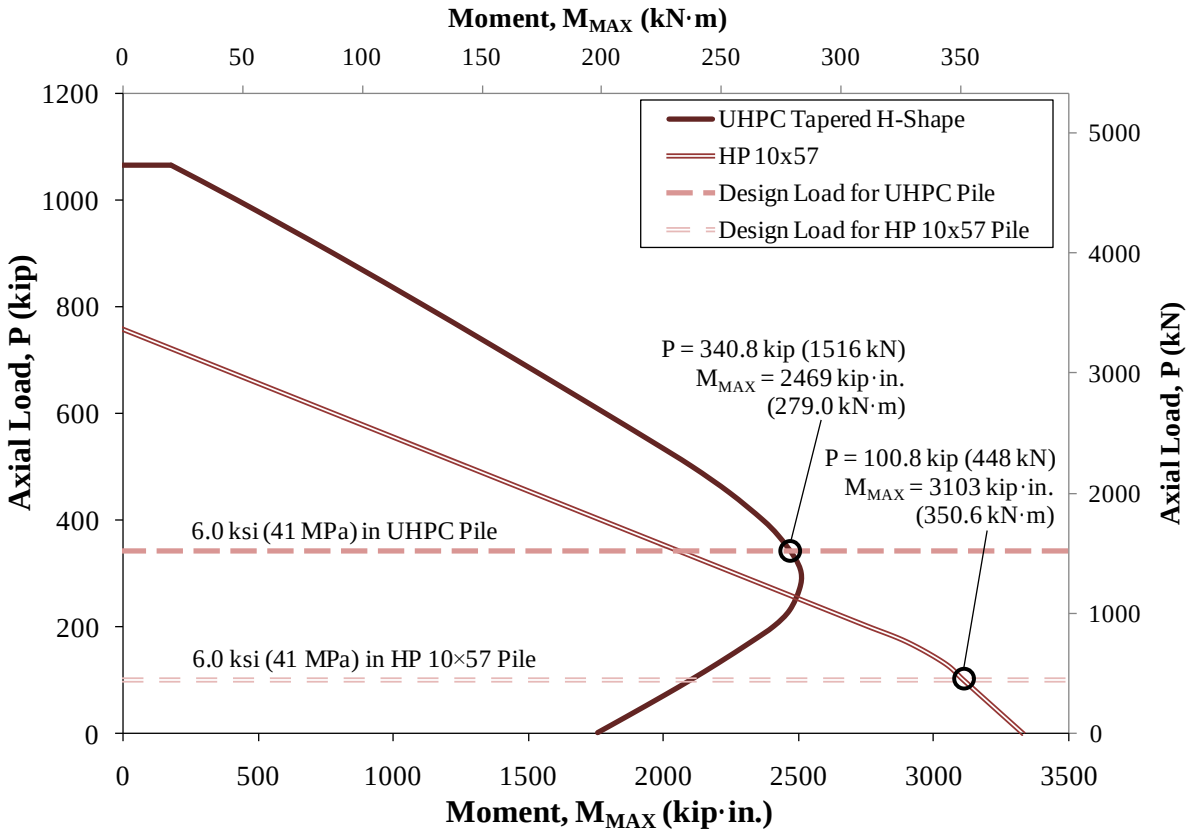

Figure 3.13. Interaction diagram of axial load and moment for UHPC and HP 10×57 pile sections with equivalent axial stresses shown

Table 3.5. Moment capacity of UHPC and HP 10×57 piles for various axial stress levels

Axial Stress ksi (MPa)	Pile Section	Axial Load kip (kN)	Moment Capacity kip·in. (kN·m)	Reduction Compared to HP 10×57
6 (41)	UHPC	340.8 (1516)	2469 (279.0)	20 %
	HP 10×57	100.8 (448)	3103 (350.6)	—
9 (62)	UHPC	511.2 (2274)	2069 (233.8)	31 %
	HP 10×57	151.2 (673)	2993 (338.1)	—
12 (83)	UHPC	681.6 (3032)	1515 (171.2)	45 %
	HP 10×57	201.6 (897)	2743 (309.9)	—

3.9. DRIVEABILITY

Although steel piles can experience significant damage during hard driving, as shown in Chapter 1, potential damage during driving due to high tensile or compressive stress is a

major concern with concrete piles. Typically, thick pile cushions composed of multiple sheets of plywood are used to prevent these high stresses. A driveability analysis can be useful in evaluating the appropriateness of the driving system and checking the predicted driving stresses against the allowable driving stresses. A simple driveability analysis has been conducted to examine whether UHPC piles can be easily driven into the ground and to identify any advantages they possess over normal concrete piling. A much more comprehensive driveability study on UHPC piles is presented in the final report for this study (Vande Voort 2008).

3.9.1. Allowable Stresses

The equations for the allowable tension and compression stresses for both steel and concrete piles have been presented in Section 2.7.3. Since the tensile and compressive strengths of UPHC are much higher and a higher level of prestressing may be used, the allowable stresses for UHPC piles are also much higher. For example, consider a standard Iowa Department of Transportation 12-in. (300-mm) square 5.0 ksi (35 MPa) concrete pile with four ½-in. (13-mm) prestressing strands. The allowable tension and compression stresses are 0.8 ksi (5.5 MPa) and 3.5 ksi (24 MPa), respectively. If a conservative tensile strength of 1.0 ksi (6.9 MPa) for UHPC is substituted for the tension term in the allowable tension stress equations, stress limits of 5.5 ksi (38 MPa) for tension and 17.5 ksi (121 MPa) for compression could be specified for the UHPC pile, an increase of over four times compared to normal prestressed concrete piles.

3.9.2. Modifications at the Top of the UHPC Piles

The cross-section over the top 18 in. of each UHPC modeled in the driveability analysis was modified by flaring the section out over a 9-in. (230-mm) length to a solid 10-in. (250-mm) square section that extended 9-in. (230-mm) further to the top of the pile, as shown in Figure 3.14. The expanded section was used to increase the area over which any driving tension force was distributed, since prestressing is not fully effective at the ends of the piles due to the prestress transfer length. Since the strand configuration was not changed, the extra effort required for forming this region is not substantial. The modification increased

the allowable tensile force at the pile top by 78 percent. The UHPC piles produced for this study included the modified pile top, as shown in Chapter 4, but subsequent driveability analysis results and observations from driving the UHPC piles in the field show tensile driving stresses at the top of the pile will not typically be high enough to require this modification.

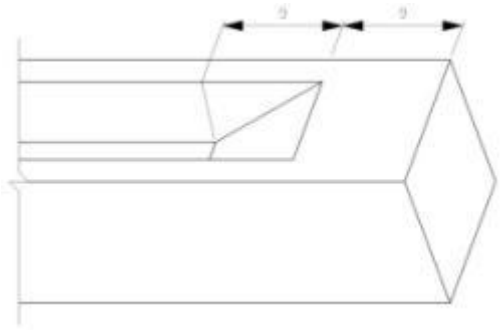

Figure 3.14. Expanded region at top of UHPC piles to minimize driving stresses

3.9.3. Driveability Analysis results

The wave equation analysis software GRLWEAP (PDI 2005) has been used to analyze UHPC and other piles during driving. A simple example is included here to demonstrate the possible advantages of UHPC.

An HP 10×57 steel pile, the 12-in. (300-mm) square normal concrete pile discussed previously, and the tapered H-shaped UHPC pile were analyzed using the same driving system in the same soil profile. A Delmag D19-42 hammer, a single-acting diesel hammer with a rated energy of 48.7 ft·lb (66 kJ) and a ram weight of 4.0 kip (18 kN) was used. Since the analysis determined that the normal concrete pile required a 4.0-in. (100-mm) thick pile cushion, a 4.0-in. (100-mm) thick cushion was used on the UHPC pile as well. The assumed soil profile was uniform sand with an SPT N-value of 20 to a depth of 59.5 ft, underlain by a thick claystone layer, which had an undrained shear strength of 80 ksf (3.8 MPa). The length of penetration used for each pile was 60 ft (18 m), so the piles were modeled as being driven to bearing on the claystone layer. Table 3.6 compares the maximum tensile and compression stresses from the driving analysis and shows the capacity of each of the piles.

Table 3.6. Maximum driving stresses and allowable stresses for piles driven in uniform soil profile

Pile Type	Tension			Compression		
	Actual Stress ksi (MPa)	Allow. Stress ksi (MPa)	Actual/ Allow. %	Actual Stress ksi (MPa)	Allow. Stress ksi (MPa)	Actual/ Allow. %
12" Concrete	0.45 (3.1)	0.82 (5.7)	54.9 %	2.4 (17)	3.6 (25)	66.8 %
10" UHPC	0.49 (3.4)	5.54 (38.2)	8.9 %	5.0 (34)	17.6 (121)	28.3 %
HP 10 x 57	2.53 (17.4)	45.0 (310)	5.6 %	19.7 (136)	45.0 (310)	43.8 %

The ratios of actual driving stress to the allowable stress for each pile, expressed as a percentage in Table 3.6, are significantly lower for the UHPC pile compared to the normal prestressed concrete pile. In fact, the ratio in tension is close to that of the steel pile, and the ratio is even lower for the UHPC pile in compression than it is for the steel pile. The low actual stress to capacity ratios suggest UHPC may be able to be driven with a reduced pile cushion thickness or with no pile cushion, similar to current steel pile driving practice.

The driveability of the UHPC pile was then modeled using the same driving system and soil profile but with pile cushion thicknesses of 2.0 in (50 mm) and 0 in. (0 mm). Table 3.7 shows that even with no cushion, the actual tension and compression stresses in the UHPC only slightly increase. In fact, the actual stresses do not exceed 14 percent of capacity in tension or 33 percent of capacity in compression, indicating that UHPC may be able to be driven without any pile cushion.

Table 3.7. Maximum driving stresses for UHPC pile with varying cushion thickness

Cushion Thickness in. (mm)	Tension			Compression		
	Actual Stress ksi (MPa)	Allow. Stress ksi (MPa)	Actual/ Allow. %	Actual Stress ksi (MPa)	Allow. Stress ksi (MPa)	Actual/ Allow. %
4.0 (100)	0.49 (3.4)	5.54 (38.2)	8.9 %	5.0 (34)	17.6 (121)	28.3 %
2.0 (50)	0.71 (4.9)	5.54 (38.2)	12.9 %	5.2 (36)	17.6 (121)	29.5 %
None	0.78 (5.3)	5.54 (38.2)	14.0 %	5.8 (40)	17.6 (121)	32.8 %

CHAPTER 4: PRODUCTION OF UHPC PILE UNITS

4.1. DESCRIPTION

The UHPC pile units needed for use in both laboratory and field tests in this study were prefabricated. The laboratory tests on UHPC units were used to verify the structural behavior of the UHPC pile section under combined axial load and bending moment. Results from the laboratory tests are not included in this report but can be found in Vande Voort et al. (2008). Field tests on the UHPC piles were used to prove the viability of producing, transporting, and driving the piles and to examine the vertical and lateral load behavior of driven UHPC piles. A total of five separate UHPC test units were cast: three small-scale test units for the laboratory testing and two full-scale test piles for the field tests.

4.1.1. Laboratory Test Units

Two 8-ft (2.4-m) long UHPC test units, designated L1 and L2, were designed and fabricated for laboratory tests involving combined axial load and bending moment. The test units had the same basic cross-sectional shape as the UHPC section described in Chapter 3 but were produced at ¾-scale, yielding 7.5 by 7.5 in. (19 by 19 cm) overall dimensions. Figure 4.1 shows the ¾-scale section and the full-scale section side-by-side, and Table 4.1 compares the properties of these sections. A smaller section was used so that the test units could be loaded to failure in flexure without exceeding the capacity of a steel base that simulated a fixed connection at the base of the unit. More details on the laboratory tests and the test set-up can be found in Vande Voort et al. (2008). Top and side views of the 8-ft (2.4-m) long laboratory test units are shown in Figure 4.2.

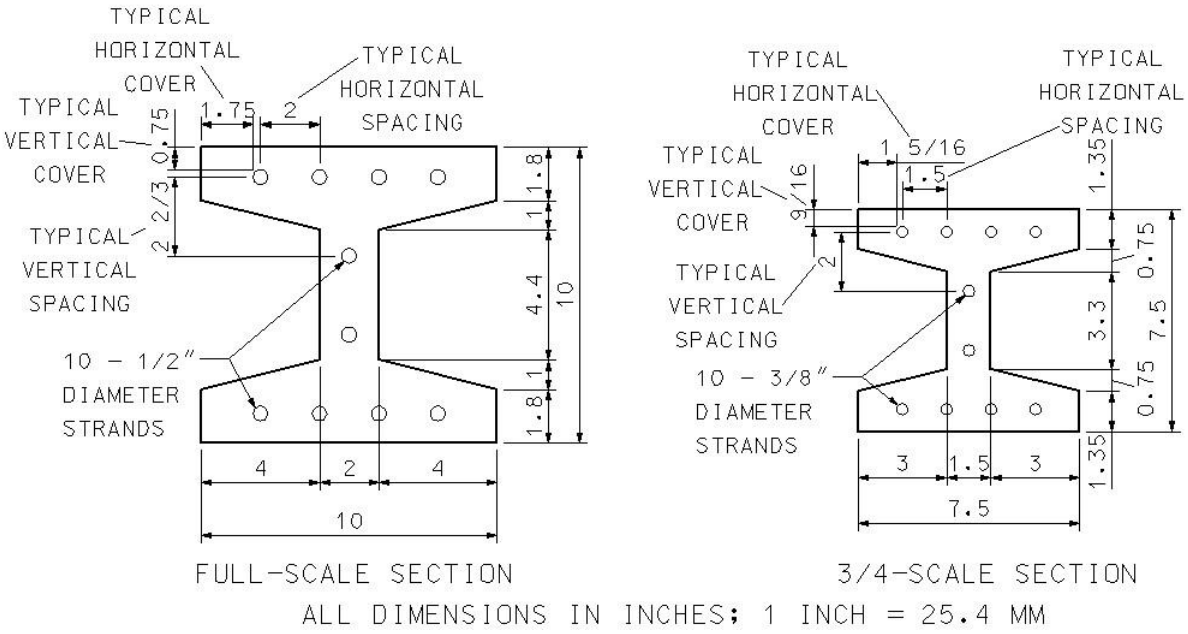

Figure 4.1. Full-scale and ¾-scale UHPC tapered H-shaped sections

Table 4.1. Property comparison between full-scale and ¾-scale UHPC sections

Property	Full-Scale Section	¾ -Scale Section	Ratio of ¾-Scale to Full-scale
Area	56.8 in^2 (366 cm^2)	32.0 in^2 (206 cm^2)	0.56
Area of Prestressing	1.53 in^2 (9.9 cm^2)	0.85 in^2 (5.5 cm^2)	0.56
Moment of Inertia	775 in^4 (3.23×10^8 mm^4)	245 in^4 (1.02×10^8 mm^4)	0.32

As seen in Figure 4.2, the 7.5 by 7.5 in. (19 by 19 cm) tapered H-shaped section was expanded to a solid 7.5-in. (19-cm) wide by 10-in. (25-cm) deep section for the bottom 15 in. (38 cm) of each test unit. The expanded section at the bottom was used to reduce the bearing stresses on the steel base and, more importantly, to move the critical moment region away from the base so that the moment-curvature behavior of the pile section could be appropriately characterized. With the critical section for moment located 15 in. (38 cm) from the member end, the prestress is also assured to be fully effective at the critical section. The threaded rods at the top (left end) of the test units were used to attach a beam across the top of the test unit through which the pile test unit was post-tensioned to simulate an axial load.

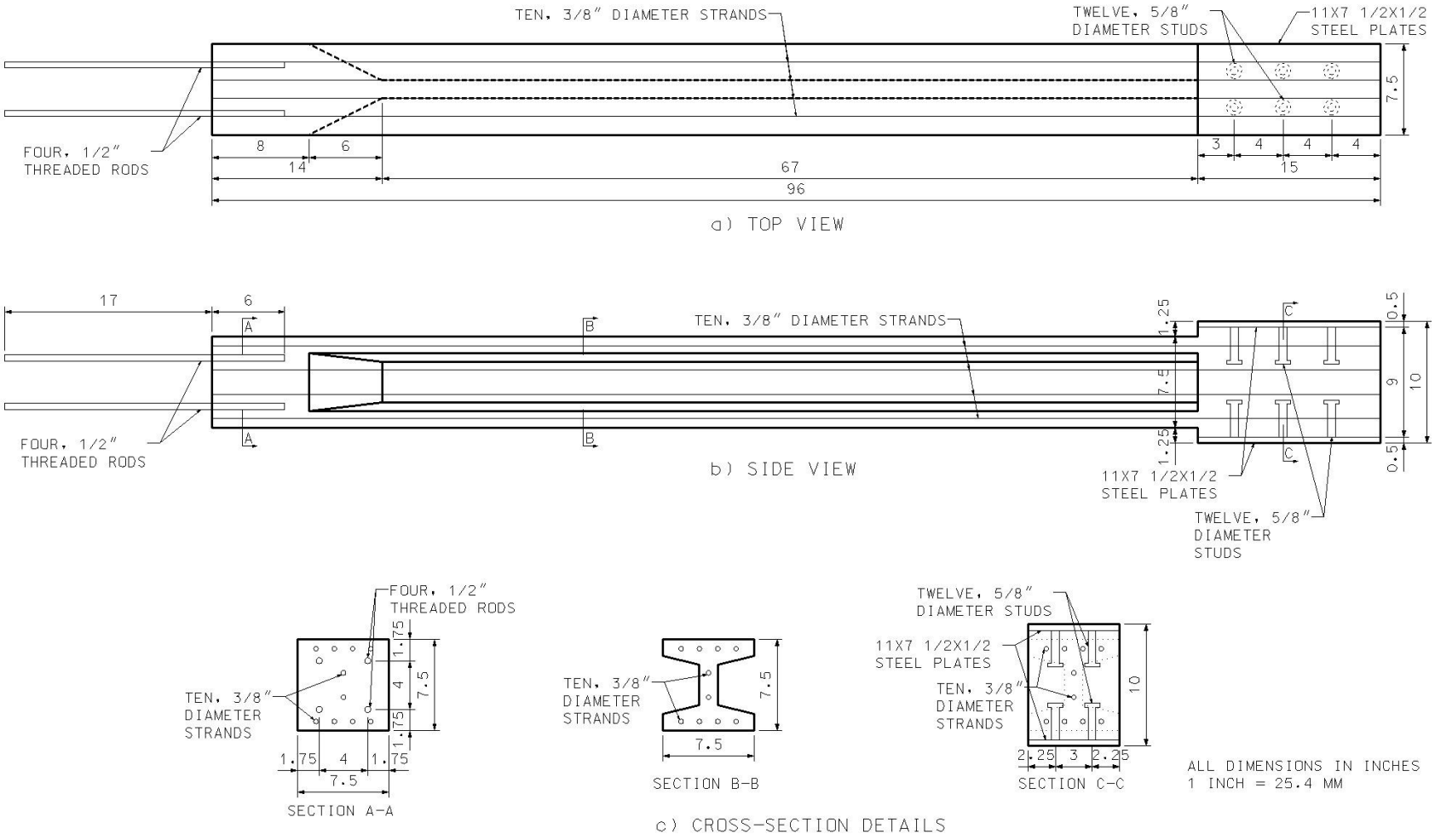

Figure 4.2. Dimensions and reinforcement details of the 8-ft (2.4-m) long UHPC pile units for laboratory tests

In addition to the ¾-scale UHPC pieces designed to study the behavior of the pile section under combined loading, a 10-ft (3.0-m) long UHPC beam was designed to examine the behavior of the UHPC pile section under pure bending. Top and side views of the 10-ft (3.0-m) piece are shown in Figure 4.3. The 10-ft (30-m) piece had the 10 by 10 in. (25 by 25 cm) tapered H-shaped cross-section at full-scale as described in Chapter 3, Section 6, details of which are shown in Figure 4.3. Due to problems during the casting of this test unit, it was decided not to conduct the laboratory tests on this unit (see Chapter 4, Section 3.3).

4.1.2. Field Test Piles

Two full-scale 35-ft (10.7-m) long UHPC test piles were designed to be driven at a bridge site in Iowa and load tested under axial and flexural actions. Several potential test sites under consideration at the time of casting featured soil profiles consisting of soft soils underlain by bedrock at a depth of 30 to 40 ft (9 to 12 m). The 35-ft (10.7-m) pile length was chosen so the test piles could be installed at one of these sites, and the chosen pile length proved to be ideal for the site where the piles were eventually driven and tested.

Top and side views of the UHPC field test piles are shown in Figure 4.4. Each pile used the 10 by 10 in. (25 by 25 cm) tapered H-shaped section at full-scale throughout their length, except for the top 18 inches. This top segment was expanded to a solid 10 by 10 in. (25 by 25 cm) section to minimize driving stresses in consideration of the transfer length of the prestressing strands in UHPC. (See Chapter 3, Section 9.2 for more details on the expanded section.)

4.2. DESCRIPTION OF INSTRUMENTATION

4.2.1. Laboratory Test Units

Laboratory test unit L1 was instrumented with 14 strain gages, and test unit L2 was instrumented with 13 strain gages. The strain gauges were attached to the prestressing strands in the test pieces, and most were located near the critical moment region of the test units. Two of the strain gauges in each test unit were located near the top of the test piece to examine the transfer length of the prestressing strands in the UHPC.

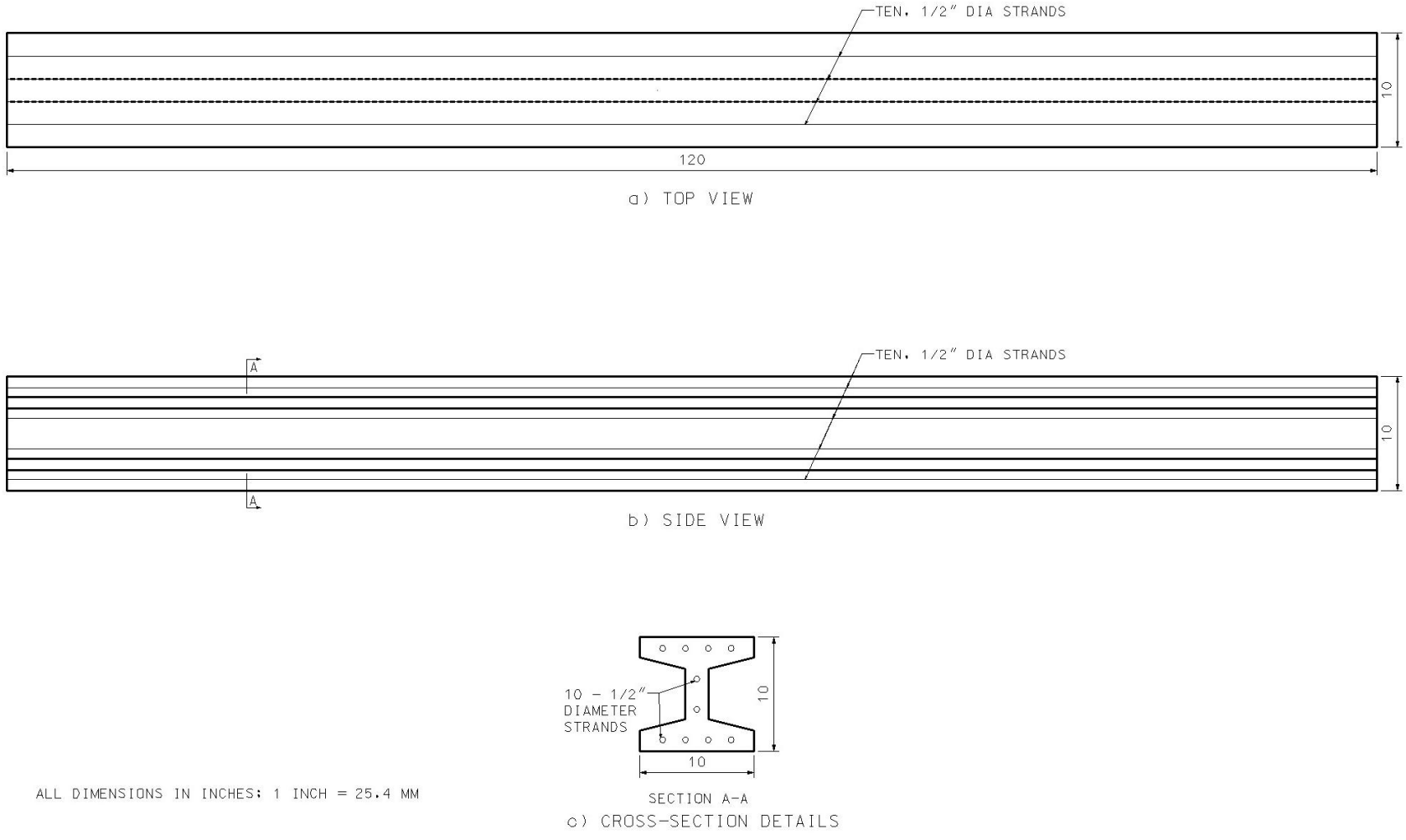

Figure 4.3. Dimensions and reinforcement details of the 10-ft (3.0-m) long UHPC pile units for laboratory tests

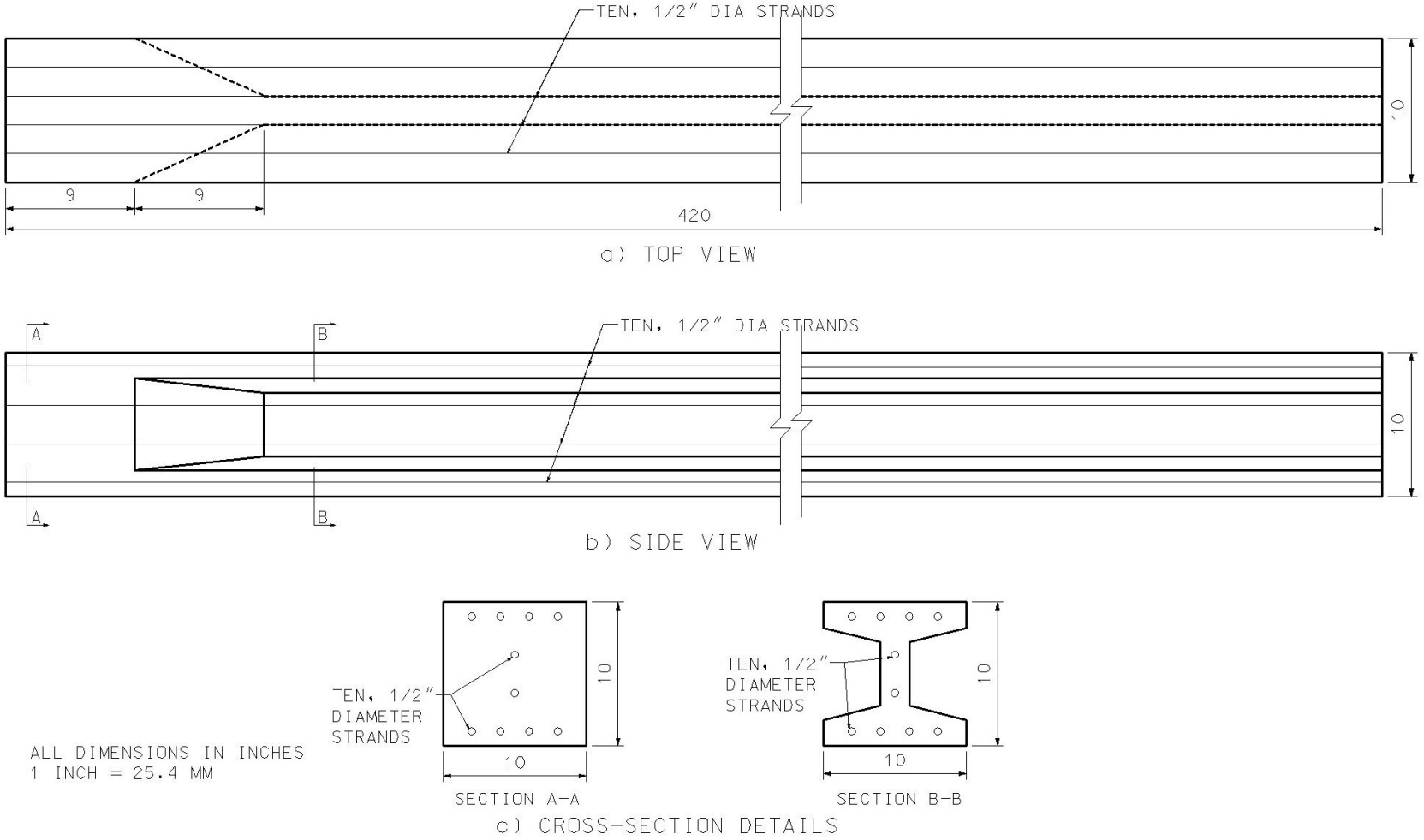

Figure 4.4. Dimensions and reinforcement details of the 35-ft (10.7-m) long UHPC piles for field tests

Couplers were also cast into the UHPC test units within the critical moment region. The couplers enabled externally mounted displacement gauges to be installed on opposite sides of the cross-section in order to compute the average strain and curvature over 6-in. (150-mm) long distances.

The list of instruments and instrument mounting equipment installed in the 8-ft (2.4-m) long laboratory test pieces included the following, which are shown in their final locations after the initial prestressing in Figure 4.5 and Figure 4.6 for test units L1 and L2, respectively: strain gauges LV01 to LV14 on the prestressing strands of test unit L1 and LV16 to LV28 on the strands of test unit L2; and six ¼-in. (6-mm) diameter couplers in each test unit for curvature measurement. Note that the prefix "LV" identifies the gauges for the laboratory test units, as opposed to the gauges for the field test piles which are identified with the prefix "FL." Strain gauge LV15 was omitted from the gauge numbering sequence. Figure 4.5 and Figure 4.6 also show a cross-sectional diagram indicating which strands in each test unit were instrumented. If the strands in each section are numbered from left to right and from top to bottom, strands 1, 2, 3, and 9 were instrumented in L1. Strands 2, 3, and 8 were instrumented in L2.

4.2.2. Field Test Piles

Field test pile P1 was instrumented with 11 strain gauges, while pile P2 was instrumented with 12 strain gauges. The strain gauges in these test piles were also attached to the prestressing strands, and all of the strain gauges were located near the top of each pile since the critical moment region during the lateral load tests was expected to occur near the top end of each pile. Test pile P1 also contained six "sister bars," which are vibrating wire strain gauges that are usually installed in pairs and measure the average strain over a 6-in. (15-cm) gauge length. The three pairs of sister bars were installed in this pile – one near the top, one in the middle, and the third one near the bottom of the pile. These gauges were expected to enable calculation of the skin friction along the length of the pile. See Figure 4.7 for the locations of each pair of sister bars within pile P1. For both piles, threaded rods were installed close to the pile head so that Pile Driving Analyzer (PDA) acceleration and strain gauges could be installed externally to monitor the pile driving process.

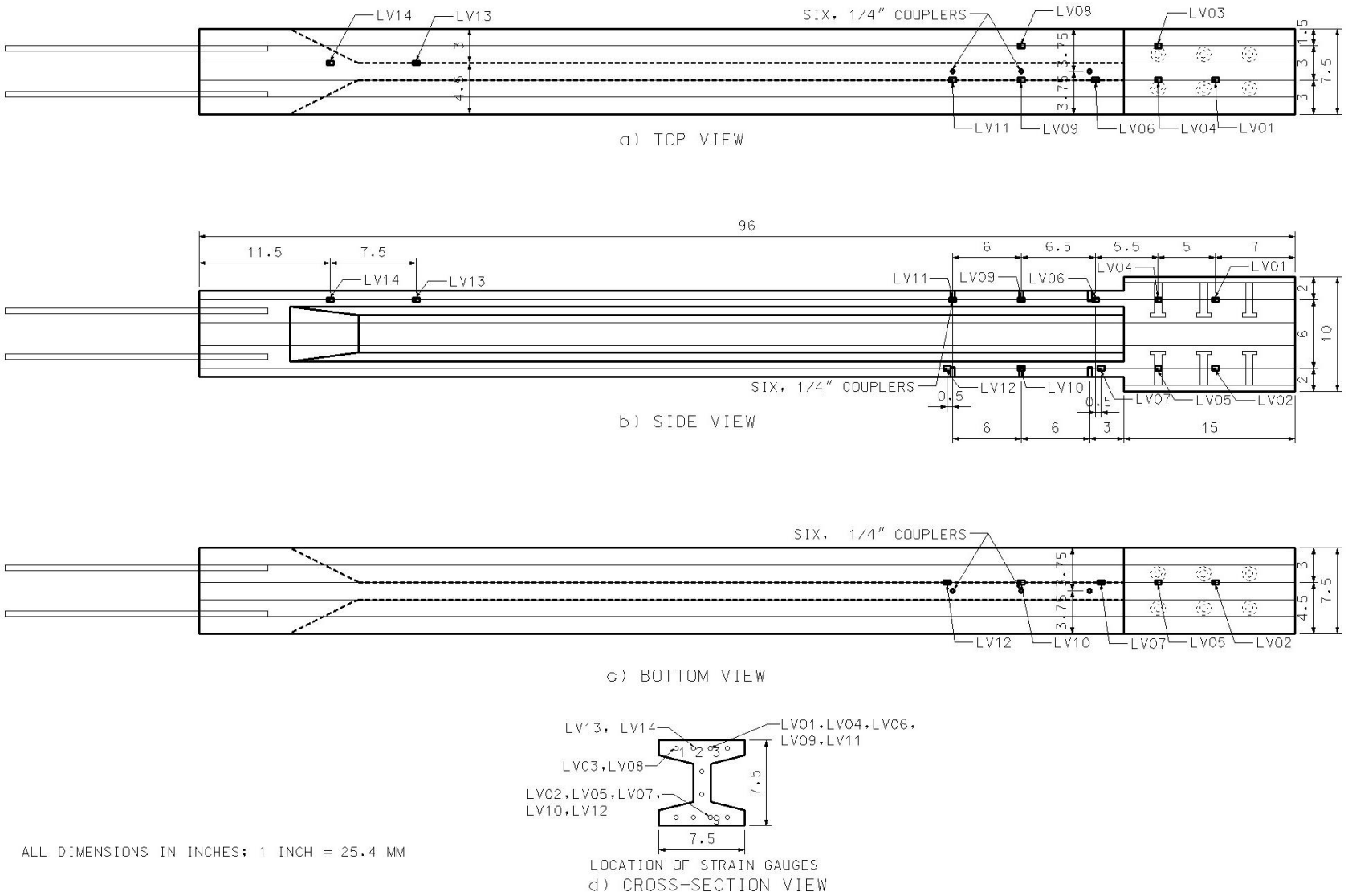

Figure 4.5. Details of instrumentation used for 8-ft (2.4-m) long UHPC laboratory test unit L1

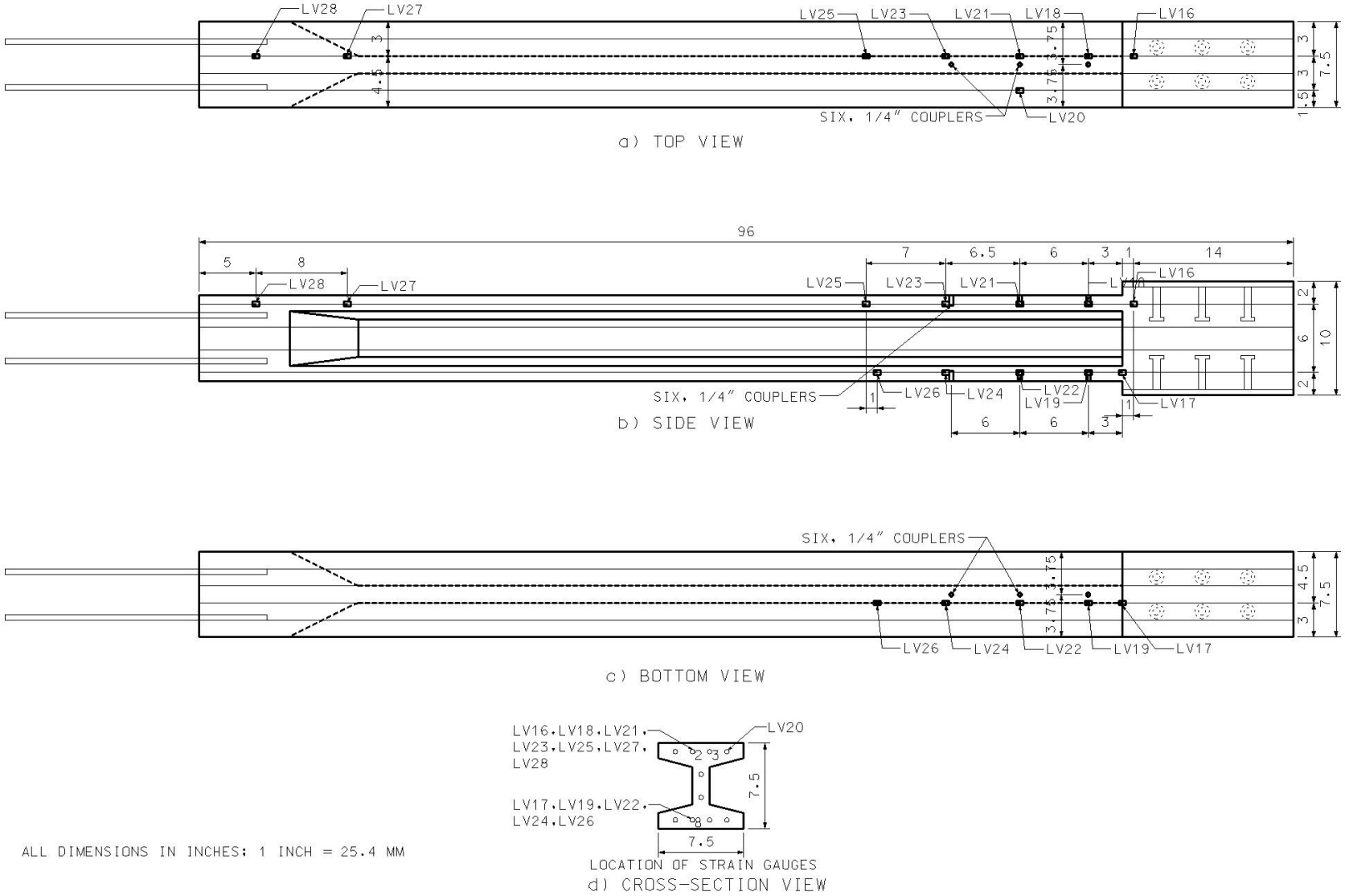

Figure 4.6. Details of instrumentation used for 8-ft (2.4-m) long UHPC laboratory test unit L2

The list of gauges and instrument mounting equipment installed in the 35-ft (10.7-m) piles includes the following, which are shown in their final locations after the initial prestress in Figure 4.7 and Figure 4.8 for UHPC test piles P1 and P2, respectively: strain gauges FL07 to FL17 on the prestressing strands of test pile P1 and FL18 to FL30 on the strands of test pile P2 (except for FL24, which was damaged during installation); sister bar vibrating wire strain gauges FL01 to FL06 for test pile P1 only; and three ¼-in. (6-mm) threaded rods in each pile for installation of PDA strain gauges and accelerometers. Strands 2, 3, 5, and 8 were instrumented for UHPC field test pile P1, and strands 1, 3, 5, and 8 were instrumented for test pile P2.

4.3. PRECAST FABRICATION

4.3.1. Casting Process

The five UHPC pile test units were cast at Coreslab Structures, Inc. in Bellevue, Nebraska. The UHPC pieces were cast in two pours due to limitations on the number of prestressing stands that could be stressed simultaneously in the end anchorages of the chosen prestressing bed. It was also desired to use the first pour as a learning experience if changes needed to be made for the second UHPC pour.

First the prestressing strands for each section were arranged in their proper configuration and a small prestressing force of approximately 3000 lb (13.3 kN) was applied to each strand to straighten and tighten the strands in place. The forms for each UHPC pile or unit were made from wood with Styrofoam inserts to create the desired tapered H-shape, as shown in Figure 4.9. Before the side forms were fastened in their final position, the strain gauges and sister bars were installed on the prestressing strands at their respective locations along the pile. Figure 4.10 shows two of the strain gauges (wrapped in aluminum tape), and Figure 4.11 shows a pair of sister bars attached to the prestressing strands. Initial strain readings from the strain gauges were taken, and then the prestressing strands were stressed to their initial prestress of 202.5 ksi (1400 MPa), which was approximately 75 percent of their ultimate strength. Figure 4.12 shows the stressing of the strands for UHPC pile P1.

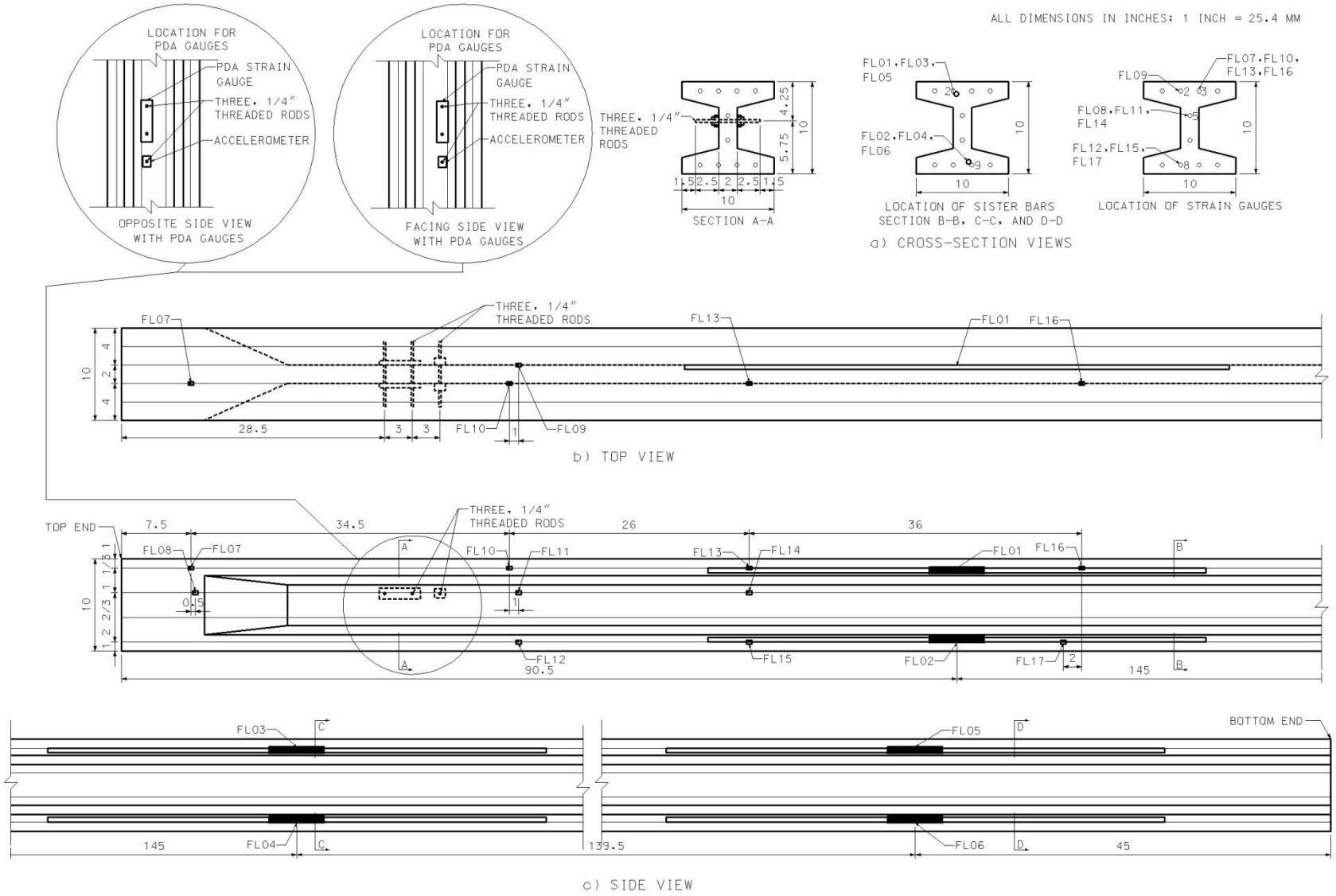

Figure 4.7. Details of instrumentation used for 35-ft (10.7-m) long UHPC field test pile P1

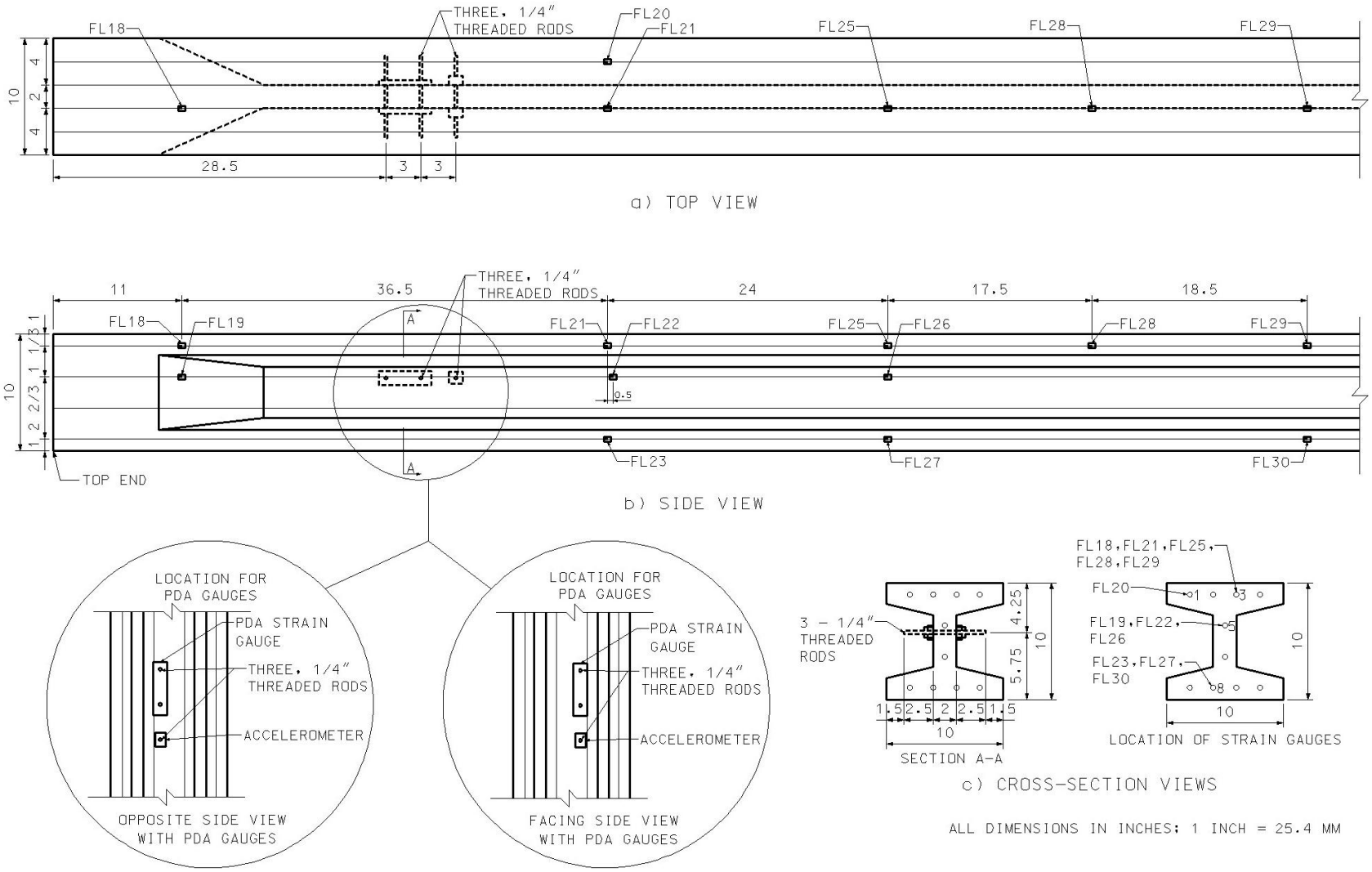

Figure 4.8. Details of instrumentation used for 35-ft (10.7-m) long UHPC field test pile P2

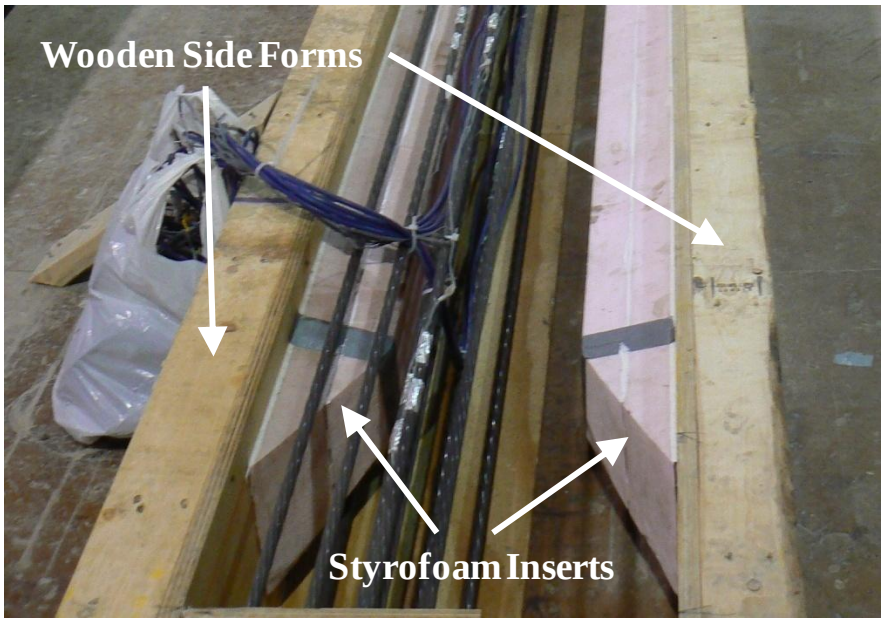

Figure 4.9. Formwork used for casting of tapered H-shaped section

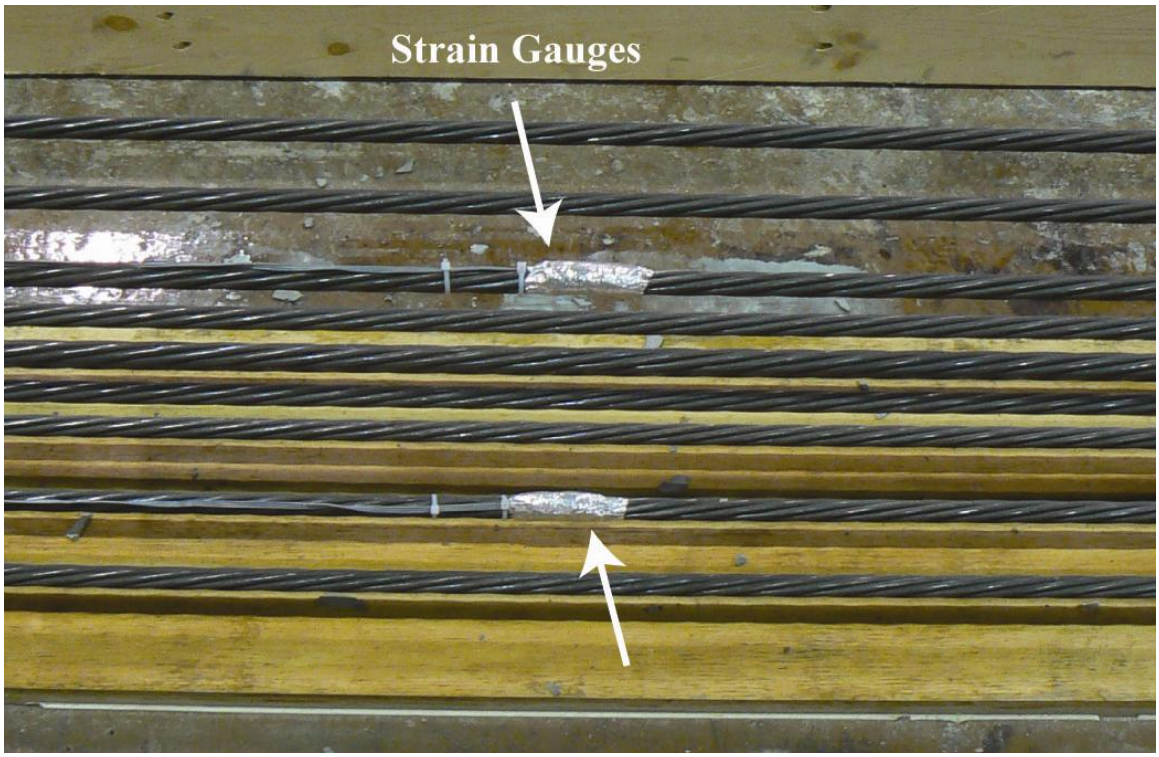

Figure 4.10. Strain gauges mounted to the prestressing strands and wrapped in aluminum tape

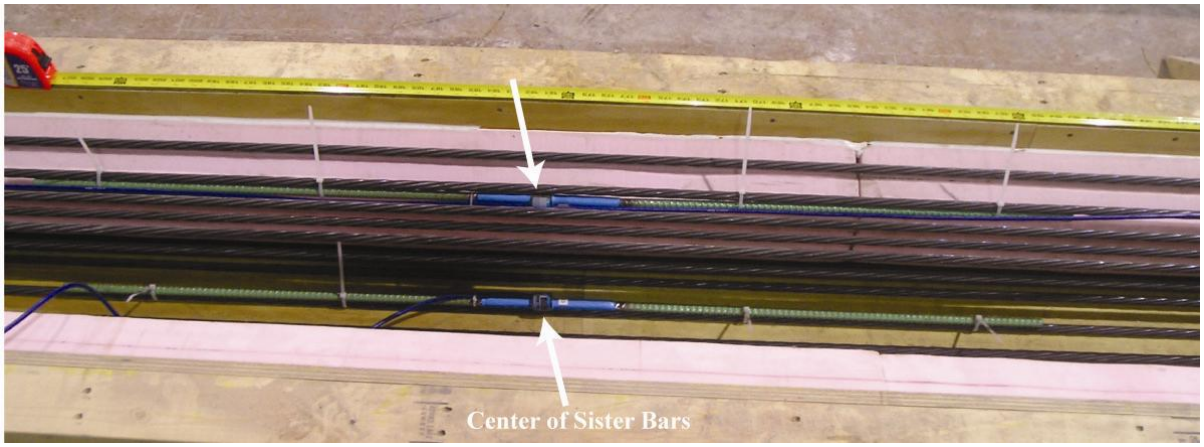

Figure 4.11. A pair of sister bars tied to prestressing strands

Figure 4.12. Stressing of prestressing strands for UHPC pile P1

After stressing all the strands, another set of strain readings were taken. Then the side forms were locked in place, and the UHPC mixing began. The UHPC was mixed at the precaster's batch plant in a 4.0 yd^3 (3.1 m^3) mixer. A total of 2.0 yd^3 (1.5 m^3) of Ductal® was donated by Lafarge North America, and approximately 1.0 yd^3 (0.8 m^3) of UHPC was produced for each of the two pours.

When the UHPC had been mixed, it was poured into the forms for each pile test unit. The UHPC being poured into the forms was kept behind its own leading edge as it flowed through the section. In this way, the fibers in the UHPC were oriented with the flow along the longitudinal axis of the piles test units, providing the maximum ultimate tensile strength

in the axial direction of each member, as in the study by Grünewald (2004). Immediately after the UHPC was poured in the forms, the exposed top surfaces of the UHPC units were covered with plastic wrap to prevent moisture loss, as shown in Figure 4.13.

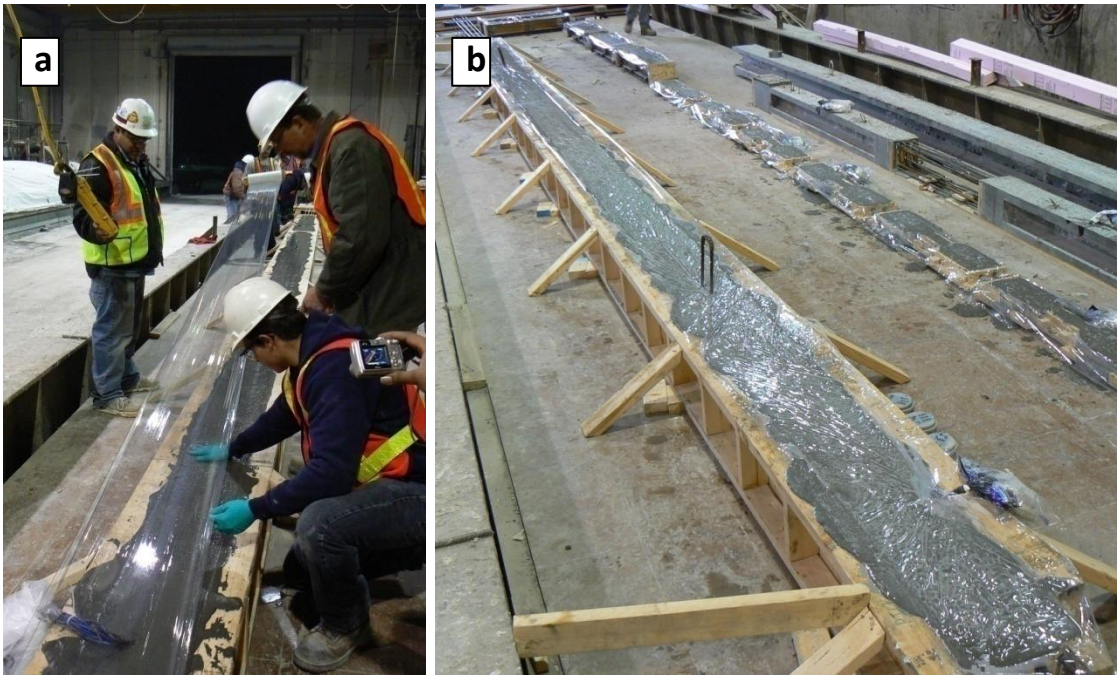

Figure 4.13. a) Covering cast top surfaces of a UHPC pile with plastic to prevent moisture loss and b) a cast and covered UHPC pile

The UHPC units were then covered under a tarp, and propane heaters were used to provide an initial curing at 86°F (30°C). Several 6-in. (15-cm) diameter, 12-in. (30-cm) tall UHPC cylinders and 2-in. (51-mm) cubes were also cast with each pour. The precaster tested the cylinders periodically during the initial curing of UHPC to determine the compressive strength of the mix. When the cylinders reached a compressive strength of 5.0 ksi (35 MPa), the side forms were released to allow unrestrained shrinkage of the UHPC, since the rate of shrinkage in UHPC rapidly increases beyond this point. Figure 4.14 shows the stripped second 35-ft (10.7-m) UHPC pile undergoing initial curing, with the propane heaters shown in the background. Note that since Styrofoam inserts comprised most of the formwork surfaces in contact with the UHPC piles, stripping of the side formwork at 5.0 ksi (35 MPa) compressive strength was probably not necessary. The Styrofoam would compress easily

without significantly restraining shrinkage of the UHPC units. After reaching a compressive strength of 14 ksi (97 MPa), the prestressing strands were cut at the member ends to release the prestressing to the UHPC, as shown in Figure 4.15. The strands were cut in the sequence shown in Figure 4.16 to avoid any unnecessary distressing in the end regions of the pile due to temporary eccentricity of prestress.

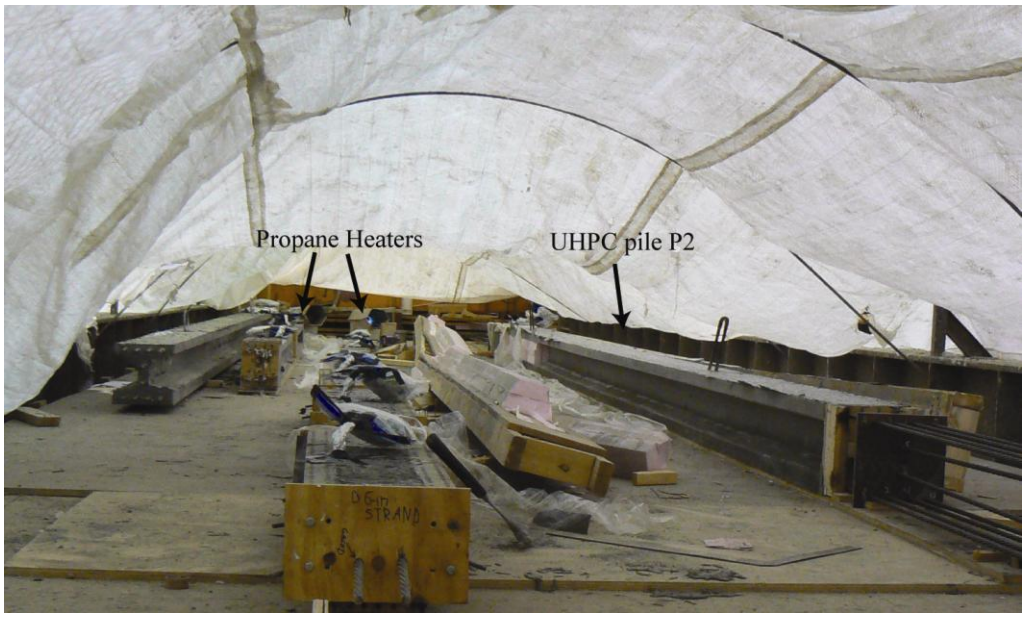

Figure 4.14. Stripped UHPC pile P2 undergoing initial curing with the help of propane heaters under tarp

Figure 4.15. Strands released at end of UHPC pile P2

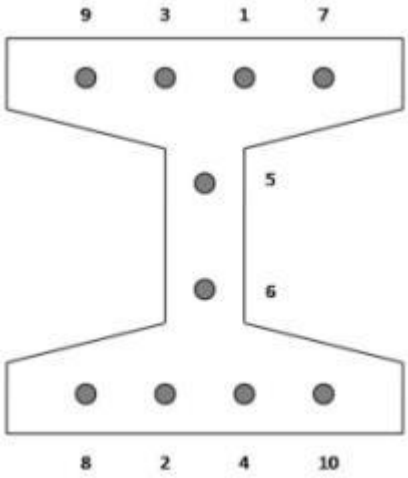

Figure 4.16. Strand release sequence used for UHPC pile test units

4.3.2. Details of First Pour

The first pour of UHPC piles and test pieces took place on November 28, 2007. The 35-ft (10.7-m) test pile P1, the two 8-ft (2.4-m) test units L1 and L2, and the 10-ft (3.0-m) test unit were cast using one batch of UHPC. The layout of the forms immediately prior to casting is shown in Figure 4.17.

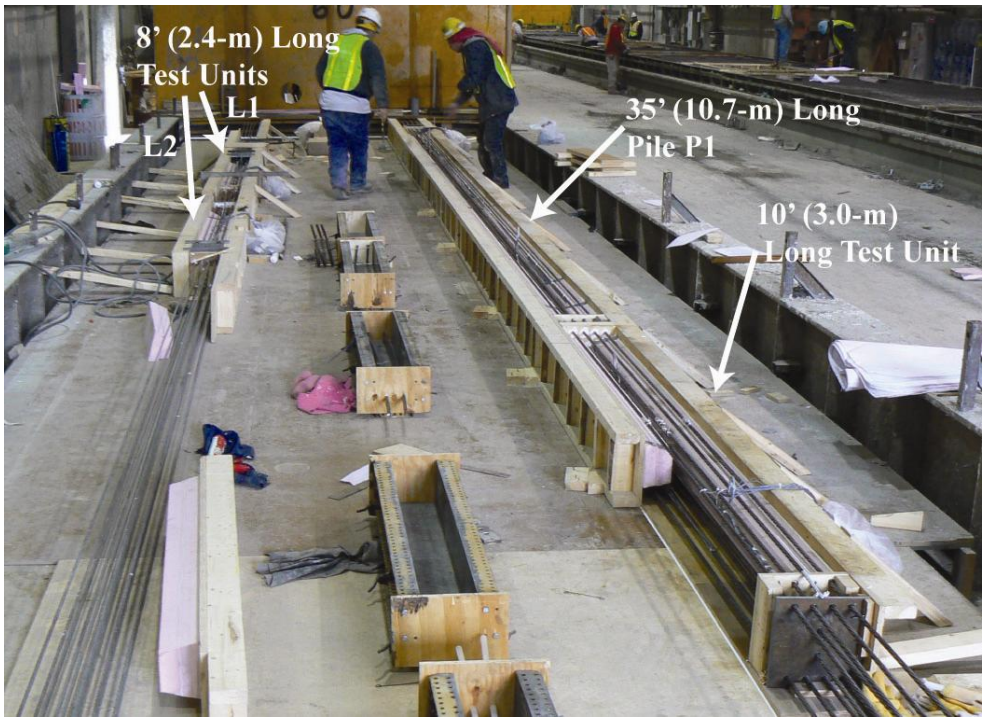

Figure 4.17. Layout of UHPC units for the first pour at Coreslab Structures in Bellevue

As the steel fibers for the first UHPC batch were added to the mixer, the fibers clumped in the rubber sleeves used to add the fibers to the mix. Clumping also occurred when the fibers were alternatively added to the mix using a skip hoist. The fibers were eventually all added, however, and dispersed throughout the mix. Typically, a dry mixer should be used for UHPC, but since the mixer at the precasting plant had been cleaned with water just prior to mixing, the water content of the UHPC mix was reduced by 2.0 gallons (7.6 L) to account for the moisture in the mixer.

The temperature of the UHPC during mixing was approximately 47°F (8°C), which is a fairly cool internal temperature for application of UHPC. A low temperature indicates a low reaction rate for UHPC, and so the mix tends to be more fluid at lower temperatures. This was clearly the case for the UHPC from the first pour, which had a static flow of 10.0 in. (255 mm). The dynamic flow was measured on a 10-in. (25-cm) flowtable using a standard flowtable test, according to ASTM C 230/C 230M – 03, and the resulting flow was greater than 10.0 in. (255 mm), since the material flowed off the edge of the flowtable.

The flowability of the UHPC allowed it to be poured in the forms quite easily. Figure 4.18 and Figure 4.19 show the UHPC being poured into a pile form. No vibration was used during casting of the first pour. Casting was a fairly quick process, and the UHPC members were then covered and heated at approximately 86°F (30°C) for the next 36 hours. The UHPC was stripped at a compressive strength of approximately 7.5 ksi (52 MPa). The mix reached a compressive strength of 14 ksi (97 MPa) approximately 36 hours after casting, according to compression tests performed by the precaster on 6-in. (150-mm) diameter cylinders, and the strands were then released.

4.3.3. Problems with the 10-ft (3.0-m) Laboratory Test Unit

Upon stripping, the 10-ft (3.0-m) laboratory test unit was found to be missing large sections of its web. The UHPC mix was so fluid that it flowed entirely across the top and bottom flanges, filling them completely, but the 2.0-in. (51-mm) thick web, which also contained two ½-in. (13-mm) prestressing strands, was only filled with UHPC over about a third of the unit's length. It is suspected that the UHPC did not immediately fill the confined spaces in the web, and as the material flowed across the top flange, air was probably trapped

in the web. The gaps in the web were not detected until the test unit was stripped. As expected, the partial web of the 10-ft (3.0-m) long test unit fractured longitudinally when the prestressing strands were released, as shown in Figure 4.20, and so this test unit was abandoned.

Figure 4.18. Beginning of first pour of UHPC units

Figure 4.19. Pouring of 35-ft (10.7-m) long UHPC pile P1

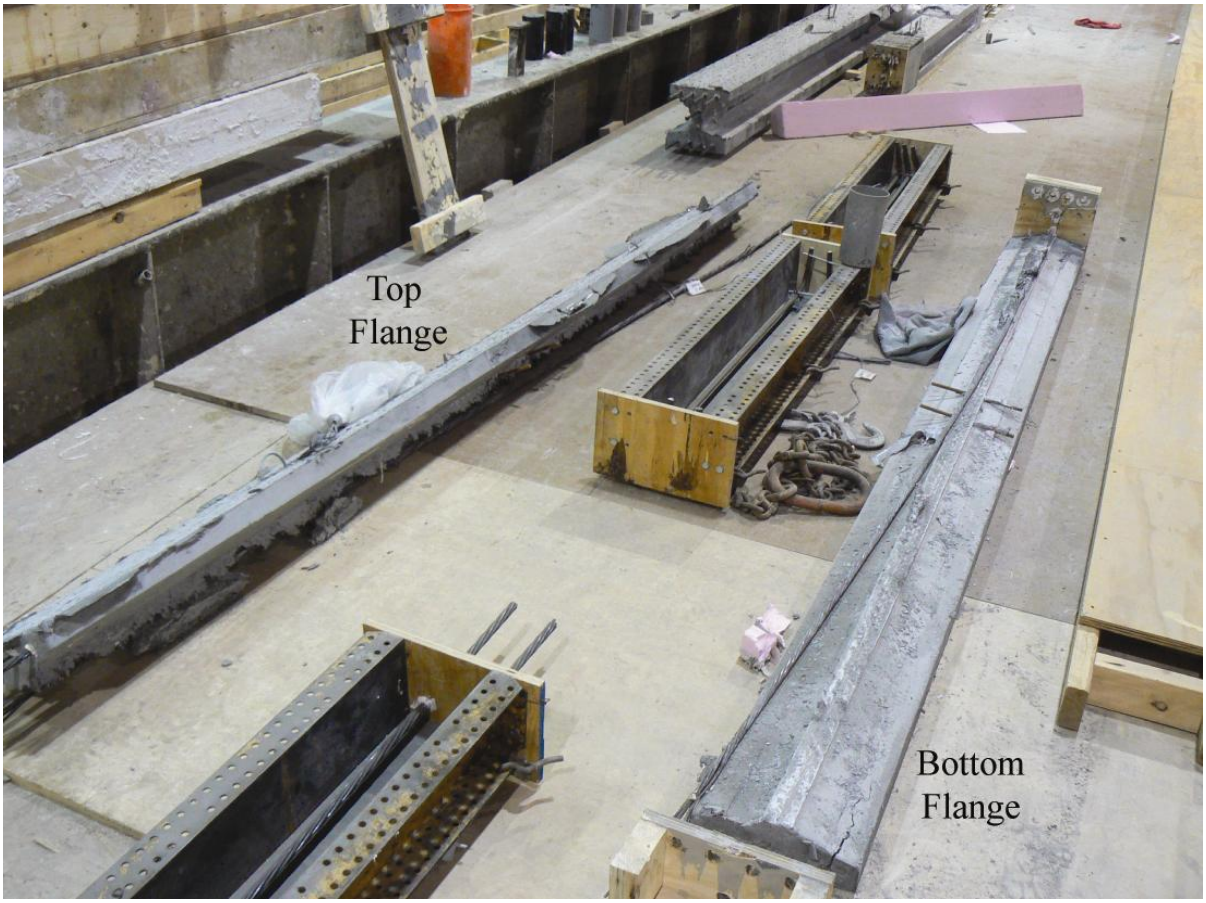

Figure 4.20. Top and bottom flanges of 10-ft (3.0-m) long test unit after release of prestressing strands

The other two laboratory test units, L1 and L2, will allow adequate moment-curvature data to be obtained, and not enough UHPC remained after the first pour to attempt to cast the full-scale 10-ft (3.0-m) long test unit again.

The 35-ft (10.7-m) long pile P1 from the first pour also exhibited some minor pocketing near the flange-web interface, as shown in Figure 4.21. These pockets are suspected to have formed in somewhat the same manner as the gaps in the web of the 10-ft (3.0-m) long test unit, but the air became trapped in the web to a much lesser degree than in the 10-ft (3.0-m) long test unit. The minor pocketing in the 35-ft (10.7-m) long pile P1 was not a source of concern for the overall strength and behavior of the UHPC pile.

Figure 4.21. Minor pocketing observed in the web of UHPC pile P1

4.3.4. Details of the Second Pour

The second pour of the UHPC piles and test units took place on December 6, 2007. The second 35-ft (10.7-m) UHPC field test pile P2 was cast along with some small UHPC samples used for a separate study. The layout of the pile and small samples cast in the second pour is shown in Figure 4.22.

The mixing process went smoothly, including the addition of the steel fibers since care was taken to add the fibers gradually. Also, since the mixer had not been rinsed immediately prior to casting, the water content did not have to be modified. A flowtable measurement for the second pour was not available, but the mix was much stiffer than the mix used for the first pour. The most likely reason for the decreased flowability of the second batch, according to a representative of Lafarge North America, is that the mixing of UHPC was stopped prematurely. Stopping mixing slightly prematurely will not affect the final properties of the hardened UHPC, although it will make the mix stiffer and somewhat more difficult to pour. A visual comparison between the flowability of each mix is shown in Figure 4.23.

Since problems with pocketing were experienced with the very flowable first UHPC pour, extra precautions were taken for the stiff second pour. As the UHPC was poured into the forms, a worker used a #3 reinforcing bar to push the UHPC mix vertically through the web of test pile P2, as shown in Figure 4.24, to ensure the filling of the web with UHPC.

After the pile was cast, it was also vibrated for several seconds every 5 to 10 feet (1.5 to 3.0 m) along the pile length, as shown in Figure 4.25. When test pile P2 was stripped, it showed no air pockets in the web or flanges. Therefore, the "rodding" and vibrating were helpful in ensuring the UHPC completely filled the section despite the increased viscosity of the mix.

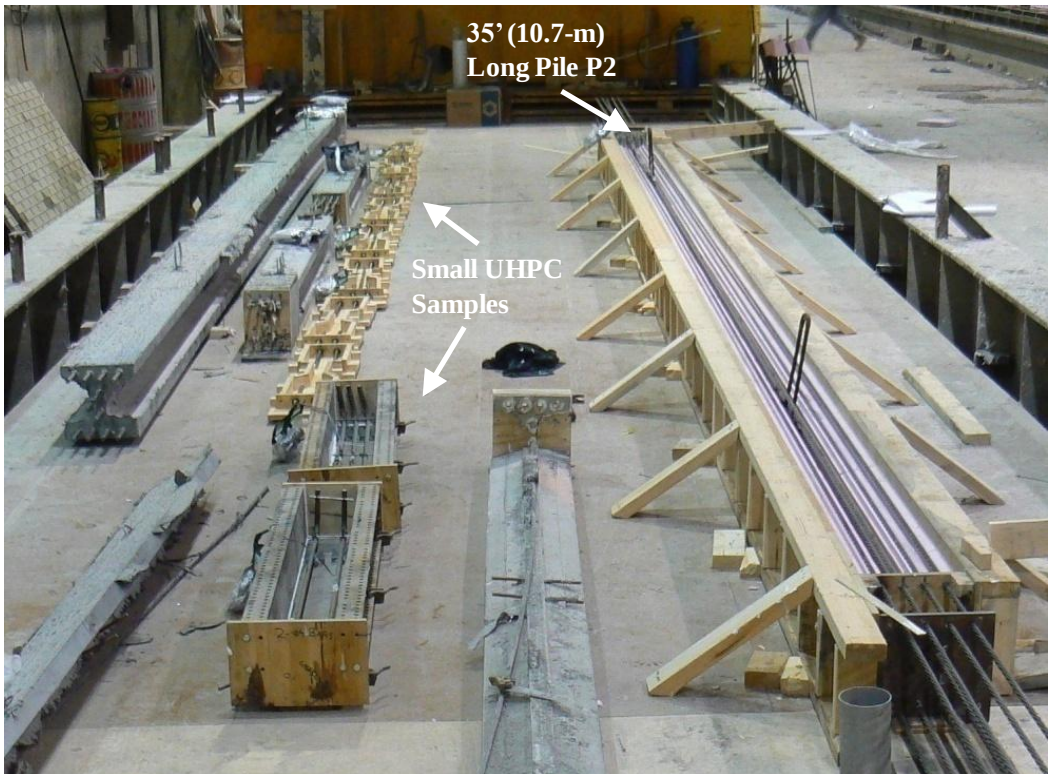

Figure 4.22. Layout of UHPC pile P2 and small samples for the second pour

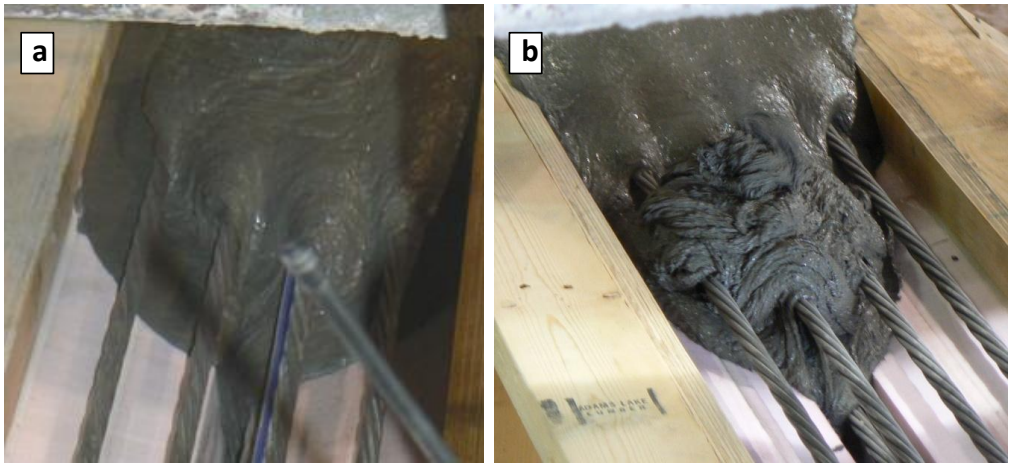

Figure 4.23. Comparison of flowability of a) first and b) second pour of UHPC

Figure 4.24. "Rodding" through the web of UHPC to eliminate formation of possible air pockets

Figure 4.25. Vibrating freshly cast UHPC to ensure complete filling of forms

After casting, test pile P2 and the small UHPC samples were covered and heated with propane heaters for approximately the next 84 hours. The UHPC had achieved a compressive strength of only about 11 ksi (76 MPa) by Saturday morning, December 8, 2007, 42 hours after casting. Since the second UHPC pour had not achieved the required 14 ksi (97 MPa)

compressive strength at transfer by Saturday morning, the UHPC pile was kept in the initial curing stage with the propane heaters for the rest of the weekend. It is likely that the UHPC achieved the transfer strength approximately 48 to 54 hours after casting. This delay in the development of the UHPC compressive strength of the second pour compared to the first pour can most likely be attributed to the difference in the ambient temperature. The ambient outdoor temperature at the time of the second pour was about 20°F (11°C) colder than that of the first pour. It is possible that the internal temperature of the UHPC was close to freezing, possibly delaying the start of the chemical reactions in the mix. The temperature inside the precasting building was also much colder compared to the previous pour, and so it may have taken longer for the propane heaters to bring the temperature under the tarp up to 86°F (30°C). This delay in the initial curing could have contributed to the longer time required for the UHPC from the second pour to develop the 14 ksi (97 MPa) transfer strength.

4.3.5. Steam Curing and Instrumentation Performance

After the release of the prestressing strands in the UHPC test pile P2, all of the UHPC members from both pours were steam-cured at 194°F (90°C) for 48 hours at the precasting plant. Of the 23 strain gauges installed in the two UHPC test piles, only two gauges, FL08 in test pile P1 and FL26 in test pile P2, stopped working after the initial stressing of the prestressing strands. The remaining 21 gauges continued to function after the steam curing, giving an instrumentation success rate of 91 percent at the end of the curing process.

4.4. HANDLING OF UHPC MEMBERS

Two lifting hooks were cast into each UHPC pile test unit at the locations shown in Figure 4.26a. Lifting each UHPC pile test unit by one or both hooks caused no harm to the UHPC members during handling at the precasting plant. In fact, a UHPC pile designed with the 10 by 10-in. (25 by 25-cm) tapered H-shaped cross-section could be up to 210-ft (64-m) long with one lifting hook (b) or 140-ft (43-m) long with two lifting hooks (a) in the configurations shown in Figure 4.26 without cracking during lifting. Note that for

calculations with one lifting hook, the UHPC pile is assumed to be supported at its far end by the ground.

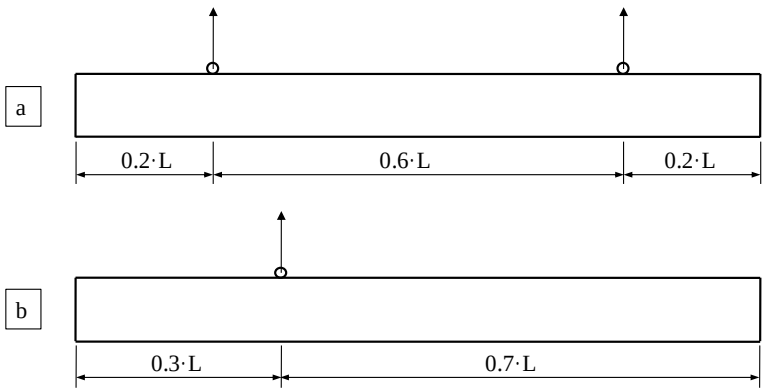

Figure 4.26. Locations of a) two or b) one lifting points for UHPC piles

4.5. MATERIAL PROPERTIES

4.5.1. Prestressing Strands

4.5.1.1 Ultimate Strength and Strain

Two 0.375-in. (9.5-mm) and two ½-in. (13-mm) diameter, 270 ksi (1860 MPa) low-relaxation strands that were used in UHPC test units were tested in uniaxial tension at Iowa State University. The ultimate strength of the 0.375-in. (9.5-mm) strands, which were used in the laboratory test units L1 and L2, was not obtained due to premature failure of the strands. The chucks used to grip the strands during the tests pinched the wires making up the strand, eventually fracturing the strands in the chucks before plastic stress-strain behavior was observed in both tests. The ultimate strength of the ½-in. (13-mm) strands was obtained, however, and those strands reached an average ultimate strength of 274 ksi (1890 MPa) before failing in tension. Figure 4.27 shows the stress-strain relationship obtained for one of the ½-in. (13-mm) prestressing strands. Note that this strand also failed in the chucks, so the ultimate tension strain value is expected to be higher than the 0.032 measured in the middle of the strand at failure.

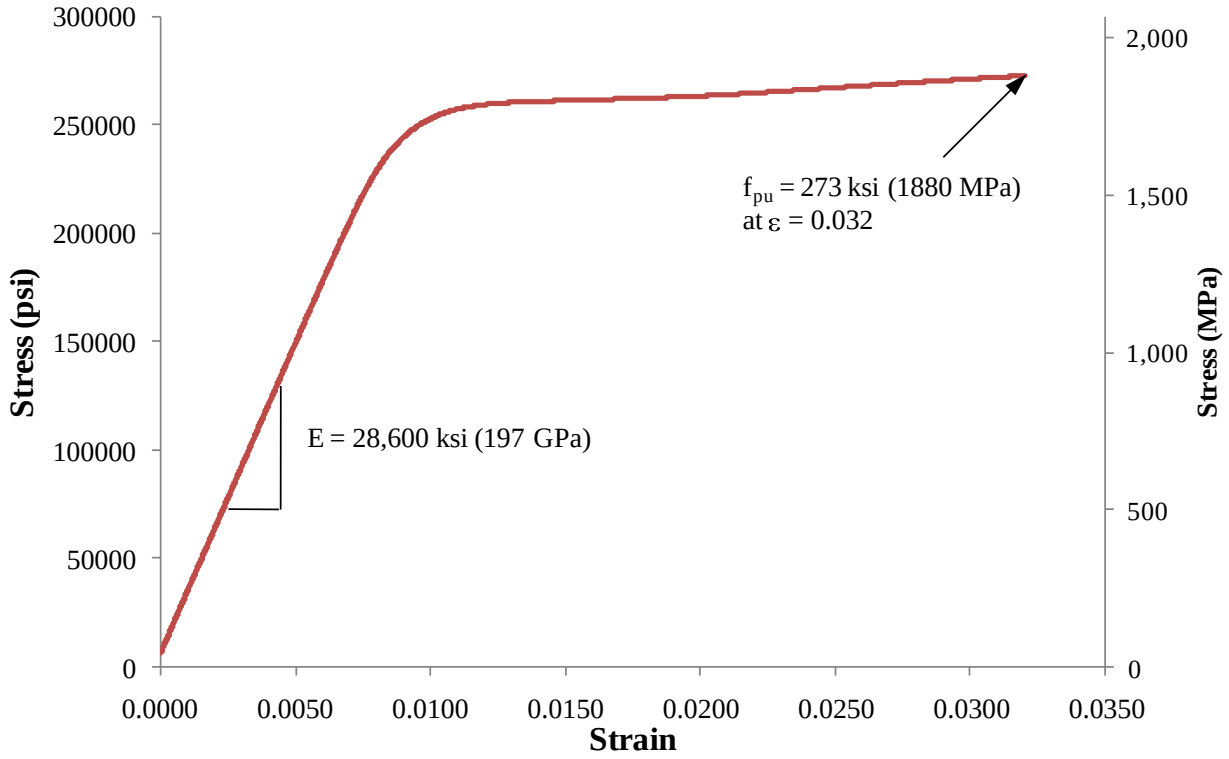

Figure 4.27. Measured stress-strain behavior of a ½-in. (13-mm) diameter low relaxation prestressing strand

4.5.1.2 Elastic Modulus

The initial elastic modulus of both strand sizes was also obtained, using the elastic portion of the stress-strain curve, which was obtained for all of the strands that were tested. The 0.375-in. (9.5-mm) strands had an average elastic modulus of 29,600 ksi (204 GPa), while the ½-in. (13-mm) strands had an average elastic modulus of 29,000 ksi (200 GPa).

4.5.1.3 Initial Prestress

The target initial prestress was $0.75 \cdot f_{pu}$, or 202.5 ksi (1400 MPa). Taking into account the initial 3000 lb (13 kN) load used to straighten the tendons prior to taking the initial strain readings, the actual initial prestress in each instrumented strand was computed using the measured elastic modulus of each size of prestressing strand. Table 4.2 shows the average initial prestress for each UHPC member, which was within 8 percent of the target value in each case.

Table 4.2. Initial prestress in UHPC test units and piles

Unit	Pour	Measured Initial Prestress ksi (MPa)
8-ft (2.4-m) Test Unit L1	First	195 (1344)
8-ft (2.4-m) Test Unit L2	First	200 (1377)
35-ft (10.7-m) Pile P1	First	193 (1329)
35-ft (10.7-m) Pile P2	Second	186 (1286)

4.5.2. UHPC

4.5.2.1 Compressive Strength

The 2.0-in. (51-mm) UHPC cubes that were cast and cured with the UHPC units were tested in compression at Iowa State University at an age of approximately five months, or 150 days. Note that since UHPC achieves nearly its full compression strength at the end of casting, little difference is expected between strengths at any ages after the end of curing. Four samples were used to establish the compressive strength of each pour. The measured strength of each cube and the average value are shown in Table 4.3. The design compressive strength of the UHPC mixes was 26 ksi (179 MPa), and results show that this average strength was achieved for the UHPC from both pours. The stiffer second pour of UHPC provided a compressive strength that was approximately 10 percent higher than the design strength.

Table 4.3. Compressive strength of UHPC cubes from each pour

	Cube 1	Cube 2	Cube 3	Cube 4	Average
First Pour	27,573 psi 190.11 MPa	27,288 psi 188.14 MPa	25,443 psi 175.42 MPa	25,232 psi 173.97 MPa	26,384 psi 181.91 MPa
Second Pour	29,195 psi 201.29 MPa	28,640 psi 197.47 MPa	29,560 psi 203.81 MPa	28,032 psi 193.27 MPa	28,857 psi 198.96 MPa

4.5.2.2 Elastic Modulus

The elastic modulus for each UHPC pour was calculated according to Equation 4.1, reported by Graybeal (2007), based on experimental testing of Ductal® UHPC cubes that were also subjected the standard heat-treatment at 194°F (90°C) for 48 hours for UHPC. The

resulting elastic moduli for the first and second pour of the UHPC cubes were 7500 ksi (51.7 GPa) and 7850 ksi (54.1 GPa), respectively.

$$E = 46,200 \cdot \sqrt{f'_c} \qquad (E = 3840 \cdot \sqrt{f'_c}) \qquad (4.1)$$

4.6. SUMMARY OF CASTING

The casting experiences with the UHPC piles test units further confirms the ability of UHPC to be successfully cast in a precasting plant. The thin section elements in the 10 by 10-in. (25 by 25-mm) tapered H-shaped cross-section can be successfully filled as UHPC is poured if precautions are taken, even with a very stiff mix. Some limited vibration of the mix and/or "rodding," as described in Section 4.3.4, may be appropriate to ensure smooth casting of UHPC piles. The target strength of UHPC was achieved for both pours, even though the two pours displayed very different flowability. The high initial strength and low weight of cast UHPC members eliminates any concerns with the handling of the UHPC piles.

CHAPTER 5: FIELD TESTING OF UHPC PILES

The two 35-ft (10.7-m) UHPC piles were driven into the ground and load tested to verify their potential for application in bridge substructures. The UHPC piles were installed next to a bridge under construction near Oskaloosa, Iowa. UHPC test pile P2, cast in the second UHPC pour at the precasting plant, was installed first. Test pile P1, cast in the first pour, was installed second, 5 ft (1.5 m) to the north of pile P1. An HP 10×57 steel pile was also installed and load tested so that it could be compared with the UHPC piles. Details of the driving and load testing of the piles are included in the following sections.

5.1. PILE DRIVING

5.1.1. Test Site

The bridge constructed at the Oskaloosa site is a three-span continuously welded plate girder bridge carrying future expansion of northbound US 63 across Union Pacific railroad located at 41° 20’ north latitude and 92° 39’ west longitude. The total bridge length is 407-ft (124-m), and HP 10×57 steel piles were designed to support the two abutments and the two piers of the bridge. The bridge is oriented in the northwest to southeast direction, and the test piles were installed on the north end of an access path for the southern pier of the bridge, as shown in Figure 5.1.

5.1.2. Soil Profile

Two Standard Penetration Tests (SPT) were conducted by the Iowa Department of Transportation near each abutments of the bridge. The location of the test piles is slightly closer to the SPT test conducted near the north abutment of the bridge, located approximately 250 ft (75 m) to the west of the test piles (see Figure 5.1). The research team hired Geotechnical Services, Inc. (GSI) to conduct two Cone Penetration Tests (CPT) at the bridge site. One CPT, referred to henceforth as CPT1, was located approximately 40 ft (12 m) south of the test piles, and the second, CPT2, was located 9 ft (2.7 m) south of the southernmost UHPC test pile. Figure 5.2 shows the CPT testing truck from GSI performing CPT2 near the test piles.

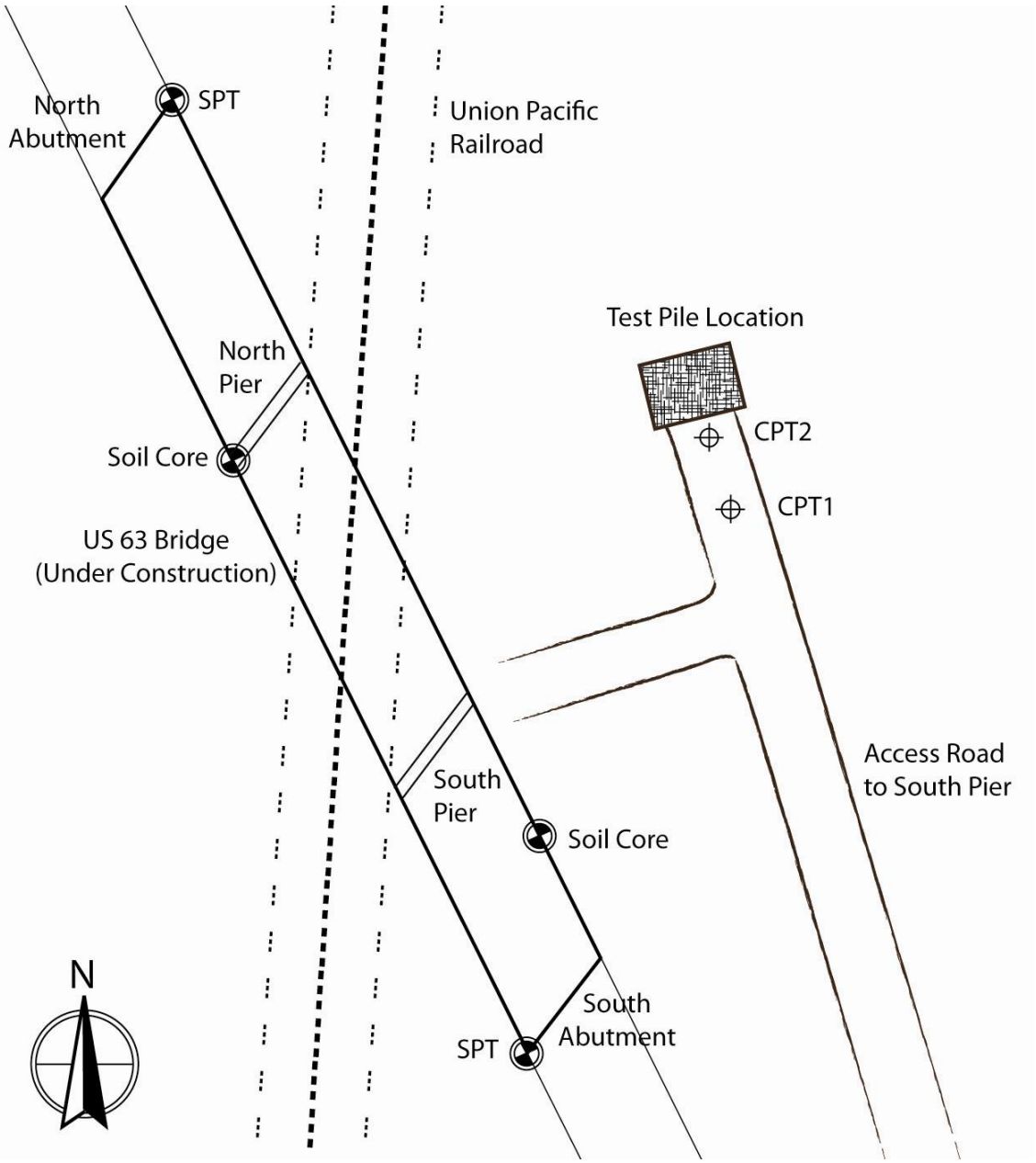

Figure 5.1. Plan view of the Oskaloosa bridge site including locations of test piles

The soil at the Oskaloosa bridge site consists of a loess soil – mostly clay with some sensitive fine grained material – underlain by Pre-Illinoian glacial till, which is classified primarily as sandy silt to clayey silt with intermediate layers of sand, silty sand to sand, clay, very stiff fine grained material, and sand to gravelly sand. The glacial till is underlain by a very hard layer, which may be bedrock. The CPT results indicate that the loess at the location

of the test piles is about 15 ft (4.6 m) deep, and the bedrock is located at a depth of 35 to 36 ft (10.7 to 11.0 m) below the ground surface. Results from the SPT at the north abutment and CPT2 on the site are shown in Figure 5.3. Since the SPT was located approximately 250 ft (75 m) from CPT, as noted previously, some variation in the depth of the soil layers in the soil profile was expected. Interestingly, however, if the SPT results are shifted downward by approximately 4 ft (1.2 m), the locations of hard layers from the CPT2 and SPT results line up very well. The SPT results shown in Figure 5.3 have therefore been adjusted downward by 4 ft (1.2 m). SPT and CPT2 results show a hard layer at a depth of approximately 26 ft (8 m) and bedrock at a depth of 36 ft (10.9 m). Observations during driving confirmed the locations of these layers, as discussed in Section 5.1.5.2.

Figure 5.2. View of CPT2 test in progress, located 9 ft (2.7 m) south of UHPC pile P2

The water table was located at a depth of approximately 10 ft (3 m) according to the Iowa Department of Transportation soil report for a borehole near the south pier, approximately 200 ft (60 m) from the test piles. A unit weight of 98.3 pcf (1574 kg/m^3) was measured from the loess soil samples taken near the ground surface next to the north pier (approximately 200 ft (60 m) from the test piles), and a unit weight of 130 pcf (2080 kg/m^3) was assumed for the glacial till. The Iowa Department of Transportation also reported a coefficient of consolidation of 0.37 ft^2/day (0.034 m^2/day), and a moisture content of 26 percent for the soil sample near the north pier.

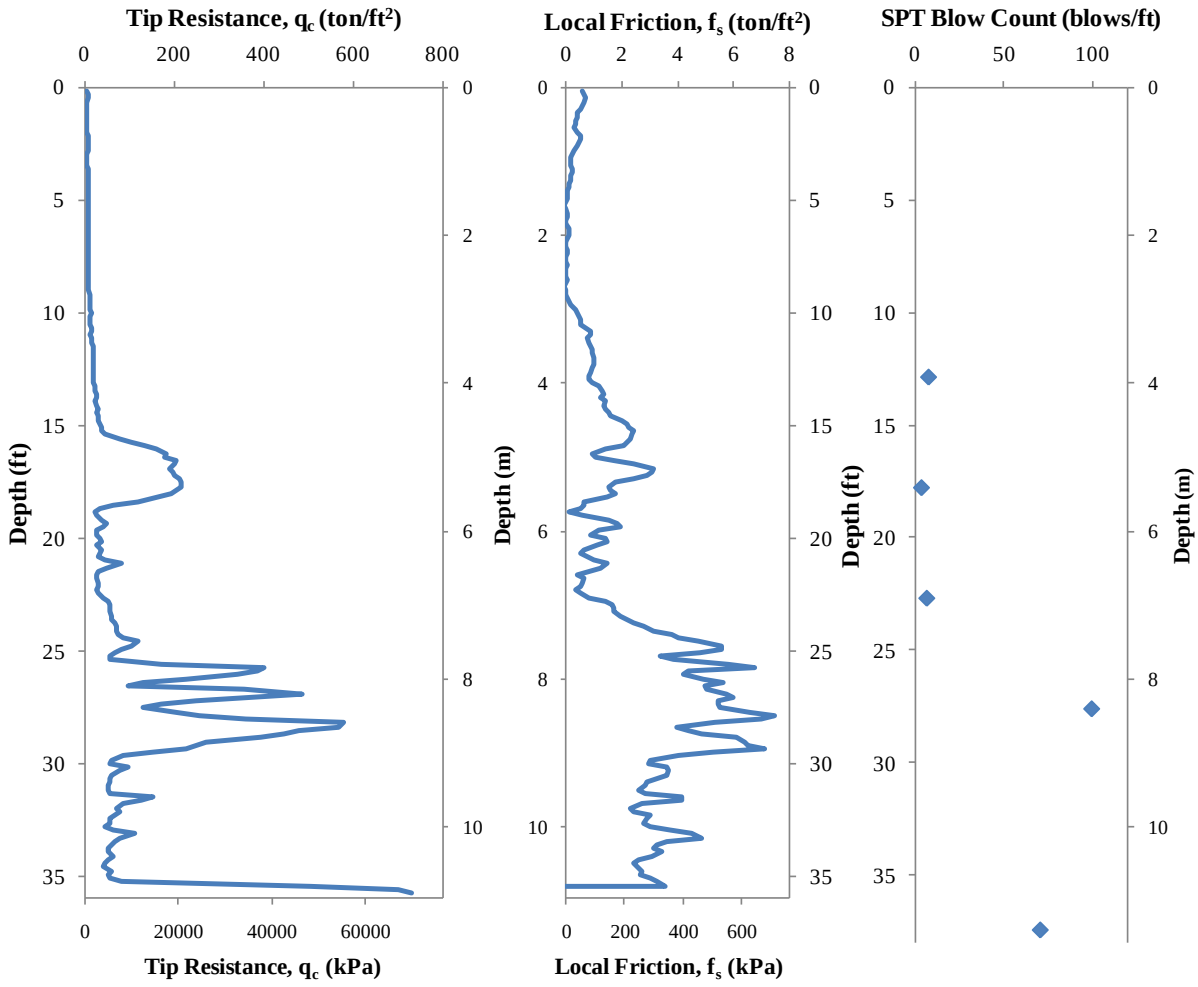

Figure 5.3. CPT2 and SPT results for soils on Oskaloosa test site

Figure 5.4 shows the soil classification reported by the Iowa Department of Transportation based on SPT and the classification by GSI based on CPT2. Both the SPT and CPT2 show that the glacial till contains intermediate hard layers composed of sand, gravel, and/or boulders, the most noticeable of which, as discussed previously and shown in Figure 5.3, occurred at a depth of approximately 26 ft (8 m).

Figure 5.4 also shows the undrained shear strength for each soil layer, which was calculated from the average of the undrained shear strengths calculated from CPT1 and CPT2. The undrained shear strength for each layer was determined using the "total" cone resistance from the CPT data and an empirically based approach described by Lunne et al. (1997). The CPT1 data showed layers of similar soil types to CPT2 but at different depths,

indicating some horizontal variation in the soil profiles. The data from the two CPTs were thus averaged over the same soil type, and the depths and layer thickness from CPT2 were used. The average results from the two CPT tests helped to reduce possible errors in CPT data caused by the rate of the test or obstructions in the soil profile and so created a better model of the resistance provided by the soil to a pile. For the average CPT results, the undrained shear strength ranged from 8.2 to 19.8 psi (57 to 136 kPa) for the loess layers (depths from 0 to 15.4 ft (0 to 4.7 m)) and from 37 to 232 psi (254 to 1600 kPa) for the glacial till layers (depths from 15.4 to 35.4 ft (4.7 to 10.8 m)). The Iowa Department of Transportation measured a cohesion of 6.4 psi (44 kPa) using a Consolidated-Undrained Triaxial Compression test on a soil sample taken from the top soil layer near the north pier.

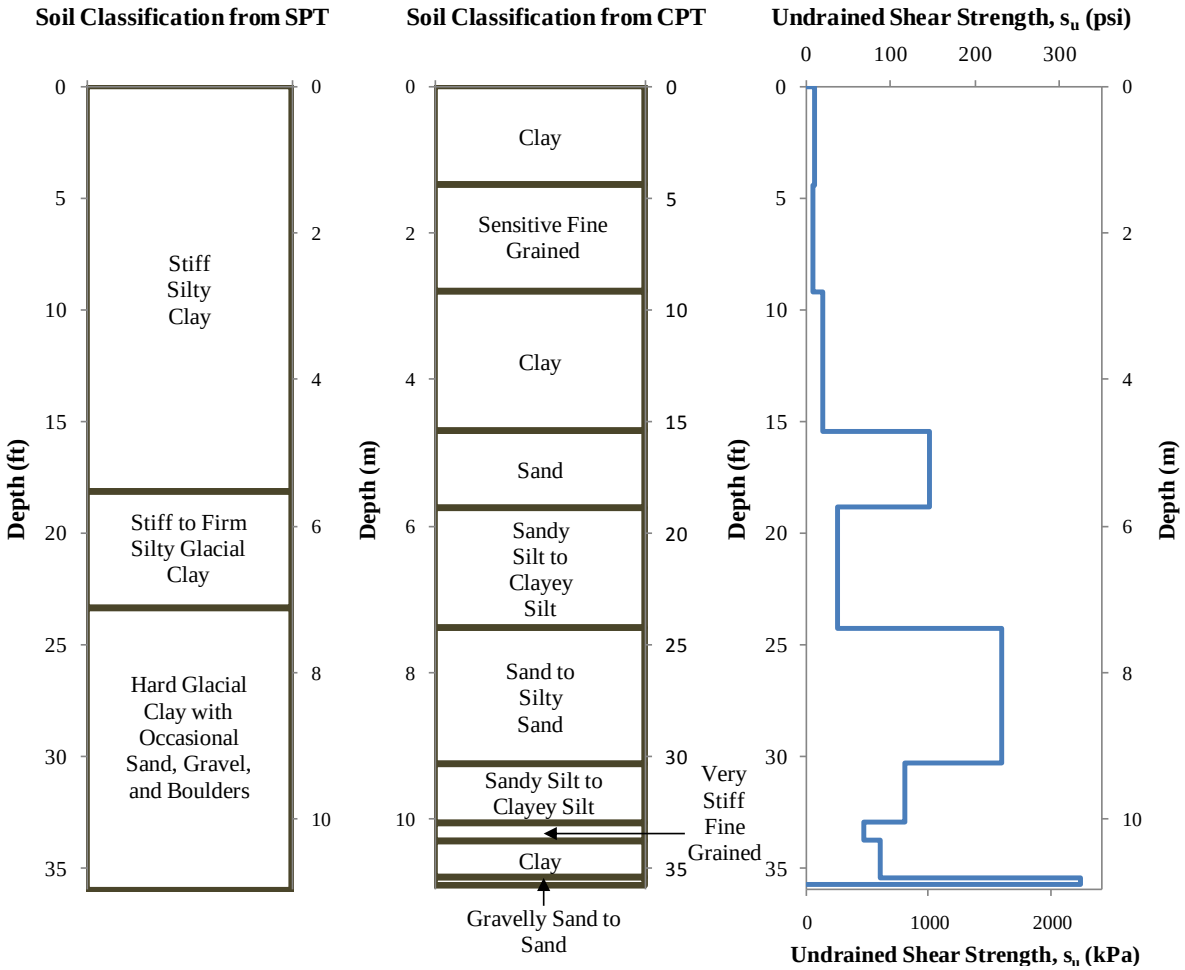

Figure 5.4. Soil classification from SPT and CPT and undrained shear strength calculated from CPT data

5.1.3. Driving System

A Delmag D19-42 hammer was used to drive the steel and UHPC piles used at the site. The D19-42 is an open-ended diesel hammer with a maximum stroke of 10.8 ft (3.3 m), a maximum combustion pressure of 1520 psi (10.5 MPa), a ram weight of 4.0 kips (18.2 kg), and a maximum rated energy of 48.7 ft·kip (66 kN·m) (Delmag 2007). A 2.0 kip (9.1 kg) driving helmet was used between the hammer and the piles. For the driving of the steel piles, an attachment at the bottom of the helmet was used which had four steel spikes. The spikes helped keep the thin-walled steel piles in place in the helmet during driving (see Figure 5.5). This attachment was removed for driving the UHPC piles since the solid 10 by 10-in. (250 by 250-mm) cross-section would not fit between the points. A 2.0-in. (51-mm) thick aluminum and micarta hammer cushion was used between the hammer and helmet for driving all of the piles.

Figure 5.5. Driving helmet with guiding spikes used for steel piles

The anchor piles were driven first, followed by the steel HP 10×57 pile, UHPC pile P2, and finally UHPC pile P1. A 2.25-in. (57-mm) thick plywood cushion was used while driving pile P2, which was the first UHPC pile driven into the ground at the site, and a 3.75-

in. (95-mm) thick cushion was used for pile P1. Even though, driveability analysis, described in the following section, indicated UHPC pile stresses due to driving were well within allowable values with no pile cushion even at the maximum hammer stroke, the pile cushion was used for the UHPC piles as a precautionary measure.

5.1.4. Driveability Analysis

In addition to the hammer properties described above, an elastic modulus of 430 ksi (3000 MPa) and a coefficient of restitution of 0.8 were assumed for the hammer cushion, and an elastic modulus of 30 ksi (207 MPa) and a coefficient of restitution of 0.5 were assumed for the plywood cushions, according to Iowa Department of Transportation guidelines (Dirks and Kam 2003). The soil shaft and toe resistances on the UHPC piles during driving were calculated using the undrained shear strengths calculated for CPT2 in the FHWA computer program "DRIVEN," which is used to calculate the vertical capacity of the UHPC piles and HP 10×57 steel pile (Matthias and Cribbs 1998). DRIVEN uses the Nordland and α-methods for determining the pile capacity in cohesionless and cohesive soil layers, respectively, and details of each of these methods can be found in Hannigan et al. (1998). Using DRIVEN, the predicted driving resistance of each UHPC pile was 148 kip (657 kN), and the predicted driving resistance of the steel pile was 111 kip (494 kN).

Driveability analysis with a variable hammer stroke was conducted with GRLWEAP, and the resulting maximum predicted stresses during driving for the UHPC and steel piles are shown in Table 5.1. The table shows the expected tensile stresses were not a source of concern since the allowable tensile stress of the prestressed UHPC piles is 5.5 ksi (38 MPa) and of the steel pile is 45 ksi (310 MPa). The compression stresses were also well below the allowable stresses of 17.5 ksi (121 MPa) for the UHPC pile and 45 ksi (310 MPa) for the steel pile.

Four additional HP 12×53 steel piles were required to anchor the loading frame used for the vertical load tests on the UHPC and steel piles. Neither Driven capacity analysis nor GRLWEAP driveability analysis was conducted for these piles, but they were designed as 40-ft (12.2-m) long piles with 35 ft (10.7 m) of penetration into the ground to achieve a total skin friction capacity of 120 kip (530 kN) each pile, according to Dirks and Kam (2003).

Table 5.1. UHPC and steel pile stresses predicted by driveability analysis

Stress	UHPC Pile – No Cushion ksi (MPa)	UHPC Pile – 2.25-in. Cushion ksi (MPa)	UHPC Pile – 3.75-in. Cushion ksi (MPa)	Steel Pile – No Cushion ksi (MPa)
Compression	8.5 (59)	6.8 (47)	6.6 (45)	26.5 (183)
Tension	0.04 (0.3)	0.04 (0.3)	0.11 (0.7)	0.09 (0.6)

5.1.5. Driving Process

5.1.5.1 Steel Piles

The four HP 12×53 anchor piles for the load test frame were driven at the test site on December 17, 2007. The HP 10×57 test pile and the two UHPC piles were driven the next day. A Pile Driving Analyzer (PDA) was used to monitor the driving of the HP 10×57. The PDA used two strain gauges and two accelerometers to measure the force and velocity imparted to the pile by the hammer. This allowed the driving resistance of the pile to be calculated using wave equation theory. The strain gauges and accelerometers were installed on the steel pile by bolting through drilled holes in the web approximately 36 in. (91 cm) from the pile head. (Note that the top 12 in. (30-cm) of the steel pile were cut off after driving.) The two strain gauges were located opposite to each other on either side of the web, and the accelerometers were located on the left side of each of the strain gauges, as shown in Figure 5.6. Wires extended from the gauges to a PDA unit provided and operated by the Iowa Department of Transportation. Results from the PDA analysis are reported in Section 5.2.

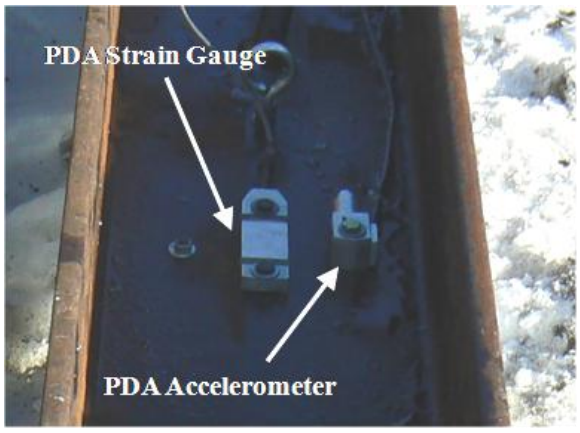

Figure 5.6. PDA strain gauge and accelerometer attached to the web of the HP 10×57 steel pile

The steel piles were lifted into position by cutting a hole in the web and passing a lifting chain through it. The lifting chain was attached to the lower end of the hammer, such that as the hammer was raised, the pile was lifted into a vertical position beneath it. The hammer leads were then positioned in the desired location and adjusted until they were perfectly vertical. Figure 5.7 shows the leads, hammer, and pile lifted into position. When the leads and pile were vertical, a worker climbed the ladder on the side of the leads to guide the hammer helmet onto the top of the pile as the hammer and helmet were lowered. When the leads, hammer, and pile were in place, the ram of the hammer was lifted manually by the crane and dropped. Since the resistance provided to the pile by the soil was minimal for approximately the first 8 to 10 ft (2.4 to 3.0 m) of penetration, the ram usually had to be raised manually several times before the hammer was able to develop enough combustion pressure to continue operating.

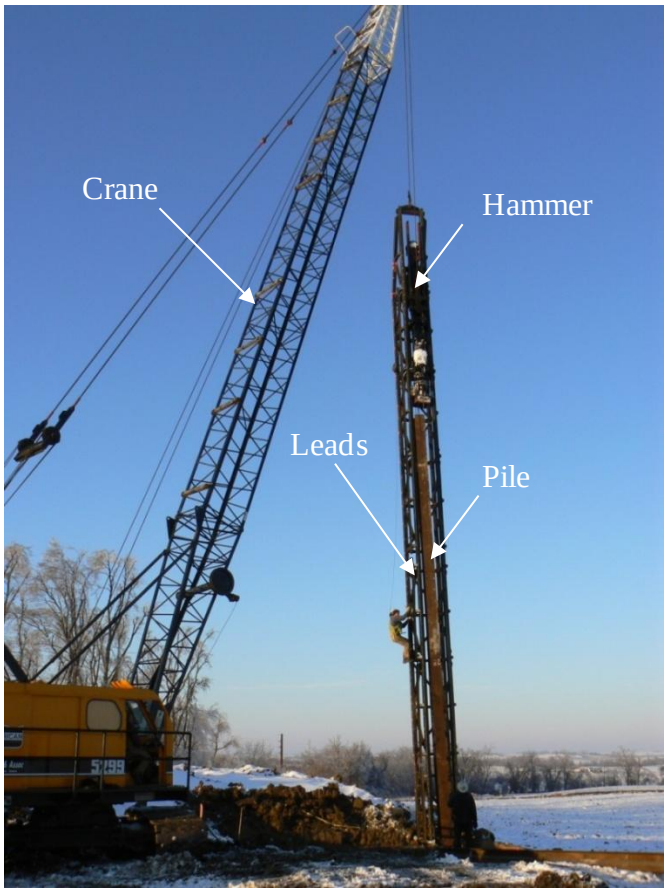

Figure 5.7. Crane, leads, hammer, and anchor pile lifted and ready for driving

Several of the piles experienced minimal local buckling or bending in the flanges near the pile top, as shown in Figure 5.8. The HP 10×57 test pile was originally 36-ft (10.9-m) long, and the top 12 in. (30 cm) was cut off to provide a level and even surface for the load testing of this pile. Although the anchor piles were not load tested, some of the bent flanges had to be cut off to allow the load frame to be correctly constructed and attached securely to the anchor piles.

Figure 5.8. Local buckling and bending damage to two steel anchor piles due to driving

5.1.5.2 UHPC Piles

The UHPC piles were driven on the same day as the steel test pile. The PDA was also used to monitor the driving of the UHPC piles, and the strain gauges were installed opposite to each other on either side of the pile web using threaded rods cast through the web. The accelerometers were installed opposite each other on the web just below the strain gauges, as shown in Figure 5.9, since the web was not wide enough for the accelerometers to be installed next to the strain gauges.

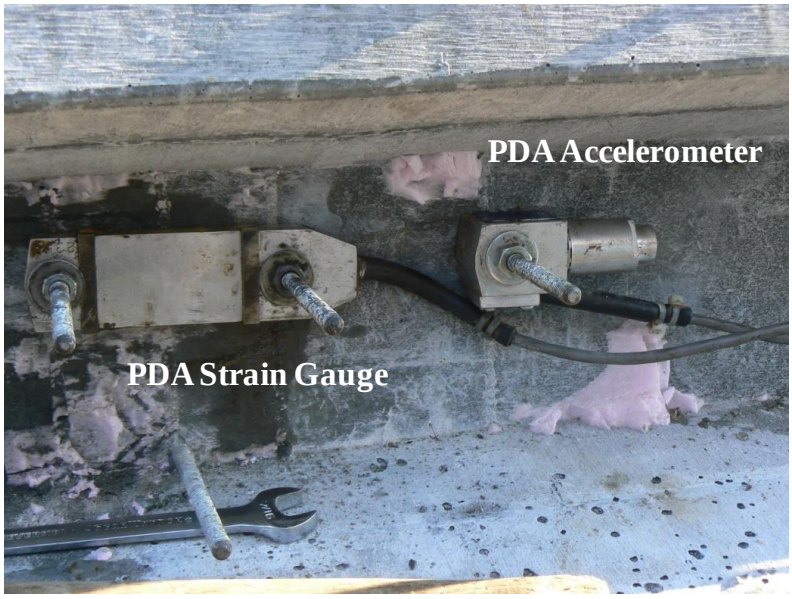

Figure 5.9. PDA strain gauge and accelerometer on one side of the UHPC pile web

The lifting hook cast into the UHPC piles was designed to allow the piles to be raised into position with a lifting chain, similarly to the steel piles. Since the hook was located 7 ft (2.1 m) from the pile top, the UHPC piles could not be safely lifted using this hook without the risk of the pile top colliding with the hammer leads. Instead, a lifting strap was used to hold the head of the UHPC pile and connected to the hammer and helmet to raise the pile into position as the hammer was lifted. For pile P1, driven after pile P2, the steel fibers protruding from the uncast edge of the pile cut through the lifting strap, causing it to break when the pile was positioned vertically in the leads. The pile driving crew was able to manually position the pile under the helmet so that it could be driven.

The contractor suggested improving the lifting procedure of the UHPC piles by casting a lifting hook much closer to the pile head. In fact, if an expanded section near the pile head is not used for future UHPC piles, two lifting hooks could be located on either side of the pile web within a short distance from the top of the pile, allowing for very easy and uniform lifting without interfering with the leads during lifting or driving.

The driving of the UHPC piles was similar to that of the steel piles. The low soil resistance at the beginning of driving required the ram to be raised manually several times before the hammer was able to develop enough combustion pressure to run continuously. A

hard layer was also observed after about 25 ft (7.6 m) of driving for the UHPC piles. Figure 5.10 shows the UHPC pile P2 being driven.

A 2.25-in. (57-mm) plywood pile cushion was used for this pile, but the pile cushion disintegrated rather abruptly at a pile penetration of approximately 28 ft (8.5 m), near or during the penetration through the hard soil layer. The deterioration of the cushion is shown in Figure 5.11. Instead of replacing the cushion with a new cushion, however, the pile was driven with essentially no cushion over the last 4 ft (1.2 m) of penetration. No damage occurred along the observable length of pile P2 or to the top of the pile (see Figure 5.12) after the deterioration of the pile cushion, though the pile was driven through hard sand and stiff fine-grained soil layers at the tip depth.

Figure 5.10. First UHPC pile being driven at the Oskaloosa test site

Even though no problems were encountered when the 2.25-in. (57-mm) plywood cushion disintegrated, a thicker 3.75-in. (95-mm) cushion was used for pile P1 as a precautionary measure and attempt to avoid or reduce the deterioration of the cushion. This pile cushion also deteriorated near the end of driving at a pile penetration of approximately 30 ft (9.1 m), leaving no cushion for the last 2 ft (0.6 m) of driving through relatively hard soil layers. Figure 5.13 shows that UHPC pile P1 also experienced no damage to the top of the pile after the pile cushion deteriorated. This further suggests that UHPC can be driven without a pile cushion if supported by driveability analysis results.

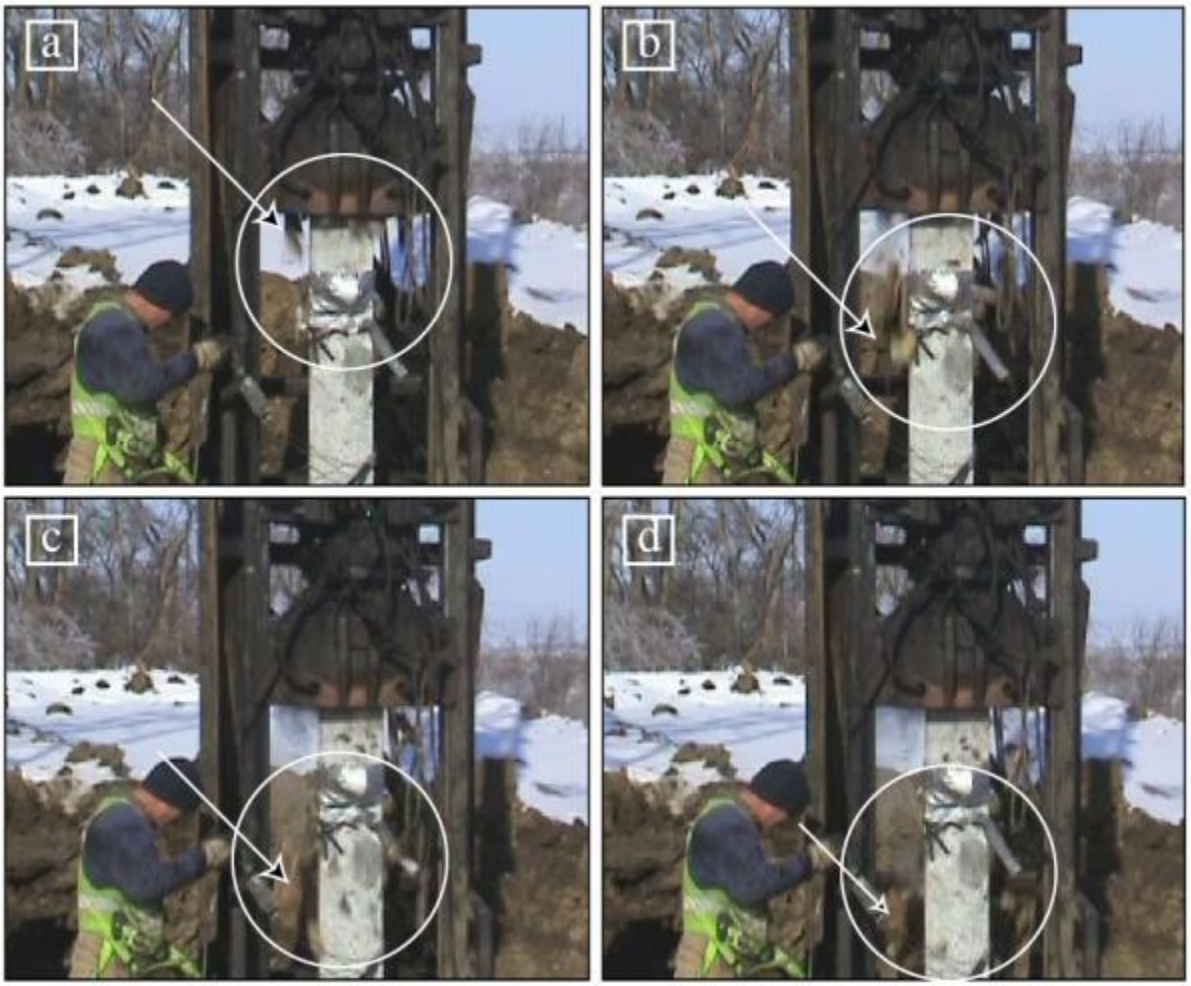

Figure 5.11. Rapid deterioration of UHPC pile cushion for first pile driven, Pile 2 (total elapsed time from frame a) to frame d) is 0.14 seconds)

Figure 5.12. Condition of pile head at the end of driving pile P2

Figure 5.13. Condition of pile head at the end of driving pile P1

Strain readings were taken for each pile after driving. Only two of the 21 remaining strain gauges had stopped working after driving, giving an overall instrumentation success rate of 83 percent. Strains remained virtually unchanged from measurements taken shortly before driving, indicating minimal residual stresses in the piles. Overall, the UHPC piles performed extremely well during driving and experienced no cracking or crushing.

5.2. PILE DRIVING ANALYZER (PDA) RESULTS

5.2.1.1 Steel Pile

The PDA recorded a total of 175 hammer blows during driving of the steel pile. The only soil variable required for the PDA analysis was the Case damping factor. The soil layer at the final tip elevation of the steel pile (approximately 32 ft (9.8 m) below the ground surface) was clayey silt, so damping factors ranging from 0.4 to 0.7 were examined for the steel pile, as recommended by Rausche et al. (1985) for clayey silt and silty clay soils. PDA results further confirm the location of a hard soil layer, probably sand, at a depth of approximately 25 to 26 ft (7.6 to 7.9 m) below the ground surface. The PDA also confirmed that the steel pile was not damaged during driving, based on the shape of the force and velocity waves recorded at the pile head.

The maximum compressive stress developed in the steel pile during driving was 26.6 ksi (183 MPa), and the maximum tensile stress was 4.9 ksi (34 MPa). Driveability analysis, reported in Section 5.1.4, calculated the compressive stress well within an error of less than 1 percent. The tension stress was underestimated by the driveability analysis but was still well below the allowable tensile stress of 45 ksi (310 MPa) for the steel pile. The PDA results gave a total capacity of the steel pile of 138 to 145 kips (614 to 645 kN) for the range of Case damping factors examined.

5.2.1.2 UHPC Piles

The PDA strain gauges rattled loose at the beginning of the driving pile P2 (the first UHPC pile driven). The nuts were further tightened when pile P1 was driven, and good data were obtained for most of the driving of that pile. One of the strain gauges did become loose at hammer blow number 244 out of a total of 275 blows recorded for the UHPC pile P1, but good results were still obtained from the remaining working gauge beyond that point. The PDA results confirm the integrity of UHPC pile P1 throughout driving. The loose PDA gauges from UHPC pile P2 provided no conclusive information on the integrity of that pile.

Since the final pile tip elevation was the same as that of the steel pile, the same range of Case damping factors (i.e., 0.4 to 0.7) was used in the PDA analysis. The maximum compressive stress in the UHPC pile during driving as measured by the PDA gauges was 8.2

ksi (57 MPa), and the maximum tension stress during driving was 0.4 ksi (2.8 MPa) according to the PDA. The driveability analysis with no pile cushion had an error of only 4 percent for the maximum compression stress and also predicted that maximum tension stress would be almost zero. The PDA results estimated a total axial capacity for the UHPC pile in the range of 208 to 222 kips (925 to 989 kN), approximately 50 percent greater than the capacity of the steel pile.

5.3. VERTICAL LOAD TESTS

5.3.1. Load Frame and Test Set-up

One UHPC pile and one steel pile were load tested vertically, and the same load test frame was used for both of the vertical load tests without moving the frame in between tests. The planned layout of the test piles and anchor piles is shown in Figure 5.14. The actual installed locations varied by up to 8 in. (20 cm) from those shown. A center-to-center spacing of 7·D, where D is the pile section depth, was maintained between the two vertically tested piles and between each test pile and the adjacent anchor piles. The two UHPC piles had a center-to-center spacing of slightly less than 6·D.

Top and profile views of the test frame are shown in Figure 5.15 and Figure 5.16, respectively. After the anchor piles had been driven, shorter pile segments, labeled as "side pile pieces" in Figure 5.15 and Figure 5.16, were welded onto the sides of the anchor piles, as shown in Figure 5.17. The side pile pieces were positioned so that the top of each piece was at the same elevation, providing level supports for the main reaction beam. The main reaction beam was lifted and placed on the protruding flanges of the side pile pieces, and the clamping beams and height adjusters were then placed on top of the main reaction beam. The 3-in. (7.6-cm) diameter rods were then lowered through the holes in the height adjusters and clamping beams and through the spaces between each side pile piece web and each corresponding anchor pile web. Finally, sleeved rod nuts were tightened against the bottom plate directly underneath each side pile piece. The completed load frame is shown in Figure 5.18.

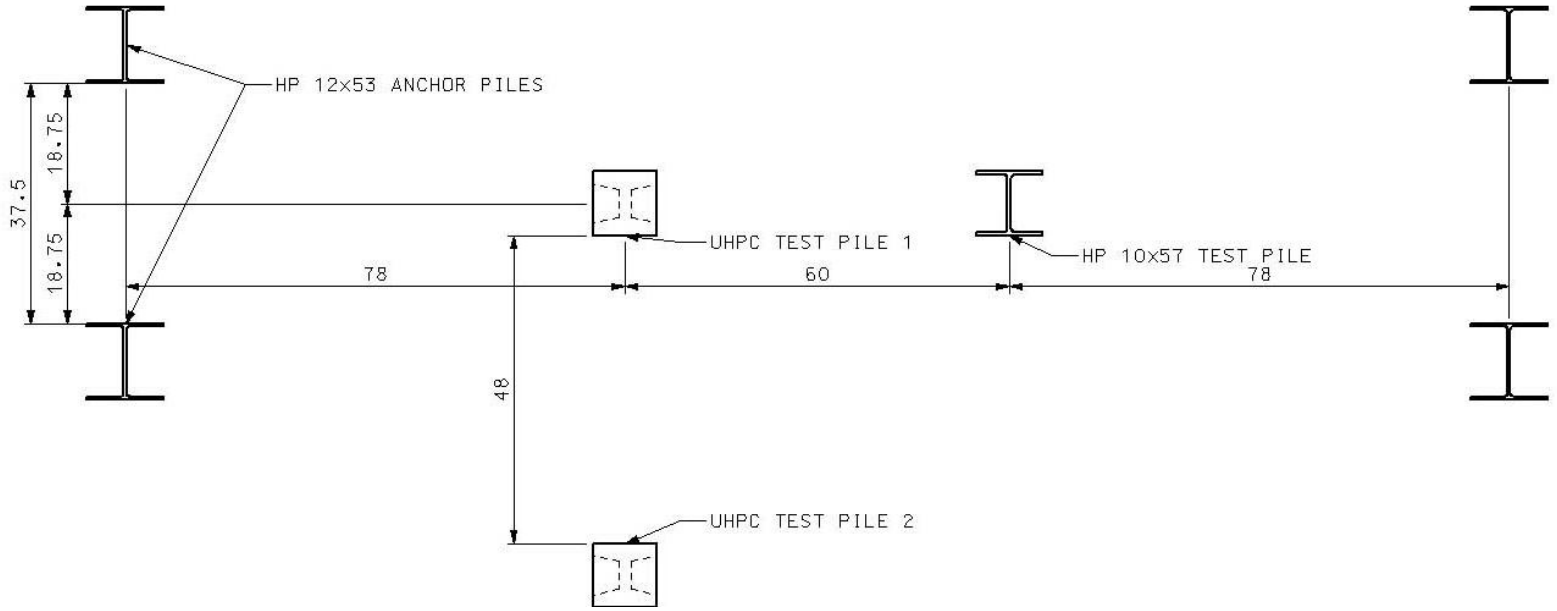

Figure 5.14. Configuration of the test and anchor piles

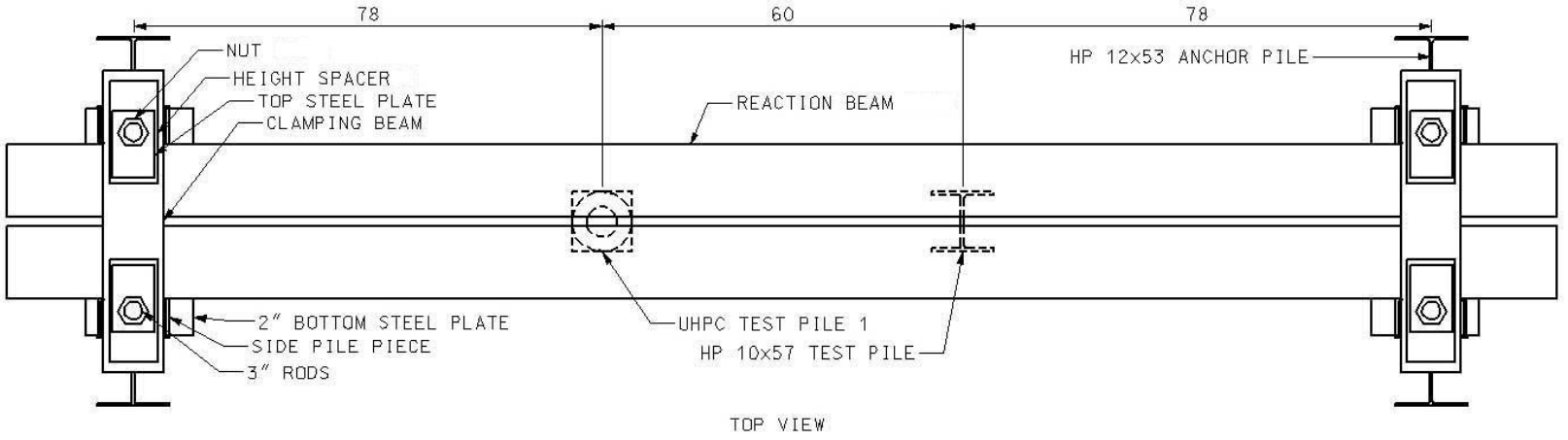

Figure 5.15. Top view of the pile test configuration for the vertical load test

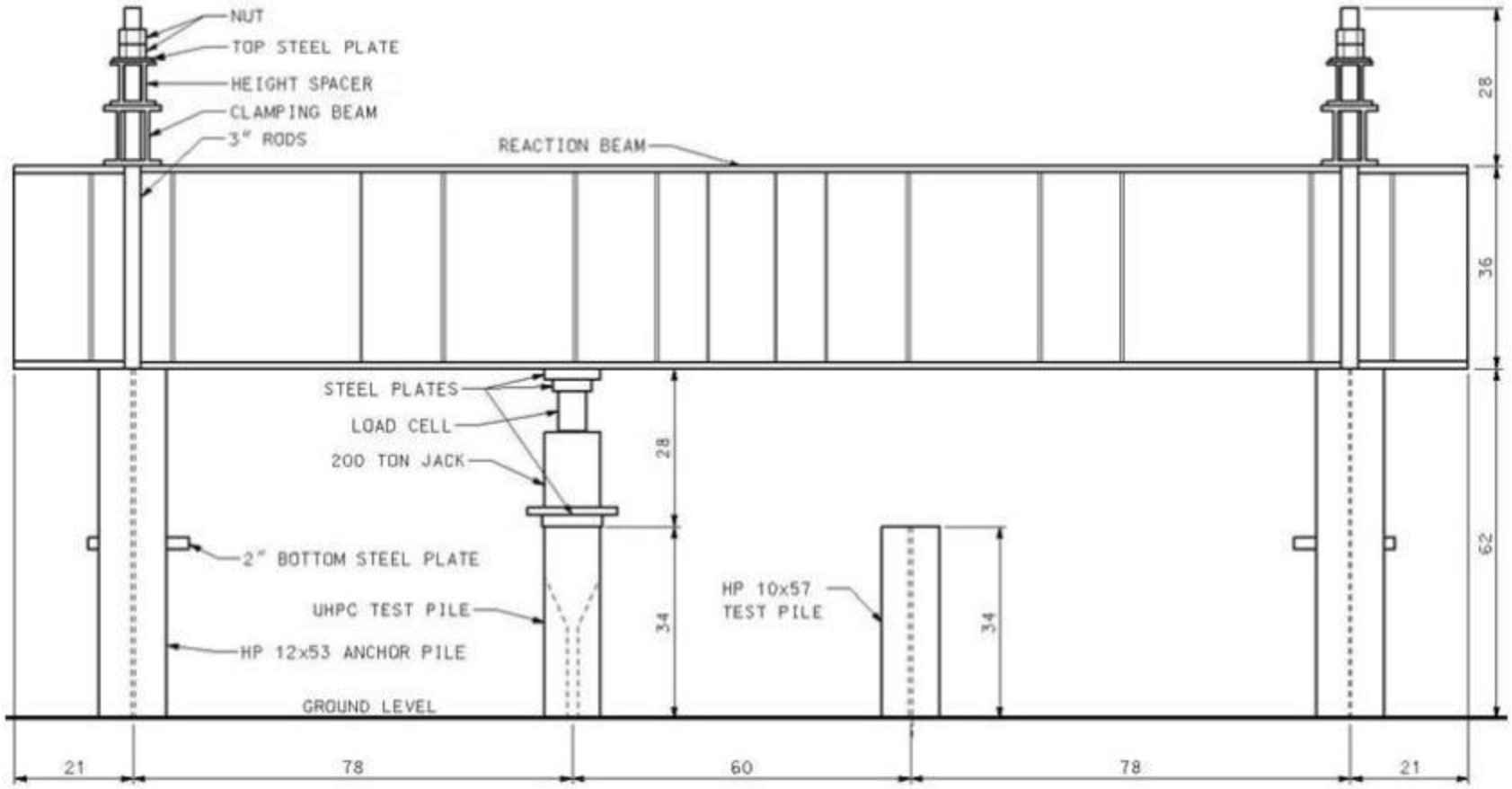

Figure 5.16. Elevation view of vertical load test frame and loading setup

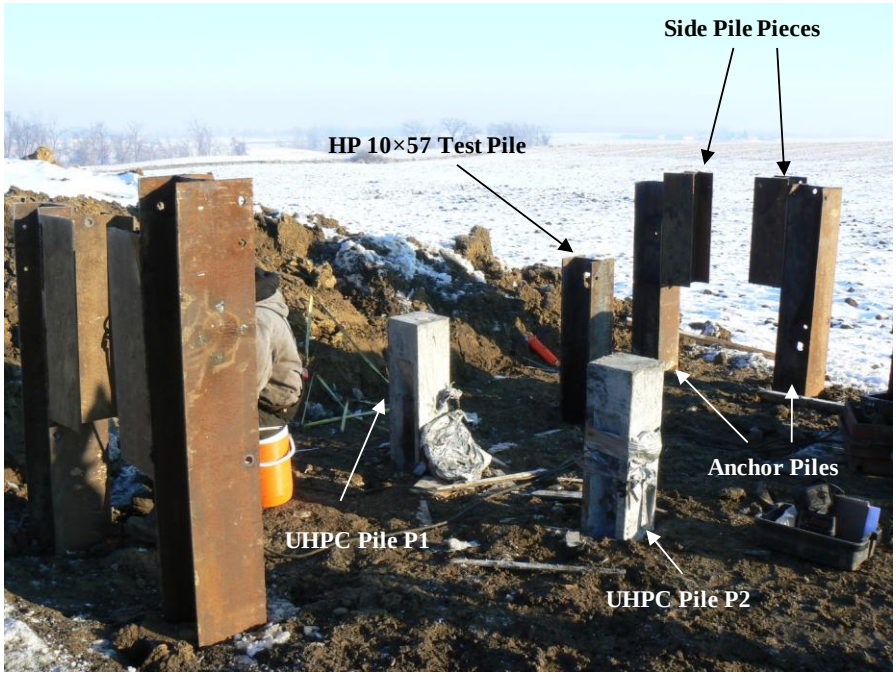

Figure 5.17. Piles at completion of driving, including side pile pieces welded onto facing flanges of anchor piles

Figure 5.18. Completed vertical load test frame at the Oskaloosa test site

The hydraulic jack was used to apply a vertical load on the test pile and imposed an equal load vertically upward on the main reaction beam. The main reaction beam reacted upward against the clamping beams extending across the top of each of its ends. The upward force on the clamping beams was transferred to the 3-in. (7.6-cm) diameter rods on either side of the main reaction beam. The rods reacted against the plates on the bottoms of each side pile piece, and the welds transferred the vertical load from the side pile pieces to the anchor piles, subjecting them to axial tension.

The load capacity of the test frame is controlled by the friction capacity of the anchor piles. Using a safety factor of 3.0 on the capacity of the anchor piles, the maximum load that could be applied to either test pile was 125 kips (556 kN). If the friction capacity of the anchor piles was not exceeded first, the load test frame could be used to apply a load of 680 kips (3000 kN) to either test pile. This maximum load was controlled by the tension capacity of the 3-in. (7.6-cm) diameter rods.

5.3.2. Testing Equipment

A 200 ton (203 tonne) hydraulic jack was used to apply the vertical load on the test piles, as noted previously, and a 300 kip (1330 kN) load cell was used to measure the applied load. Four 10-in. (250-mm) stroke displacement transducers were used to measure the vertical displacement of the top of each pile. These transducers were mounted on 2×4-in. (4×9 cm) wooden reference beams, which were supported approximately 4 ft. (1.2 m) away from the pile on either side by securing to short ladders as shown in Figure 5.19. The ladders were driven several inches into the soil to prevent any movement or instability. This allowed the researchers to measure the movement of the pile independent of the movement of the loading frame. The transducers were connected to the top of the pile using eye-hooks screwed into wooden blocks that were glued to the test piles in the field, as shown in Figure 5.20.

Figure 5.19. Wooden reference beams supported by ladders (steel pile)

Figure 5.20. Displacement transducers and eye-hooks mounted to a UHPC pile

The 11 functioning strain gauges in UHPC pile P1, which were zeroed before the load test began, were used to calculate strains at various depths near the top of the pile. Throughout the depth of the pile, the vibrating wire strain gauges of the sister bars provided strain measurements. Data from the load cell, deflection transducers, and strain gauges were collected using a Megadac data acquisition system, and the sister bar data were collected using a Campbell Scientific, Inc. datalogger.

5.3.3. Test Procedure

Vertical load testing followed the "Quick Test" procedure outlined in ASTM D 1143/D 1143 M – 07. Accordingly, the test pile was loaded in five percent increments up to the anticipated failure load. The load was kept relatively constant during each load step until deflection readings had stabilized, which was at least 4 minutes and at most 15 minutes for each step. Deflection, strain, and load measurements were recorded electronically and by hand at 1, 2, and 4 minutes after each loading increment and at two minute intervals thereafter for any remaining duration of each step. The piles were unloaded in five to eight equal steps (eight for the first test on the UHPC pile and five for the second test on the UHPC pile and the test on the steel pile), and the same measurement recording intervals that were used for loading the piles were used for the unloading steps. The load step durations were also increased for the failure load and the final zero load, as recommended by ASTM, to monitor creep and rebound behavior, respectively.

The load-displacement behavior of each pile was monitored throughout the vertical load test. The Davisson failure criterion was used to determine the ultimate capacity of the pile and terminate the load test, but the criterion was only reached for the vertical load test on the steel pile. The Davisson failure criterion states that the ultimate load of a pile subjected to a vertical load test is the load at which the displacement of the pile exceeds the elastic compression of the pile by 0.15+D/120 in. (3.8+D/120 mm), where D is the pile depth or diameter (Davisson 1972). The elastic compression is simply the length of the pile divided by its elastic modulus and cross-sectional area (i.e., the pile stiffness), then multiplied by the applied load.

5.3.3.1 UHPC pile P1 – Vertical Load Test 1

UHPC pile P1 was load-tested under vertical load on March 19, 2008 at the Oskaloosa site. A view of the UHPC during this test is shown in Figure 5.21. The calculated failure loads for the UHPC pile P1 were approximately 150 kips (670 kN) and 179 kips (800 kN), according to Dirks and Kam (2003) and the DRIVEN computer program (based on undrained shear strengths from averaged CPT results (see Section 5.1.2)), respectively. A maximum load of 125 kips (556 kN) was planned for the test, however, to maintain a factor of safety of three on the anchor piles. The actual loading sequence of the UHPC pile is shown in Table 5.2. The duration of each load step was increased from 4 minutes to 8 minutes starting at the 101 kip (449 kN) load step to allow deflection measurements to completely stabilize.

Figure 5.21. A view of the UHPC pile P1 during vertical load test 1

The actual loads applied to UHPC pile P1 varied slightly from those shown in Table 5.2. The electric pump used with the 200 ton (203 tonne) jack applied the load very quickly, and small load adjustments were not possible. Also, a combination of soil creep and a small amount of leakage in the hydraulic system caused the applied load at each load step to diminish slightly over the duration of the load step. The magnitude of the load change increased with increasing load step duration and applied load. This behavior, which normally occurs during load tests, can be seen in the step-like (or jagged regions) of the load-displacement results shown in Section 5.3.4.1.

The anchor piles did not show noticeable movement when the planned maximum load of 125 kips (556 kN) was reached, so the load on the UHPC pile was increased further in larger load increments of 15 kips (67 kN) each up to a final load of 200 kip (890 kN). Even at the load of 200 kip (890 kN), the Davisson criterion for pile failure was not reached for pile P1. The 200 kip (890 kN) load was maintained for over 50 minutes, and then the pile was unloaded in 25 kip (111 kN) increments. Since it was difficult to control the rate of unloading, the pile was unintentionally unloaded to 80 kips (356 kN) after the maximum load step and then reloaded to 175 kips (778 kN). The pile was unloaded completely during the next unloading step and was then reloaded slowly to 150 kips (667 kN). A valve on the electric pump was adjusted, and the rest of the unloading proceeded smoothly. Measurements were recorded for 20 minutes after the final load step that brought the load on the pile to 0 kips to observe the rebound behavior of the pile.

5.3.3.2 UHPC Pile – Vertical Load Test 2

UHPC pile P1 was vertically load tested again on March 28, 2008. The steel pile had been tested that morning and since the anchor piles had experienced no noticeable movement under the applied load of 215 kips (956 kN) on the steel pile, the maximum vertical load on the UHPC pile during this test was increased to 300 kips (1334 kN). The anchor piles did not show any indication of pulling out even at the 300 kip (1334 kN) load, but the capacity of the load cell prevented an increase above this load level.

Table 5.2. Load steps used for the first vertical load test of UHPC pile P1

Approximate % of Predicted Failure Load	Actual Load (kip)	Actual Load (kN)	Load Step Duration (min)
5	7	31	4
10	14	62	4
15	21	93	4
20	28	125	4
25	35	156	4
30	41	182	4
35	47	209	4
40	53	236	4
45	59	262	4
50	65	289	4
55	71	316	4
60	77	343	4
65	83	369	4
70	89	396	4
75	95	423	4
80	101	449	8
85	107	476	8
90	113	503	8
95	119	529	8
100	125	556	8
Overloading	140	623	8
Overloading	155	689	8
Overloading	170	756	8
Overloading	185	823	8
Overloading	200	890	52
Unloading	175	778	4
Unloading	150	667	4
Unloading	125	556	4
Unloading	100	445	4
Unloading	75	334	4
Unloading	50	222	4
Unloading	25	111	4
Unloading	0	0	20

The load sequence used for the second vertical load test of the UHPC pile is shown in Table 5.3. Larger load steps of 50 kips (222 kN) were used to load pile back up to its previous maximum load of 200 kips (890 kN). The load increment was then reduced to 15 to 25 kips (67 to 111 kN) as the pile was loaded to approximately 300 kips (1334 kN). Note that

the test procedure used larger load steps than those specified by ASTM due to time constraints on the day of testing and the fact that this pile had already been load tested per the ASTM standard. Deflection measurements stabilized within 4 minutes for every load step during this test. As in the other load tests, the actual applied loads varied from those shown in Table 5.3 due to the electric pump sensitivity and the small load changes over the duration of the load steps.

The first time the pile was loaded to 300 kips (1334 kN), the soil creep and hydraulic leakage caused the load to reduce to 282 kips (1255 kN) over the 4 minute duration. The load on the pile was increased to 300 kips (1334 kN), and the load this time dropped to 287 kips (1274 kN) in 4 minutes. When the load on the pile was adjusted one more time to 300 kips (1334 kN), the load decreased to about 288 kips (1281 kN) in 4 minutes. Displacement increased slightly for each of these load steps as reported in Section 5.3.4.2. The final 300 kip (1334 kN) load step was maintained for 15 minutes, and then the pile was unloaded in 60 kip (267 kN) increments. Measurements were recorded for 15 minutes after the final load step that brought the load on the pile to 0 kips to observe the rebound behavior of the pile.

Table 5.3. Load steps used for second vertical load test of UHPC pile P1

Approximate % of Total Load	Actual Load		Load Step Duration (min)
	(kip)	(kN)	
17	50	222	4
33	100	445	4
50	150	667	4
67	200	890	4
75	225	1001	4
83	250	1112	4
90	270	1201	4
95	285	1268	4
100	300	1334	4
100	300	1334	4
100	300	1334	15
80	240	1068	4
60	180	801	4
40	120	534	4
20	60	267	4
0	0	0	15

5.3.3.3 Steel Pile – Vertical Load Test

The HP 10×57 steel pile was also load tested vertically on March 28, 2008 at the Oskaloosa site. The predicted failure load for the steel pile was approximately 110 kips (489 kN) from both the "Foundation Soils Information Chart" (Dirks and Kam 2003) and Driven. The complete loading sequence of the steel pile is shown in

Table 5.4. Load step durations were increased from 4 minutes to 8 minutes from the 155 kip (689 kN) load step and then further increased to 15 minutes starting from the 185 kip (823 kN) load step to allow deflection measurements to stabilize. Again, the actual applied loads varied from those shown due to the electric pump sensitivity and the small load changes that occurred over the duration of the load step due to soil creep and hydraulic leakage.

After the predicted failure load of 110 kips (489 kN) was reached, the load on the steel pile was increased in larger load increments of 15 kips (67 kN) each up to a maximum load of 215 kips (956 kN). By the end of the 215 kip (956 kN) load step, the load had dropped to approximately 198 kips (881 kN) over the 15 minute duration due to soil creep and hydraulic leakage. The research team then attempted to apply a load of 230 kips (1023 kN) to the pile, but the pile moved downward rapidly, meeting the Davisson failure criterion at a load of approximately 198 kips (881 kN). The 198 kip (881 kN) load was maintained for 20 minutes, and then the pile was unloaded in 40 kip (178 kN) increments. Measurements were recorded for 20 minutes after the final load step that brought the load on the pile to 0 kips to observe the rebound behavior of the pile.

5.3.4. Test Results

5.3.4.1 UHPC Pile P1 – Vertical Load Test 1

The load-displacement behavior of UHPC pile P1 is shown in Figure 5.22. The figure shows the areas where the load decreased with little change in displacement, as described previously, as well as the unloading and reloading behavior of the load-displacement curve due to the problems encountered during initial unloading. The figure also shows that the pile was loaded to a maximum value of 199 kips (886 kN) and experienced a maximum

displacement of 0.21 in. (5.4 mm) during this load step. The exact load at the maximum displacement was 195 kips (867 kN).

Table 5.4. Load steps used for vertical load test of steel pile

Approximate % of Predicted Failure Load	Actual Load (kip)	Actual Load (kN)	Load Step Duration (min)
5	6	27	4
10	12	53	4
15	18	80	4
20	24	107	4
25	30	133	4
30	36	160	4
35	42	187	4
40	48	214	4
45	54	240	4
50	60	267	4
55	65	289	4
60	70	311	4
65	75	334	4
70	80	356	4
75	85	378	4
80	90	400	4
85	95	423	4
90	100	445	4
95	105	467	4
100	110	489	4
Overloading	125	556	4
Overloading	140	623	4
Overloading	155	689	8
Overloading	170	756	8
Overloading	185	823	15
Overloading	200	890	15
Overloading	215	956	15
Overloading	198	881	20
Unloading	160	712	4
Unloading	120	534	4
Unloading	80	356	4
Unloading	40	178	4
Unloading	0	0	20

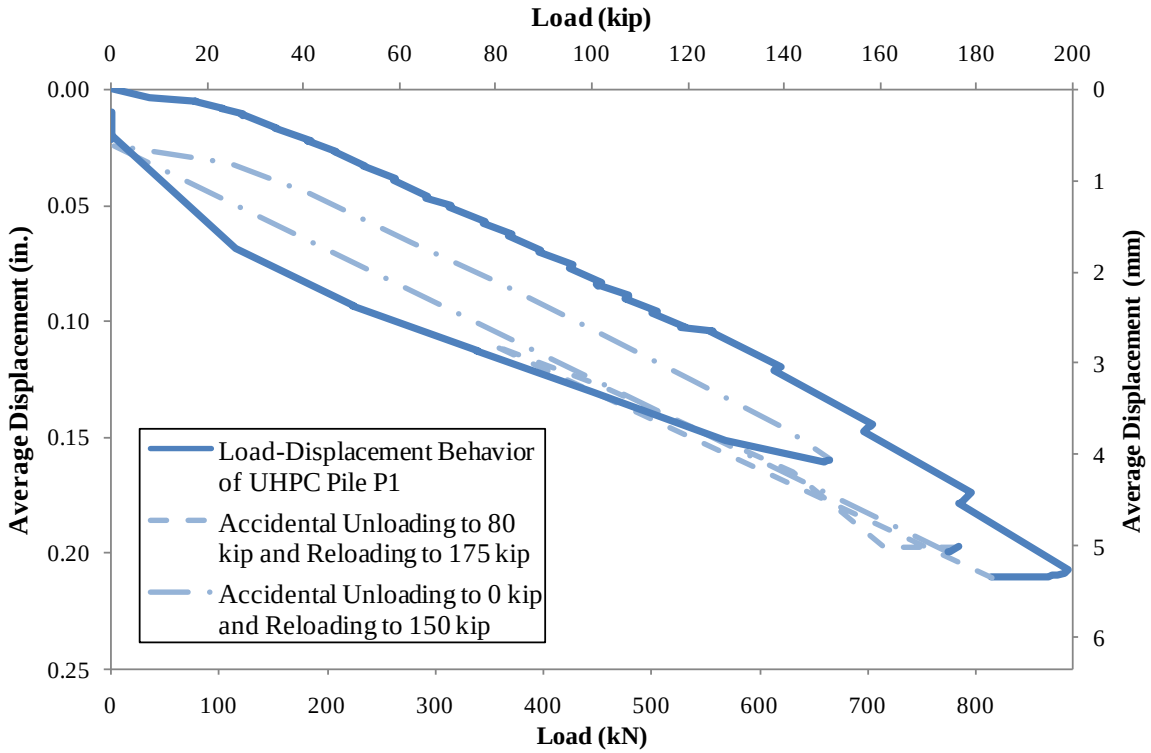

Figure 5.22. Observed load-displacement behavior for UHPC pile P1 during vertical load test 1

UHPC pile P1 experienced a permanent set of only 0.01 in (0.3 mm) at 20 minutes after the pile was completely unloaded. This low amount of set indicates that the soil had not experienced significant plastic deformation. The load-displacement relationship can also be shown in a simplified form by connecting the maximum load points from each load step of the pile load test. This load-displacement relationship is shown in Figure 5.23 along with the Davisson failure criterion for UHPC pile P1. Since the measured load-displacement of the pile does not cross the Davisson failure line, the ultimate load corresponding to the Davisson criterion was not determined from the recorded data.

The strain gauges and sister bars embedded in the UHPC pile provided information about the skin friction along the UHPC pile. The loads in the pile at the location of each set of strain gauges and sister bars were calculated by multiplying average strains from each set of gauges by the elastic modulus and cross-sectional area of the pile. The resulting loads are shown in Figure 5.24. The strain gauges located at 0.6 ft (20 cm) from the top of the pile were discarded due to erroneous measurement as were the sister bars located at 7.5 ft (230

cm) from the top of the pile. The figure shows that the strain gauges at 3.5 ft (110 cm) depth in the pile show lower strains and thus lower loads than those at 5.7 ft (170 cm) and 8.7 ft (260 cm), but the differences in strain between those gauges were less than 20×10^{-6} throughout the load test.

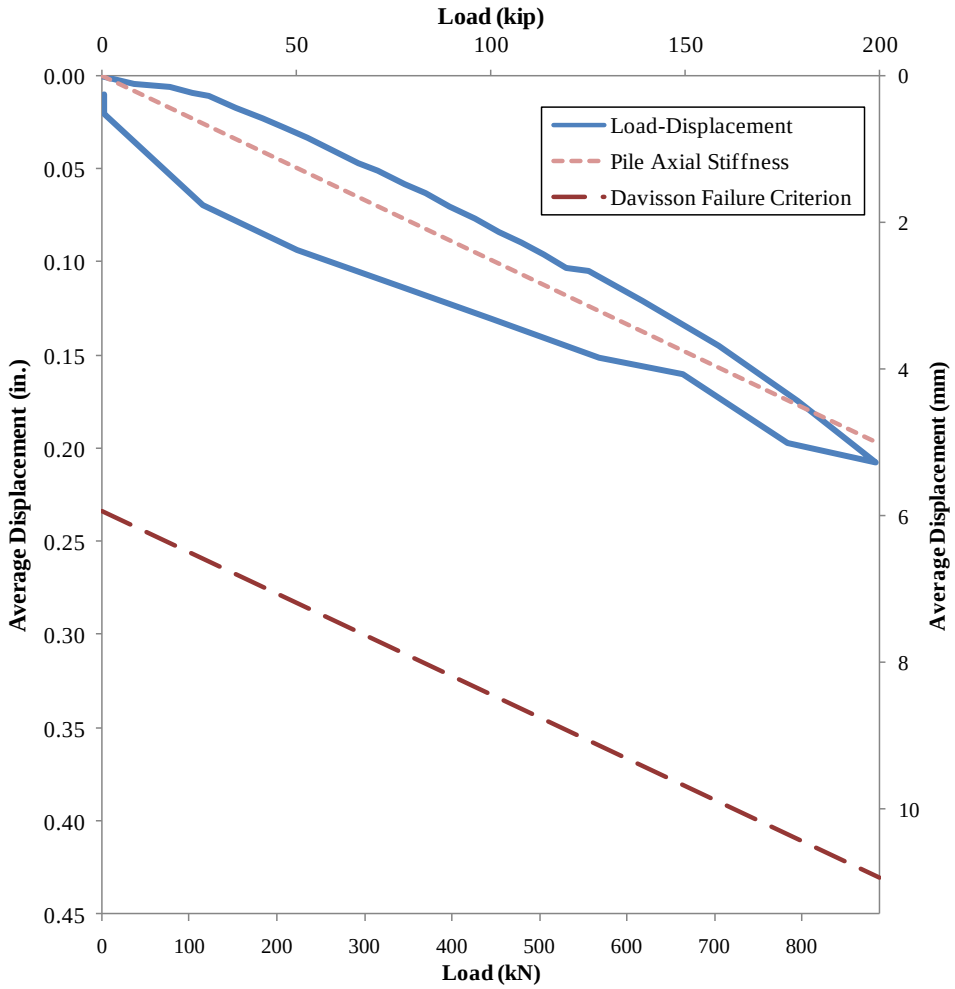

Figure 5.23. Load-displacement behavior established from the maximum load points and Davisson failure criterion for the first vertical load test of UHPC pile P1

The results from the sister bars located at 19.6 ft (6.0 m) and 31.3 ft (9.6 m) from the top of the pile (or 15.4 ft (4.7 m) and 3.7 ft (1.1 m) from the bottom of the pile, respectively) allow the total percent skin friction during the load test to be calculated as well as the distribution of that skin friction along the pile. The total percent skin friction and the skin friction for the top 19.6 ft (6.0 m) of the pile are shown in Figure 5.25. The strain gauges at

19.6 ft (6.0 m) from the pile top were located approximately 1.4 ft (0.4 m) below the location of the transition between the upper loess soil layers and the deeper glacial till layers. In other words, the skin friction percentage calculated from the strains at 15.4 ft (4.7 m) from the bottom of the pile (19.6 ft (6.0 m) from the top of the pile) is a good approximation of the portion of the total resistance provided by skin friction of the loess soil layers. Figure 5.25 also indicates that the skin friction percentage reaches its maximum at a very small displacement of 0.006 in. (0.15 mm).

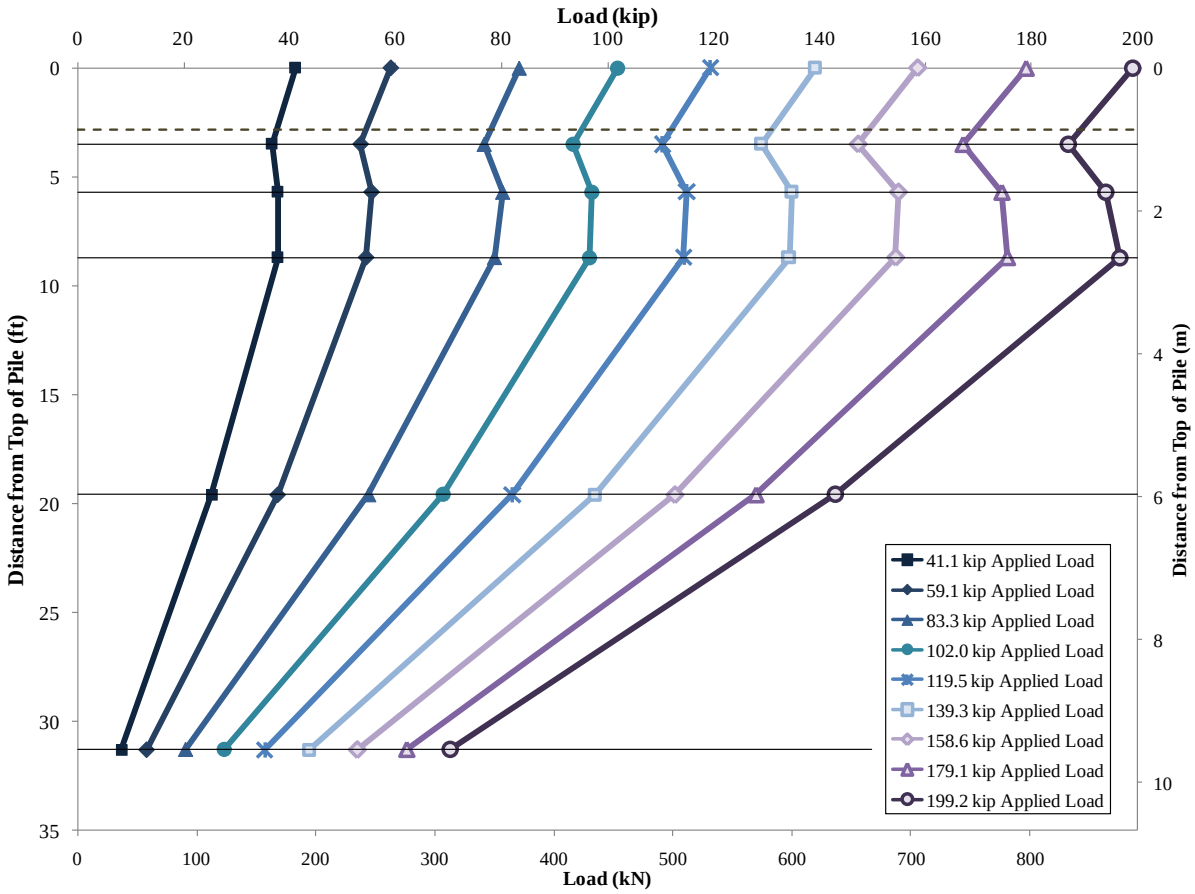

Figure 5.24. Loads throughout the depth of the UHPC pile, calculated from strain measurements

The total skin friction varies between 83 percent near the beginning of the test to 63 percent at the maximum load. The total percent skin friction calculated by the DRIVEN computer program from CPT data was 67 percent, which agrees well with experimental

results. The skin friction provided primarily by the loess soil layers to a depth of 16.8 ft (5.1 m), varies between 40 percent of the total resistance near the beginning of the test and 27 percent at the maximum load. From Driven results, the skin friction from the upper 16.8 ft (5.1 m) of soil was calculated to be 34 percent of the total resistance for the UHPC pile, again indicating good correlation with experimental results from the sister bar data. Finally, approximately 55 percent of the total skin friction occurs over the lower 15.4 ft (4.7 m) of the pile. From CPT results, Driven predicts that 49 percent of the total skin friction occurs over this region of the pile, again indicating a good agreement.

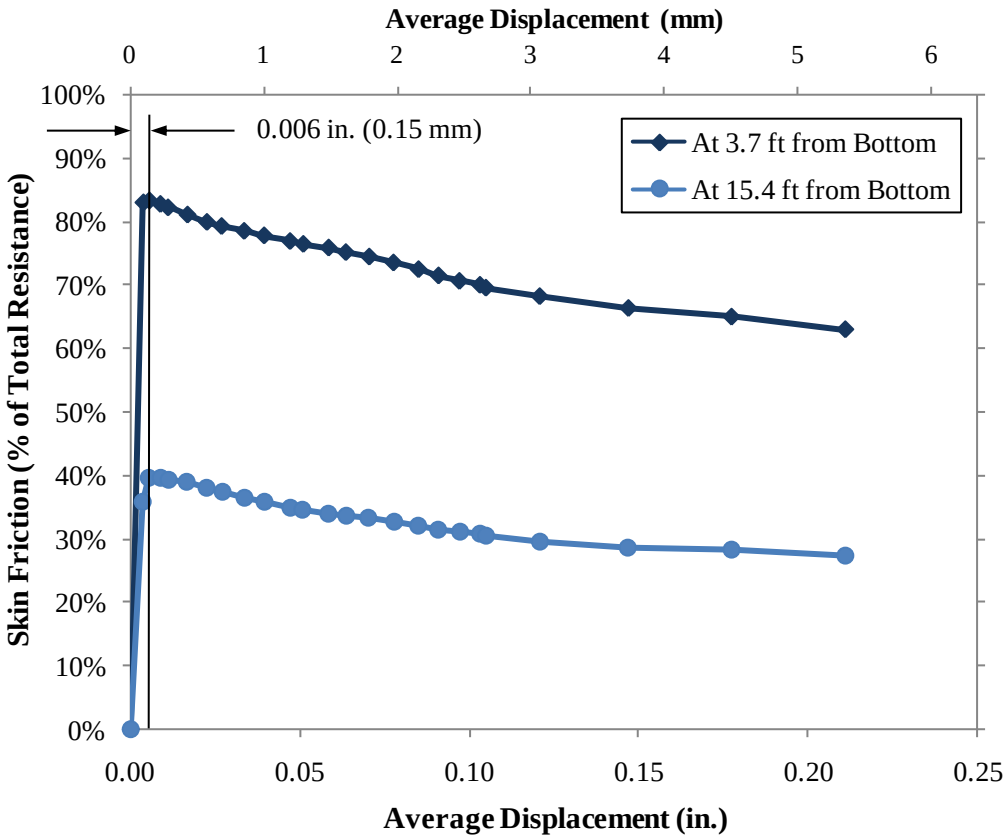

Figure 5.25. Total skin friction and skin friction for loess soil layers, both expressed as a percentage of the total load resisted by UHPC pile P1

5.3.4.2 UHPC Pile P1 – Vertical Load Test 2

The simplified load-displacement relationship of UHPC pile P1 from the second load test on the pile is shown in Figure 5.26. The figure shows the pile was loaded to a maximum

of 300 kips (1334 kN) and also shows that the Davisson failure criterion for the UHPC pile was again not reached for this load test. UHPC pile P1 had a greater permanent set at the end of the second load test than it did at the end of the first load test, remaining at 0.05 in. (1.3 mm) displacement 15 minutes after the pile was completely unloaded. The load-displacement results for vertical load test 2 were extrapolated to estimate the ultimate load of the UHPC pile according to the Davisson failure criterion, as shown in Figure 5.26. The extrapolation followed the procedure from the 1999 FHWA report by Paikowsky and Tolosko. This theoretical ultimate load was found to be 368 kips (1600 kN) for the UHPC pile.

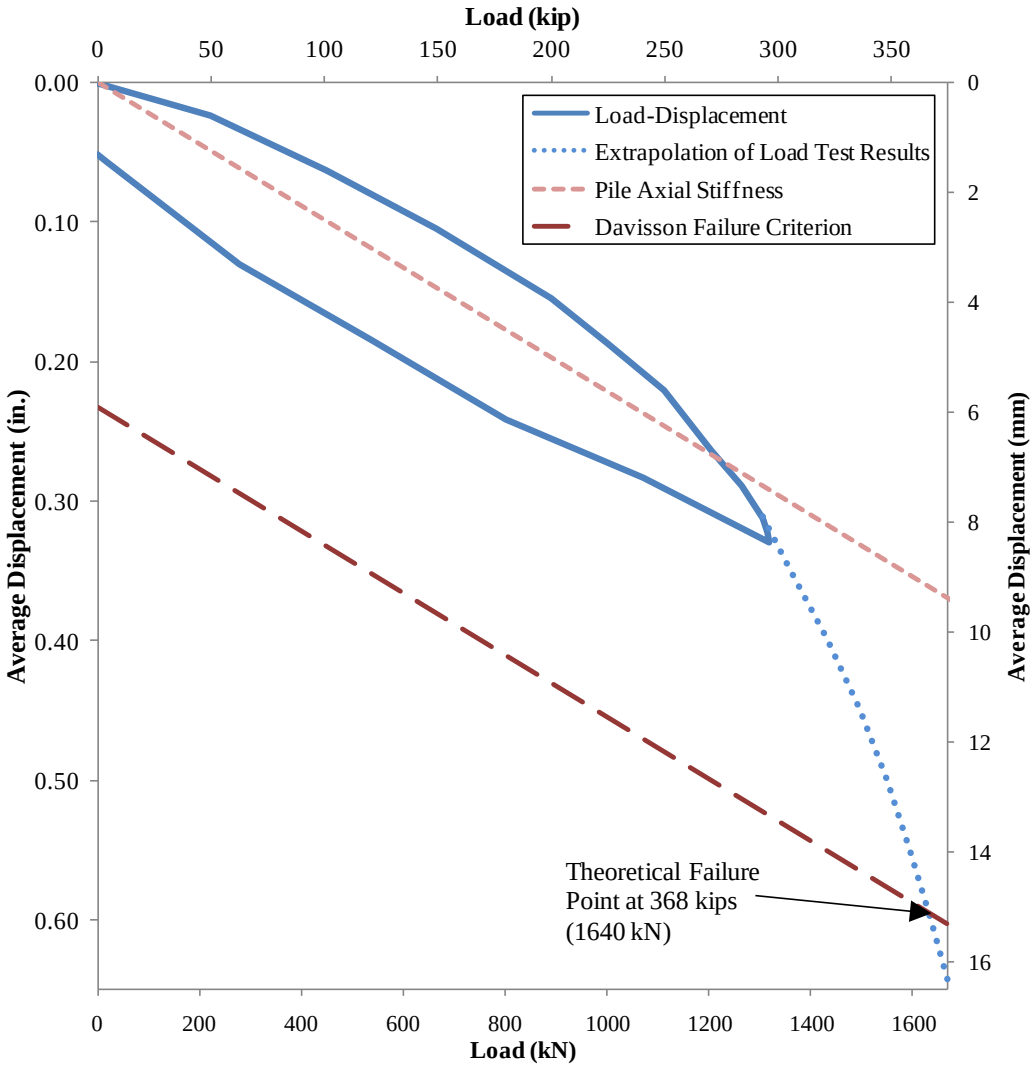

Figure 5.26. Load-displacement behavior and Davisson failure criterion for the second vertical load test of UHPC pile P1

5.3.4.3 Steel Pile – Vertical Load Test

The simplified load-displacement relationship of the HP 10×57 steel pile is shown in Figure 5.27. The original data from the beginning of the 215 kip (957 kN) load step to the beginning of the 198 kip (882 kN) load step is also shown to more accurately represent the ultimate load of the steel pile where it crosses the Davidson failure criterion. Figure 5.27 shows that the pile was loaded to a maximum of 215 kips (957 kN) and the Davisson failure criterion for the steel pile was reached at a load of 198 kips (882 kN). During this 198 kip (882 kN) load step, the pile experienced a maximum displacement of 0.70 in (17.9 mm). The steel pile experienced a permanent set of 0.55 in (14.0 mm) according to measurements taken 20 minutes after the pile was unloaded. This permanent soil deformation indicates that the soil supporting the UHPC pile experienced plastic behavior during the load test.

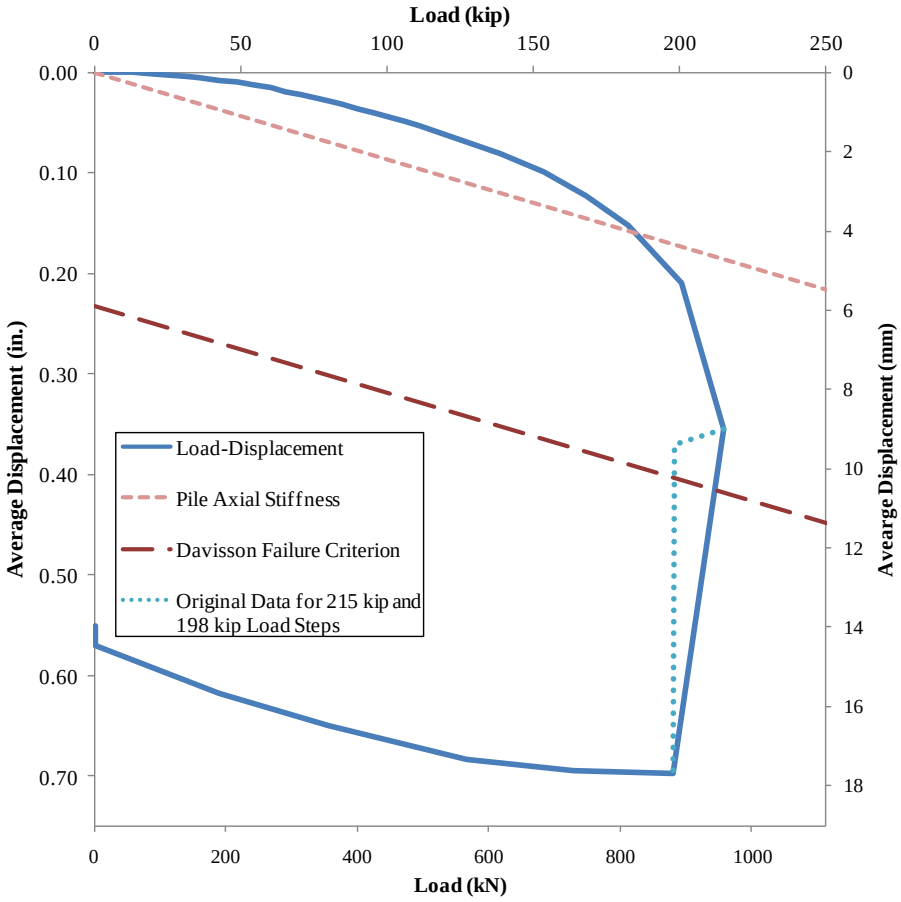

Figure 5.27. Load-displacement behavior and Davidson failure criterion for vertical load test of steel pile

5.3.4.4 Load-Displacement Comparison

The load-displacement relationships for each pile are plotted together in Figure 5.28. The second vertical test on the UHPC pile is shown as a second cycle of the first load test, so the figure shows the total displacement of the UHPC pile relative to the beginning of the first test.

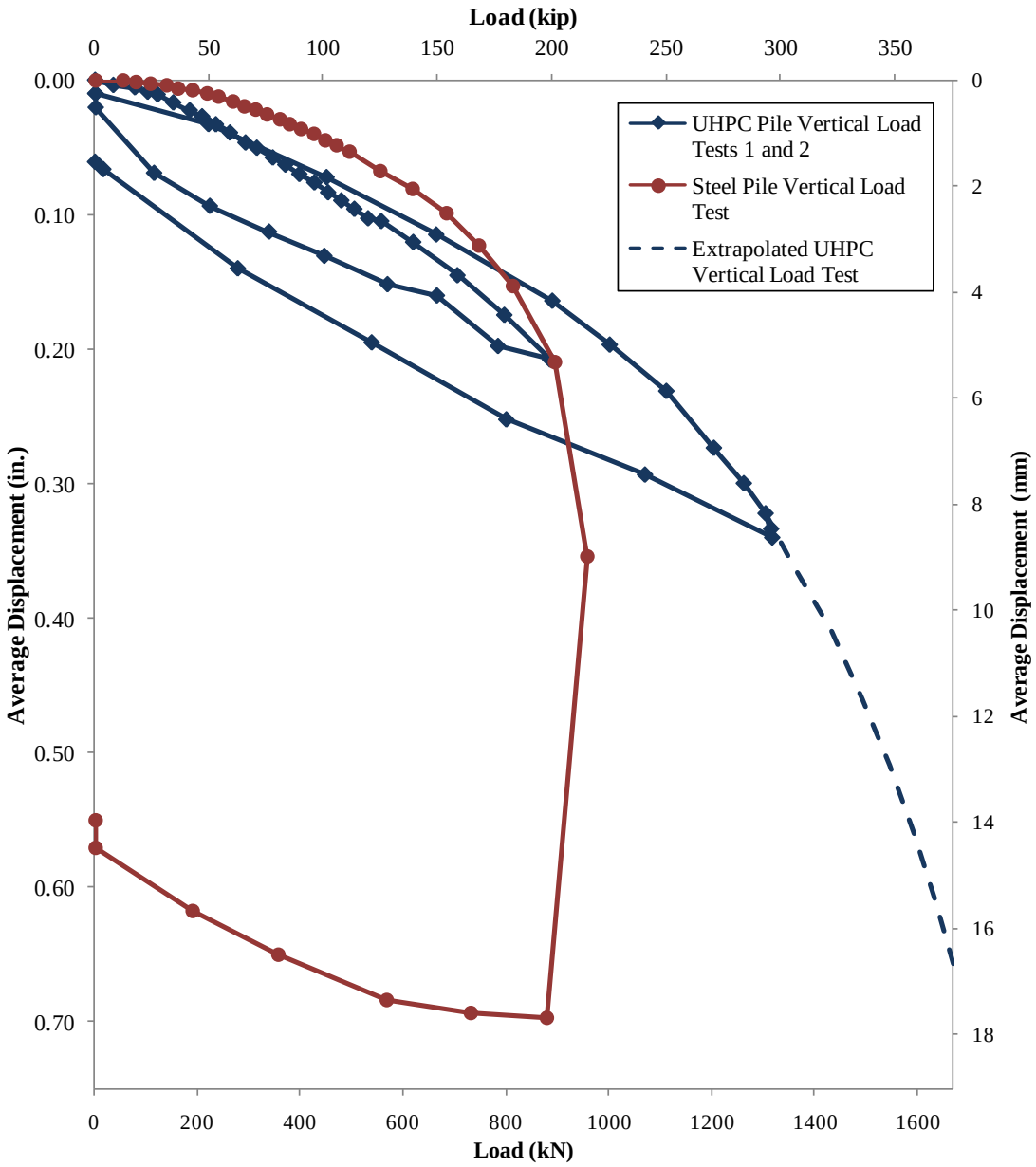

Figure 5.28. Comparison of load-displacement behaviors f vertical load test and UHPC pile P1 vertical load tests 1 and 2

Initially, the steel pile shows a stiffer load-displacement response than the load tests on the UHPC pile. A possible explanation for this is the 14 percent greater axial stiffness of the steel pile compared to the UHPC pile. The second vertical load test on the UHPC pile also shows a stiffer initial response than the first vertical load test. With an estimated ultimate load of 360 kips, the capacity of UHPC pile P1 is 80 percent higher than the capacity of the steel HP 10×57 pile. The increased capacity of the UHPC pile compared to the steel pile may be attributed to an increase in the total resistance at the pile tip of the UHPC pile, since the cross-sectional area of the UHPC pile is 3.4 times larger than that of the steel pile.

5.3.4.5 Cost Comparison

Interestingly, if the ultimate load of the UHPC pile is assumed to be 368 kips (1640 kN), a comparison on the basis of cost per unit load can be made between the UHPC and steel piles. The material costs for each pile are based on the costs reported in the literature review (see Section 2.5.5.2) of $810/ton ($800/tonne) for structural steel and $2000/yd^3 ($2600/m^3) for UHPC in North America. Table 5.5 shows the cost comparison, indicating that though the initial cost of the UHPC pile material is greater, the cost per unit load is reduced by 32 percent compared to the steel pile. Note that the table gives only material costs. UHPC will have a higher labor cost than steel since it must be produced in a precasting plant. The higher load capacity of the UHPC piles should lead to reductions in the number of piles required for a typical bridge foundation, which may provide an overall cost savings even in the initial cost of the structure. As noted previously, the extremely high durability of UHPC suggests the UHPC piles may enjoy greatly reduced maintenance costs as well.

Table 5.5. Cost per unit load comparison between UHPC and steel piles

Pile	Approx. Material Cost of Pile	Load Capacity (failure load from load test)	Cost per Unit Load
Steel HP 10×57	$810	198 kip (882 kN)	$4.09/kip ($0.92/kN)
UHPC Pile 1	$1020	368 kip (1640 kN)	$2.77/kip ($0.62/kN)

5.4. LATERAL LOAD TEST

5.4.1. Testing Setup

For the lateral load test on the UHPC piles, a 100 kip (445 kN) actuator was used to apply a lateral load to both UHPC piles simultaneously. A view of the lateral load test setup is shown in Figure 5.29. The actuator was placed on a stiffened wooden beam supported by two steel supports, and wooden wedges prevented the actuator from rotating and shifting off of the cross-beam during the test. The distance between the center of the actuator and the top of the piles was approximately 10 in. (25-cm). A 300 kip (1330 kN) load cell was used to measure the applied load, which was positioned on the cross-beam in line with the actuator, and steel plates were used to fill in the remaining space between the two UHPC piles.

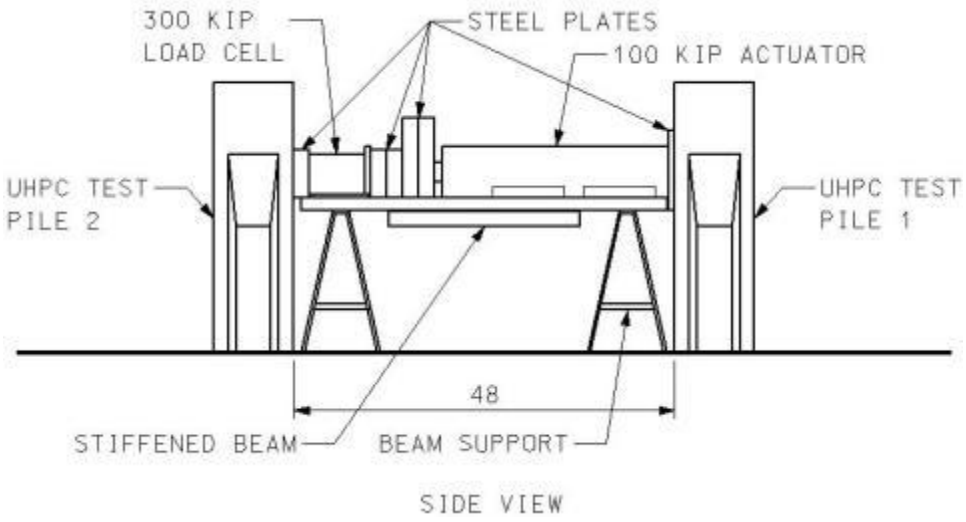

Figure 5.29. A view of lateral load test setup used for the UHPC piles

Two 10-in. (250-mm) displacement transducers were used to measure the lateral displacement at the top of each pile. The transducers were nearly fully extended at the beginning of the test, thereby allowing over 9 in. (23 cm) of displacement per pile. The displacement capacity of the lateral load test was also controlled by the actuator, which had an 18-in. (46-cm) stroke, allowing each pile to be displaced up to 9 in. (23 cm) simultaneously. The displacement transducers were mounted to 2×4-in. (4×9 cm) wooden reference beams, which were supported approximately 4 ft. (1.2 m) from the pile on either end on tripods as shown in Figure 5.30. The transducers were connected to the top of the pile using wooden blocks glued to the piles and eye-hooks, as shown in Figure 5.31, and the displacements of each pile could thus be measured independent of one other.

Figure 5.30. Displacement transducers attached to a wooden reference beam supported on tripods

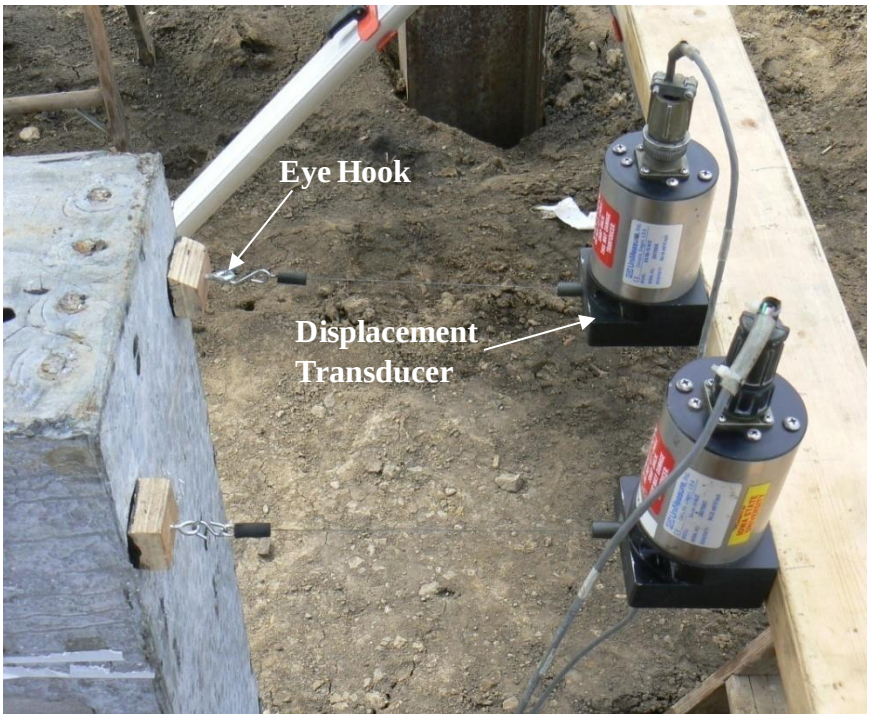

Figure 5.31. Displacement transducers and eye hooks used to measure displacement at the pile head.

A total of 23 strain gauges installed near the top of the UHPC piles were used to measure the strains at different depths. Throughout the length of UHPC Pile 1, the sister bar vibrating wire strain gauges also provided strain measurements. Data from the load cell, deflection transducers, and strain gauges were again collected using the Megadac data acquisition system, and the sister bar data was collected using the Campbell Scientific, Inc. datalogger. Figure 5.32 shows the setup used for collecting data during the lateral load test.

Figure 5.32. Data collection system used during the lateral load test

5.4.2. Test Procedure

The lateral load test followed the "Standard Loading" procedure outlined in ASTM D 3966 – 07 as detailed in Table 5.6. The ASTM procedure recommends loading to 200 percent

of the design lateral load, but no specific design lateral load had been established for the UHPC pile as the design focused only on the vertical load. LPILE software was therefore used to predict the maximum lateral load that the UHPC piles would develop in the soil before either experiencing flexural failure or exceeding the 9-in. (23-cm) lateral displacement capacity of the testing equipment. The LPILE analysis used the moment-curvature relationship of the pile section, which was calculated following the procedure presented in Section 3.7 and was based on measured material properties of each UHPC pile. The undrained shear strengths calculated from CPT results were also used in the LPILE analysis to model the soil surrounding the pile. The maximum lateral load calculated for each UHPC pile was approximately 30 kips (133 kN) and was controlled by the 9-in. (23-cm) lateral displacement capacity of the testing equipment. A design load of less than half of this maximum load, or 12 kips (53 kN), was chosen so that 200 percent of the design lateral load could safely be applied without exceeding the capacity of the testing equipment. The researchers modified the ASTM procedure slightly by increasing displacements in 1.0-in. (2.5-cm) intervals after the 24 kip (107 kN) (200 percent of design load) load step until the maximum displacement capacity of the testing equipment was reached.

Table 5.6. Lateral load sequence established as per for testing the UHPC piles

% of Design Load	Load Step Duration (min)
25	10
50	10
75	15
100	20
125	20
150	20
170	20
180	20
190	20
200	60
150	10
100	10
50	10
0	—

During each loading step, the load was kept relatively constant until deflection measurements had stabilized for a duration of at least 10 minutes and at most 20 minutes. Deflection, strain, and load readings were recorded at 1, 5, and 10 minutes after the load for each load step was applied and at five minute intervals for any remaining duration. The piles were unloaded in four equal load steps, with measurements recorded at the same intervals for the unloading steps as for the loading steps. The load step durations were increased for the failure load and the final zero load to monitor the creep and rebound behavior, respectively.

5.4.2.1 UHPC Piles – Lateral Load Test

The UHPC piles were load-tested laterally on March 29, 2008. The layout of the lateral load test set-up is shown in Figure 5.33, and a view of the piles at the beginning of the lateral test is shown in Figure 5.34.

Figure 5.33. Overall layout at beginning of lateral load test on UHPC piles

Figure 5.34. View showing the lateral load test set-up at the beginning of the load test

The complete loading sequence of the UHPC pile is shown in Table 5.7. Due to time constraints on the day of testing, load step durations were decreased from the recommended 20 minutes to 15 minutes beginning at a load of 18 kips (80 kN). The actual applied loads varied slightly from those shown in Table 5.7 since the electric hydraulic pump was used, and, as noted for the vertical tests in Section 5.3.3, the electric pump loaded too quickly to allow for small load adjustments. Again, a combination of minor leakage in the hydraulic system and soil creep caused the applied load at each load step to drop slightly over the duration of each load step. The magnitude of the load reduction increased with increasing load step duration and applied load.

By the end of the 22 kip (98 kN) load step, the load had decreased to approximately 20.6 kips (91.6 kN) over 15 minutes. The research team then attempted to apply a load of 23 kips (102 kN) to the piles, but a shear crack developed in the web of UHPC pile P1 approximately 19 in. (48 cm) below the top of the pile. More information on the development of this shear failure is presented in Section 5.4.3.3. The displacement of pile P2, which did not experience a similar shear failure, could no longer be increased at this point due to the failure of pile P1. Because the shear cracks in pile P1 were opening widely as the pile was displaced, the test was paused at a lateral load of 23 kips (102 KN) without unloading the piles. The displacement of pile P1 had increased by almost 1.9 in. (4.8 cm) since the end of

the previous load step, yet the lateral load that the cracked pile was able to sustain was virtually unchanged at approximately 20.4 kips (90.7 kN). After a 10 minute pause, the actuator was extended further to increase the displacement of the shearing pile. UHPC pile P1 reached a maximum displacement of almost 8 in. (20 cm) before the loading was stopped. Pile P1 could still sustain a lateral load of over 18 kips (80 kN) at this point. The duration of this load step was extended to 20 minutes to allow the deflection measurements to stabilize. The pile was then unloaded in four approximately equal increments. Measurements were recorded for 25 minutes after piles had been completely unloaded to assess their rebound behavior.

Table 5.7. Actual loading procedure of UHPC piles for lateral load test

Approximate % of "Design Load"	Actual Load		Load Step Duration
	(kip)	(kN)	(min)
25	3	13	10
50	6	27	10
75	9	40	15
100	12	53	20
125	15	67	20
150	18	80	15
170	20	89	15
180	22	98	15
170 (shear failure)	20	89	10
160	18	80	20
125	15	67	10
80	10	44	10
40	5	22	10
0	0	0	25

Figure 5.35 shows the gap between each pile and the adjacent soil early in the test, midway through the test, and after the shear failure occurred to pile P1. Note that the magnitudes of the lateral displacements were similar for the two piles until the shear failure of pile P1. Even after the shear failure of pile P1, UHPC pile P2 remained did not experience any visible signs of distress at the end of the lateral load test, as shown in Figure 5.36.

Figure 5.35. Soil gaps due to lateral pile movement next to a) P1 and b) P2 early in the test, c) P1 and d) P2 midway through the test, and e) P1 and f) P2 after the shear failure of pile P1

Figure 5.36. Condition of pile P2 at the end of the lateral load test

5.4.3. Test Results

5.4.3.1 Load-Displacement

The load-displacement envelopes from the lateral load test for each UHPC are shown in Figure 5.37. The figure shows that a maximum load of 22.8 kips (101.3 kN) was applied to each pile. UHPC pile P1 showed a much greater maximum deflection than pile P2 due to experiencing shear failure at a lateral load of 20.5 kips (91.2 kN). After the shear failure began to occur, pile P1 was able to undergo a total displacement of 7.92 in. (20.1 cm) while sustaining a lateral load of approximately 18 kips (80 kN). Pile P2 reached a maximum displacement of 2.54 in. (6.45 cm) at a lateral load of 20 kips (89 kN). Pile P2 was expected to sustain larger lateral loads and displacements but could not be loaded further after the shear failure of pile P1.

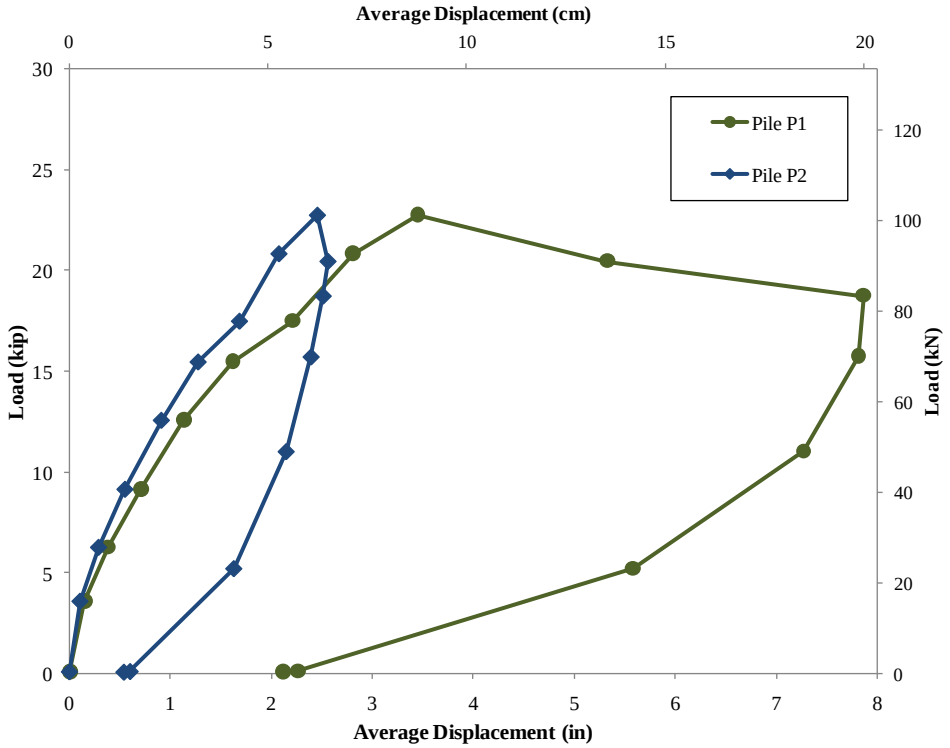

Figure 5.37. Load displacement behavior for lateral load test of UHPC piles

5.4.3.2 Moment Profile

The flexural tensile strain measurements along the depth of the pile were obtained from the strain gauges in each pile and the sister bars in pile P1. These measurements may be used to illustrate the bending moment profile along the pile length under the lateral loading. Figure 5.38 shows the tensile strain at various lateral loads measured from the strain gauges on Strand #3 in pile P1. Figure 5.39 shows the tensile strain under different lateral loads measured from the sister bars next to Strand #2 in the same pile. Figure 5.40 shows the tensile strain at various lateral loads measured from the strain gauges on strand #8 in pile P2. The strain gauges for which results are shown in Figure 5.38 and Figure 5.40 were located approximately 4 in. (100 mm) from the horizontal centroidal axis of the pile cross-section, while the sister bars used for Figure 5.39 were approximately 3.5 in. (90 mm) from the centroidal axis. Therefore the strains measured by the strain gauges were expected to be higher than the strains measured by the sister bars for a section with each type of instrumentation subjected to the same bending moment. Also note that sister bars measure an

average strain over a 6-in. (15-cm) length, but the gauge length for strain gauges is much shorter, at 0.04 in. (1 mm). See Figure 5.41 for cross-sections showing the locations of the numbered instrumented strands.

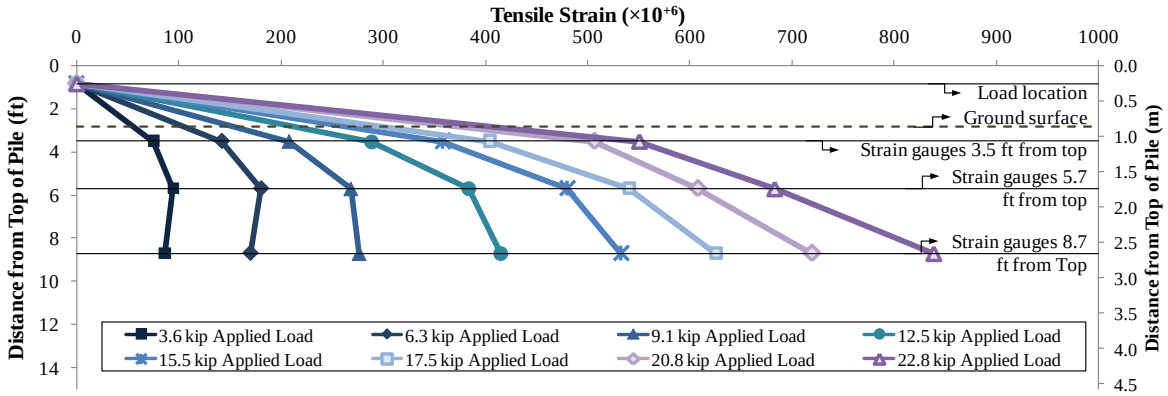

Figure 5.38. Tensile strain along the length of strand #3 in UHPC pile P1 during lateral load test

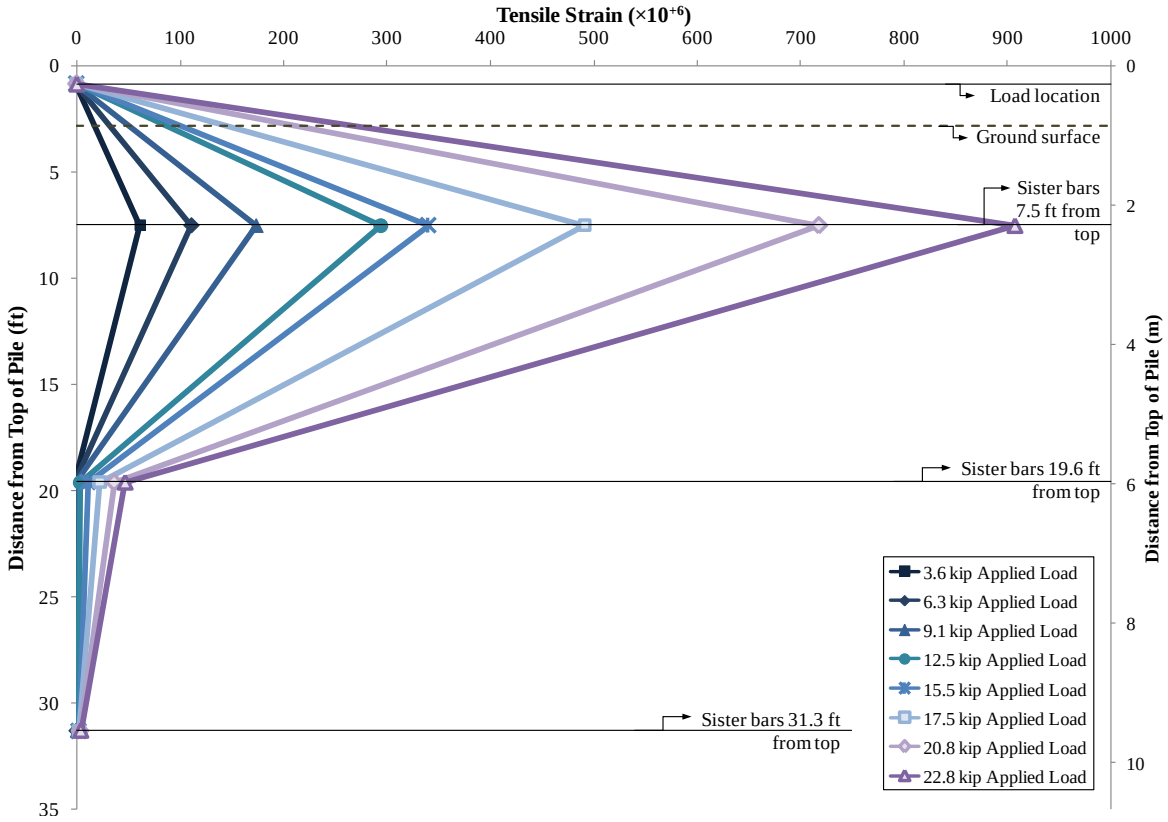

Figure 5.39. Tensile strain along the length strand #2 in UHPC pile P1 during lateral load test

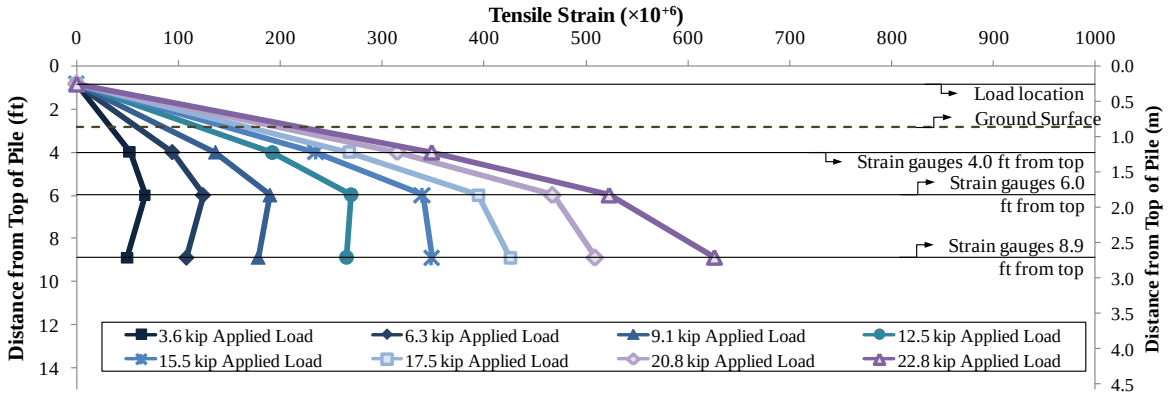

Figure 5.40. Tensile strain along the length of strand #8 in UHPC pile P2 during lateral load tests

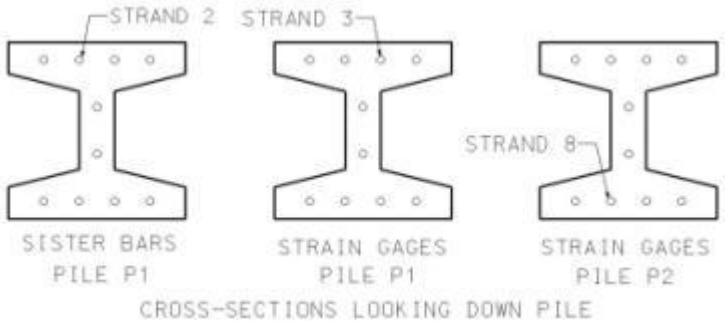

Figure 5.41. Cross-sections of pile P1 and P2 showing instrumented strand locations for tensile strain results

The tensile and compressive strains measured from the strain gauges in both UHPC piles and the sister bars in pile P1 were used to calculate the curvature along the depth of each pile. The theoretical moment corresponding to each measured curvature was calculated using moment-curvature analysis, as described in Section 3.7. Figure 5.42 shows the moment along the depth of each UHPC pile at the maximum lateral load of 22.8 kips (101.3 kN). The maximum moments corresponding to the curvatures calculated from the measured strains were 1120 kip·in. (127 kN·m) in pile P1 at a depth of 7.5 ft (2.3 m) from the top of the pile and 960 kip·in. (108 kN·m) in pile P2 at a depth of 8.9 ft (2.7 m).

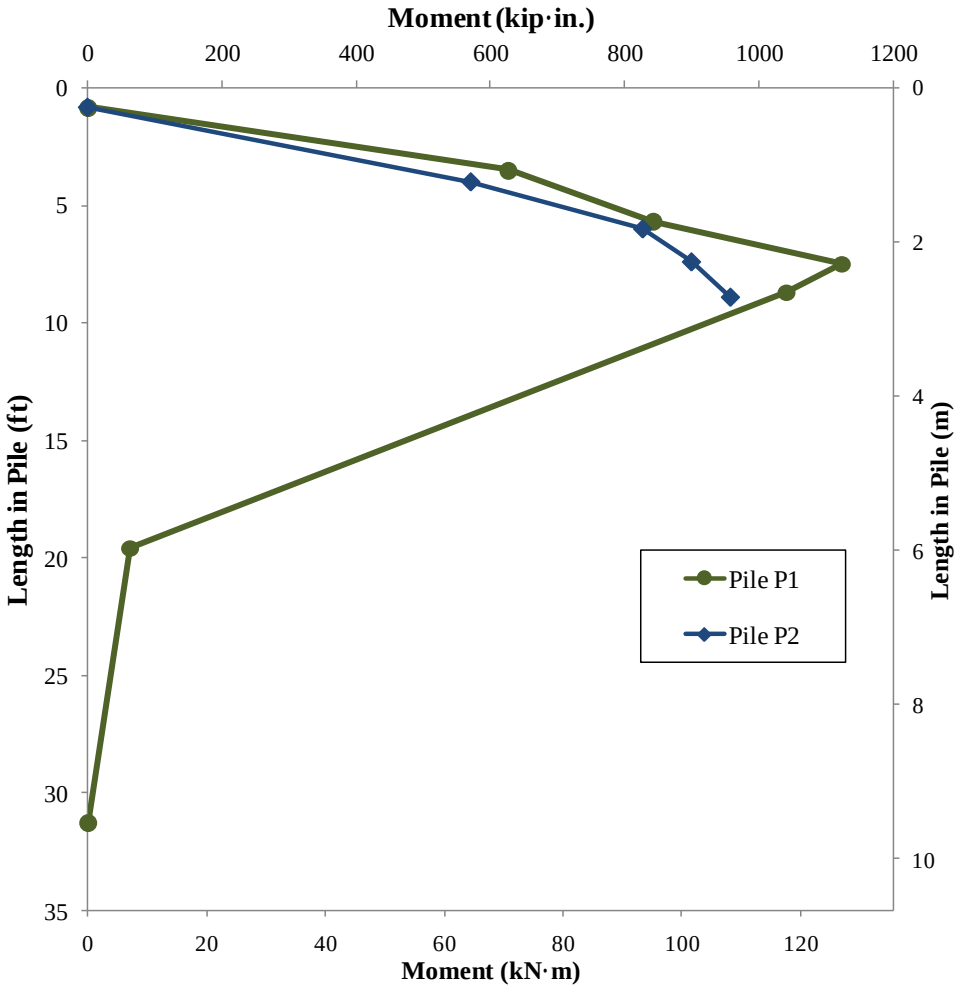

Figure 5.42. Moment along the length of UHPC piles P1 and P2 from measured curvature during lateral load test

5.4.3.3 Shear Failure of UHPC Pile P1

The initial shear cracks that developed on the west side of the web of UHPC pile P1 are shown in Figure 5.43. The location of the initial shear cracking was just below the center of the actuator and approximately 1.0 in. (2.5 cm) below the transition region between the tapered H-shaped section and the solid square section at the top of the pile. From Figure 5.44, which shows the shear cracking on the opposite side of the web, it can be observed that the shear cracks penetrated completely through the web as the lateral displacement of pile P1 was increased from 3.45 in. (87.6 mm) to 7.87 in. (200.0 mm). A crack also developed on the back flange of the UHPC pile as displacements increased, as shown in Figure 5.45. The

bending of UHPC pile P1 due to the shear failure can be clearly seen in Figure 5.46. The extent of the web shear cracking of pile P1 at the end of the lateral load test is shown in Figure 5.47.

Figure 5.43. Initial shear cracking in web of UHPC pile P1 at a lateral load of 22.8 kip (101.3 kN)

Figure 5.44. Views of the shear cracking on the east side of the web of UHPC pile P1

Figure 5.45. Cracking of back flange of UHPC pile P1

Figure 5.46. Bending of UHPC pile P1 under a lateral displacement of 7.87 in. (200.0 mm) after the shear failure began to occur

Figure 5.47. Damaged region of UHPC Pile 1 at the end of the lateral load test

The shear failure in UHPC pile P1 was not expected at magnitude of the lateral loads applied in the load test. In fact, principle stress analysis indicated that the UHPC piles should each be able to sustain a lateral load of 43 kips (191 kN) before experiencing shear cracking. As noted in Section 2.4.2, because UHPC is fiber-reinforced, it also possesses some post-cracking tensile strength.

Though analysis showed the UHPC pile section could withstand a lateral load of 43 kips (191 kN) without experiencing shear cracking, UHPC pile P1 cracked after sustaining a lateral load of 22.8 kips (101.3 kN). It is believed that UHPC pile P1 was weakened at the critical section for shear. A significant amount of the area of the pile section, especially the web area, was ineffective due to the presence of six sister bar wires and 11 strain gauge wires bundled through the web, as shown in Figure 5.48. Figure 5.49 shows that the thick bundle passed directly through the region of the web where the shear failure initiated.

The initial shear crack in pile P1 occurred at an angle of approximately 30 degrees. Principle stress analysis shows that at a lateral load of 22.8 kips (101.3 kN), a loss of a 0.8-in. (20-mm) thick strip of the web could result in a principle tensile stress that exceeds the 1.3

ksi (12 MPa) tensile cracking strength of UHPC. The bundle of wires was of sufficient thickness to cause this magnitude of section loss in UHPC pile P1.

Figure 5.48. Bundle of instrumentation wires passing through the web and out of the flange of UHPC pile P1

Contrary to typical shear failures in normal concrete, the shear failure in UHPC pile P1 was not a brittle failure mechanism. After the shear cracking initiated at a displacement of 3.45 in. (87.6 mm), the pile was displaced laterally a further 4.42 in. (11.2 cm) and could sustain a load of 18.8 kips (83.6 kN))(or 82 percent of the maximum lateral load) at that displacement.

Figure 5.49. Shear failure region of UHPC pile P1 after the lateral load test with some cracked UHPC pieces removed

5.4.4. LPILE Analysis

5.4.4.1 Load-Displacement Response

The LPILE computer program was used to establish the load-displacement behavior of the UHPC piles at the test site. The average undrained shear strengths calculated from CPT1 and CPT2 were used for in analyses as well as the moment-curvature analysis calculated for each UHPC pile based on the measured material properties.

Figure 5.50 shows the measured load-displacement response of UHPC pile P2 and the load-displacement obtained from LPILE. (Pile P1 is not compared to the theoretical LPILE analysis because the loss of stiffness due to the wire bundle in that pile made the moment-curvature analysis of the pile P1 section inaccurate.) The LPILE computed response corresponds extremely well with the measured results. Note again that UHPC pile P2 could

not be pushed to higher loads or displacements because of the premature shear failure in pile P1. Also, note that the pile would experience a maximum lateral load of only 30 kips (133 kN) in this soil, and thus the theoretical lateral load capacity of 43 kips (191 kN) would be adequate.

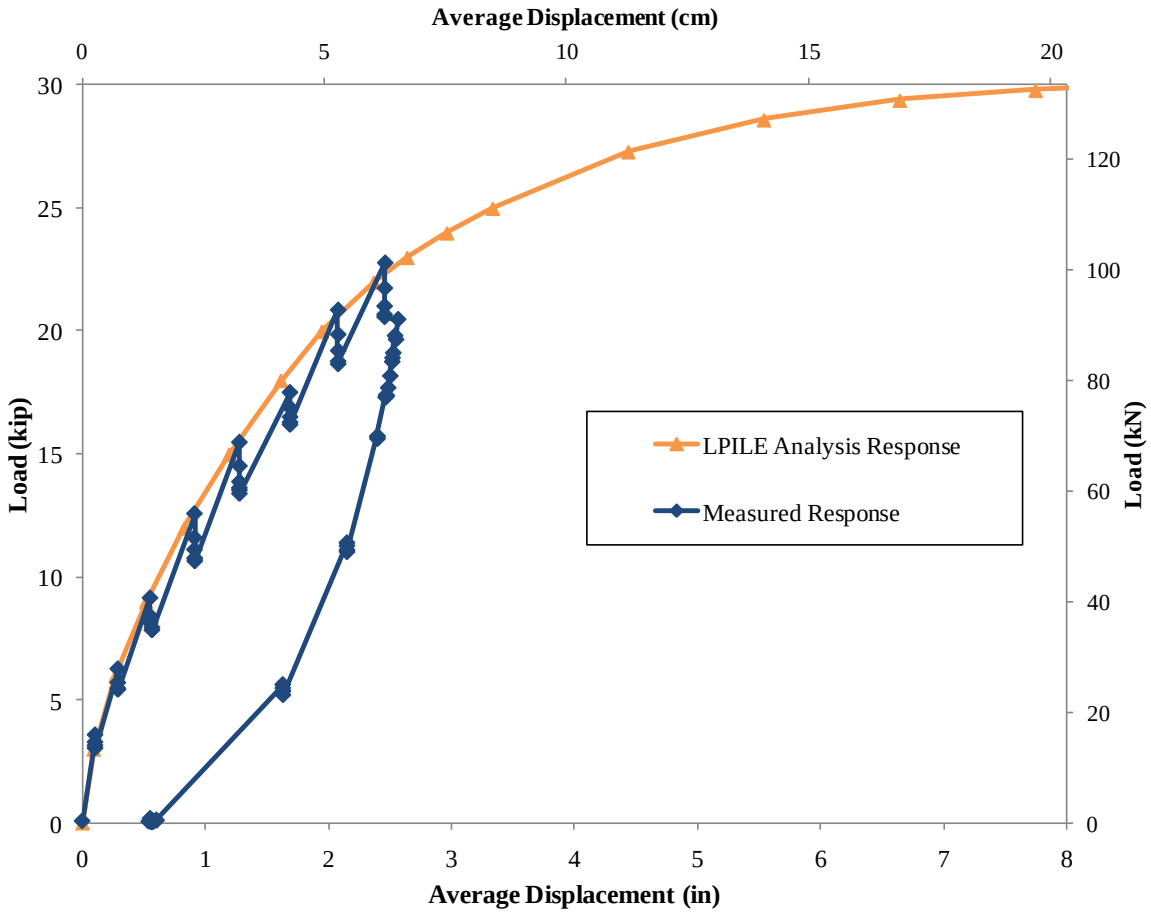

Figure 5.50. Measured and calculated load-displacement response of pile 2

5.4.4.2 Moment Profile

LPILE was also used after the lateral load test had been completed to calculate moments along the length of each UHPC pile for the actual loads applied to the piles during the lateral load test. Figure 5.51 shows the moments calculated from the measured strains at each gauge location in the UHPC piles as reported in Section 5.4.3.2 and the moment profile obtained from LPILE at the maximum lateral load of 22.8 kips (101.3 kN).

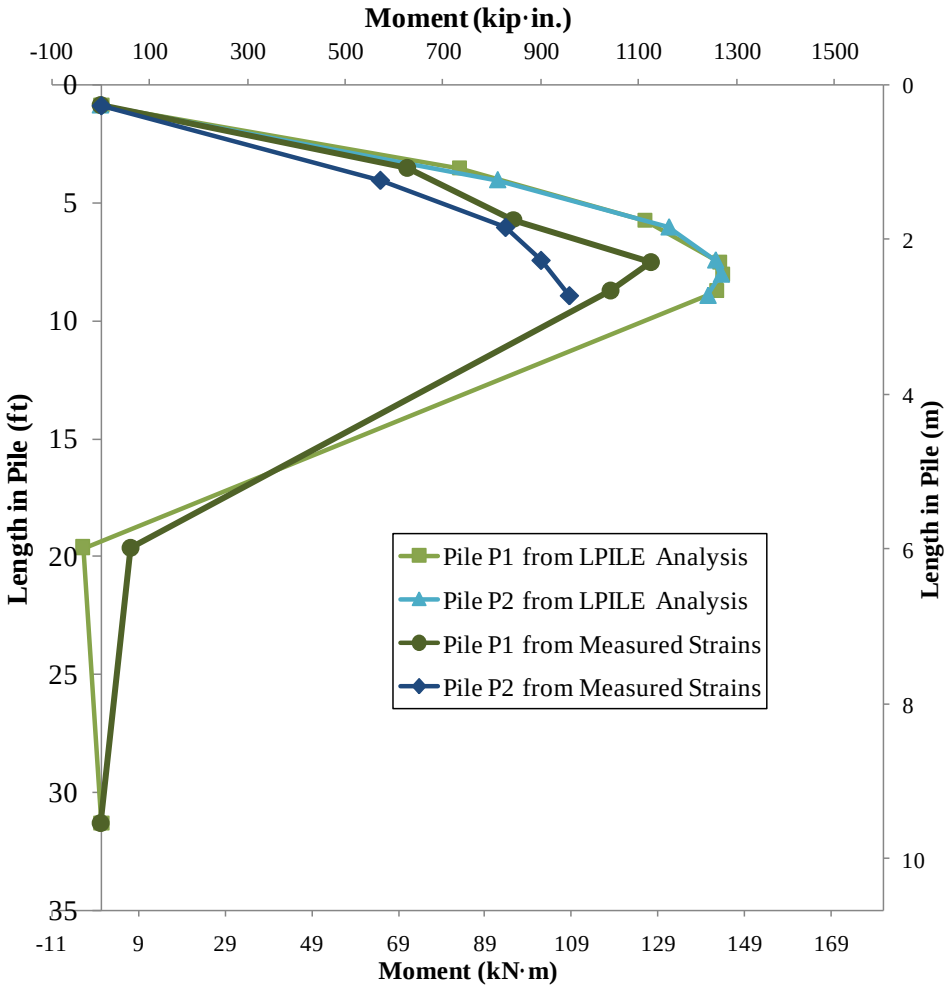

Figure 5.51. Comparison of moment profile established from LPILE analysis with those calculated from measured strains along the length of UHPC piles P1 and P2 at 22.8 kip (101.3 kN) lateral load

The maximum moments from the LPILE analysis occurred at 8.0 ft (2.4 m) from the top of the pile for both UHPC piles. The maximum moment values were 1272 kip·in. (143.7 kN·m) for pile P1 and 1268 kip·in. (143.3 kN·m) for pile P2. The largest moments calculated from the measured strains for each pile can be directly compared with the LPILE moments at the same location, as presented in Table 5.8 for the 22.8 kip (101.3 kN) lateral load.

Table 5.8. Comparison of largest moment calculated from measured strains and moment from LPILE analysis at the corresponding depth

Pile	Location from Top of Pile	Largest Moment from Measured Strains	Moment from LPILE Analysis at Same Depth	LPILE % Error
P1	7.4 ft (2.3 m)	1124 kip·in. (127.0 kN·m)	1267 kip·in. (143.1 kN·m)	13%
P2	8.9 ft (2.7 m)	958 kip·in. (108.2 kN·m)	1241 kip·in. (140.2 kN·m)	30%

CHAPTER 6: SUMMARY AND CONCLUSIONS

6.1. SUMMARY OF RESEARCH

The challenges associated with bridge pile types currently used in the United States have been discussed in the Chapter 1, emphasizing how high performance materials like UHPC can help to achieve the AASHTO Strategic Plan for Bridge Engineering's grand challenges of extending bridge service life and optimizing structural systems. A review of published literature in Chapter 2 has shown that the excellent durability and material properties of UHPC make it an ideal material for deep foundation applications. Factors that control pile design and driveability have been discussed in Sections 2.6 and 2.7, including the allowable stresses and corrosion prevention measures used by state departments of transportation. Chapter 3 has shown how a tapered H-shaped prestressed UHPC pile section was designed with a unit weight similar to that of a commonly used steel pile having the same overall dimensions. Moment-curvature and driveability analysis results for the UHPC pile section have been presented, showing the high bending moment capacity and good driving performance for the proposed UHPC pile. The successful casting of UHPC field test piles and laboratory test units has been presented in Chapter 4, verifying the ability of UHPC to be used in a precasting plant to produce high quality members with high compressive strength. The driving of UHPC test piles on a bridge site in Iowa has been discussed in Chapter 5, and PDA results have verified the driving resistance of the piles. Vertical load tests have been performed to compare the axial load capacity of the UHPC pile to a similarly sized steel pile. The results of lateral load tests have also determined the lateral load capacity of the UHPC piles.

6.2. CONCLUSIONS

6.2.1. Section Design

An optimized prestressed UHPC pile section has been successfully designed with no mild steel reinforcement. The 10 by 10-in. (25 by 25-cm) tapered H-shaped UHPC pile

section achieves a weight approximately the same as that of a similarly sized HP 10×57 steel pile without a significant reduction in moment capacity compared to the steel pile. Based on a driveability study with a wide range of materials, soils, and driving hammers, it is concluded that driving stresses are well below allowable limits in UHPC piles in most conditions, and the required pile cushion thickness for UHPC piles may be reduced compared to HPC or normal concrete piles.

6.2.2. Pile and Test Unit Production

UHPC can be successfully cast in a precasting plant, even in members with small cross-sections. High strengths of 26 to 29 ksi (179 to 200 MPa) are achievable when the standard heat treatment procedures for UHPC are followed. Vibration of UHPC during casting is recommended to eliminate the possibility of air pocketing in UHPC members, and with vibrating, even a stiff UHPC mix can be used to produce high-quality specimens.

6.2.3. Theoretical Behavior

Results from PDA measurements during the driving of the UHPC and steel piles confirmed that the driveability analysis accurately calculated the driving stresses. CPT test results also provided a good prediction of soil resistance during pile driving. LPILE analysis for the laterally loaded UHPC piles appeared to be sensitive to small changes in the input soil parameters. LPILE results using averaged soil properties from two CPT locations at the test site showed good correlation with measured lateral deflections and moment profile at the maximum load in the UHPC piles.

6.2.4. Feasibility of Using UHPC for Driven Piles

Observations and measurements during driving confirm that UHPC piles can be driven with the same driving equipment as steel piles of the same size and weight. UHPC piles were successfully driven without a pile cushion for a distance of approximately 2 to 4 ft (0.6 to 1.2 m) through sand to silty sand and sandy silt to clayey silt soil layers. Neither cracking nor any damage was observed on the UHPC piles after driving, and the condition of the top of each pile at the end of driving was better than that of most of the steel piles driven at the test site.

The axial load capacity of the UHPC pile was 1.8 times greater than that of the steel pile, mainly due to the larger cross-sectional area of the UHPC pile. This suggests that the use of UHPC piles may reduce the total number of piles required for a bridge foundation. The initial cost of a UHPC pile foundation could thus be lower than that of a steel pile alternative in some situations, and the maintenance costs for UHPC piles are expected to be significantly lower than those associated with other types of piles. Though one of the UHPC piles failed in shear during the lateral load test because of a weakened region containing a large bundle of instrumentation wires, a higher shear capacity is expected for a UHPC pile without this loss of section.

6.3. FUTURE RESEARCH

The moment-curvature behavior of the UHPC pile section will be further studied by the research team though experimental laboratory tests. The results of these tests will be presented in Vande Voort et al. (2008). Further research on the stress-strain behavior of UHPC, particularly of confined UHPC, would be useful in developing more accurate moment-curvature analysis.

UHPC piles should be driven at test sites with other soil profiles to verify the driving performance of the piles. The installed UHPC piles should be load tested vertically and laterally to determine the vertical load capacity and the displacement ductility of the piles under lateral load, respectively, in different types of soils. A driven UHPC pile should also be excavated after driving to inspect the pile for damage, particularly to examine the pile tip if it is driven to bedrock.

The shear capacity of the tapered H-shaped UHPC pile section should be tested to determine the actual shear capacity of a fully effective UHPC pile section. The weak-axis bending behavior of the tapered H-shaped UHPC pile section should be studied to determine whether the maximum ductility of the pile is achieved with strong-axis or weak-axis bending. The behavior of UHPC piles under cyclic loads similar to those that would be experienced in an integral abutment due to the temperature movements of a bridge should be studied. If the UHPC piles do not exhibit the progressive cracking damage and section loss that currently

prevents normal concrete piles from being used to support integral abutments in some states (e.g., Iowa), the UHPC piles should then be used for integral abutments in an actual bridge application, and their performance under cyclic temperature loading should be monitored. The UHPC pile described in this report could be installed in a non-integral bridge foundation application without further testing, but the performance of the pile should be monitored.

REFERENCES

Abdel-Sayed, F.K., Soghair, H.M., El-Wafa, A.A., and A.M. Yousry. 2002. Safe Limits Against Lateral Instability of RC Slender Beams Cast of Normal, High, and Ultra High Performance Concrete. *Innovations and Developments in Concrete Materials and Construction: Proceedings of the International Conference Held at the University of Dundee, Scotland, UK on 9-11 September*. London: 805-818.

Acker, P. 2001. Micromechanical analysis of creep and shrinkage mechanisms. *Creep, Shrinkage and Durability Mechanics of Concrete and other Quasi-Brittle Materials*. Ed. by Ulm, F.-J., Bažant, Z.P., and F.H. Wittmann. Elsevier: 15-25.

Acker, P. 2004. Why Does Ultrahigh-Performance Concrete (UHPC) Exhibit Such Low Shrinkage and Such Low Creep? *Autogenous Deformation of Concrete*: 141-153.

Acker, P., and M. Behloul. 2004. Ductal® Technology: A Large Spectrum of Properties, *Ultra High Performance Concrete, Kassel, Germany, Sept. 13-15*: 11-23.

Aïtcin, P.-C. 2000. Cements of yesterday and today – Concrete of tomorrow. *Cement and Concrete Research*, Sept., Vol. 30, No. 9: 1349-1359.

Aïtcin, P.-C., Delagrave, Y., and R. Beck. 2000. A 100-m High Prefabricated Concrete Pole: Why not? Proceedings of the IEEE International Conference on Transmission and Distribution, Construction, and Live Line Maintenance: 365-374.

Alaska Department of Transportation and Public Facilities (DOT&PF). 2005. *Highway Design*. Alaska Highway Preconstruction Manual.

American Concrete Institute (ACI). 1992. *Report on High-Strength Concrete (ACI 363R-92)*. ACI, Farmington Hills, Michigan.

American Concrete Institute (ACI). 2005. *Building Code Requirements for Structural Concrete (ACI 318-05) and Commentary (ACI 318R-05)*. ACI, Farmington Hills, Michigan.

American Association of State Highway and Transportation Officials (AASHTO). 2002. *Standard Specifications for Highway Bridges*, Seventeenth Ed. AASHTO.

American Association of State Highway and Transportation Officials (AASHTO). 2004. *AASHTO LRFD Bridge Design Specifications, Customary U.S. Units*, Third Ed. AASHTO.

AASHTO. 2005. Grand Challenges: A Strategic Plan for Bridge Engineering. AASHTO Subcommittee on Bridges and Structures, June.

American Society of Civil Engineers (ASCE). 1996. *Standard Guidelines for the Design and Installation of Pile Foundations*, ASCE 20-96, New York.

Arizona Department of Transportation (ADOT), Intermodal Transportation Division. 2001. *Bridge Design Guidelines*. http://www.azdot.gov/Highways/bridge/Guidelines/DesignGuidelines/ index.asp.

Arsoy, S., Duncan, J.M., and R.M. Barker. 2002. Performance of Piles Supporting Integral Bridges. *Soil Mechanics*. Transportation Research Record, No. 1808: 162-167.

Association Française de Génie Civil (AFGC). 2002. *Ultra High Performance Fibre-Reinforced Concretes - Interim Recommendations*, Jan. AFGC.

Ay, L. 2004. Curing tests on ultra high strength plain and steel fibrous cement based composites. *Proceedings of the International Symposium on Ultra High Performance Concrete, Kassel, Germany, Sept. 13-15*: 695-701.

Bayard, O., and O. Plé. 2003. Fracture mechanics of reactive powder concrete: material modelling and experimental investigations. Engineering Fracture Mechanics, May, Vol. 70, No. 7-8: 839-851.

Behloul, M. 1996. Les micro-bètons renforces de fibers. De l'éprouvevette aux structures, XIVèmes Journées de l'AUGC.

Bierwagen, D., and A. Abu-Hawash. 2005. Ultra High Performance Concrete Highway Bridge. *Proceedings of the 2005 Mid-Continent Transportation Research Symposium, Ames, IA, August*.

Bindiganavile, V., Banthia, N., and B. Aarup. 2002. Impact Response of Ultra-High-Strength Fiber-Reinforced Cement Composite. *ACI Materials Journal*, Nov./Dec., Vol. 99, No. 6: 543-548.

Billon, P., Ed. 2006. Saint-Pierre-la-Cour: A railway bridge that is twice as light. *Ductal® Solutions*, The Lafarge Ductal® Newsletter, No. 3, March: 3.

Blais, P.Y., and M. Couture. 1999. Precast, Prestressed Pedestrian Bridge – World's First Reactive Powder Concrete Structure. *PCI Journal*, Sept., Vol. 44, No. 5: 60-71.

Bonneau, O., Poulin, C., Dugat, J., Richard, P., and P.-C. Aïtcin. 1996. Reactive Powder Concretes: From Theory to Practice. *Concrete International*, Apr., Vol. 18, No. 4: 47-49.

Bonneau, O., Lachemi, M., Dallaire, E., Dugat, J., and P.-C. Aïtcin. 1997. Mechanical Properties and Durability of Two Industrial Reactive Powder Concretes. *ACI Materials Journal*, July-Aug., Vol. 94, No. 4: 286-290.

Bonneau, O., Vernet, C., Moranville, M., and P.-C. Aïtcin. 2000. Characterization of the granular packing and percolation threshold of reactive powder concrete. *Cement and Concrete Research*, Dec., Vol. 30, No. 12: 1861-1867.

Bridge Engineering Center. 2007. News, 2006 Concrete Bridge Award, Iowa State University, July 30. http://www.bec.iastate.edu/.

Bristow, B. and S. Sritharan. Uniaxial and Cyclic Behavior of Ultra-High Performance Concete. To be submitted to the *ACI Materials Journal*.

Brown, J.L. 2006. Highway Span Features Ultra-High-Performance Concrete. *Civil Engineering*, July, Vol. 76, No. 7: 24-26.

Cadoni, E., Teruzzi, T., Muttoni, A., Suter, R., and E. Brühwiler. 2004. FRC in Switzerland: research, applications and perspectives. *International Workshop on Advanced Fiber Reinforced Concrete, Bergamo, Italy*. École Polytechnique Fédérale de Lausanne, *IS-Beton*. http://is-beton.epfl.ch/Publications/2004/ Cadoni04.pdf.

California Department of Transportation (Caltrans). 2007. *California Amendments to the AASHTO LRFD Bridge Design Specifications*. http://www.dot.ca.gov/hq/esc/techpubs/manual/bridgemanuals/ca-to-aashto-lrfd-bds/caalbds.html.

Castellote, M., Llorente, I., Andrade, C., and C. Alonso. 2003. Accelerated leaching of ultra high performance concretes by applications of electrical fields to simulate their natural degradation. *Materials and Structures*, March, Vol. 36: 81-90.

Comité Euro-International du Béton. 1993. *CEB-FIP Model Code 1990*.

Cement and Concrete Association of Australia. 2002. Drying Shrinkage of Cement and Concrete. Cement and Concrete Association of Australia, July. http://www.concrete.net.au/search.php?category=cement&menu=2.

Chan, Y.-W., and S.-H Chu. 2004. Chu. Effect of silica fume on steel fiber bond characteristics in reactive powder concrete. *Cement and Concrete Research*, July, Vol. 34, No. 7: 1167-1172.

Cheyrezy, M., Maret, V., and L. Frouin. 1995. Microstructural Analysis of RPC (Reactive Powder Concrete). *Cement and Concrete Research*, Oct., Vol. 25, No. 7: 1491-1500.

Cheyrezy, M., Roux, N., Behloul, M., Ressicaud, A, and A. Demonte. 1998. Bond strength of reactive powder concrete. *Proceedings of the 13th FIP Congress on Challenges for Concrete in the Next Millenium*, Amsterdam, Netherlands, 23-29 May, Vol. 1: pp. 65-68.

Cheyrezy, M. 1999. Structural Applications of RPC. *Concrete*, Jan., Vol. 33, No. 1. London: 20-23.

Cheyrezy, M., and M. Behloul. 2001. Creep and Shrinkage of Ultra-High Performance Concrete. *Creep, Shrinkage and Durability Mechanisms of Concrete and other Quasi-Brittle Materials – Proceedings of the Sixth International Conference CONCREEP-6@MIT*, Cambridge, MA, USA, 20-22 August. Ed. By Ulm, F.-J., Bažant, Z.P., and F.H. Wittmann. Elsevier: 527-538.

Collepardi, S., Coppola, L., Troli, R., and M. Collepardi. 1997. Mechanical Properties of Modified Reactive Powder Concrete. *Enco Journal*. http://www.encosrl.it/enco%20srl%20ITA/servizi/pdf/high/12.pdf.

Colorado Department of Transportation (CDOT). 2002. *Bridge Design Manual*. http://www.dot.state.co.us/Bridge/DesignManual/BridgeDesignManual.htm.

Construction Innovation Forum. 2003. Ultra-High Performance Concrete with Ductility – The World's First Long-Span Roof Constructed in Ductal®. Construction Innovation Forum, 2003 Nova Award Nomination. http://www.cif.org/Nom2003/Nom22_03.pdf.

Cornfield, G.M. 1980. *Steel Bearing Piles*, British Steel Corporation, Middlesbrough, United Kingdom.

Cwirzen, A. 2007. The effect of the heat-treatment regime on the properties of reactive powder concrete. *Advances in Cement Research*, Jan., Vol. 19, No. 1: 25-33.

Das, B. 2004. Principles of Foundation Engineering. Brooks/Cole-Thomson Learning, United States.

Dallaire, E., Aïtcin, P.-C., and M. Lachemi. 1998. High-Performance Powder. *Civil Engineering*, Jan., Vol. 68, No. 1: 48-51.

Davisson, M.T. 1972. High Capacity Piles. *Proceedings, Soil Mechanics Lecture Series on Innovations in Foundation Construction*, ASCE, Chicago: 81-112.

Davisson, M.T., Manuel, F.S., and R.M. Armstrong. 1983. Allowable Stresses in Piles. FHWA/RD-83/059, Dec.

de Larrard, F., and T. Sedran. 1994. Optimization of Ultra-High-Performance Concrete by the Use of a Packing Model. *Cement and Concrete Research*, June, Vol. 24, No. 6: 997-1009.

Deem, S. 2002. Concrete Attraction – Something new on the French menu—concrete. *Popular Mechanics*, June.

Degen, B.E. 2006. Shear design and behavior of Ultra-High Performance Concrete. Master of Science Thesis, Iowa State University.

Delmag. 2007. Diesel Pile Hammer – Technical Details (Brochure). Germany, Mar.

DiMillio, A. 1998. *A Quarter Century of Geotechnical Research*. FHWA-RD-98-139. Dec. http://www.fhwa.dot.gov/engineering/geotech/ pubs/century/index.cfm.

Dirks, K. and P. Kam. 2003. Foundation Soils Information Chart – Pile Foundation. Iowa Department of Transportation, Office of Road Design, Ames, Iowa, United States.

Dowd, W.M., and C.E. Dauriac. 1996. Reactive Powder Concrete. Construction Specifier, Dec., Vol. 49, No. 12: 47-52.

Droll, K. 2004. Influence of additions on ultra high performance concretes – grain size optimisation. *Proceedings of the International Symposium on Ultra-High Performance Concrete, Kassel, Germany, Sept. 13-15*: 285-301.

Dugat, J., Roux, N., and G. Bernier. 1996. Mechanical Properties of Reactive Powder Concretes. *Materials and Structures*, May, Vol. 29: 233-240.

Engineering News Record (ENR). 2007. Construction Economics, *ENR*, McGraw Hill Companies, Nov. 26: 77-78.

Engineering News Record (ENR). 2008. Construction Economics, *ENR*, McGraw Hill Companies, Jan. 7/14: 28-33.

Federal Highway Administration (FHWA). 2002. A New and Improved High-Performance Concrete. *Focus*, Feb. http://www.tfhrc.gov/focus/feb02/highperformance.htm.

Federal Highway Administration (FHWA). 2004. Achieving the Promise of Ultra-High-Performance Concrete. *Focus*, Nov. http://www.tfhrc.gove/focus/nov04/01.htm.

Feng, X., Deng, L.-P., Cao, Z.-L., and L.-D. Huang. 2006. Static Loading Investigation on Well Cover of Reactive Powder Concrete. *Key Engineering Materials*, Jan., Vol. 302-303: 556-560.

Feylessoufi, A., Tenoudji, F.C., Morin, V., and P. Richard. 2001. Early ages shrinkage mechanisms of ultra-high-performance cement-based materials. Cement and Concrete Research, Nov., Vol. 31, No. 11: 1573-1579.

Florida Department of Transportation (FDOT), Structures Design Office. 2008. *Structures Manual – Vol. 1: Structures Design Guidelines*. Jan. http://www.dot.state.fl.us/ structures/StructuresManual/CurrentRelease/StructuresManual.htm.

Gao, R., Liu, Z.-M., Zhang, L.-Q., and P. Stroeven. 2006. Static Properties of Reactive Powder Concrete Beams. *Key Engineering Materials*, Jan., Vol. 302-303: 521-527.

Georgia Department of Transportation (GDOT), Office of Bridge and Structural Design. 2007. Bridge and Structures Design Policy Manual. Oct. http://www.dot.state.ga.us/ dot/preconstruction/R-o-a-d-s/DesignPolicies/documents/pdf/GDOT%20Bridge%20and%20Structures%20Policy%20Manual.pdf.

Gilliland, S.K. 1996. Reactive Powder Concrete (RPC), A New Material for Prestressed Concrete Bridge Girders. *Structures Congress - Proceedings, Vol. 1, Building an International Community of Structural Engineers*: 125-132.

Gowripalan, N., and R.I. Gilbert. 2000. *Design Guidelines for RPC Prestressed Concrete Beams*. The University of New South Wales.

Graff, C.R. 1965. The Wave Equation and Pile Driving. *Foundation Facts*, Vol. 1, No. 2: 8-9, 18.

Granger, S., Loukili, A., Pijaudier-Cabot, G., and G. Chanvillard. 2006. Experimental characterization of the self-healing of cracks in an ultra high performance cementitious material: Mechanical tests and acoustic emission analysis. *Cement and Concrete Research*, Apr., Vol. 37, No. 4: 519-527.

Graybeal, B. 2005. Characterization of the Behavior of Ultra-High Performance Concrete. PhD dissertation, University of Maryland.

Graybeal, B.A. 2006. Material Property Characterization of Ultra-High Performance Concrete. FHWA-HRT-06-103, Aug.

Graybeal, B. 2007. Compressive Behavior of Ultra-High-Performance Fiber-Reinforced Concrete. *ACI Materials Journal*, Mar.-Apr.: 146-152.

GRL Engineers. 2001. Pile Driving Wave Equation Workshop – course notes. March 21, Iowa State University, Ames, Iowa, United States.

Grogan, T. 2007. Inflation Bows to Sub-Prime Crisis, *ENR*, McGraw Hill Companies, Dec. 17: 26-28.

Grünewald, S. 2004. *Performance-based design of self-compacting fibre reinforced concrete*. Delft University Press, Deflt, The Netherlands.

Habel, K., Charron, J.-R., Denarié, E., and E. Brühwiler. 2006a. Autogenous Deformations and Viscoelasticity of UHPFRC in Structures. *Magazine of Concrete Research*, April, Vol. 58, No. 3: 135-145.

Habel, K., Viviani, M., Denarié, E., and E. Brühwiler. 2006b. Development of the Mechanical Properties of an Ultra-High Performance Fiber Reinforced Concrete (UHPFRC). *Cement and Concrete Research*, July, Vol. 36, No. 7: 1362 – 1370.

Hannigan, P.J., Goble, G.G., Thendean, G., Likins, G.E., and F. Rausche. 1998. Design and Construction of Driven Pile Foundations – Volume I. Goble Rausche Likins and Associates, Inc., FHWA-HI-97-013, Nov.

Hassan, A., and M. Kawakami. 2005. Steel-Free Composite Slabs Made of Reactive Powder Materials and Fiber-Reinforced Concrete. *ACI Structural Journal*, Sept./Oct., Vol. 102, No. 5: 709-718.

Hegger, J., Tuchlinski, D., and B. Kommer. 2004. Bond Anchorage Behavior and Shear Capacity of Ultra High Performance Concrete Beams. *Proceedings of the International Symposium on Ultra-High Performance Concrete, Kassel, Germany, Sept. 13-15*: 351-360.

Heinz, D., and H.-M. Ludwig. 2004. Heat Treatment and the Risk of DEF Delayed Ettringite Formation in UHPC. *Proceedings of the International Symposium on Ultra-High Performance Concrete, Kassel, Germany, Sept. 13-15*: 717-730.

Herold, G., and H.S. Müller. 2004. Measurement of porosity of Ultra High Strength Fibre Reinforced Concrete. *Proceedings of the International Symposium on Ultra-High Performance Concrete, Kassel, Germany, Sept. 13-15*: 685-694.

Holschemacher, K., and S. Klotz. 2003. Ultra High Strength Concrete under Concentrated Load. *Leipzig Annual Civil Engineering Report (LACER)*, No. 8: 231-242.

Holschemacher, K., Wieße, D., and S. Klotz. 2005. Bond of Reinforcement in Ultra High-Strength Concrete. *7th International Symposium on Utilization of High Strength High Performance Concrete*, Vol. 1: 513-528.

Huck, R.W., and J.R. Hull. 1971. Resonant Driving in Permafrost. *Foundation Facts*, Vol. 7, No. 1: 11-15.

Huh, S.-B., and Y.-J. Byun. 2005. Sun-Yu Pedestrian Arch Bridge, Seoul, Korea. *Journal of the International Association for Bridge and Structural Engineering (IABSE)*, Feb., Vol. 15, No. 1: 32-34.

Illinois Department of Transportation. 2006. *Bridge Manual Design Guides – LRFD Geotechnical Pile Design Procedure Guide 3.10.1*. Nov. http://www.dot.il.gov/bridges/Design%20Guides/3.10.1%20-%20LRFD%20Pile%20Design.pdf.

Iowa Department of Transportation. 2007. *ASD/LFD Bridge Design Manual*. Iowa Department of Transportation, July. http://www.dot.state.ia.us/bridge/manualasd.htm.

Jones, T., and B. Cather. 2005. Ultra-High Performance Fibre-Reinforced Concrete. *Concrete Engineering International*, Spring, Vol. 9, No. 1: 59-61.

Jungwirth, J., and A. Muttoni. 2004. Structural Behavior of Tension Members in UHPC. École Polytechnique Fédérale de Lausanne, *IS-Beton*. http://is-beton.epfl.ch/Person/Anciens/Jungwirt/Paper%20JJ%20Kassel%20UHPC.pdf.

Juran, I., and U. Komornik. 2006. Behavior of Fiber-Reinforced Polymer (FRP) Composite Piles under Vertical Loads. August. http://www.fhwa.dot.gov/engineering/geotech/pubs/04107/index.cfm.

Kakizaki, M., Edahiro, H., Tochigi, T., and T. Niki. 1992. *Fly Ash, Silica Fume, Slag, and Natural Pozzolans in Concrete: Proceedings, Fourth International Conference, Istanbul, Tukery, May*. Ed. By V.M. Malhotra. American Concrete Institute, Detroit, MI: 997-1016.

Klemens, T. 2004. Flexible Concrete Offers New Solutions. *Concrete Construction*, Dec. FindArticles.com. http://findarticles.com/p/articles/mi_m0NSX/is_12_49/ai_n8590896.

Kosmatka, S.H., Kerhoff, B., and W.C. Panarese. 2002. *Design and Control of Concrete Mixtures*, 14th Ed. Portland Cement Association, Shokie, IL.

Lafarge North America. 2006. LCM's Precast operations in Winnipeg produces the world's first Ductal® bus shelters. Lafarge North America. http://www.lafarge-na.com/wps/wcm/resources/file/eb9b2002009d964/busshelter.pdf.

Lafarge North America. 2006. Structural Columns to Support a Suspended Floor in a 185-ft Silo. Imagineductal.com. http://www.imagineductal.com/imagineductal/public/eng/pdf/Detroit-Columns.pdf.

Lafarge North America. 2007. Product Information. http://www.lafargenorthamerica. com.

Lafarge. 2007. Ductal® - Applications and References. http://www.ductal-lafarge.com/wps/portal/Ductal/ApplicationsAndReferences/.

Lee, M.-G., Chiu, C.-T., and Y.-C. Wang. 2005. The Study of Bond Strength and Bond Durability of Reactive Powder Concrete. *Journal of ASTM International*, July/Aug., Vol. 2, No. 7: 104-113.

Lee, N.P., and D.H. Chisholm. 2006. *Reactive Powder Concrete*. Branz. http://www.branz.co.nz/branzltd/publications/pdfs/SR146.pdf.

Louisiana Department of Transportation and Development (DOTD), Bridge Design Section. *LRFD Bridge Design Manual, First Ed*. Sept. 1. http://www.dotd.louisiana.gov/highways/project_devel/design/bridge_design/documents/LRFD_Bridge_Design_Manual-version_2006.1.pdf.

Loukili, A., Khelidj, A., and P. Richard. 1999. Hydration Kinetics, Change of Relative Humidity, and Autogenous Shrinkage of Ultra-High-Strength Concrete. *Cement and Concrete Research*, Apr., Vol. 29, No. 4: 577-584.

Lubbers, A. 2003. Bond Performance Between Ultra-High Performance Concrete and Prestressing Strands, Master's Thesis, Ohio University.

Lunne, T., Powell, J.J.M., and P.K. Robertson. 1997. *Cone Penetration Testing in Geotechnical Practice*. Taylor and Francis.

Ma, J., and H. Schneider. 2002. Properties of Ultra-High-Performance Concrete. *Leipzig Annual Civil Engineering Report (LACER)*, No. 7: 25-32.

Ma, J., Dietz, J., and F. Dehn. 2003. Ultra High Performance Self Compacting Concrete. *3rd International Symposium on Self-Compacting Concrete, Reykjavik, Iceland, 17-20 August*: 136-142.

Ma, J., Orgass, M., Dehn, F., Schmidt, D., and N.V. Tue. 2004. Comparative Investigations on Ultra-High Performance Concrete with and without Coarse Aggregates. *Proceedings of the International Symposium on Ultra-High Performance Concrete, Kassel, Germany, Sept. 13-15*: 205-212.

Massachusetts Highway Department (Mass Highway). 2005. *Bridge Manual – Part I*. May. http://www.mhd.state.ma.us/downloads/bridge/CHAPTER%203%202007.pdf.

Matte, V., and M. Moranville. 1998. Leaching of the Reactive Powder Concretes: Results on Transfer Properties. Nondestructive Characterization of Materials in Aging Systems: Symposium Held November 30-December 4, 1997, Boston, Massachusetts, Vol. 503. Ed. by Crane, R.L., Achenbach, J.D., Shah, S.P., Matikas, T.E., Khuri-Yakub, P., and R.S. Gilmore. Materials Research Society: 145-150.

Matte, V., and M. Moranville. 1999. Durability of Reactive Powder Composites: influence of silica fume on the leaching properties of very low water/binder Pastes. Cement & Concrete Composites, Feb., Vol. 21, No. 1: 1-9.

Matthias, D. and M. Cribbs. 1998. Driven 1.0: A Microsoft Windows Based Program for Determining Ultimate Vertical Static Pile Capacity (User's Manual). FHWA-SA-98-074, May.

Minnesota Department of Transportation. 2007. *LRFD Bridge Design Manual*. Oct. 5. http://www.dot.state.mn.us/bridge/Manuals/LRFD/index.html.

Missouri Department of Transportation (MoDOT). 2007. LRFD Manual General – 751.36 Driven Piles. http://epg.modot.org/index.php?title=751.36_Driven_Piles.

Montana Department of Transportation (MDT) Bridge Design Section. *Montana Structures Manual*. http://www.mdt.mt.gov/other/bridge/external/structures-manual/part_II/chp-20-final.pdf.

Morin, V., Cohen-Tenoudji, F., Feylessoufi, A., and P. Richard. 2002. Evolution of the capillary network in a reactive powder concrete during hydration process. Cement and Concrete Research, Dec., Vol. 32, No. 12: 1907-1914.

Morley, J. 1979. The corrosion and protection of steel piling, *British Steel Corporation*, Teesside Laboratories.

Morley, J. and D.W. Bruce. 1983. Survey of steel piling performance in marine environments, final report. Commission of the European Communities, Document EUR 8492 EN.

Nebraska Department of Roads (NDOR) Bridge Division. 2005. *Bridge Operations, Policies, & Procedures*. http://www.nebraskatransportation.org/design/bridge/bopp/2005_BOPP_Manual.pdf.

Nevada Department of Transportation. 2005. *Geotechnical Policies and Procedures Manual*. Feb. 14. http://www.nevadadot.com/reports_pubs/Geo_PPManual/pdfs/Geo_PPM.pdf.

Nevada Department of Transportation. 2008. *Structures Manual*. Jan.

New York State Department of Transportation (NYSDOT). 2007. LRFD Blue Pages – US Customary. Sept.

Nielsen, C.V.1998. Triaxial Behavior of High-Strength Concrete and Mortar. *ACI Materials Journal*, Mar./Apr., Vol. 95, No. 2: 144-151.

Paikowsky, S.G., and T.A. Tolosko. 1999. Extrapolation of Pile Capacity from Non-Failed Load Tests. FHWA-RD-99-170, Dec.

Pando, M.A., Ealy, C.D., Filz, G.M., Lesko, J.J., and E.J. Hoppe. 2006. A Laboratory and Field Study of Composite Piles for Bridge Substructures. FHWA-HRT-04-043, Mar. http://www.tfhrc.gov/structur/pubs/04043/index.htm#toc.

Pennsylvania Department of Transportation (PENNDOT). 2007. Design *Manual – Part 4, Structures*, Sept.

Perry, V. 2001. Reactive Powder Concrete. *PCI Journal*, July/Aug., Vol. 46, No. 4: 118.

Perry, V., and D. Zakariasen. 2004. First Use of Ultra-High Performance Concrete for an Innovative Train Station Canopy. *Concrete Technology Today*, Aug., Vol. 25, No. 2: 1-2.

Perry, V. 2006. Ductal® - A Revolutionary New Material for New Solutions. Association of Professional Engineers and Geoscientists of the Province of Manitoba (APEGM). http://www.apegm.mb.ca/pdnet/papers/ductal.pdf.

Pile Dynamics, Inc (PDI). 2005. *GRLWEAP – Wave Equation Analysis of Pile Driving, Procedures and Models*, Cleveland, OH.

Pinkham, M. 2006. Structurals Build Staying Power, *Metal Center News*, June.

Port Strategy. 2007. Treating your piles. Nov. 14. http://www.portstrategy.com/archive/2007/november/marine_engineering_corrosion_control/treating_your_piles.

Porteneuve, C., Zanni, H., Vernet, C., Kjellsen, K.O., Korb, J.-P., and D. Petit. 2001. Nuclear Magnetic Resonance Characterization of High- and Ultrahigh-Performance Concrete: Application to the Study of Water Leaching. *Cement and Concrete Research*, Dec., Vol. 31, No. 12: 1887-1893.

Porteneuve, C., Korb, J.-P., Petit, D., and H. Zanni. 2002. Structure-texture correlation in ultra-high-performance concrete: A nuclear magnetic resonance study. *Cement and Concrete Research*, Jan., Vol. 32, No. 1: 97-101.

Poulos, H. 2006. Course on Analysis and Design of Piles, University of Canterbury, Christchurch, New Zealand, Sept.

Prakash, S. and H. Sharma. 1990. *Pile Foundations in Engineering Practice*, Wiley-Interscience, New York.

Precast/Prestressed Concrete Institute (PCI). 1999. *PCI Design Handbook: Precast and Prestressed Concrete*, 5th Ed. PCI, Chicago, IL.

Racky, P. 2004. Cost-effectiveness and Sustainability of UHPC. Proceedings of the International Symposium on Ultra High Performance Concrete, Kassel, Germany, Sept. 13-15: 797-805.

Rausche, F., Goble, G.G., and G.E. Likins. 1985. Dynamic Determination of Pile Capacity. *Journal of Geotechnical Engineering*, ASCE, Vol. 111, No. 3: 367-383.

Reda, M.M., Shrive, N.G., and J.E. Gillott. 1999. Microstructural Investigation of Innovative UHPC. *Cement and Concrete Research*, Mar., Vol. 29, No. 3: 323-329.

Rebentrost, M., and B. Cavill. 2006. Reactive Powder Concrete Bridges. AustRoads Conference, Perth, Australia, 12-15 Sept.

Reineck, K.-H., Lichtenfels, A., and S. Greiner. 2004. Concrete Hot Water Tanks for Solar Energy Storage. *Structural Engineering International: Journal of the International Association for Bridge and Structural Engineering (IABSE)*, Aug., Vol. 14, No. 3: 232-234.

Reineck, K.-H., and S. Greiner. 2004. Tests on ultra-high performance fibre reinforced concrete designing hot-water tanks and UHPFRC-shells. *Proceedings of the International Symposium on Ultra High Performance Concrete, Kassel, Germany, Sept. 13-15*: 361-374.

Richard, P., and M.H. Cheyrezy. 1994. Reactive Powder Concretes with High Ductility and 200-800 MPa Compressive Strength. *Concrete Technology: Past, Present, and Future – Proceedings of V. Mohan Malhotra Symposium*. American Concrete Institute, Detriot, MI.

Richard, P., and M. Cheyrezy. 1995. Composition of Reactive Powder Concretes. *Cement and Concrete Research*, Oct., Vol. 25, No. 7: 1501-1511.

Road and Traffic Authority, New South Wales (RTA NSW). 2005. Blandford Bridge. Heritage and Conservation Register. http://www.rta.nsw.gov.au/cgi-bin/index.cgi?action=heritage.show&id=4305023.

Romanoff, M. 1962. Corrosion of Steel Pilings in Soils, *Journal of Research of the National Bureau of Standards - C. Engineering and Instrumentation*, United States Department of Commerce, National Bureau of Standards Monograph 58, Vol. 66C, No. 3, July-Sept.

Rossi, P. 2005. Development of New Cement Composite Materials for Construction. *Proceedings of the Institution of Mechanical Engineers, Part L: Journal of Materials: Design and Applications*, Feb., Vol. 219, No. L1: 67-74.

Roux, N., Andrade, C., and M.A. Sanjuan. 1996. Experimental Study of Durability of Reactive Powder Concretes. *Journal of Materials in Civil Engineering*, Feb., Vol. 8, No. 1: 1-6.

Richardson, J.G. 1986. Supervision of Concrete Construction. Vol. 1, Taylor and Francis.

Salgado, R. 2006. *The Engineering of Foundations*. McGraw-Hill.

Schmidt, M., Fehling, E., Teichmann, T., Bunje, K., and R. Bornemann. 2003. Ultra-High Performance Concrete: Perspective for the Precast Concrete Industry. *Concrete Precasting Plant and Technology*, Vol. 69, No. 3: 16-29.

Schmidt, M., and E. Fehling. 2005. Ultra-High-Performance Concrete: Research, Development and Application in Europe. *7th International Symposium on Utilization of High Strength High Performance Concrete*, Vol.1: 51-77.

Semioli, W. 2001. The New Concrete Technology. *Concrete International*, Nov., Vol. 23, No. 11: 75-79.

Smith, E.A. 1962. Pile-Driving Analysis by the Wave Equation. *Transactions*, American Society of Civil Engineers, Vol. 127: 1145-1171.

Sobolev, K. 2004. The development of a new method for the proportioning of high-performance concrete mixtures. *Cement and Concrete Composites*, Oct., Vol. 26, No. 7: 901-907.

Soutsos, M.N., Millar, S.G., and K. Karaiskos. 2005. Mix Design, Mechanical Properties, and Impact Resistance of Reactive Powder Concrete (RPC). *International RILEM Workshop on High Performance Fiber Reinforced Cementitious Composites in Structural Applications, Honolulu, HI, May*. http://www.hpfrcc-workshop.org/HPFRCC-workshop/Papers/F/Soutsos_ReactivePowderConcrete.pdf.

Spasojevic, A. 2006a. Possibilities for Structural Improvements in the Design of Concrete Bridges. *6th International PhD Symposium in Civil Engineering, Zurich, Aug 23-26*. http://is-beton.epfl.ch/Publications/2006/Spasojevic06.pdf.

Spasojevic, A. 2006b. Possibilities of Innovation in Bridge Design. École Polytechnique Fédérale de Lausanne, *IS-Beton*. http://sar2.epfl.ch/JDoctorants/Posters2006/ 48.pdf.

Sritharan, S., Bristow, B., and V. Perry. 2003. Characterizing an Ultra-High Performance Material for Bridge Applications under Extreme Loads. *Proceedings of the 3rd International Symposium on High Performance Concrete, Orlando, Florida*.

Talebinejad, I., Bassam, S.A., Iranmanesh, A. and M. Shekarchizadeh. 2004. Optimizing Mix Proportions of Normal Weight Reactive Powder Concrete with Strengths of 200 – 350 MPa. *Proceedings of the International Symposium on Ultra High Performance Concrete, Kassel, Germany, Sept. 13-15*: 133-141.

Tang, M.-C. 2004. High Performance Concrete – Past, Present, and Future. Ultra High Performance Concrete (UHPC). *Proceedings of the International Symposium on Ultra High Performance Concrete, Kassel, Germany, Sept. 13-15*: 3-9.

Teichmann, T., and M. Schmidt. 2004. Influence of the packing density of fine particles on structure, strength and durability of UHPC. *Proceedings of the International Symposium on Ultra-High Performance Concrete, Kassel, Germany, Sept. 13-15*: 313-323.

Tennessee Department of Transportation (TDOT) Structures Division. Structure Design Sections. http://www.tdot.state.tn.us/Chief_Engineer/assistant_engineer_design/structures/design.htm.

Texas Department of Transportation (TxDOT). 2006. *Geotechnical Manual*. Aug. ftp://ftp.dot.state.tx.us/pub/txdot-info/gsd/manuals/geo.pdf.

Toutlemonde, F., and J. Sercombe. 1999. FRC Containers Design to ensure Impact Performance. *Structures Congress – Proceedings*: 183-186.

Tuchlinski, D., Heqqer, J., and B. Kommer. 2006. Studies on prestressed concrete beams made from UHPC. *Concrete Precasting Plant and Technology*, Vol. 72, No. 1: 14-20.

van Breugel, K., and Y. Guang. 2004. Analyses of hydration processes and microstructural development of UHPC through numerical simulation. *Proceedings of the International Symposium on Ultra-High Performance Concrete, Kassel, Germany, Sept. 13-15*: 253-264.

Vande Voort, T., Sritharan S., and M Suleiman. 2008. Design and Performance Verification of UHPC Piles for Deep Foundations. Yet to be published.

Vernet, C.P. 2004. Ultra-Durable Concretes: Structure at the Micro- and Nanoscale. *MRS Bulletin*, May, Vol. 29, No. 5: 324-327.

Virginia Department of Transportation (VDOT). 2006. VDOT Modifications to AASHTO Standard Specifications for Highway Bridges, Sixteenth Edition. http://www.extranet.vdot.state.va.us/locdes/electronic%20pubs/VDOTMODASD/VDMASD.pdf.

Voo, J.Y., Foster, S.J., Gilbert, R.I., and N. Gowripalan. 2001. Design of Disturbed Regions in Reactive Powder Concrete Bridge Girders. *High Performance Materials in Bridges: Proceedings of the International Conference, Kona, Hawaii, July 29 – August 3*. Ed. by Azizinamini, A., Yakel, A., and M. Abdelrahman. American Society of Civil Engineers, Reston, VA: 117-127.

Voo, J.Y., Foster, S.J., and R.I. Gilbert. 2003. Shear Strength of Fibre Reinforced Reactive Powder Concrete Girders without Stirrups. *UNICIV Report No. R-421*, Nov. The University of New South Wales. http://www.civeng.unsw.edu.au/research/publications/uniciv/R-421.pdf.

VSL Proprietary Limited. 2003. Introduction to Ductal® – Frequently Asked Questions. VSL Proprietary Limited. http://www.ductal.com/Introduction%20to%20 Ductal.pdf.

Walraven, J.C. 2002. From Design of Structures to Design of Materials. Innovations and Developments in Concrete Materials and Construction: Proceedings of the International Conference Held at the University of Dundee, Scotland, UK on 9-11 Sept. London: 805-818.

Walraven, J.C. 2004. Designing with ultra high strength concrete: basics, potential and perspectives. *Proceedings of the International Symposium on Ultra-High Performance Concrete, Kassel, Germany, Sept. 13-15*: 853-864.

Walraven, J.C., and P. Schumacher. 2005. Applications for Ultra-high Performance Concrete. *TIEFBAU*, No. 4: 230-234

Walraven, J.C. 2007. Futuro del hormigon con fibras. Applicaciones estructurales de hormigon con fibras, Oct. 9, Barcelona.

Washington State Department of Transportation (WSDOT). 2006. *Geotechnical Design Manual*. http://www.wsdot.wa.gov/fasc/EngineeringPublications/Manuals/GDM/GDM.htm.

Wen-yu, J., Ming-zhe, A., Gui-ping, Y., and W. Jun-min. 2004. Study on Reactive Powder Concrete Used in the Sidewalk System of the Qinghai-Tibet Railway Bridge. *International Workshop on Sustainable Development and Concrete Technology, Beijing, China, May 20-21*. http://www.cptechcenter.org/publications/sustainable/jireactive.pdf.

White, D.J., Mekkawy, M.M., Sritharan, S., and M. Suleiman. 2007. Underlying Causes for Settlement of Bridge Approach Pavement Systems. *Journal of Performance of Constructed Facilities*, ASCE, July/Aug.: 273-282.

Xing, F., Huang, L.-D., Cao, Z.-L., and L.-P. Deng. 2006. Study on Preparation Technique for Low-Cost Green Reactive Powder Concrete. *Key Engineering Materials*, Jan., Vol. 302-303: 405-410.

Yan, Z.-G., and G.-P. Yan. 2006. Experimental Study and Finite Element Analysis of RPC Footwalk Braces. *Key Engineering Materials*, Jan., Vol. 302-303: 713-719.

Yazici, H. 2006. The effect of curing conditions on compressive strength of ultra high strength concrete with high volume mineral admixtures. *Building and Environment*, May, Vol. 42, No. 5: 2083-2089.

Yin, J., Zhou, S., Xie, Y., Chen, Y., and Q. Yan. 2002. Investigation on compounding and application of C80–C100 high-performance concrete. *Cement and Concrete Research*, Feb., Vol. 32, No. 2: 173-177.

Zanni, H., Cheyrezy, M., Maret, V., Philippot, S., and P. Nieto. 1996. Investigation of Hydration and Pozzolanic reaction in Reactive Powder Concrete (RPC) Using ^{29}Si NMR. *Cement and Concrete Research*, Jan., Vol. 26, No. 1: 93-100.